Solid Oxide Fuel Cells Operating on Alternative and Renewable Fuels

Final Technical Report

DOE Cooperative Agreement No. DE-NT0004396

Reporting Period:
October 1st, 2008 - September 30th, 2014

Xiaoxing Wang, Wenying Quan, Jing Xiao, Emanuela Peduzzi, Mamoru Fujii, Funxia Sun, Cigdem Sentorun-Shalaby, Yan Li, Chao Xie, Xiaoliang Ma, David Johnson, Jeong Lee, Mark Fedkin, Mark LaBarbera, Debanjan Das, David Thompson, Serguei Lvov (co-PI), and Chunshan Song* (PI)

The Pennsylvania State University

EMS Energy Institute and Department of Energy and Mineral Engineering

C211 CUL, University Park, PA 16802

*E- Mail: csong@psu.edu / Tel: 814-863-4466 / Fax: 814-865-3573

December 31st, 2014

DISCLAIMER

ACKNOWLEDGEMENT

We gratefully acknowledge the support by the United States Department of Energy, National Energy Technology Laboratory under award number DE-NT0004396. We wish to thank Ms Heather Quendenfeld, Director, Power Systems Division; Shailesh Vora, Technology Manager; Mr. Joseph Stoffa, Program Manager; Mr. Travis Shultz, and Mr. Wayne Surdoval.

Table of Contents

A. List of Tables and Figures page

Tables

Figures

B. Executive Summary

This DOE project at the Pennsylvania State University (Penn State) initially involved Siemens Energy, Inc. to (1) develop new fuel processing approaches for using selected alternative and renewable fuels – anaerobic digester gas (ADG) and commercial diesel fuel (with 15 ppm sulfur) – in solid oxide fuel cell (SOFC) power generation systems; and (2) conduct integrated fuel processor – SOFC system tests to evaluate the performance of the fuel processors and overall systems. Siemens Energy Inc. was to provide SOFC system to Penn State for testing. The Siemens work was carried out at Siemens Energy Inc. in Pittsburgh, PA. The unexpected restructuring in Siemens organization, however, led to the elimination of the Siemens Stationary Fuel Cell Division within the company. Unfortunately, this led to the Siemens subcontract with Penn State ending on September 23rd, 2010. SOFC system was never delivered to Penn State. With the assistance of NETL project manager, the Penn State team has since developed a collaborative research with Delphi as the new subcontractor and this work involved the testing of a stack of planar solid oxide fuel cells from Delphi.

The Penn State work was carried out in the EMS Energy Institute involving the faculty members and students in the Department of Energy and Mineral Engineering and the Department of Chemical Engineering and involving collaborative discussion with the Penn State Waste Water Treatment Facility in the Office of Physical Plants. The work at Penn State focused on the development of fuel processors for both ADG and commercial diesel fuels and SOFC tests for integration with SOFC power generation systems. Penn State is responsible for the development of the sorbents for sulfur removal from commercial diesel fuel and ADG, and sulfur-tolerant and carbon-resistant reforming catalysts formulations, testing in lab system, and analyzing the trace level contaminants.

Delphi delivered ten button cells of 1" diameter and two 5-cell stacks instead of 9-cell stack to Penn State for testing on the alternative fuels as planned. The 9-cell stack was replaced by the 5-cell stack due to ease of handling and the fact that there is not a significant difference in the electrochemical properties between the two. Penn State conducted a detailed electrochemical characterization of the Delphi solid oxide fuel cell (SOFC) and stack unit including fuel composition analysis, fuel utilization, air utilization, open circuit voltage, thermal cycle degradation, Electrochemical Impedance Spectroscopy (EIS) analysis on the individual cells as well as the 5-cell stack both under open circuit conditions as well as under power generation regimes, and voltage degradation tests to provide feedback on SOFC operation and further help to optimize the stack design and parameters.

The project achievements are highlighted below:

- The literature review on ADG cleanup technology and diesel reforming in fuel processing for solid oxide fuel cells has been completed and submitted.
- A new flow adsorption system for evaluation of adsorbents/sorbents performance in ADG cleanup has been designed, built and used for the project.
- Commercially available adsorbents including activated carbon from Cabot, HTZ-5 from Haldor Topsoe, SulfaTrap R7 and SulfaTrap R8 adsorbents from the TDA Research and SulfaTreat adsorbent from A Smith/Schlumberger Company have been obtained and evaluated for ADG cleanup from simulated ADG gas containing 200 ppmv H_2S, 10% N_2, 40%

CO_2 and 50% CH_4. It was found that the TDA SulfaTrap R7 adsorbent showed the best performance at room temperature, while at 350 °C HTZ-5 was more effective for sulfur removal. None of them have the capability to remove CO_2 from ADG gas.

- A new mesoporous alumina support (surface area, 244 m^2/g; pore volume, 0.99 cm^3/g; and pore size, 6.5 nm) has been synthesized and used as the support for ZnO adsorbents. The meso-Al_2O_3 supported ZnO showed a better H_2S adsorption capacity than unsupported ZnO and the commercial Al_2O_3 supported ZnO adsorbent.
- A series of metal oxide based adsorbents have been developed for H_2S removal from ADG stream and found that TiO_2-CeO_2 adsorbents were effective for sulfur removal. Further, with the addition of copper oxide, the developed CuO-TiO_2-CeO_2 adsorbent showed much higher sulfur adsorption capacity compared to TiO_2-CeO_2 adsorbent. It was also better than the commercially available adsorbent, TDA SulfaTrap R7, which is the best among the commercial adsorbents studied in this project.
- The developed CuO-TiO_2-CeO_2 adsorbent showed good performance for H_2S removal from simulated ADG stream at room temperature and under atmospheric pressure, which can treat 150 L-ADG/g (i.e., 39.2 mg-S/g or 3.92 wt%) with H_2S concentration reduced from 200 ppmv to less than 10 ppbv. The adsorbent material is regenerable. After 5 cycles of regeneration at 350 °C with air, a sulfur capacity of 3.04 wt% was retained.
- The study showed that the sulfur adsorption performance of the CuO-TiO_2-CeO_2 adsorbent was influenced by the preparation method and procedure, and the adsorbent composition. There may be a synergetic effect on the H_2S adsorption performance for the ternary CuO-TiO_2-CeO_2 adsorbent and the intimate interaction between these three components may play a critical role for achieving high capacity for H_2S adsorption.
- Novel molecular basket sorbents (MBS) have been developed for ADG cleanup on the basis of the concept of "molecular basket", by loading CO_2 and H_2S-philic polymer such as polyethylenimine (PEI) on a nanoporous support, such as SBA-15, and evaluated in the in the flow adsorption system at room temperature using a simulated ADG gas containing 200 ppmv H_2S- 10 v% N_2-40 v% CO_2-50 v% CH_4. It was found that the prepared sorbent can remove both CO_2 and H_2S from the ADG gas and the sorbent is regenerable at 100 °C.
- The characterization showed that at PEI loading below 50 wt%, PEI was completely filled into the mesoporous channels. The addition of PEI can improve the dispersion of the SBA-15 particles. PEI loading higher than 50 wt % resulted in the aggregation of sorbent particles.
- Other molecular basket sorbents (MBS) have been developed using some typical amine compounds including Polyallyamine (PA), polyethylenimine (PEI) and N, N, N′, N′-Tetramethyl-1,6-hexanediamine (TMHD) and evaluated at room temperature and atmospheric pressure. The prepared MBSs are able to adsorb H_2S from 2000 ppmv to below 1 ppmv.
- The effects of amine structure, i.e., primary, secondary and tertiary amine groups, has been studied, the inlet H_2S concentration, adsorption temperature, porous properties of the support and polymer loading were systematically studied in this project. It was also found that the presence of CO_2 can significantly inhibit H_2S sorption over MBS materials.
- Another series of molecular basket sorbents called NH_3-MBS by loading acidic polymer over nanoporous support have been developed for ammonia removal from the ADG gas stream. It was found that the polymer loading has a profound impact on the NH_3 sorption capacity of the NH_3-MBS sorbents.

- Although silica gel could remove siloxane from the ADG gas stream, the novel mesoporous materials such as MCM-41 and SBA-15 are more effective for siloxane removal.
- Based the novel adsorbent developed for deep desulfurization, ammonia adsorption and siloxane removal, a conceptual design of ADG fuel gas processer containing three sorption units is proposed and illustrated.

- More than 40 metal-oxide-based adsorbents and 40 activated carbon materials have been prepared and tested in a batch adsorption system and in the fixed-bed flow adsorption system for their adsorption performance in sulfur removal from a commercial diesel fuel.
- The Ni-adsorbents were prepared by different methods and evaluated in a fixed-bed flow system for adsorptive desulfurization of ultra-low sulfur diesel. The ultrasonic aid in the preparation could improve the performance significantly, by a factor of more than 18. Loading 20 wt% of Ni gave the best sorbent for sulfur removal from liquid low-sulfur diesel.
- The adsorption selectivity of Ni20/MCM-48 adsorbent for different sulfur compounds in ULSD and the possible adsorption mechanism over the Ni-based adsorbents has been investigated. Over Ni-based adsorbents, sulfur compounds are likely adsorbed on the adsorbent surface directly through an interaction between the sulfur atom and the exposed nickel atoms, and a part (~6 %) of the adsorbed sulfur compounds react further with the surface nickel to release the corresponding hydrocarbons. The results also imply that the desulfurization reactivity of the alkyl dibenzothiophenes is dependent on not only the number of alkyl groups, but also the size of the alkyl substituent groups at the 4- and 6-positions of the alkyl dibenzothiophenes.
- The new TiO_2-CeO_2 mixed metal-oxide-based adsorbent has been prepared by using a commercial fumed silica (EH-5) and mesoporous silica including SBA-15, MCM-41 and MCM-48 as a support, and applied for adsorptive desulfurization (ADS) of ultra-low sulfur diesel (ULSD) at room temperature. MCM-48 supported adsorbent showed the best adsorption performance among the supports examined. It was found that both the surface area and the pore structure of the mesoporous silica support influence the adsorption performance of the supported mixed metal oxide adsorbents.
- Through the comparison of the adsorption performance of the 15 wt% CeO_2/MCM-48, 15 TiO_2/MCM-48 and 15 wt% $Ti_{0.9}Ce_{0.1}O_2$/MCM-48, we found that Ce and Ti oxides have a strong synergetic effect on the performance of the Ti-Ce-O/MCM-48 adsorbent.
- We developed a novel air-promoted adsorptive desulfurization (ADS) approach over TiO_2-CeO_2 mixed oxides from ultra-low sulfur diesel (ULSD) at ambient conditions, in which air can significantly promote ADS over TiO_2-CeO_2 mixed oxides from ULSD at room temperature under atmospheric pressure, with 9 fold increase in ADS breakthrough capacity at 1 ppmw-S.
- We have further developed another novel approach for ultra-deep desulfurization of diesel fuel, in which the original fuel was treated by light irradiation before adsorptive desulfurization (ADS) over the TiO_2–CeO_2/MCM-48 adsorbent under ambient conditions. A superior capacity of 95 cm^3-fuel/g-adsorbent (32 times higher than that with the original fuel) was achieved. The promoting effect of light irradiation was likely through in situ peroxides generation in fuel under visible light/sunlight, which may oxidize organosulfur to form strongly adsorbed sulfones over the adsorbent.
- The method for fuel-steam mixing and preheating has been investigated for steam reforming of diesel fuel. It was found that our design using high temperature steam to preheat and

gasify diesel could efficiently avoid early carbon deposition before catalyst bed during diesel steam reforming.

- Several CeO_2-Al_2O_3 supports and Al_2O_3-supported Ni, Ni-Co, Ni-Fe catalysts with or without potassium (K) modification have been prepared and evaluated for steam reforming of commercial diesel with 15 ppmw sulfur at 800 °C. It was found that the addition of K and Co could improve the performance of Ni/Al catalyst. The Ni-Fe catalyst showed better activity and reforming performance than both Ni and Ni-Co catalysts. The addition of iron can promote the resistance to both carbon deposition and sulfur poisoning.
- The prepared catalysts have been characterized by N_2 physisorption method to obtain the BET surface area and pore volume data, and by H_2 temperature programmed reduction method to obtain the reducibility of metals and understand the metal-metal and metal-support interactions. The results indicate that the proper metal-support interaction may play a vital role to achieve high resistance to sulfur poisoning and carbon deposition over Ni based catalyst.
- The spent catalysts after steam reforming of commercial diesel with 15 ppmw sulfur at 800 °C have been analyzed to obtain the carbon deposit information. It showed that the addition of K can significantly suppress the carbon formation. The presence of Co can contribute to carbon formation.
- The prepared catalysts were characterized by sulfur and carbon K-edge XANES, which indicate that the presence of Fe may hinder sulfur adsorption on reforming catalysts, thus improve sulfur tolerance of Ni-Fe catalyst. While the addition of K can enhance the gasification of deposit carbon and therefore reduce the carbon accumulation on the 10Ni-5Fe-5K/Al reforming catalyst.
- A conceptual design of a diesel fuel processor including adsorbent unit and reforming unit for solid oxide fuel cell and will be reported in the next period. In this conceptual design of the diesel fuel processor, it involves two units, i.e., the desulfurization unit and the reforming unit. The air-regenerable TiO_2-CeO_2 mixed oxide adsorbent for deep desulfurization of diesel fuel down to below 1 ppm and the highly carbon-resistant and sulfur-tolerant Fe-Ni based catalyst for diesel steam reforming developed in this project are applied in the desulfurization unit and the reforming unit, respectively.

- A literature review was performed specifically with respect to the issues of fuel cell degradation while operating with hydrocarbon fuels as the basis for analyzing the SOFC performance stability and degradation with the reformed fuels.
- With regards to the development of a lab-scale single SOFC test system, electrochemical impedance spectroscopy (EIS) analysis was tuned for detailed *in situ* MEA degradation studies and the technical solution for mounting and sealing the single ring cells for the electrochemical testing was optimized.
- A new technique, Electrochemical Frequency Modulation (EFM) has been applied as a preliminary trial to study kinetic effects and estimate kinetic parameters on the SOFC stack.
- The results from EFM technique have been compared with EIS, LSV and LPR (Linear Polarization Resistance) to make a comparative treatment of the obtained data and used to estimate the extent of accuracy and deviation between values from the three methods.
- It was observed that the values from the above mentioned techniques were close to each other and were of the same order of magnitude.

- Delphi has completed the two tests on 2 Delphi Gen 4 Stacks using the five fuel conditions agreed upon by Delphi and Penn State.
- One year of daily Anaerobic Digester Gas volumetric production data has been obtained from Penn State's Waste Water Treatment Plant.
- The technical progress review meetings with DOE project manager, Mr. Joseph Stoffa, were held at Penn State on July 7, 2010, and July 31st, 2013, respectively.
- With the support of this project, 9 graduate and 1 undergraduate students and 6 research associates/assistants have been educated and/or benefited from the project research on fuel processing and fuel cell technologies.
- The research of this project has generated 20 referred journal publications and 9 conference papers, with more manuscripts in the chain of publication.

C. Introduction

This DOE research project entitled "Solid Oxide Fuel Cells Operating on alternative and Renewable Fuels" was formally established at Penn State late in October 2008 including a subcontract to Siemens Energy Inc. However, the internal restructuring within Siemens led to the elimination of the Siemens Stationary Fuel Cell Division in the US. Unfortunately, this led to the Siemens subcontract with Penn State ending on September 23, 2010. With the help of DOE management, Penn State then actively searched the industrial partner and teamed up with Delphi to develop a collaborative research project involving testing of a commercial stack of planar solid oxide fuel cells. The PSU research team and Delphi team had a project kick-off teleconference on Aug 3rd, 2012 to discuss the project tasks, timeline and milestones and agreed to have regular teleconference every month.

The objectives of this DOE project at the Pennsylvania State University (Penn State) involving the industrial partner Delphi are: 1) to develop new fuel processing approaches for using selected alternative and renewable fuels – anaerobic digester gas (ADG) and commercial diesel fuel (with 15 ppm sulfur) – in solid oxide fuel cell (SOFC) power generation systems; and 2) to conduct integrated fuel processor –SOFC system tests to evaluate the performance of the fuel processors and overall systems. With the Delphi team joining the project the work is to demonstrate the feasibility of integrated fuel processor-solid oxide fuel cell system using diesel fuel and bio-gas fuel for electrical power generation in support of DOE SECA program mission.

After detailed discussions between Delphi and Penn State, it was finalized that instead of the initially proposed 9-cell stack, a 5-cell stack will be tested and analyzed at PSU. This was mainly due to that a 5-cell stack is much lighter and easier to handle. In terms of technical details, they do not have much difference except the fact that a 5-cell stack has a lower OCP of about 5 V. A 5-cell debug stack was sent to PSU, to first check on the testing procedures, systems and experimental setup before working with the actual SOFC stack. Delphi team has conducted two Gen 4 Stack tests under the conditions agreed upon by Penn State and Delphi. The five typical fuel compositions covering the possible fuel compositions of ADG reformate and diesel fuel reformate after the ADG and Diesel fuel processors were applied for testing. The results from these tests have been summarized and compared in this report.

The work at Penn State EMS Energy Institute focused on the development of fuel processors for both ADG and commercial diesel fuels, respectively, for integration with Siemens SOFC power generation systems, and Penn State team is responsible for the development of the sorbents and reforming catalysts formulations, testing in lab system, analyzing the trace level contaminants focusing on fuel processing processor for ADG and commercial diesel fuel. Penn State has developed several novel metal oxide based adsorbents for deep sulfur removal from both ADG gas and commercial diesel (10 ppb-S for ADG and 1 ppmw-S for commercial diesel) and novel polymeric sorbents for the removal of CO_2 and H_2S. The developed adsorbents are effective and efficient for sulfur removal, exhibited much better performance than the commercially available adsorbents selected and evaluated in this project. Novel approaches for deep desulfurization of diesel fuel using air promotion and/or light-irradiation have been proposed. It was also demonstrated that iron-Ni catalyst was effective for steam reforming of diesel fuel with high sulfur-tolerance and carbon-resistance. In addition, PSU team has performed Electrochemical Impedance Spectroscopy (EIS) analysis on the individual cells as well as the 5-cell stack both under open circuit conditions as well as under power generation regimes.

The details on the technical progress are provided as follows.

D. Technical Progress

1. Research and Development for Alternative Fuel Processing

1.1. Development of Single SOFC Testing System

In preparation for the routine SOFC testing required to validate the cleaning and reforming methods, lab scale test equipment has been ordered, and the main components of the system are being designed. The single SOFC studies include measurements of fuel cell performance, durability, and degradation. In addition to voltage-current response, electrochemical impedance spectroscopy (EIS) is considered a key technique of SOFC characterization in this study.

Electrochemical impedance spectroscopy can be utilized for the investigation of double-layer capacitance, electrode processes and complex interfaces in various electrochemical systems [1]. Electrochemical impedance is determined by the response of electrochemical cell to a small sinusoidal AC amplitude. The current signal resulting from the applied AC potential can be measured and will be a sinusoid at equivalent frequency in shifted phase [2].

In detail [2-3], the sinusoidal potential can be expressed as,

$$E = E_o \sin(\omega t) \quad (1)$$

where E_o is the amplitude of the signal and ω is angular frequency (i.e. 2π times conventional frequency). The current signal as a response is given by

$$I = I_o \sin(\omega t + \phi) \quad (2)$$

where ϕ is phase angle separated between potential and signal phase.
The potential can be written as a sum of potential drop across the resistor and capacitor,

$$E = E_R + E_C \quad (3)$$

where E_R and E_C are potential drops, respectively, in the resistor and capacitor.
Here, E_C can be expressed using complex function as,

$$E_C = -jX_C I \quad (4)$$

where Xc is the capacitive reactance ($1/\omega C$).
Thus, E can be represented as

$$E = I (R - jX_C) \quad (5)$$

$$E = I \mathbf{Z} \quad (6)$$

A vector $\mathbf{Z}$ ($= R - jX_C$) is called *impedance* which is composed of both real and imaginary parts of impedance and is rewritten as

$$\mathbf{Z} = Z_{Re} - jZ_{im} \quad (7)$$

where Z_{Re} and Z_{im} represent IR and IX_C, respectively.

These impedance measurements of the electrochemical systems allow for differentiating the contributions from a series of processes in the cell including charge transfer (electrode kinetics), electrolyte and mass transfer resistances [4]. Polarization measurements (i.e. current-voltage measurements) are commonly used for electrochemical characterization and can be useful in the evaluation of the fuel cell performance; with time these results can monitor the performance degradation. However, polarization measurements are unable to provide insight on the extent of individual effects of each process in the cell on polarization behavior. With this regard, AC impedance spectroscopy results in parallel with the polarization analysis of the cell are required to better understand the mechanism and microscopic information of electrochemical system.

The characteristics of an electrochemical system can be represented by an equivalent electrical circuit. The system can be regarded as simple impedance to sinusoidal perturbation. The equivalent circuit consists of two classes of elements according to the dependence on frequency. The frequency independent elements can be composed of resistance, inductance, and capacitance whereas the frequency dependent elements include Warburg elements and constant-phase elements. Warburg elements represent the resistance to mass transfer and constant-phase elements represent the circuit elements that show a constant phase angle [5]. By establishing an equivalent circuit that models the electrochemical cell, the specific components that comprise the system can be identified. It is noted that the impedance analysis can offer valuable information on the interface between electrolyte and catalyst, component structure, and reaction kinetics which are necessary for catching the mechanism of possible degradation of the solid oxide fuel cell operating on hydrocarbon based fuels.

There were a number of studies with EIS used for monitoring of the SOFC performance. EIS regarded as a powerful technique for cell life and degradation studies [6, 7]. Also it was used for examination of electrode kinetics [8], allowing differentiation between the anode and cathode performances, and also for studying response of the SOFC to changes of experimental variables, such as fuel or oxygen partial pressures [9]. One of the critical steps in applying EIS is data interpretation via circuit modeling. The impedance spectra can be fitted to an equivalent circuit composed of a series of resistances, inductance and frequency dependent elements. In the spectra of Nyquist plots (Z_{imag} vs. Z_{real}) obtained by impedance measurements, the arcs generated in low frequency region (0.1-100 Hz) represent diffusion and gas conversion, while the arcs measured in high frequency region (100-10K Hz) are associated with the electrode polarization resistance in the anode and cathode processes and the intercept at high frequency is determined by the resistance of electrolyte and interface between the electrodes and electrolyte. The electrode polarization resistance indicates the anode and cathode polarization loss and reaction kinetics. Thus, the possible degradation in SOFC electrodes during long term fuel cell test can be monitored by impedance measurements with respect to the change in the electrode kinetics and diffusion resistance as a function of time [10,11]. Furthermore, it is known that different frequency region in the impedance spectra can indicate the reaction mechanism in the cell. The high frequency spectrum is ascribed to the charge transfer of oxide ions from the interface between electrode and electrolyte to the vacancies in the electrolyte. The spectra observed at the medium and low frequencies can be attributed to dissociation of oxide ions and diffusion of oxide ions to the electrode/electrolyte interface [12,13]. The differentiation of each anode and cathode characteristics can be also feasible using different cell configurations where a symmetric

cell (e.g. cathode/electrolyte/cathode) or a thick electrolyte half cell (cathode/electrolyte/Pt) can be constructed for characterization [14,15].

The currently designed SOFC button cell tests was performed with the NextCell™ samples (Fuel Cell Materials), 20-mm in diameter. The sample cells are based on 120-μm thick YSZ electrolyte support with applied electrodes 12.5 mm in diameter which provided the electrode area of 1.23 cm^2 on both anode and cathode sides. The cathode material is represented by the lanthanum strontium manganite (LSM), and the anode material is represented by the nickel-YSZ cermet (**Figure 1a**). Each of the electrode layers is ~50 μm in thickness. As current collectors, gold wire coil was attached onto the anode with gold ink, and a platinum mesh with platinum wire was attached onto the cathode with platinum ink, and the cell was sintered at 850 °C for 1 hour. For the test, the cell was mounted on an alumina tube using CAP-552 SOFC sealing paste (Fuel Cell Materials Inc.), anode positioned towards inside the tube, and the whole assembly was step-cured at 93 and 260 °C for 2 hours at each temperature. The mounted cell (**Figure 1b**) was installed in a tube furnace. These standard-component cells are convenient options for reference performance tests. We will be able to compare the obtained performance characteristics with the manufacturer's calibrations. This approach would allow us to ensure the proper operation of the experimental system before testing the reformed fuels.

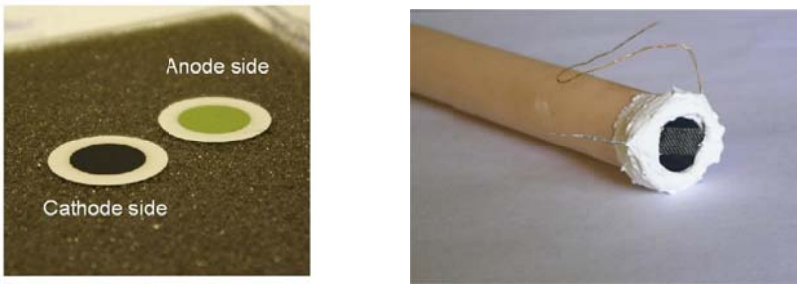

(a) (b)

Figure 1. SOFC samples: (a) button cells; (b) with attached electrodes and mounted on the alumina tube.

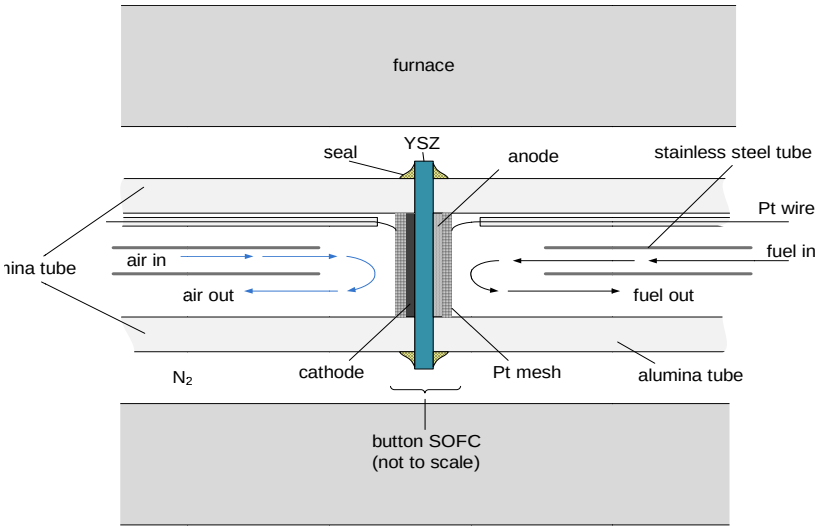

Figure 2. Design of the button SOFC fixture.

For the performance tests, a special fixture to accommodate the button SOFC in the furnace is being designed (**Figure 2**). A button cell will be sealed between the two alumina tubes using a gas-tight ceramic sealant (**Figure 1b**). The separate tube channels are designed to provide the maximum separation of the cathodic and anodic feed gases. The Pt mesh attached to each side of the button cell serves as a current collector, and the attached Pt leads are insulated using ceramic straws. The designed fixture should allow precise control of both fuel gas and air flow rates. Nitrogen gas is used to provide the background atmosphere.

The first SOFC tests were run with two types of reference fuels to experimentally simulate the above-mentioned boundary conditions: (1) H_2/N_2 (1:1) gas mixture and pure H_2 and (2) ethanol-water (1:1) blend as an example of unreformed liquid fuel. When directly utilized in SOFC with Ni-YSZ anodes, ethanol fuel is known to cause carbon deposition and consequent cell degradation, but this process can be suppressed by mixing ethanol with water [16-18]. It is inferred that operating temperature for ethanol-fueled SOFC may be an important tuning factor, since, on one hand, it controls the kinetics of the in-situ reforming reaction (more efficient conversion at higher temperature) [16], but, on the other hand, affects carbon deposition (less deposit at lower temperature) [19]. The cell was conditioned by running H_2/N_2 gas mixture and pure H_2 as fuels for 24 hours. Humidified air was supplied to the cathode side of the cell at a flow rate of 128 ml/min through a coiled capillary. Open circuit potential (OCP) measurements and performance tests were carried out repeatedly to check the cell functionality at three temperatures 650, 750, and 850 ^{o}C and ambient pressure. Electrochemical impedance spectroscopy (EIS) measurements were carried out using a Gamry Instruments Reference 600 Potentiostat /Galvanostat/ZRA to determine the ohmic resistance of the cell as well as variations in polarization resistances over time depending on temperature and type of fuel. The OCP values measured for different types of reference fuels are listed in **Table 1**.

Table 1. Open circuit potential (OCP) in volts of SOFC operated with different fuels as a function of temperature.

Temperature, ^{o}C	650	750	850
H_2/N_2 (1:1)	0.954	0.959	0.957
Ethanol-Water (1:1)	0.692	0.902	0.951

The OCP measured for higher temperatures are consistent with the values reported in the literature [16] for both ethanol water blend as well as hydrogen operating on a similar test apparatus at 800 ^{o}C. The OCP values for the ethanol-fueled SOFC approach the values obtained with hydrogen as the temperature is increased, which probably indicates more complete internal reforming of ethanol at higher temperatures. The electrochemical impedance spectra were taken in a region of high frequencies for the SOFC under open circuit conditions at different temperatures. Some of the EIS data for hydrogen gas and ethanol-water mixture as fuels are demonstrated in **Figures 3** and **4**, respectively.

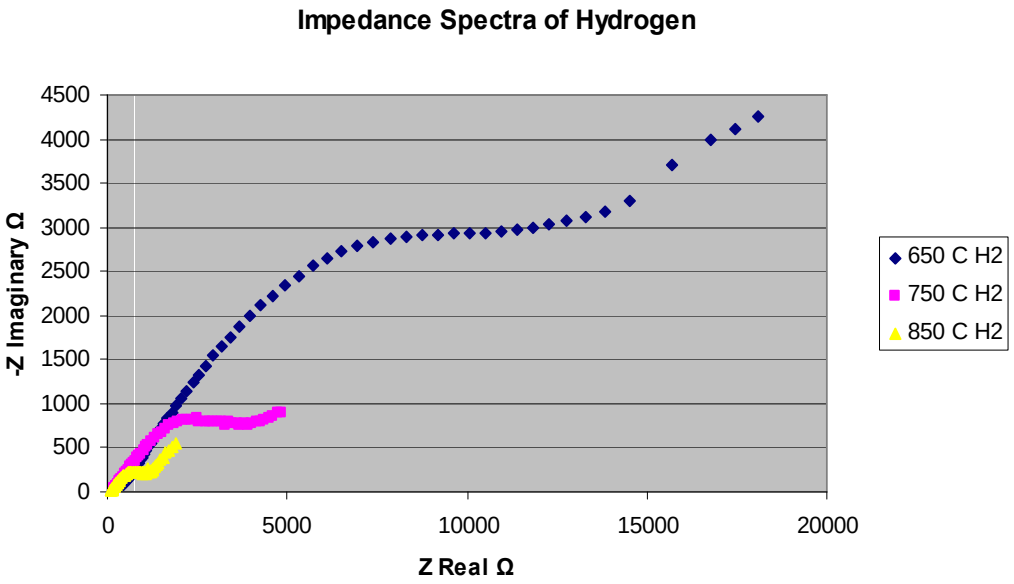

Figure 3. Electrochemical impedance spectra obtained for button SOFC operated under open circuit conditions with the reference hydrogen fuel at different temperatures.

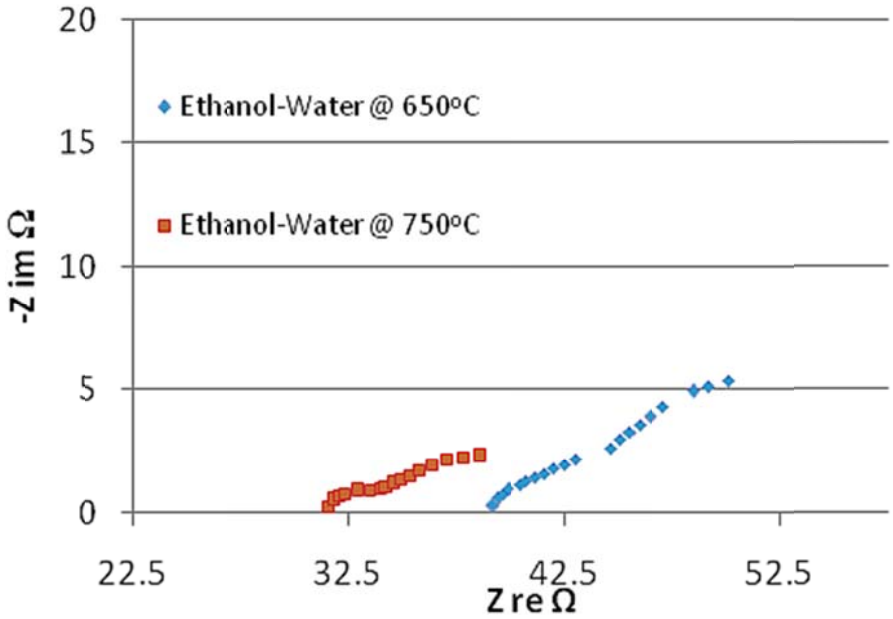

Figure 4. Electrochemical impedance spectra obtained for button SOFC operated under open circuit conditions with ethanol-water (1:1) mixture as a fuel at different temperatures.

From the obtained spectra, the ohmic resistances of the button cell were determined to be 39.1 and 31.4 ohm at 650 and 750 ^{o}C, respectively. The observed drop in the total cell resistance is due to the higher conductivity of the YSZ electrolyte. The polarization resistance of the SOFC operated with ethanol-water mixture was determined to be approximately 25 and 15 ohm at 650 and 750 ^{o}C, respectively. This tendency of decreasing the polarization resistance with increasing temperature probably indicates faster kinetics of ethanol transport at the anode, which can be in

part a result of internal reforming of ethanol to H_2-containing gaseous mixture. Traces of carbon deposited inside the fuel tube were observed after the experiment; however, the duration of the first test was relatively short.

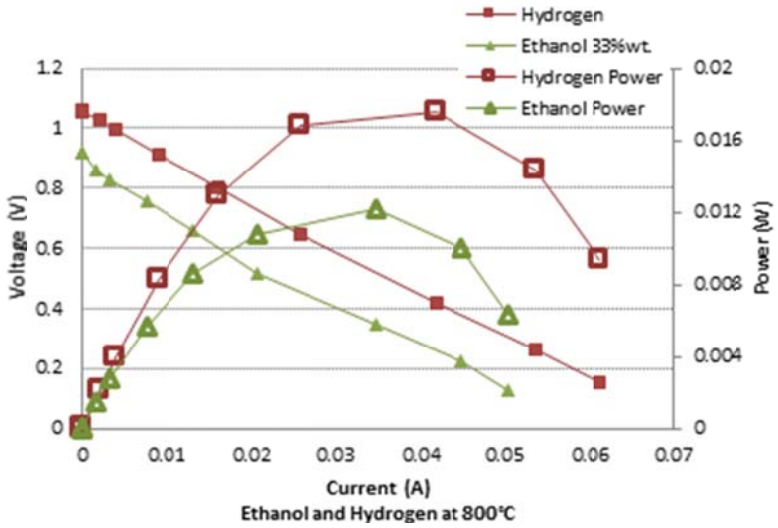

Figure 5. Polarization curves for button SOFC samples operated with hydrogen and ethanol/water fuels at 800 °C.

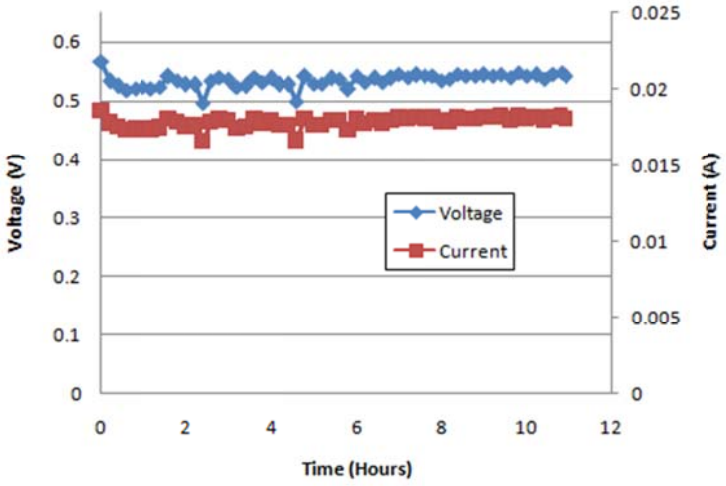

Figure 6. Performance versus time data for button SOFC operated with ethanol/water blend fuel at 800 °C.

The polarization tests were performed to compare the voltage and current produced from hydrogen and ethanol/water blend fuels. The ethanol mixture was injected via a syringe pump into N_2 gas flow (33% fuel by mass). The polarization tests were carried out at 800°C and ambient pressures. The ethanol water blend was supplied at 30 µl/min. Comparison of the polarization curves is displayed in **Figure 5**. The SOFC performance with ethanol/water fuel was monitored over time at 800 ^{o}C to study possible degradation patterns. The test illustrated in **Figure 6** was continued over 12 hours, and no significant degradation of the cell performance was observed. The durability test had to be terminated because of loss of contact.

EIS tests are conducted as an important part of degradation study. Both traditional equivalent circuit modeling and distribution function of relaxation times [20, 21], which was proved to be very efficient in distinguishing different polarization losses are involved as analytical methods for EIS data treatment. The following resistance components are considered as potential contributors to performance degradation:

R_o – Ohmic resistance of the YSZ electrolyte layer. This component is expected to be low due to small thickness and to remain relatively constant over time.

R_A – Anode polarization resistance (total), which would include

R_{A1} – fuel gas diffusion polarization will depend on the porosity of the anode substrate and will be substantially affected by carbon deposition

R_{A2} – charge transfer polarization at the triple-phase boundary and ion transport in the Ni-cermet structure

R_C – Cathode polarization losses due to ionic transport and charge transfer kinetics in the LSM structure.

For both electrodes, monitoring of these polarization resistances would be beneficial to reveal the impact of the alternative fuels (reformed or unreformed) and fuel impurities on the structure, porosity, reactivity (poisoning), and conductivity of the cathode and anode.

In this project, two methods have been refined for the preparation and operation of SOFC button cells. The main goal of both techniques is to provide an intimate electrical contact between each electrode of the cell with the current collectors and to minimize ohmic losses during power generation. We have discussed these methods with well-known experts from the University of Pennsylvania, Dr. J.M. Vohs and R.J. Gorte, who have substantial experience in preparing and analyzing the SOFC button cells. The particular issues of interest were (1) the development of SOFC MEA preparation, (2) exploring the technique for proper current collection from the SOFC cell, (3) analysis of electrochemical impedance spectroscopy data.

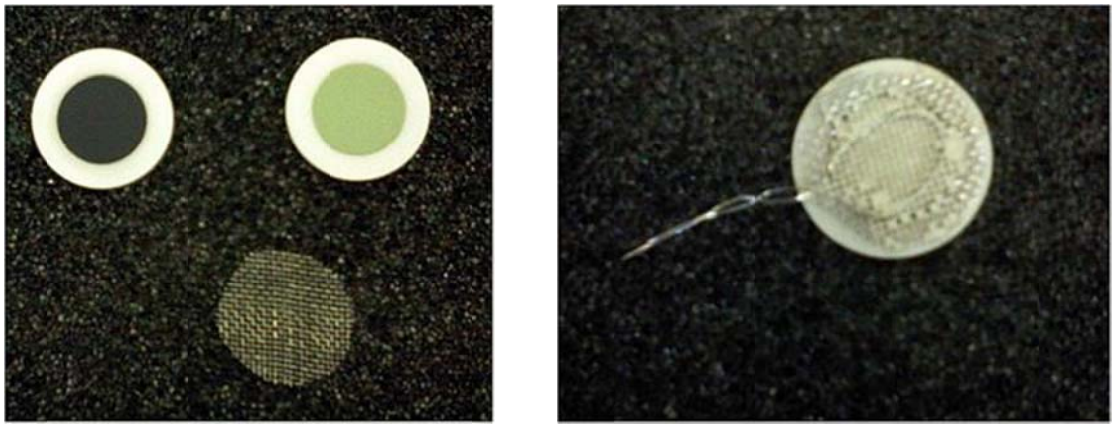

Figure 7. (Left) SOFC cathode, anode and current collector and (right) assembled SOFC button cell with current collector.

In the second method, recommended by the Fuel Cell Materials (FCM) company, the vendor for the used button SOFC samples required nickel leads, nickel current collector, and separate anode and cathode pastes for incorporating the current collector into the electrodes: Ni paste for the anode, lanthanum strontium manganite for the cathode. The nickel materials were obtained from Alfa Aesar: 0.25mm diameter, annealed, 99.98% nickel wire; 40-mesh 0.13mm diameter wire, nickel gauze. The anode paste supplied by FCM was a high purity Ni powder in a

terpineol vehicle. The cathode paste supplied by FCM was comprised of lanthanum oxide, manganese oxide, and strontium oxide powders in a terpineol vehicle. Both the nickel and LSM pastes are applied and cured individually. First the cathode has just enough LSM applied to coat the active area of the cell and provide solid contact the with the current collector; then LSM paste requires a very specific curing process to ensure proper annealing of LSM paste into the LSM cathode as well as proper porosity; the LSM paste is annealed by raising the temperature from 0-500 ^{o}C at 2 ^{o}C/min; then heating from 500-1000 ^{o}C at 3 ^{o}C/min; the cell is held at 1000 ^{o}C for 1 hour then allowed to cool to room temperature at 5 ^{o}C/min. The nickel paste is applied in a similar manner however it is only dried for 1 hour at 100 ^{o}C (final curing and reduction of nickel paste occurs after the cell is attached to the alumna tube and heated for operation).

The bench scale horizontal tube furnace system, Arbin Instruments fuel cell test station, and Solartron Analytical impedance spectroscopy systems were used to verify the performance of button SOFCs prepared by both techniques. The performance of each MEA was evaluated by open circuit potential, polarization curve (cell voltage vs. current density), limiting current density, area specific resistance, and impedance spectroscopy. The results are shown in **Figure 8**, with all the performance parameters labeled on the figure. The performance is shown to be similar to previously reported data in the Journal of the Electrochemical Society, by S. McIntosh, J.M. Vohs, and R.J. Gorte [22] (**Figure 9**).

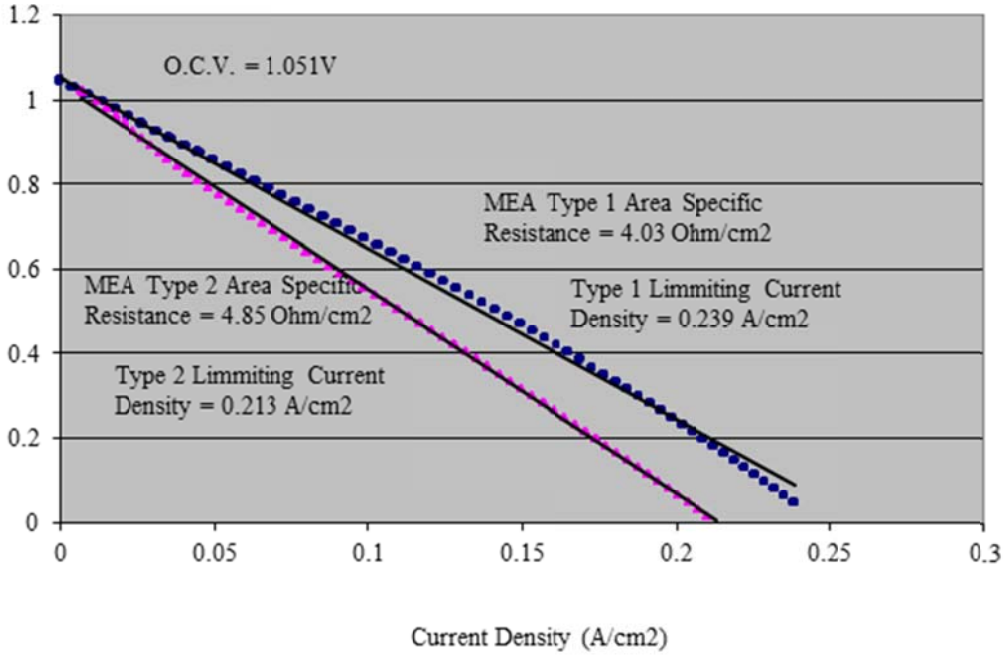

Figure 8. Polarization curves for both SOFC prepared by Method 1 (circles) and Method 2 (triangles) operating at 850 ^{o}C with 50 sccm humidified H_2.

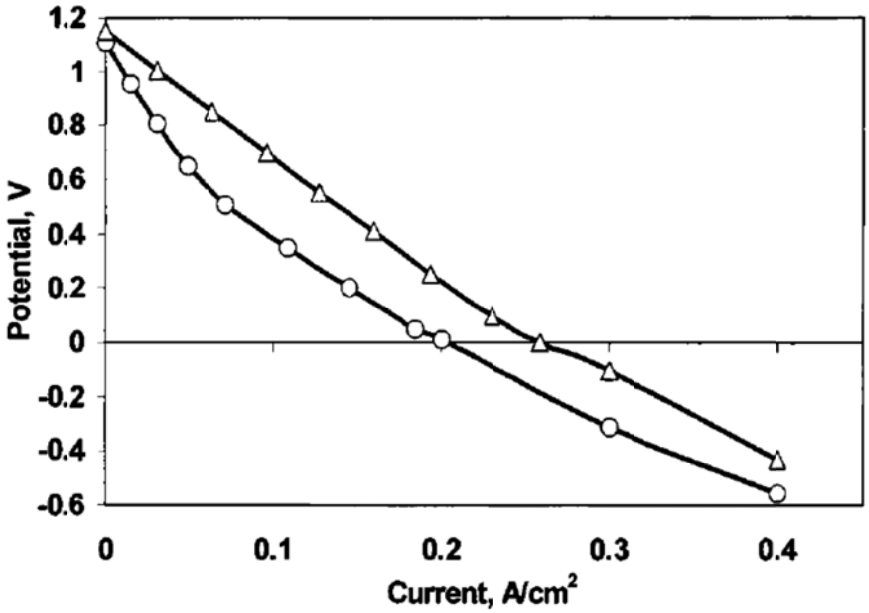

Figure 9. Polarization curves of SOFC button cells operating on H_2 and butane fuels at 983K according to McIntosh, et al. (2003) [22].

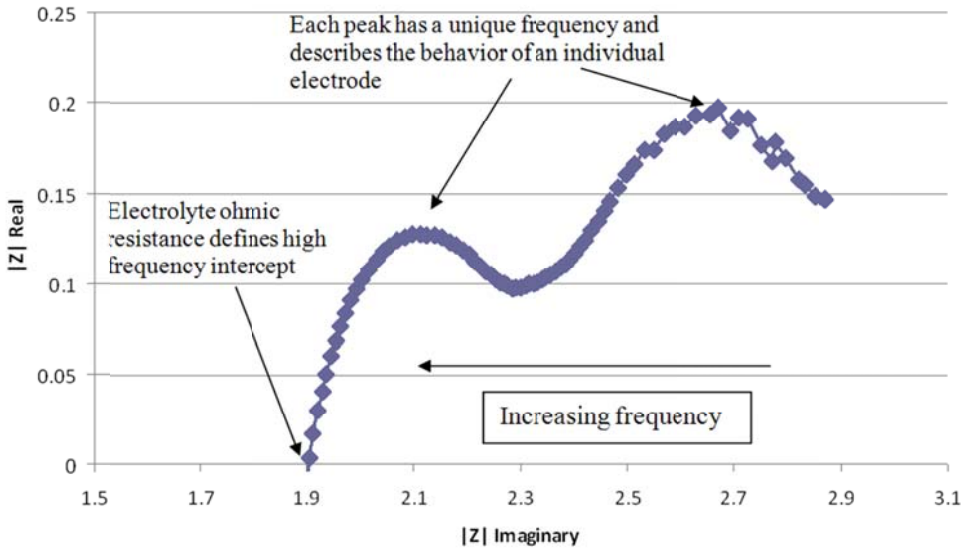

Figure 10. Electrochemical Impedance Spectrum (Nyquist Plot) for the button SOFC assembly prepared via Method 1 operating at 850 ^{o}C with 50 sccm humidified H_2.

An electrochemical impedance spectrum (Nyquist plot) obtained for the SOFC test with H_2 reference fuel is illustrated in **Figure 10**. The experiment to generate the Nyquist plot is to apply an alternating voltage in the system and monitor the current response, this response has a characteristic time delay; this time delay is a function of the frequency of the applied potential. From these measurements impedance is split into both real and imaginary components and plotted against each other to form the Nyquist plot. This data can be used to generate equivalent circuit data for the modeling and monitoring of the cell in operation.

Figure 11a is the Nyquist plot displaying the monitored dynamic current in response to a variety of frequency potential oscillations around a potential of OCV of 200 mV. This allows us to distinguish the real and imaginary parts of the electrical impedance and ultimately to monitor the behavior of each electrode in a nondestructive *in situ* test. Then, by applying a circuit model to the data generated from the Nyquist plot we can isolate the MEA Ohmic resistance to ion transfer, as well as the charge transfer resistances of the anode and cathode independently. As demonstrated in **Figure 11b**, a mathematical model of the Nyquist plot shows a strong correlation to the cells Nyquist behavior presented in **Figure 11a**. In this model there are three intercepts with the x-axis: from left to right (or low to high real impedance) the first intercept is the impedance reading as the frequency approaches infinity, this measures the Ohmic resistance of the membrane to oxygen ions only; the distance between the first and second intercept shows the charge transfer resistance occurring at one of the two electrodes; the distance between the second and third intercept (this being very low frequency) is the charge transfer resistance of the other electrode. Distinguishing which electrode is which need only be done once and can be determined by running the test with considerably different concentrations or compositions of fuel, the arc that grows or shrinks is the anode. The location of the 3rd intercept (or the sum of the aforementioned three resistances) is exactly the slope of the polarization curve at the tested current density. This approach is based on the Kramers-Kronig method of data analysis and utilizes a 2-component Voigt electrical model; so long as the polarization curve is linear in the immediate neighborhood of the current density the theory holds; as evident in **Figure 11b** the polarization behavior of a SOFC is almost always linear. The data fitting here is carried out by complex non-linear least square techniques, which have shown very accurate results, specifically, when using reliable software such as Z-view.

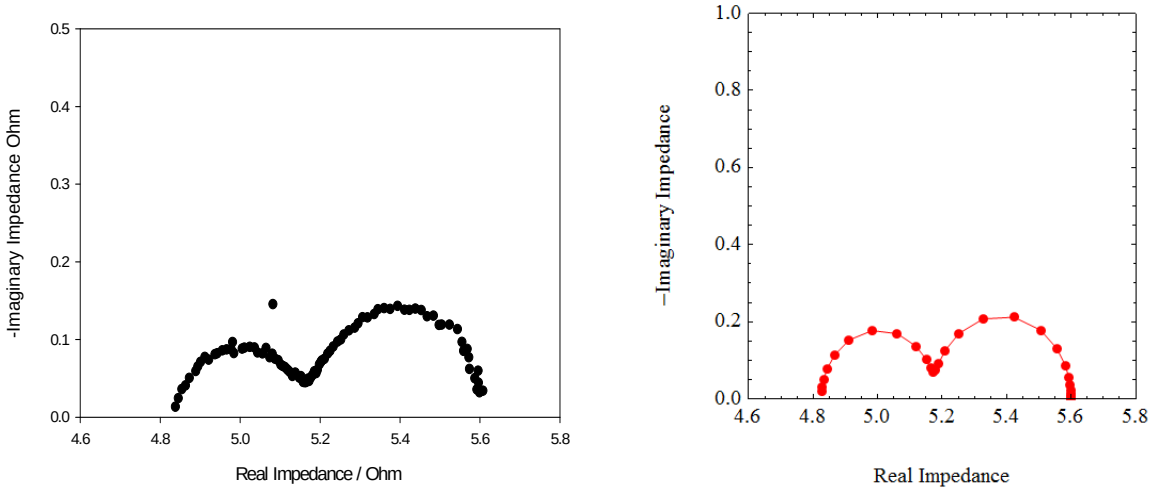

(a) (b)

Figure 11. (a) Nyquist plot of SOFC generating power at OCP of 200 mV under hydrogen, and (b) Nyquist plot of a circuit model used in data analysis.

An EIS test is carried out at OCV of 200 mV to determine the behavior of each electrode operating on the reformate fuel, the polarization data for the SOFC operating under ethanol and water fuel is shown in **Figure 12**. To simulate the degradation expected in a large-scale SOFC system, our cell is then allowed to generate power at or near its maximum power density for several hours and days with periodic EIS testing (this testing does not interrupt the generation of

power). By monitoring the change in EIS results with time and properly analyzing the data we can gain a more detailed view into the nature of possible cell degradation.

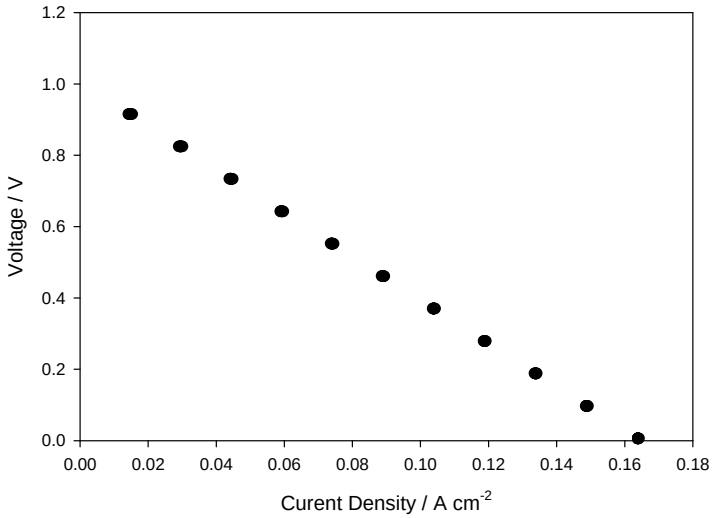

Figure 12. Polarization Curve for SOFC Operating on Ethanol-Water Model Reformate.

1.2. Single SOFC Performance and Degradation Tests on Alternative Fuels

1.2.1 Experimental

SOFC Test Setup

The SOFC setup is a dual flow system, involving two gas inputs: fuel and oxidant into the separated cathode and the anode chambers. The anode side of the SOFC cell is connected to the fuel flow, which includes humidified hydrogen and carbon dioxide. The cathode side is connected to the oxidant supply, which is mainly air (79 % N_2 + 21 % O_2). The solid oxide fuel cells for these experiments are NextCell^{TM} electrolyte supported button cells (Fuel Cell Materials). The membrane electrode assembly (MEA) is supported by a dense 150 micron YSZ (8 mol. % yttria-stabilized zirconia) membrane, supporting a porous 50 micron Ni-YSZ anode, and a porous 50 micron LSM cathode.

The fuel cell setup comprises of two alumina tubes of different diameter and length. The shorter and thinner alumina tube is used for mounting the SOFC cell with the anode side facing towards the inside of the tube. The cell is mounted using a high-temperature alumina cement (Aremco Ceramabond^{TM} 552 High Temperature Ceramic adhesive). The larger and longer diameter alumina tube spans across the entire length of the horizontal tube furnace and allows the air to flow into the concentric system from the other end towards the cathode side of the button cell mounted on the smaller alumina tube (**Figure 13**). Insulation materials like glass wool are provided on both ends of the furnace to maintain steady operating temperature inside the tube furnace and minimize heat loss from the system.

The Membrane Electrode Assembly (MEA) is prepared through the following approach. A very thin film of silver paste is applied on both electrodes the anode and cathode and acts as the current collector serving the purpose of an interconnect in an SOFC stack. Circular gold wires are spot-welded on to the electrode surfaces and connected to silver wires long enough which act as leads and therefore are connected to the Solartron electrochemical test station for further data recording, treatment, and analysis.

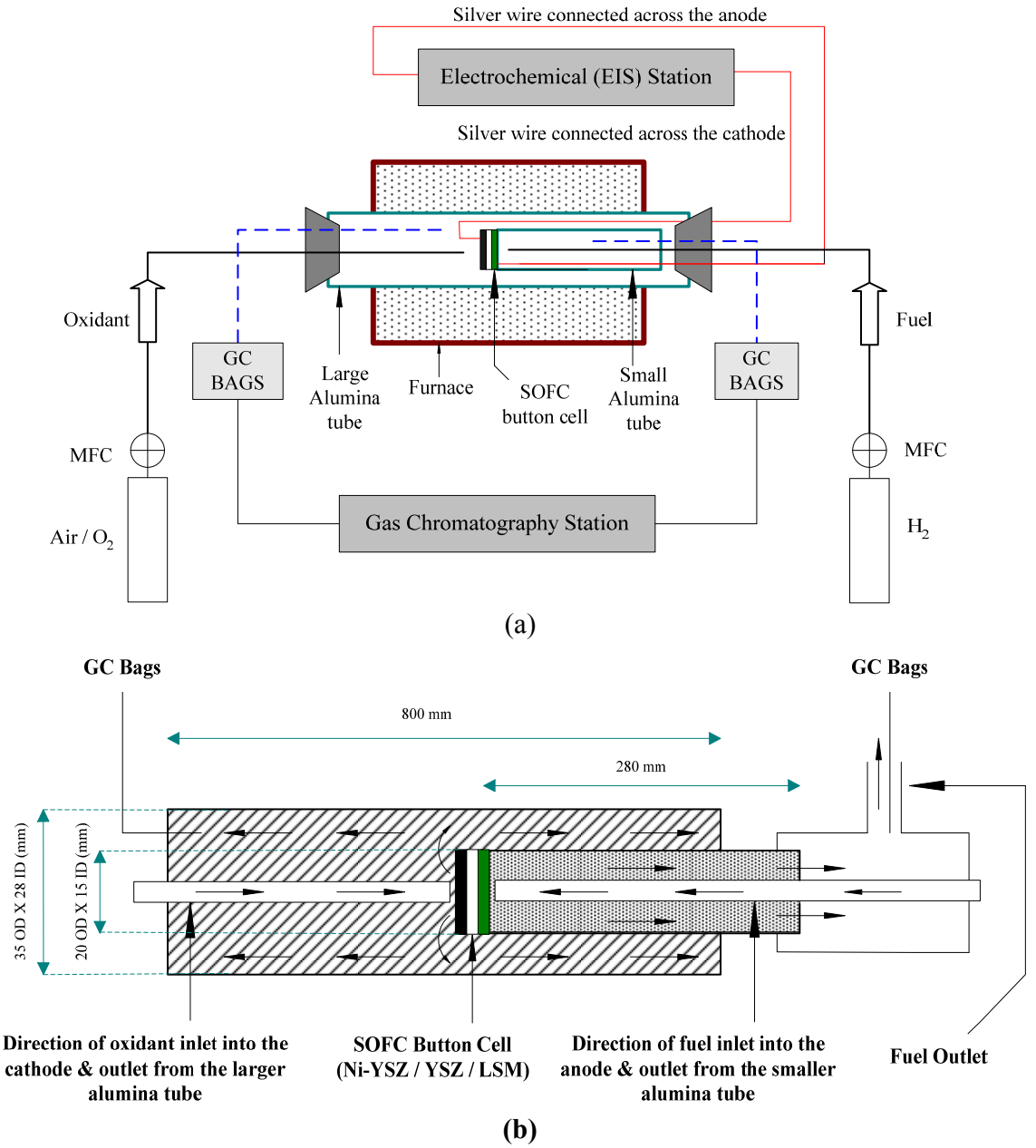

Figure 13. (a) Experimental Setup of the Single-SOFC Testing System; (b) Magnified View of the Cell Assembly Showing the Gas Flow Directions in and out of the System.

Test Procedure and Equipment

A Solartron Analytical 1470E Cell Test System Potentiostat and Solartron Analytical 1252A Frequency Response Analyzer operated via Cell Test software is used to control all electrical testing carried out in this study. An Arbin Instruments Fuel Cell Test Station controls the system's flow rates, pressures, and humidification. A Barnstead Thermolyne 21100 tubular furnace is employed in this study to control the operating temperature with the help of a thermocouple inserted into one of the ends of the furnace. The experimental temperature is maintained at 900 °C with a precision of ± 1.0 °C and ambient air is used for SOFC cathode. The

heating of the fuel cell system is carried out from room temperature to 900 °C at a rate of 10 °C min^{-1} under 50 cm^3s^{-1} argon anode flow. Another important point worth noting is that the EIS & Polarization equipment, which is currently in the lab, has a maximum voltage measurement range of 10 V and maximum current measurement range of 4 A.

GC sampling bags will be used to collect the gas samples from exhaust lines of the fuel and oxidant outlet. The samples will be analyzed by gas chromatography (GC) to quantify the amount of fuel and oxidant utilization in the anode and cathode side electrochemical reaction respectively. If possible perhaps after testing with initial apparatus, a high temperature zirconia oxygen sensor could also be used to estimate the concentration of oxygen inside the larger diameter tube to evaluate the difference on oxygen concentration in the oxidant after the electrochemical reaction takes place at the cathode.

The sold oxide fuel cells used in these experiments were NextCell-B button cells with 1.256 cm^2 active area (Fuel Cell Materials). The SOFC membranes in these cells were 150 μm dense yttria stabilized zirconia (YSZ), 8 mol. % yttria. The anode layer was a porous 50 μm nickel-YSZ cermet, and the cathode layer was a porous 50 μm lanthanum strontium manganite (LSM).

For the recent tests, the SOFC membrane electrode assemblies were prepared in the following manner. A 99.99 % purity gold wire (Alfa-Aesar), used as current collector, was adhered to both the anode and cathode sides of the button cell by covering the wire and electrode with a silver paste (SPI supplies). The SOFC was then pasted onto an alumina tube using Armeco ceramabond, alumina paste, with the anode side facing into the tube. This method so far provided the most efficient contact between the electrode and current collector.

Control and analysis software and data logging

System software which are Cell Test (EIS System) and MITS Pro 5.0 (Arbin gas flow system); compatible to the equipment used, are installed in the setup computer which provide real time intuitive control of the testing system. These software packages provides real time indications of all the measured parameters and allow plotting of cell voltage, current and impedance data obtained directly from the fuel cell stack. Real time variable monitoring and control is very important because it will allow us to have quick access to useful information and thus estimate any discrepancies in the parameters of a particular ongoing experiment. ZView, an EIS analysis software from Scribner Associates, will also be used at the post-experimental stage, for further EIS equivalent circuit modeling, fitting and simulation of both individual and the Delphi SOFC stack.

Electrochemical characterization – EIS testing and modeling

To measure the effects of the internal processes occurring within a solid oxide fuel cell is a difficult and arduous task. Hence, modeling and simulation provides a valuable capability of predicting cell performance and understanding how it is influenced by external factors such as the flow rate of fuel and oxidant streams, the stoichiometric composition of both streams, variation in temperature, or changes in the electrical current drawn from the cell.

As a first step towards the project, a literature review has been completed on electrochemical impedance spectroscopy and its application to solid oxide fuel cells to extract the key parameters. The experimentally obtained data will be modeled using the commercially available ZView software V3.2c. The data will be tested with Kramers-Kronig transformations to check for internal consistency and further analysis will be done to account for degradation

over long periods of time. Equivalent circuit modeling approach will be used for treating the data where the distributed parameters will account for the different physical processes controlling the system. Sensitivity analysis will be conducted by varying decision variables such as cell area, thickness of channels, interconnects etc. This process of optimization is expected to indicate a clear trade-off between compactness and temperature, which is directly related to degradation. Identification and quantification of key processes in the fuel cell stack, such as gas diffusion, oxygen surface exchange kinetics and O^{2-} diffusivity in cathode, gas diffusion in anode, charge transfer reaction and ionic transport, is critical to the overall impedance analysis.

1.2.2 Test results

1.2.2.1 Test results on single SOFC

A Ni-YSZ anode SOFC button cell fueled with pure ADG is used to generate electrical power in **Figure 14**. Stable power generation was observed for greater than 80 hours. The initial increasing power density is a result of the membrane electrode assembly preparation method. This power density plot demonstrates the first 80 hours of power generation from the SOFC button cell across a 5 Ω external load. The power generation from ADG showed no significant carbon deposition on the anode or in the system. AGD that has had H_2S sufficiently removed is feasible for long-term stable power generation in Ni-YSZ anode SOFCs.

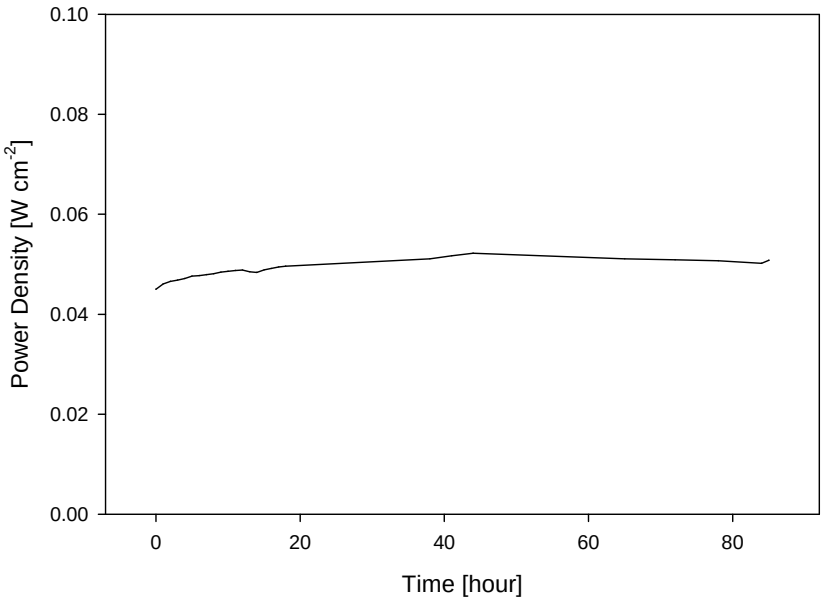

Figure 14. Power Density of Single SOFC Operated with ADG Fuel at 5 Ω External Load Recorded Over Time: T = 900 °C, P = 1.0 bar, Air Fed LSM Cathode.

Performance curves of Ni-YSZ anode SOFC button cells fueled by ADG and hydrogen are compared in **Figure 15**. The diagram plots the cell voltage *vs.* current density and specifies the open circuit potential (OCP), area specific resistance (ASR) and peak power density obtained from these data. The maximum power density generated with anaerobic digester gas was 89.4% that of hydrogen. The use of ADG directly or co-fed with hydrogen as a fuel in SOFCs is feasible for stable power generation.

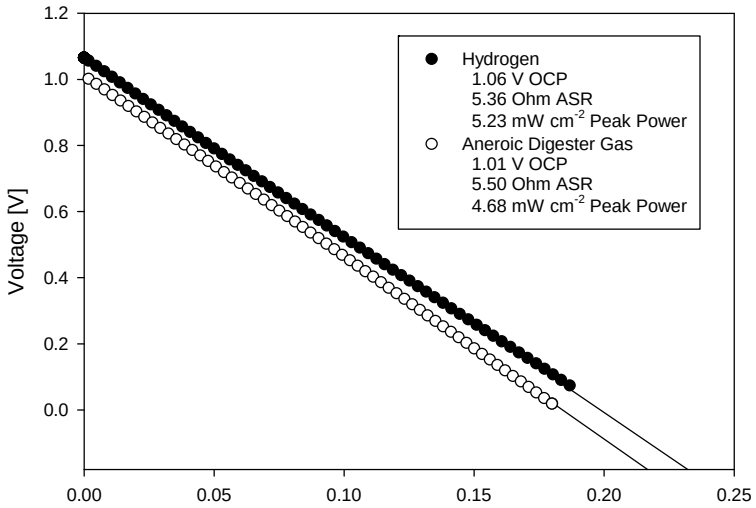

Figure 15. Polarization Curves for SOFC Operated with Hydrogen and Anaerobic Digester Gas fuel. T = 900 °C; P = 1.0 atm; Air Fed Cathode.

Figure 16 shows the example of the data collected from the SOFC operating on ADG fitted to an electrical equivalent circuit model before and after H_2S poisoning. The data were taken *in situ* during a power generation test. The equivalent circuit model under development is designed to separate reaction kinetic effects from mass transport effects in the SOFC, as well as to identify the effects of H_2S in ADG powered SOFCs. The electrical equivalent circuit model used to fit the impedance data plotted in **Figure 16** is shown in **Figure 17**.

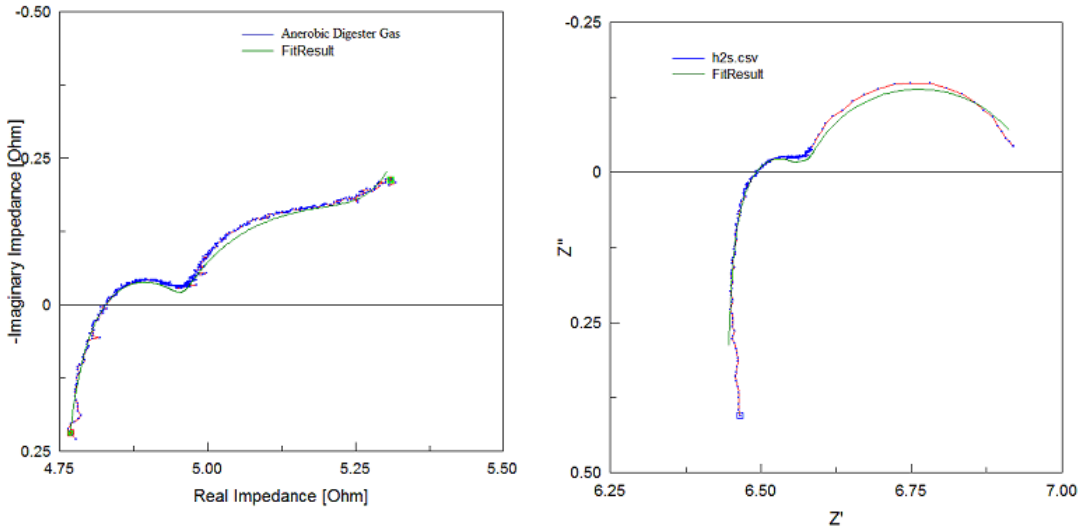

Figure 16. Nyquist plot displaying real vs. imaginary impedance over a frequency range of 30 kHz to 0.1 Hz fitted with an electrical equivalent circuit model shown in Fig. 4. Pure ADG is fed to the Ni-YSZ anode before and after H_2S poisoning (left before, right after). The shown EIS data were obtained during SOFC operation under 5Ω external load. Fuel: ADG /air, T = 900 °C, P = 1.0 bar.

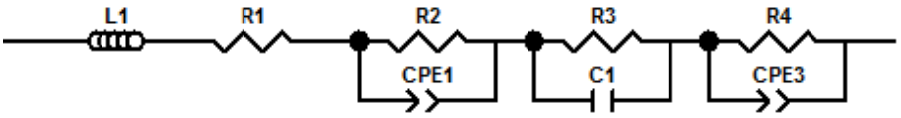

Figure 17. Equivalent electrical circuit model used for Figure 16.

A commercial diesel steam reformation system has been integrated with the single SOFC button cell test system. The system consumed a 3:1 diesel to water ratio to generate 100 cm^3 min^{-1} reformate in an 800 °C reformer. The reformate was then fed to a 900 °C Ni-YSZ anode SOFC system where power densities of 0.2 W cm^{-2} were generated. The performance of the diesel reformate fuel was evaluated by three parameters: open circuit potential, maximum power density, and limiting current density. A photo and scheme of the integrated diesel steam reformer and SOFC test system are provided in **Figure 18**.

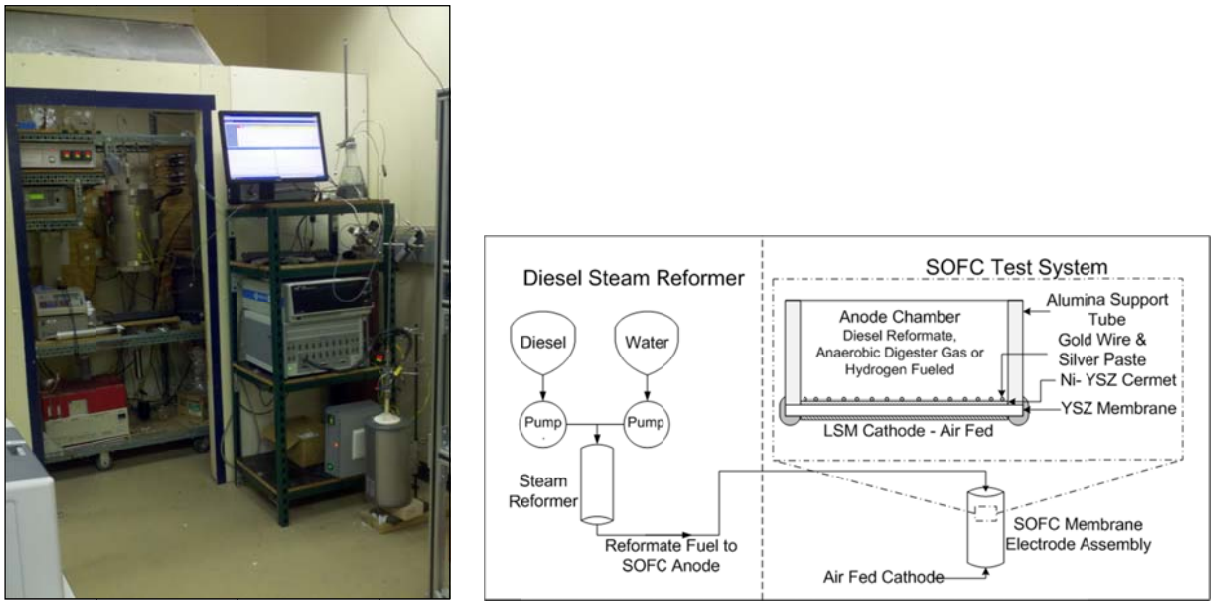

(a) **(b)**

Figure 18. (a) Photo of the integrated Diesel Steam Reformer – SOFC system, and (b) a scheme of the integrated diesel steam reformer - SOFC system, including detailed membrane electrode assembly design.

A model anaerobic digester gas (ADG), with the composition 45% CH_4 (the active fuel) in 55% CO_2 (diluent) was used in a series of SOFC performance tests. This composition was based on the desulfurized product gas from the Penn State Waste Water Treatment Center. The SOFC data obtained with ADG were further compared to those obtained with hydrogen as benchmark fuel and commercial diesel reformate. As for the commercial diesel steam reformate, it was prepared in the following manner. The Ni-Fe catalyst was used in the steam reforming process The reforming reaction was performed at 800 ºC. Both water and fuel were pumped via HPLC pumps through a pre-heater and then into the reactor at volumetric flow rates of 4.08 and 1.38 mL/h, respectively, for a steam-to-carbon molar ratio (S/C) of 3:1. The fuel employed in this study was commercially available diesel with 15 ppmw (parts per million by weight) sulfur. The composition of the commercial diesel reformate was determined to be approximately 70 %

H_2, 20 % CO, 5 % CO_2, 2 % CH_4, 3 % H_2O and less than 5 ppm sulfur (all percent by weight). The voltage-current density and power density-current density relationships demonstrated by each fuel are shown in **Figure 19**. The limiting current density and maximum power densities obtained in these tests are presented in **Table 2**.

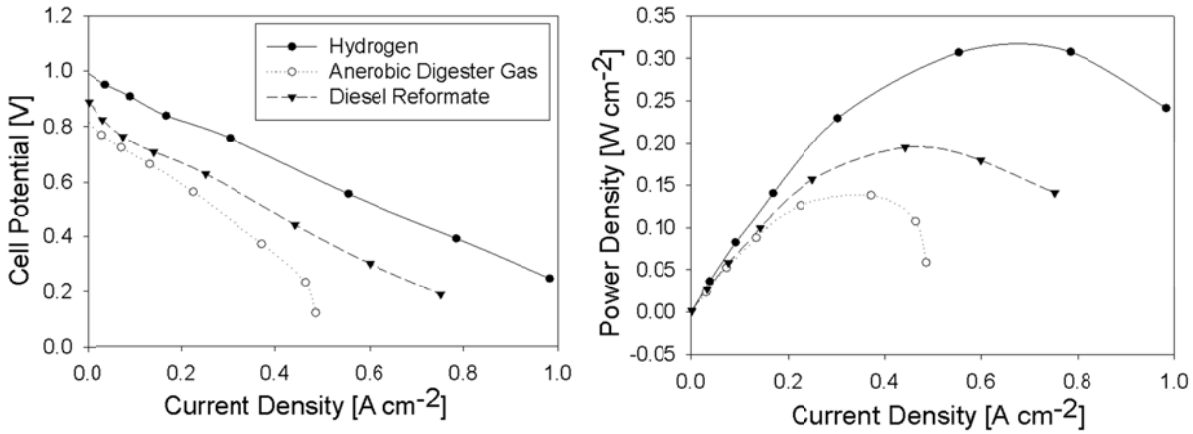

Figure 19. SOFC performance with hydrogen, anaerobic digester gas, and diesel reformate at 900 ^oC: (left) Cell voltage – Current density; (right) Power density – Current density.

Table 2. Comparative Analysis of Alternative Fuels in Solid Oxide Fuel Cell.

Fuel	Limiting Current Density	Maximum Power Density
Hydrogen	1.30 *	0.325
Commercial Diesel Reformate	0.90 *	0.20
Anaerobic Digester Gas	0.50	0.14

* Estimated value

The diesel reformate showed an open circuit potential (0.90 V), lower than that of hydrogen (1.30 V). The maximum powder density with diesel reformate as a fuel was 1.41 mW cm^{-2}, while it was 1.81 mW cm^{-2} with hydrogen. It should be pointed out that it contains about 72% of hydrogen, 18% carbon monoxide, 1% methane and 9% carbon dioxide in the diesel reformate (dry-base). Considering the gas composition in the diesel reforming, it can be concluded that the diesel reformate performs reasonably well compared to hydrogen. Additionally, the stability of the electric power generation using the reformate directly from steam reforming of commercial diesel was tracked and it showed that the power generation is stable for over 100 hours.

1.2.2.2 Test results on Delphi SOFC button cell and stack

Penn State Experiments Performed using Delphi Provided Button Cells

Initial experiments were carried out with a simulated mixed reformate. The mixture composition was chosen after a mutual agreement between PSU and Delphi. The selected composition consists of 22% of CO_2, 3% of CH_4, 20% of N_2, 5% of H_2O, and 50% of H_2. It is assumed that this composition will be used in all future impurity tests. Experiments were recently conducted to check consistency of the procedure and the reliability of the obtained data,

which should be reproducible for better and smooth future real-time experiments applying different fuels and operating conditions. Polarization curves (**Figure 20a**) were obtained and a soak chart (**Figure 20b**) was generated at current load conditions for a period of 120 hours to check the proper functioning of the cell with the proposed simulated reformate composition during this period. The cell was kept at a current density of 0.6 A/cm^2 (1.5 A) at 750 °C. The power density at the beginning was 0.46 W/cm^2 and at the end of the 5-day period, a 4.3 % decrease was observed. The performance was considered to be stable after a web discussion of the results with Delphi.

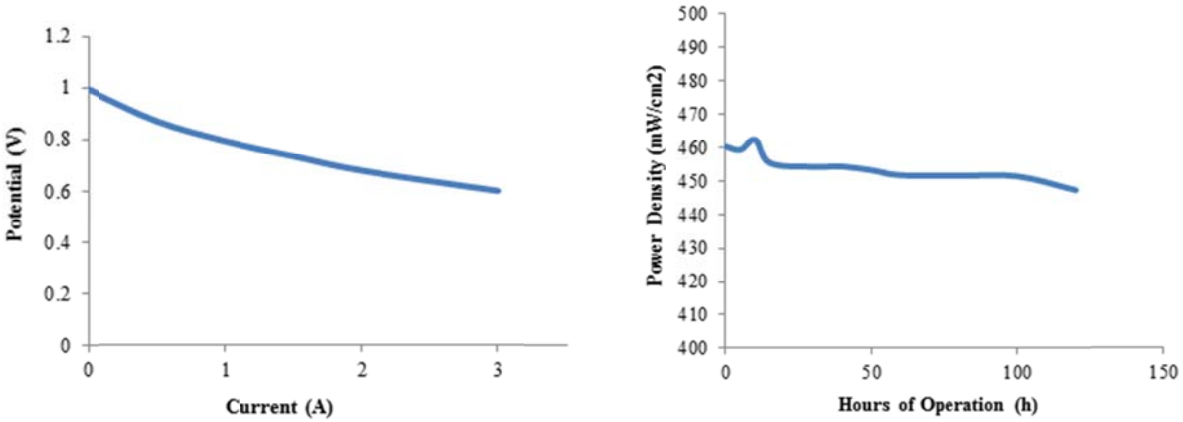

(a) (b)

Figure 20. (a) Polarization curve and (b) five day soak chart at 0.6 A/cm^2 with simulated reformate at 750 °C.

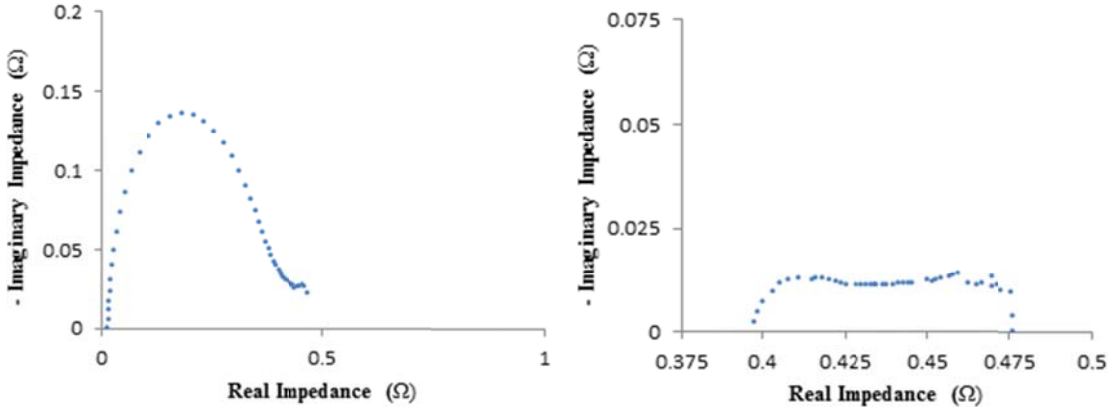

(a) (b)

Figure 21. EIS Spectra with H_2 as the Fuel at (a) OCP and (b) 0.6 A/cm^2 after 24 hours at 750 °C.

In case of H_2 as the fuel, the ohmic resistance of the cell increased over a soak period of 24 hours as expected showing that the membrane resistance increased from 0.09 Ω to 0.39 Ω. In open circuit conditions, shown in **Figure 21a**, a single arc designating the charge transfer resistance in the cell was obtained. As the cell was polarized in a galvanic mode there was a second arc, which is designating the mass transfer resistance associated with the transport process in the button cell. This is shown in **Figure 21b**. When using hydrogen, the mass transfer

resistance is convoluted with the charge transfer resistance, occurring as a single complex spectra.

In the case of simulated reformate as a fuel, the membrane resistance increased from 0.12 Ω at OCP conditions to 0.13 Ω at the end of the soak period of 120 hours. This is shown in **Figure 22a**. The difference in the increase of the membrane resistance between hydrogen and reformate could probably be due to the quality of the MEA prepared in both the cases and also because of some experimental factors such as gas flow, stability of temperature, pressure, etc. For the simulated reformate, under a load there are two distinct arcs, which could be identified and the mass transfer arc is larger than in the case of using H_2 due to a lower partial pressure of hydrogen. This is shown in **Figure 22b**.

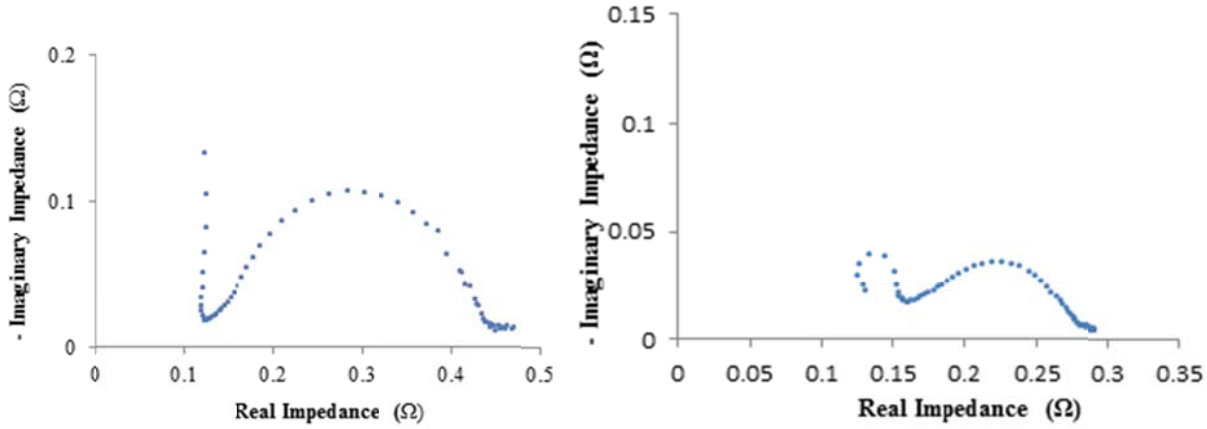

(a) (b)

Figure 22. EIS Spectra with Simulated Reformate as Fuel at (a) OCP and (b) 0.6 A/cm^2 after 120 hours at 750 °C.

Contaminant Tests of Delphi Button Cells

Contaminant tests were carried out with simulated mixed reformate. The mixture composition was chosen after a mutual agreement between PSU and Delphi. The selected composition consists of 22 % of CO_2, 3 % of CH_4, 20 % of N_2, 5 % of H_2O, and 50 % of H_2. Poisoning of the button cells with impurities at the respective concentration levels were performed for a definite amount of time. Electrochemical impedance spectra were obtained at equal intervals to track the degradation of the button cell and better understand the electrochemical processes contributing to the deterioration of the fuel cell performance. Circuit models were developed to quantify the resistances in the fuel cell, which helps us to monitoring the performance degradation both qualitatively and quantitatively.

Ammonia Testing

Ammonia was tested at concentration levels of 20, 50 and 100 ppm on the button cells. The fuel used was the simulated reformate mentioned above and fuel flow rate used was 50 sccm. The cell was kept at each concentration at a current density of 0.4 A/cm^2 for a time period of 100 hours to allow the impurity to stabilize and impedance spectra (**Figure 23**) were taken at the end of each soaking period. The circuit model used is shown previously and the best fit values of the electrochemical parameters obtained by Complex Non-Linear Least Squares (CNLS) from the ZView software is represented in **Table 3**.

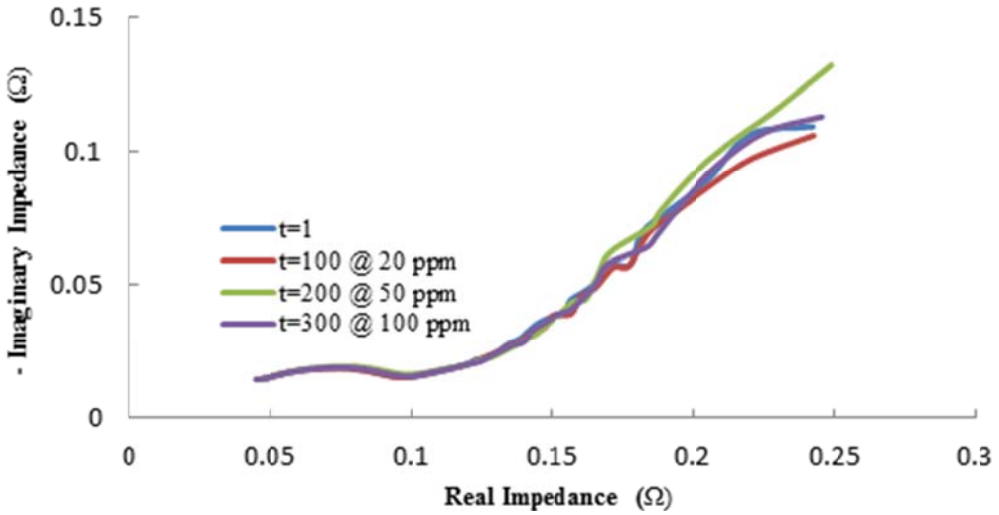

Figure 23. Impedance spectrum with equivalent circuit model for NH_3 contaminated fuel.

Table 3: Values of electrochemical parameters obtained from the best fit of the data shown in Figure 23.

	t=1	**t= 100**	**t=200**	**t=300**
R1	.03	.04	.04	.036
R2	.1690	.178	.1803	.13
CPE1-T	.696	1.08	1.21	.659
CPE1-P	.370	.26	.27	.373
R3	.185	.1753	.185	.226

It can be seen that there is no significant reduction of performance at all the three concentrations of NH_3. According to the thermodynamics of NH_3 at such high temperatures of 750 °C, it dissociates completely into N_2 and H_2. Thus there is an absence of any foreign impurities formed in the molecular or elemental state in the fuel stream which could possibly impede the electrochemical reactions taking place at the electrode/electrolyte interface. The impedance spectroscopy analysis shows that there is no observable degradation in the fuel cell as the value of the charge transfer resistance (R3) does not change much over the period of time at the increasing concentration levels. It is inferred that NH_3, even at high concentrations does not have any negative effect on the performance of the SOFC button cell. While the tests should be duplicated on a stack, much diversion from such behavior is not expected.

H_2S Testing

Sulfur is one of the major impurities present in biogas and diesel reformates and a proper understanding of its degradation effects on the Delphi stacks is essential for its successful mitigation when working at a commercial level. Even though the effects are very complex and vary with different process conditions, working with the button cells gives an initial and general idea about the expected behavior. It is also important to mention at this point that the results. Tests were carried out with button cells at relatively lower concentration of 200 ppb, 1 ppm and 4 ppm. Even though there was no significant reduction in the cell performance (**Figure 24**). The trends in resistances (**Table 4**) show a pronounced increase in the interfacial charge transfer

resistance. It can be seen that with using the 200 ppb H_2S in the fuel stream there was maximum increase of the charge transfer resistance during initial period of 100 hours. This large increase is attributed to the rapid adsorption of sulfur onto the anode surface and the triple phase boundaries, which results in the conversion of the metallic nickel to nickel sulfide. As a result, the amount of active catalytic sites for hydrogen oxidation is reduced which directly impacts the charge transfer processes. Once this change of surface composition has occurred the amount by which the surface oxidation reaction is inhibited remains constant. The change in microstructure results in an increased second arc over the entire time period of operation. A much more detailed diagnostics should be done when such tests are carried out on a stack with various process parameters and operating conditions because that is one of the major objectives of this project. The tests should also include reversibility of performance upon removal of sulfur rich fuel.

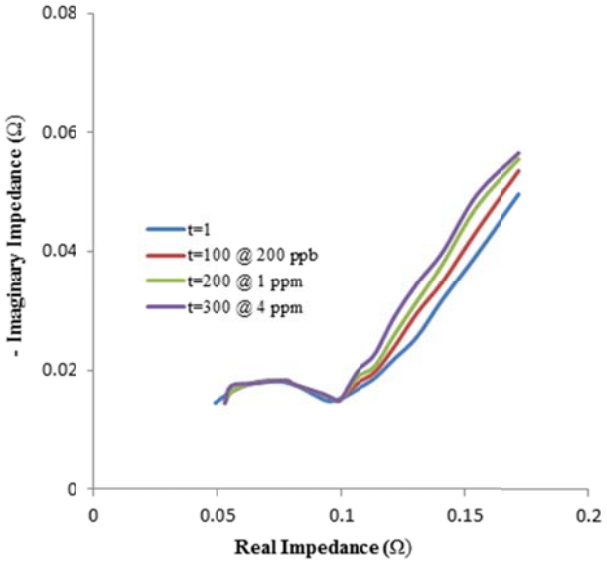

Figure 24. Impedance Spectrum for H_2S Contaminated Fuel.

Table 4: Values of electrochemical parameters obtained from the best fit of the data shown in Figure 24.

	t=1	**t= 100**	**t=200**	**t=300**
R1	.007	.007	.008	.008
R2	.149	.148	.150	.152
CPE1-T	.444	.444	.443	.444
CPE1-P	.336	.337	.337	.339
R3	.115	.223	.231	.249

To investigate the time dependence of H_2S poisoning and the regeneration of SOFC cell, a concentration of 1 ppm was selected and the cell was operated at a constant voltage and a fixed anode flow rate of the simulated reformate stream. As shown in **Figure 25**, the poisoning seems to occur at two stages. The initial sudden drop of about 14.5 % in the cell current can be attributed to the desorption of sulfur on the anode surface which is then followed by a much more sluggish and continuous performance drop of about 2.8 % (in the next 200 h) which can be attributed to slower electrochemical kinetics at the reaction triple phase boundaries because of a smaller number of the active catalytic sites are available for the electrochemical reaction. Upon

removal of H_2S from the fuel and increasing the oxygen flow at the cathode, the cell performance gradually and slowly rebound within a few hours. The recovery was not complete and the cell current was stabilized at a level of 97 % of the initial value. It was observed that the sulfur poisoning and regeneration processes strongly depend on the cell voltage. Lower the cell operating voltage, a better chance is for the highest level of recovery in the cell performance. It is evident from this study that the current passing through the cell probably might favor the electrochemical oxidation of the sulfur adsorbed on the Ni anode surface. At polarized conditions and high oxygen flow at the cathode, there is higher oxygen ion flux across the electrolyte and oxidation of the adsorbed sulfur converting it to gaseous sulfur dioxide. This may result in a rapid desorption of the sulfur species at the anode surface, which leads to maximum removal of sulfur after stopping the poisoning process by H_2S. However, it was noticed that the actual rate of poisoning process at any particular concentration would not be altered by change in cell voltage or current. Temperature increase might be helpful in this case, but due to the testing protocol to run the Delphi stack at a fixed temperature, the temperature effect was not tested.

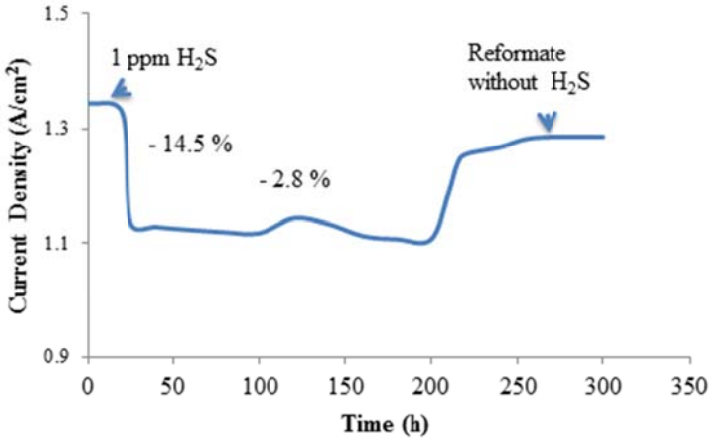

Figure 25. Sulfur poisoning and recovery process of Ni-YSZ anode in SOFC fueled by simulated reformate with 1 ppm of H_2S at potential of 0.55 V.

Siloxane - D5 (Decamethylcyclopentasiloxane) Testing

While testing the effect of siloxane on the fuel cell performance, the chosen concentration concentrations were 20, 50 and 100 ppm. In the beginning the test was carried out at 20 ppm. As shown in **Figure 26**, it was observed that 20 ppm proved to be extremely detrimental to the cell. The thermodynamics of D5 is such that it completely dissociates into silica (SiO_2) at high temperatures and silica is deposited or adsorbed onto the anode surface. This results in a formation of an insulating non-conducting oxide layer on the anode and this prevents (completely or partially depending upon the time of operation) the passage and diffusion of the fuel into the triple phase boundaries where the fuel electrochemical oxidation reaction takes place. As can be seen in **Figure 26** after the few initial hours, voltage dropped by about 20 % of the initial value and the impedance spectrum obtained was not reproducible due to the complete deactivation of the anode catalyst layer coupled with the contact leads.

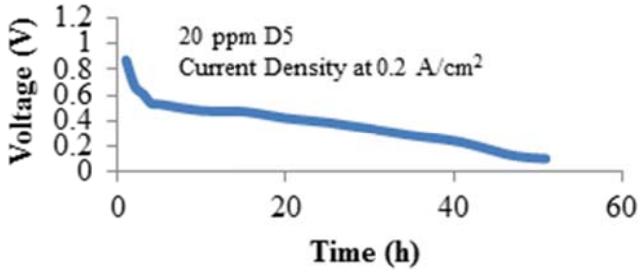

Figure 26. V-t Curve for a 20 ppm D5 on Simulated Reformate.

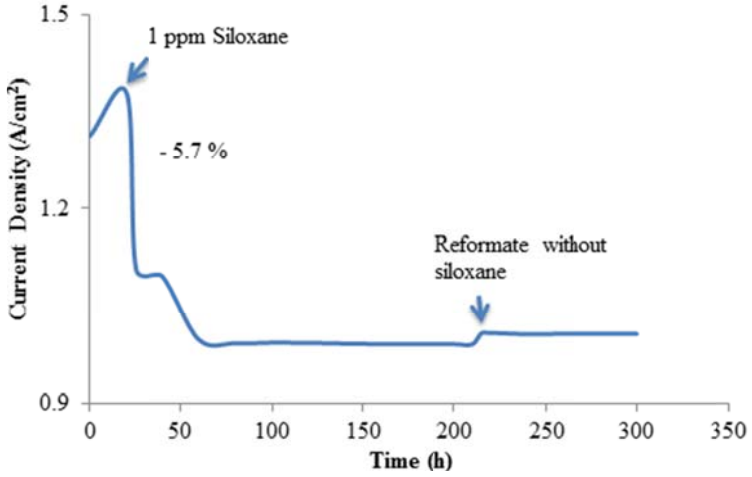

Figure 27. Siloxane poisoning process of Ni-YSZ anode in SOFC fueled by simulated reformate with 1 ppm of D5 at a potential of 0.58 V.

The time dependence of siloxane poisoning and the regeneration of SOFC cell were also studied with the selected siloxane concentration of 1 ppm for the fuel mixture since the concentration of siloxane in simulated reformate of more than 2 ppm was detrimental leading to almost permanent deactivation. As shown in **Figure 27**, it was observed an immediate reduction of the current density (about 5.7 %) and there was no gradual decrease of cell current like in case with sulfur. A possible explanation for this behavior is that siloxane after getting adsorbed also affects the kinetics of the electrochemical reaction forming some side products which results in a slow and gradual decrease of the cell current. Apparently, siloxane forms glassy and non-conducting deposits of silica on the anode surface and this leads to increasing both the ohmic and mass transfer resistances. It may not have much of an effect on the anode structure like sulfur (which forms NiS_x) but clearly forms a sort of a barrier between the anode TBP sites and the incoming anode fuel for which a percentage of fuel does not react and remains unutilized leading to a lesser conversion of the fuel for generating current. In addition, after changing the fuel to pure reformate, and removing siloxane from the stream, no observable cell recovery was observed. The main difference between sulfur and siloxane poisoning in this regard is that, the adsorbed sulfur can be oxidized at the anode during some time period by increasing oxygen flow to the cathode or maintaining a constant current in the cell. In the case of siloxane, the deposited silica adheres to the anode surface and forms a very stable oxide layer which is resistant to electrochemical oxidation and removal from the anode surface. Thus, the insulating silica layer deactivates the surface and reduces the cell performance.

The Delphi 5-cell SOFC Stack

The main focus of the project is the analysis of the degradation of the fuel cell stack under different impurities operating on diesel and bio-gas reformate. Delphi engineers arrived at the Penn State facility and installed both the debug stack and the first real stack. The main purpose of the debug stack was to simulate the actual process conditions and run dummy tests with the electrochemical equipment and the gas flow system. This was performed to ensure that if there are any issues or problems, they could be solved with the debug stack, so that smooth functioning of the actual stacks will be insured. The typical testing protocol included polarization curves, current soak tests, fuel utilization and pressure tests. The obtained data were sent to Delphi for comparison to make sure they meet the required standards. The obtained data are shown below in **Figure 28a-d**.

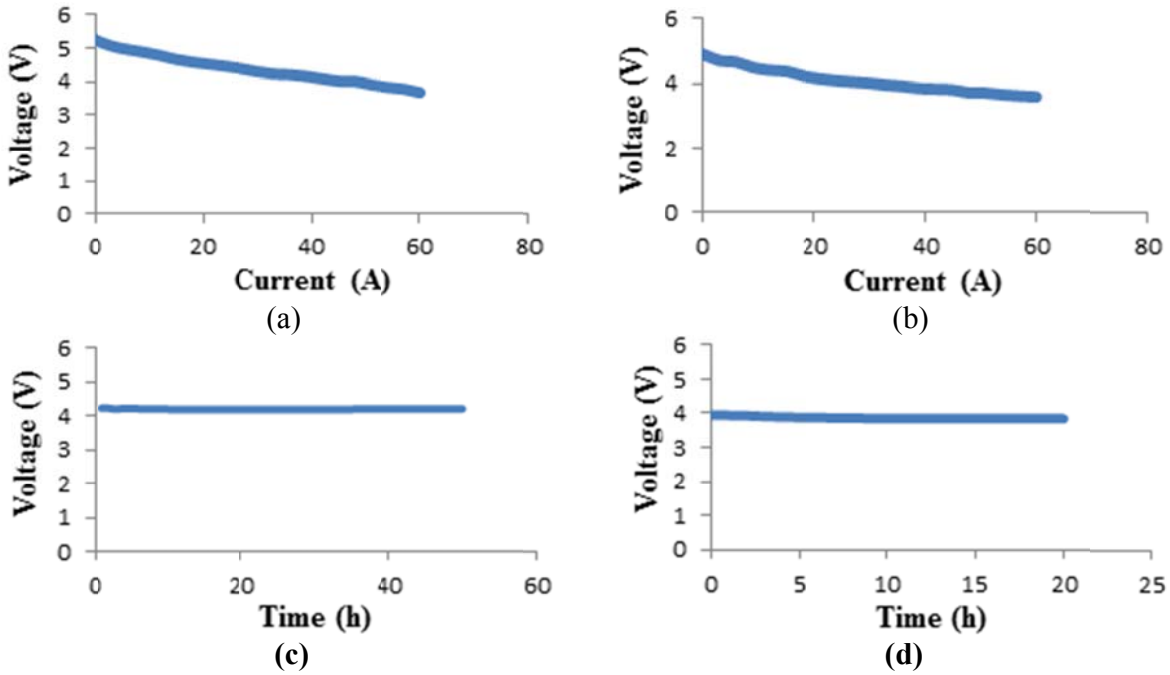

Figure 28. (a) Polarization curve with H_2/N_2 fuel, (b) Polarization curve with simulated reformate, (c) Soak chart with H_2/N_2 at 35A current and (d) Soak chart with simulated reformate at 35A current.

The first real stack was installed after all the required tests with the debug stack were finished. The EIS curves were obtained with the first stack using the Solartron EIS equipment and it was checked for any errors which might arise during the acquisition of the impedance data. The Solartron's ability to operate on all the individual cells as well as the stack was reliably confirmed. The EIS curves at both OCP and at a load were also obtained. **Figure 29** and **Figure 30** are representative impedance spectrums for the real stack at open circuit and load conditions respectively. A screenshot of the circuit models along with the value of the electrochemical parameters and their corresponding error percentages were also included below the pictures. It is to be noted, that for a good fit and acceptable model, an error percentage of less than 5 % - 8 % was selected as the baseline.

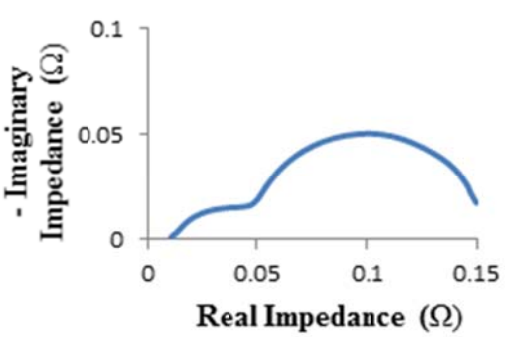

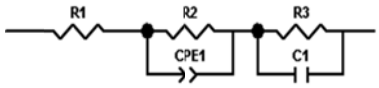

Element	Freedom	Value	Error	Error %
R1	Free(+)	0.010151	7.4051E-05	0.72949
R2	Free(+)	0.045896	0.00060292	1.3137
CPE1-T	Free(+)	0.62741	0.026375	4.2038
CPE1-P	Free(+)	0.65423	0.0062387	0.95359
R3	Free(+)	0.096867	0.00085209	0.87965
C1	Free(+)	2.748	0.042601	1.5503

Figure 29. Impedance spectrum of the real stack with H_2/N_2 fuel at OCP with screenshot showing the equivalent circuit parameters and errors between the experimental and fitting curve from the ZView software.

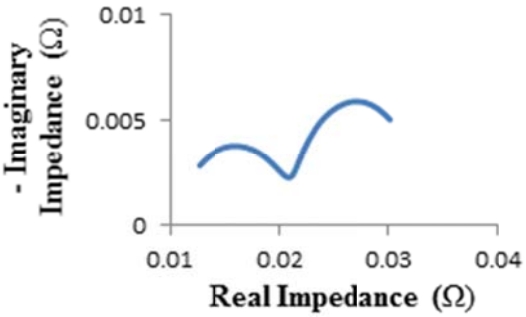

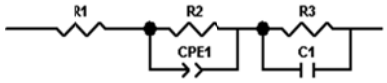

Element	Freedom	Value	Error	Error %
R1	Free(+)	0.010186	0.00011965	1.1747
R2	Free(+)	0.011467	0.00016403	1.4305
CPE1-T	Free(+)	0.35221	0.019103	5.4238
CPE1-P	Free(+)	0.73455	0.009616	1.3091
R3	Free(+)	0.011376	0.00011611	1.0207
C1	Free(+)	7.991	0.11639	1.4565

Figure 30. Impedance spectrum of the real stack with H_2/N_2 fuel at 15 A current with screenshot showing the equivalent circuit parameters and error between the experimental and fitting curve from the ZView software.

Performance tests were also carried out with diesel reformate using Delphi SOFC stack. A simulated diesel reformate was prepared to be very close to the actual reformate composition which would be obtained after reforming diesel using steam. The fuel blend consisted of around 60-70 % H_2, 5-10 % CO, 15-20 % CO_2 and 3-5 % CH_4. Steam was also added to the gas mixture to adjust the Steam/Carbon (S/C) ratio. Due to presence of CO in the fuel stream, carbon deposition is a possibility and this could drastically reduce the fuel cell efficiency. Carbon deposits block the active Ni sites and hamper the fuel cell performance. Even though carbon also oxidizes itself at a constant current condition, the removal of carbon from the anode surface is rather slow. To mitigate this effect and avoid the possible carbon deposition, a minimum S/C ratio of 2 is always maintained when working with the stack fueled by the diesel reformate. The steam was added to enhance the formation of H_2 and CO_2 by inducing the water-gas shift reaction between CO and H_2O.

Short-term performance tests of about 300 h each were carried out with various CO compositions to check the fuel cell response. It was observed using CO concentrations of 5 - 7 % that there was no significant reduction or degradation of the stack performance. Taking into account that a sufficient amount of steam was provided to the system, we speculate that there was not any rapid carbon deposition and this assumption was confirmed by observing a very small decrease of the cell potential and power density during a relatively long test time. The tests were run and data were recorded first for 100 hours and then were continued up to 300 hours. The polarization curve and the voltage-time curves are given in **Figure 31**.

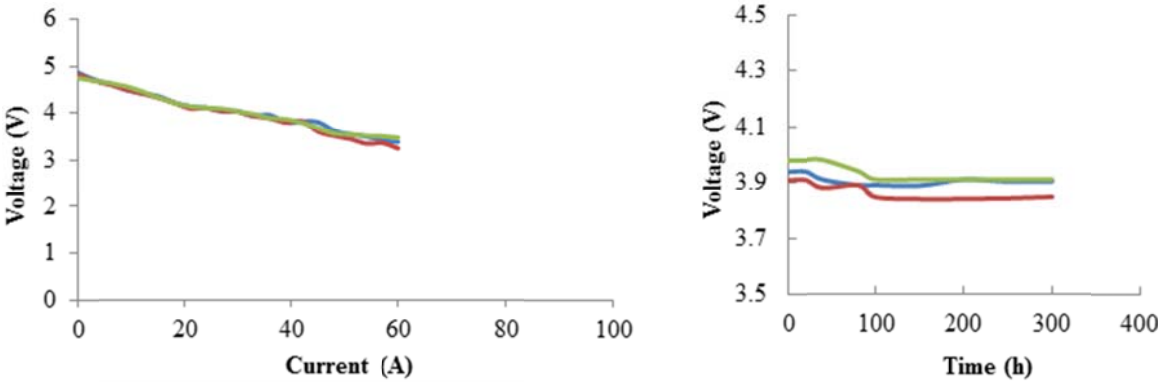

(a) (b)

Figure 31. (a) Polarization curve and (b) potential time dependence of the tests with diesel reformate. Different colors show the corresponding compositions.

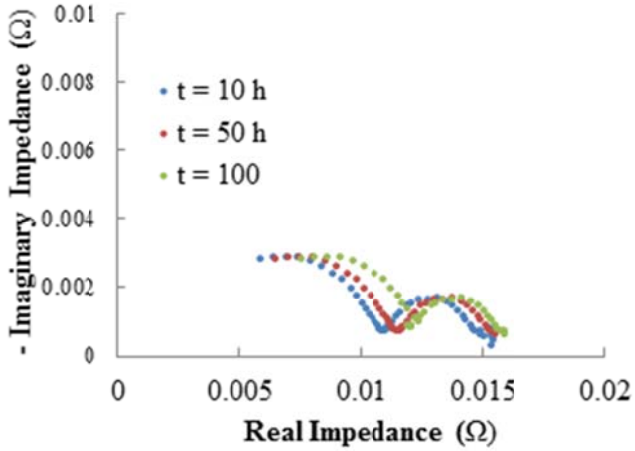

Figure 32. EIS Curves for a Single Cell (Cell 1) of the 5 Cell Stack Using a Diesel Reformate with 10% of CO.

The EIS tests, as shown in **Figure 32**, were performed to gather more information on the change in the charge transfer and interfacial resistances occurring in the fuel cell. The tests were carried out with 10 % of CO in the diesel reformate. The EIS curves were modeled using the equivalent diagram below and the obtained parameters are given in **Table 5**.

Table 5. Values for Equivalent Circuit Parameters for the Diesel Reformate Tests with 10% of CO.

	t=10	**t= 50**	**t=100**
R1	.0026	.0028	.0030
R2	.0082	.0097	.0112
CPE1-T	.1786	.1840	.1994
CPE1-P	.7811	.7800	.7823
R3	.0045	.0047	.0052
CPE2-T	66.57	67.23	67.20

No change in the ohmic resistance was observed and very negligible change of interfacial resistance, R3, (mass transfer and gas conversion resistance) was found. However, the charge transfer resistance (R2), observed over a period of 100 hours, was slightly increased. The reason could be attributed to a reduced partial pressure of hydrogen. It is evident from the performance curves and also the EIS plots that CO poisoning did not occur in the cells in these tests. Thus, we assume that the changes in the charge transfer resistance cannot be related to the CO poisoning processes at the anode.

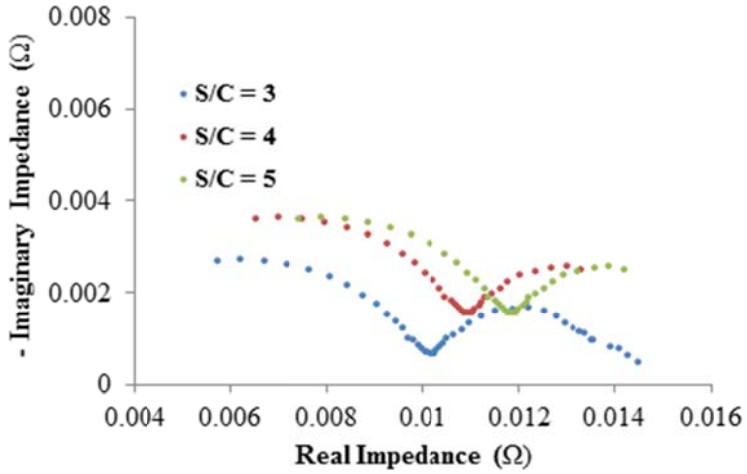

Figure 33. EIS curves for a single cell (Cell 1) of Delphi 5-Cell stack fueled by diesel reformate with 10% CO and different S/C ratios.

Note that the stack was not run in the absence of steam to avoid any possibility of the carbon deposition and the selected S/C ratio did not affect performance of the cell fueled by the diesel reformate. Tests were then conducted with varying S/C ratios, which are presented in **Figure 33**. Addition of steam is important for avoiding carbon deposition by the water-gas shift reaction but performance of the fuel cell changed drastically on increasing water content. High water content in the fuel stream initiated multiple side reactions, which affect the electrochemical reactions occurring at the anode. One of the important reactions which occurs with excess amount of water in the fuel feed is the reaction between methane and water. At nominal S/C ratios of up to 2.5, the water gas shift reaction dominates for which the CO in the fuel stream is converted to CO_2 and H_2. But in the presence of methane in the fuel stream, it reacts with the excess steam to produce CO which then have a possibility of undergoing the reverse Buodouard reaction, which might result in carbon formation and deposition. Therefore, a lot of side reactions are possible when the fuel chemistry gets complex and there is enough water content to initiate them. These side reactions may end up reducing the partial pressure of the effective fuel components and also may lead to the anode carbonization, which would reduce the performance of the fuel cell.

It is clear from the impedance curves that increasing the S/C ratio does not necessarily improve the performance of the fuel cell. The change in the impedances might not be significant but continuous application of the large S/C ratios may lead to a gradual and slow degradation by the mechanisms which was explained in the previous paragraph. All the above plots in **Figure 33** have been taken after application for a period of 50 h at a current of 35 A. **Figure 34** shows the steady-state stable performance of the cell on adjusting the S/C ratio with a slight decrease of the

potential. The reduction of potential is related to the Nernst Potential and in no way shows cell degradation. The idea here is to operate the cell without carbon deposition and also to maintain an optimum level of steam to avoid too much reduction in potential.

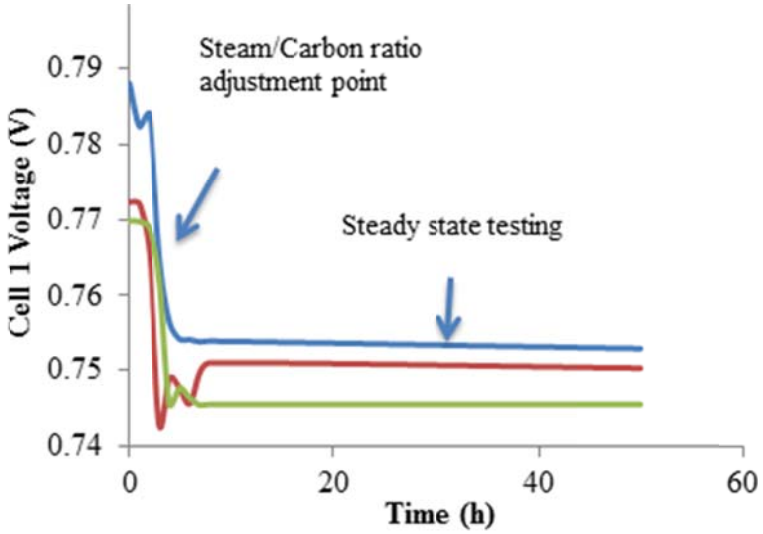

Figure 34. Cell potential as a function of time at different S/C for a single cell (Cell 1) of Delphi 5-Cell Stack [Blue: S/C =3, Red: S/C = 4, Green: S/C = 5].

1.3. Novel EFM tests with the stack

Electrochemical Frequency Modulation (EFM) has been used extensively in monitoring corrosion processes over the past decade. However, it has not been employed in obtaining any information on any kinetic parameters for fuel cells. This work demonstrates the feasibility of using this important technique in obtaining valuable information on the kinetic variables for fuel cells. EFM involves a potential perturbation signal by one or more sine waves which generate current responses at more frequencies than the frequencies of the applied signal. Current responses can be measured at harmonic and intermodulation frequencies and thus employed with empirical relations to quantify the exchange current and the respective Tafel parameters for the system under test. It should be noted that EFM is considered as a primary technique similar to EIS, in providing important information about electrochemical parameters whose knowledge is useful to better understand, improve, and optimize cell performance. EFM provides information on the exchange current, Tafel constants and causality factors. Both, Exchange Current and Tafel parameters can be independently measured using EFM. The causality factors are used to validate the data and are a kind of internal check to confirm the consistency and validity of the measurement process. There are two causality factors 2 and 3. These causality factors serve as internal checks to confirm the consistency of the obtained EFM plots and the data. Any significant deviation from these ideal values indicates the quality of the electrochemical model which has been used to calculate the implied parameters. The fundamental background theory for the electrochemical frequency modulation can be found at the end of this report.

1.3.1. Electrochemical Frequency Modulation – Fundamental Background Theory

EFM has been used as a new technique which was first proposed by Bosch et al. for online corrosion measurements. It is a nondestructive electrochemical technique that has the capability of giving values of the corrosion currents without prior knowledge of the Tafel

Constants. The original concepts of EFM can be deduced from the Butler-Volmer equation as mentioned in the early works on this technique. Similar to EIS, EFM is an AC excitation method, where a small signal is applied to the fuel cell. In EFM, two sine waves at different frequencies are generated, which is used to stimulate the cell simultaneously. It is known that current is a non-linear function of potential so that the systems also responds in a non-linear way to the potential perturbation. The electrical current contains responses from the input frequencies as well as sum, difference and multiples of the two input frequencies. The two frequencies are selected to optimize the output. The frequencies should be as high as possible so as to reduce the time of operation and be sufficiently low so that the charging of the double layer does not contribute to the current response. The amplitude of the signal excitation is also selected to be as low as possible, just like EIS. In their work, Bosch et al. described empirical relationships between the electrochemical parameters and the current responses at different intermodulation frequencies. These relations could be easily used in this case also for calculation of the exchange current density. There is also an internal check devise, named as causality factors, which helps to perform a validation of the data and estimate the presence of any background noise. The noise could be originating from the instrument or the system itself. The causality factors, 2 and 3, are used as baseline data verification to help decide if the data obtained through EFM can be analyzed further. Significant deviation from the ideal values of 2 and 3 is the result of a system probably with high background noise or an incorrect selection of electrochemical model.

Mathematical Treatment

The relation between activation overpotential (η) and current density (i) is represented by the Butler-Volmer equation at each electrode-electrolyte interface (which means that the equation is applied separately at the anode and cathode), shown here

$$i = i_0 \left[\exp\left(\frac{\alpha n F}{RT}\,\eta\right) - \exp\left(\frac{-\beta n F}{RT}\,\eta\right) \right] \quad [1]$$

In this equation i_0 is the exchange current density, α and β are the anodic and cathodic transfer coefficients respectively, n is the number of electrons transferred by the corresponding electrode reaction, F is Faraday's constant, R is universal gas constant and T is the absolute temperature.

The mathematical analysis for the EFM technique should be mentioned here as these results are important to define and estimate the exchange current, Tafel parameters and also the causality factors. A potential perturbation consisting of two sine waves of different frequencies is applied to the fuel cell:

$$\eta = U_0 \sin\omega_1 t + U_0 \sin\omega_2 t \quad [2]$$

where η is the overpotential, U_0 is the amplitude of the potential perturbation and ω_1, ω_2 are the perturbation frequencies.

The potential perturbation described in Equation (2) is substituted in Equation (1)

$$i = i_0 \left[\exp\left(\frac{\alpha n F}{RT}\,\{U_0 \sin\omega_1 t + U_0 \sin\omega_2 t\}\right) - \exp\left(\frac{-\beta n F}{RT}\,\{U_0 \sin\omega_1 t + U_0 \sin\omega_2 t\}\right) \right] \quad [3]$$

$$i = i_0 \left[\exp\left(\frac{\alpha n F}{RT}\,U_0 \sin\omega_1 t\right) \exp\left(\frac{\alpha n F}{RT}\,U_0 \sin\omega_2 t\right) - \exp\left(\frac{-\beta n F}{RT}\,U_0 \sin\omega_1 t\right) \exp\left(\frac{-\beta n F}{RT}\,U_0 \sin\omega_2 t\right)\right] \quad [4]$$

The exponential parts are expanded according to the Taylor series:

$$\exp\left(\frac{\alpha n F}{RT}\,U_0 \sin\omega_1 t\right) = 1 + \frac{\alpha n F}{RT}\,U_0 \sin\omega_1 t + \frac{1}{2}\left(\frac{\alpha n F}{RT}\,U_0 \sin\omega_1 t\right)^2$$

$$+\frac{1}{6}\left(\frac{\alpha nF}{RT}\ U_0\ \sin\omega_1 t\right)^3 + \ldots \quad [5]$$

Similarly after doing the Taylor expansion for rest of the terms and doing some algebraic manipulation yields the values of the current at the perturbation frequencies and also the harmonic and intermodulation frequencies:

$$i_{\omega 1} = i_{\omega 2} = i_0\left(\frac{\alpha nF}{RT}\ U_0\ +\ \frac{\beta nF}{RT}\ U_0\right) \quad [6]$$

$$i_{2\omega 1} = i_{2\omega 2} = \frac{1}{4} i_0\left[\left(\frac{\alpha nF}{RT}\ U_0\right)^2\ -\left(\frac{\beta nF}{RT}\ U_0\right)^2\right] \quad [7]$$

$$i_{3\omega 1} = i_{3\omega 2} = \frac{1}{24} i_0\left[\left(\frac{\alpha nF}{RT}\ U_0\right)^3\ +\left(\frac{\beta nF}{RT}\ U_0\right)^3\right] \quad [8]$$

$$i_{\omega 1 \pm \omega 2} = \frac{1}{2} i_0\left[\left(\frac{\alpha nF}{RT}\ U_0\right)^2\ -\left(\frac{\beta nF}{RT}\ U_0\right)^2\right] \quad [9]$$

$$i_{2\omega 1 \pm \omega 2} = i_{\omega 1 \pm 2\omega 2} = \frac{1}{8} i_0\left[\left(\frac{\alpha nF}{RT}\ U_0\right)^3\ +\left(\frac{\beta nF}{RT}\ U_0\right)^3\right] \quad [10]$$

Solving the equations (6 - 10), for the exchange current, i_0, both the Tafel parameters $\frac{RT}{\alpha nF}$ and $\frac{RT}{\beta nF}$,

$$i_0 = \frac{{i_{\omega 1,\omega 2}}^2}{2\sqrt{8 i_{\omega 1,\omega 2}\ i_{\omega 1 \pm 2\omega 2} - 3 {i_{\omega 1 \pm \omega 2}}^2}} \quad [11]$$

$$\frac{RT}{\alpha nF} = \frac{i_{\omega 1,\omega 2}\ U_0}{i_{\omega 1 \pm \omega 2} + \sqrt{8 i_{\omega 1,\omega 2}\ i_{\omega 1 \pm 2\omega 2} - 3 {i_{\omega 1 \pm \omega 2}}^2}} \quad [12]$$

$$\frac{RT}{\beta nF} = \frac{i_{\omega 1,\omega 2}\ U_0}{-i_{\omega 1 \pm \omega 2} + \sqrt{8 i_{\omega 1,\omega 2}\ i_{\omega 1 \pm 2\omega 2} - 3 {i_{\omega 1 \pm \omega 2}}^2}} \quad [13]$$

The current values mentioned above denote the current response to the perturbation function at those particular frequencies. Therefore, $i_{\omega 1,\omega 2}$ means the current component measured at frequencies ω_1 and ω_2. The current components are averaged and applied in the equations (11) through (13) to estimate the electrochemical parameters.

For checking the validity of the assumed model and also the data, two causality factors are defined which serves as an internal check during data analysis. The causality factors are related to the current components as follows:

$$\text{Causality factor (2)} = \frac{i_{\omega 1 \pm \omega 2}}{i_{2\omega 1}} \quad [14]$$

$$\text{Causality factor (3)} = \frac{i_{2\omega 1 \pm \omega 2}}{i_{3\omega 1}} \quad [15]$$

If there is a relation between the perturbation signal and the current response, the current components should ideally follow both the causality factor values of 2 and 3. Sometimes, measurements might by influenced by background noise which might arise from the equipment or from the system. Data validity and reliability can be easily checked by performing this simple post-test calculation.

This work is an effort to apply and introduce EFM to a fuel cell system for calculating the value of the exchange current densities and Tafel parameters. Conceptually corrosion systems and fuel cell systems are similar in nature with the similar defining kinetic models. The kinetics of a corrosion process can be explained with the Butler-Volmer equation with the "ideal" current termed as corrosion current, which is called exchange current in case of fuel cell systems. The response of an electrochemical system to a certain perturbation should follow similar non-linear behavior irrespective of whether it is a corrosion system or a fuel cell system. We expect and propose that the original theory for the technique should be similar for all electrochemical systems, such that the results generated from the technique should work for both corrosion

systems as well as fuel cell systems. The results from this technique have been compared with EIS, LSV and LPR (Linear Polarization Resistance) to make a comparative treatment of the obtained data and used to estimate the extent of accuracy and deviation between values from the three methods.

1.3.2. Electrochemical Measurement & Instrumentation

The fuel used in the experiments was pure hydrogen (3 % humidified) and all the four different measurements (EFM, EIS, LPR & LSV) were carried under similar operating conditions. After the reduction of the cells, wet H_2 was supplied to the anode side of the SOFC stack with a flow rate of 2.5 L min^{-1}, and the cathode was supplied with air at a flow rate of 5 L min^{-1}. All of the gases used were as received from Praxair Inc. For measuring the EIS at open circuit conditions, a Solartron 1252A Frequency Response Analyzer was used in conjunction with a 1470 E Cell Test System. The frequency range for which the impedance data was obtained ranged from 10 kHz to 0.1 Hz. This allows all the possible electrochemical processes to be represented in the Nyquist plots. The stack generated a large amount of current. This resulted from its larger surface area of the individual cells. The Solartron system could not be used due to its current limitations. For this reason, a HP 6060B electronic load was used to perform the linear sweep (LSV) due to its high current handling capability of 60 A. Anodic overpotential ranging from 0 mV to 400 mV was used to generate the current-overpotential data which would then be used to perform the Tafel analysis. Equivalent Circuit Modeling was performed using ZView on the obtained EIS spectra to determine the corresponding resistances associated with the fuel cell system. EFM measurements were carried out using the Gamry Reference 600 and the EFM 140 software package. The frequencies used were 2 Hz and 5 Hz. The base frequency used was 1 Hz. The values of the electrochemical parameters observed from EFM were directly obtained from the Gamry software framework system. Tests were repeated multiple times to check the consistency and repeatability.

1.3.3. EFM Results – Comparative Analysis with EIS, LSV and LPR

1.3.3.1 EIS Data and Nyquist Plots

Impedance spectra were recorded for a single cell (Cell 1) considering the conditions which were mentioned before. It was made sure that the gas flow and temperature conditions remained similar throughout the entire test schedule. Five sets of EIS data were recorded at different times of the day, each at intervals of 3 hours. This was performed to verify the obtained values drift significantly with passage of time or there is negligible change in them. A Nyquist Plot at open circuit conditions is shown in **Figure 35**. The impedance plot obtained in the figure is for $N = 3$. Plots of $N = 1$ to $N = 5$ have not been shown because it was found that the nature of the impedance spectra did not change with the specified operating conditions.

The EIS plot obtained is shown in **Figure 35**. Identification of different sections of the EIS plots gives us information on the corresponding electrode processes. Change in the spectra with changing operating conditions shows the dependency of the particular variable on the corresponding portion of the EIS spectra. It is seen that the first high frequency arc (centered around 10 Hz) is completely dependent on the partial pressure of oxygen (21 % O_2 to 100 % O_2) on the cathode side and the second mid frequency arc (centered around 0.15 Hz) is mainly dependent on the partial pressure of hydrogen and also the operating temperature on the anode side. It is thus noted that the first arc corresponds to the cathodic charge transfer kinetics and O^{2-} diffusivity. The second arc is also a function of polarization and with increasing current load on

the fuel cell, the size of the mid frequency arc decreases respectively. Therefore passage of current through the cell increases the charge transfer process, i.e., more conversion of the fuel (H_2) to water. Thus, it is inferred that the mid frequency arc corresponds to an anodic charge transfer process where hydrogen is getting oxidized. When calculating the value of exchange current densities our main focus is the region of R3. Circuit Modeling helps to analyze the impedance plots quantitatively to give near exact values of the associated resistances and capacitances of the system. The values obtained for all the electrochemical parameters after fitting of the experimental data for $N = 1$ to $N = 5$ have been shown in **Table 6**.

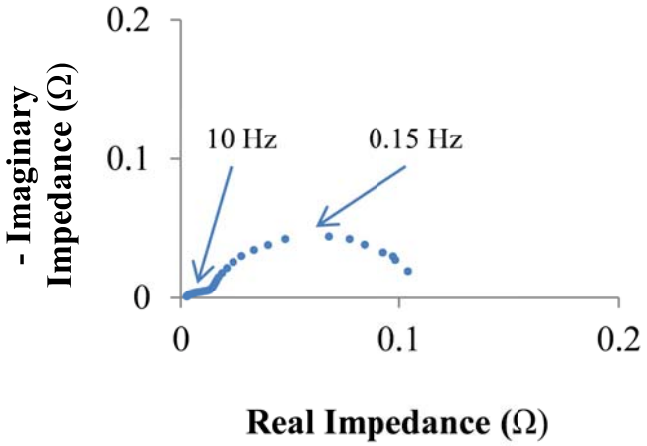

Figure 35. Nyquist plot for cell 1 at OCP with the centre frequencies for the individual arcs. Fuel: 3 % wet H_2 (2.5 SLPM), Oxidant: air (5 SLPM).

Table 6. Values of the electrochemical parameters from circuit modeling.

Data Acquisition Points	***R1* (Ω)**	***R2* (Ω)**	***CPE1-T* (F)**	***CPE1 - P* (F)**	***R3* (Ω)**	***CPE2-T* (F)**	***CPE2-T* (F)**	Error R1,R2,R3 (%)
***N* = 1**	0.001880	**0.01345**	3.218	0.64711	**0.09361**	14.86	0.96253	1.26, 1.21,0.67
***N* = 2**	0.001881	**0.01367**	3.2178	0.64325	**0.09345**	53.50	0.96401	1.24,2.37,1.98
***N* = 3**	0.001879	**0.01347**	3.2435	0.65008	**0.09392**	53.45	0.96720	4.37,2.6,0.88
***N* = 4**	0.001890	**0.01332**	3.1786	0.64721	**0.09388**	53.48	0.96750	2.99,1.1,2.7
***N* = 5**	0.001883	**0.01350**	3.1881	0.64798	**0.09455**	53.43	0.96520	3.44,2.15,1.17

Regarding EIS, the low current approximation of the Butler-Volmer equation gives the relation between the exchange current density (i_o) and the charge transfer resistance as follows:

$$i_0 = \frac{RT}{nFRct}$$

Here, R is the molar gas constant, T is the temperature of the electrochemical process, n is the number of electrons transferred during the process, F is Faraday's constant, and Rct is the area specific charge transfer resistance (sum of cathodic and anodic charge transfer resistance), which corresponds to sum of the resistive elements $R2$ and $R3$ in **Figure 36**.

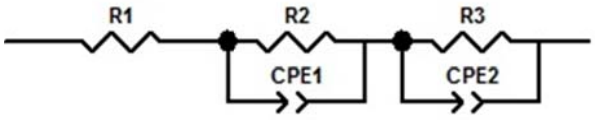

Figure 36. Circuit model to fit the experimental data obtained through EIS.

For the anodic and cathodic reaction in a solid oxide fuel cell with H_2 as fuel, we can write the following electrochemical reaction.

$$H_2(g) + O^{2-}(aq) \rightarrow H_2O(g) + 2e^- \quad \text{- Anode}$$
$$O_2(g) + 2e^- \rightarrow O^{2-}(aq) \quad \text{- Cathode}$$

Hence we can assume n equal to 2 for calculating the exchange current densities. The rest of the parameters are assumed standard values according to IUPAC recommendations. The area specific charge transfer resistance is calculated exchange current density values are directly estimated using the low current approximation as stated in equation 5.

i.e. for $N = 3$ the i_0 value can be calculated as;

$$R\text{ct} = (0.01347\ \Omega + 0.09392\ \Omega)\ (105\ \text{cm}^2) = 11.2759\ \Omega\text{-cm}^2$$

$$i_0 = \frac{(8.3145)(1023)}{(2)(96485)(11.2759)} = 3.9090\ \text{mA/cm}^2$$

The calculated values as obtained are shown in **Table 2** for each of the readings.

Table 7. Values of the exchange current density obtained from low current approximation of Butler-Volmer equation.

Data Acquisition Points	*R*ct (Ω cm^2)	(mA/cm^2)
***N* = 1**	11.1136	3.9591
***N* = 2**	11.6556	3.7750
***N* = 3**	11.2759	3.9090
***N* = 4**	11.6196	3.7867
***N* = 5**	11.6577	3.7743

1.3.3.2. LSV Data and Tafel Plot

Linear Sweep Voltammetry was performed on the same cell at the same time intervals which were considered for taking the EIS measurements. Five sets of data from $N = 1$ to $N = 5$ were observed and the corresponding Tafel Equation was formed with the current density and the overpotential as parameters. The natural logarithm of the current was chosen as the y-axis and the cell overpotential was chosen as the x-axis. After generating the current-overpotential data from the electronic load, it was transferred to graphical analysis software for plotting the relationship curve.

In order to identify the linear region in the plot, a straight line was drawn which was asymptotic to the curve and had an intercept in the y-axis. The plots which were generated for each of the measurement points were very similar and almost superimposed. For this reason, one single plot for $N = 3$ is shown in **Figure 37**. The obtained values, from the analysis of each of the plots are given in **Table 8**.

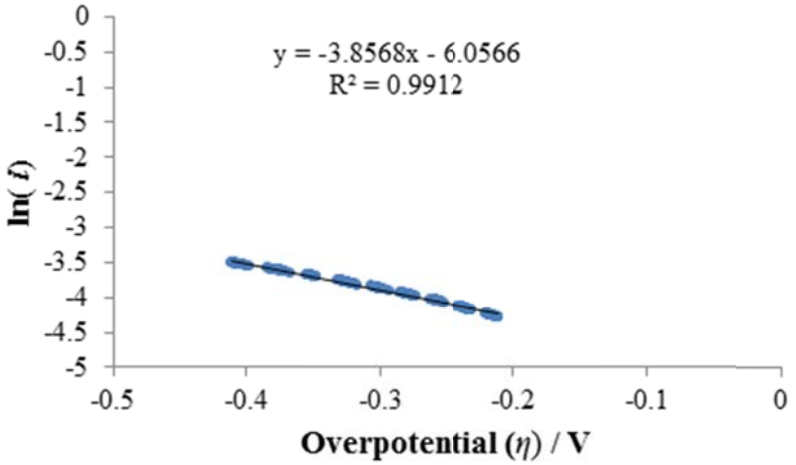

Figure 37. Tafel plot of cell 1 at $N = 3$ with the straight line showing the linear region used for calculating the y-axis intercept. Fuel: 3 % wet H_2 (2.5 SLPM), Oxidant: air (5 SLPM).

Table 8. Values of the exchange current density obtained from the intercept from the Tafel plots.

Data Acquisition Points	Y-Axis Intercept (A/cm^2)	Exchange Current Density i_o (mA/cm^2)
***N* = 1**	-6.0805	2.287
***N* = 2**	- 6.0801	2.288
***N* = 3**	- 6.0566	2.357
***N* = 4**	- 6.0673	2.317
***N* = 5**	- 6.0931	2.258

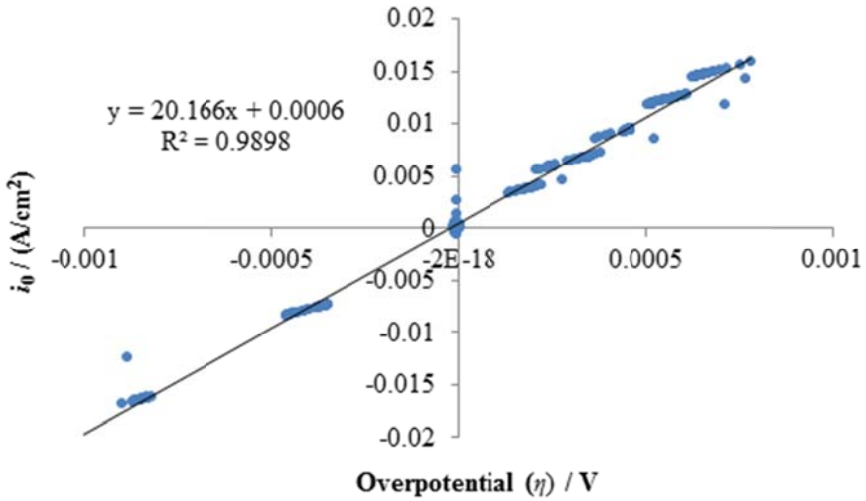

Figure 38. LPR plot of cell 1 at $N = 3$ with the straight line showing the linear region used for calculating the slope. Fuel: 3 % wet H_2 (2.5 SLPM), Oxidant: air (5 SLPM).

1.3.3.3. Linear Polarization Resistance (LPR) data

Linear polarization resistance is a very useful technique for measuring the charge transfer resistance for an electrochemical cell. At very low overpotentials, the current density follows a

linear relationship as a function of the overpotential. The slope of the linear function is approximately equal to the charge transfer resistance of the fuel cell and the low current approximation obtained from the Butler Volmer equation can be applied to estimate the exchange current density. For carrying out the test, data points were recorded within 10 mV of the open circuit potential both in galvanic and electrolytic region as shown in **Figure 38** and **Table 9**. The best fit linear equation is shown in the plot. The slope of the equation is shown as 20.166 which is simply the area specific charge transfer resistance.

Table 9. Values of the exchange current density obtained from the slope of the linear equation from the LPR test.

Data Acquisition Points	Slope of the linear equation (Ω cm^2)	Exchange Current Density i_0 (mA/cm^2)
$N = 1$	20.344	2.287
$N = 2$	20.377	2.288
$N = 3$	20.166	2.357
$N = 4$	20.314	2.317
$N = 5$	19.988	2.258

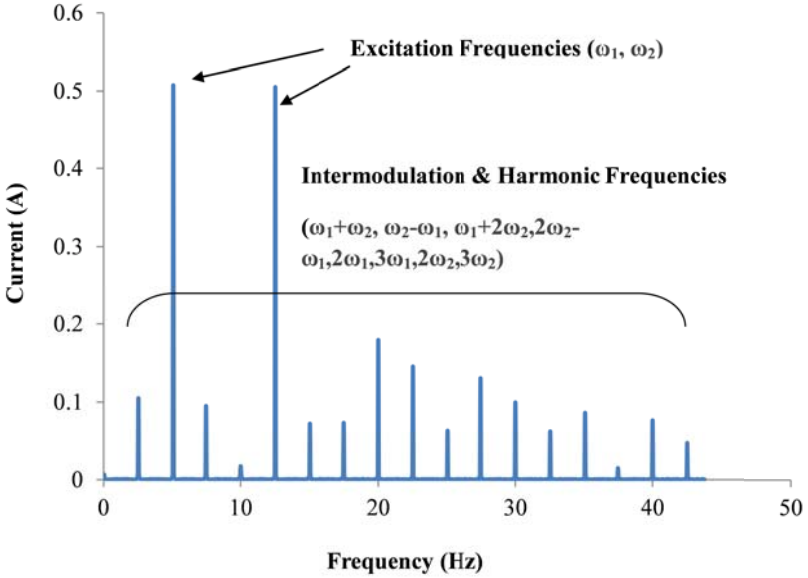

Figure 39. Intermodulation spectra of cell-1 at OCP. Fuel: 3 % Wet H_2 (2.5 SLPM), Oxidant: air (5 SLPM).

1.3.3.4. EFM Measurements

Frequency Modulation data were also recorded at similar time periods when the EIS and LSV were taken. Recording the data at the fixed time intervals gives the opportunity to test and compare the data obtained at the same time. This helps to keep the operating and process conditions to be similar when each of these 3 different sets of data was obtained. EFM is a fast technique which was completed within a few minutes. For this reason, it is expected that the overall experimental conditions do not change over the passage of the testing period. This helps to provide consistent results for each of the different methods. The exchange current values are directly calculated from the software package included in Gamry hardware. The EFM spectra is

termed as an intermodulation spectrum which has the y-axis as the current and x-axis as frequency. The spectra recorded at $N = 3$ has been shown in **Figure 39**.

Table 10. Values of the exchange current density and causality factors obtained from the Gamry EFM software**.**

Data Acquisition Points	Exchange Current Density i_0 (mA/cm^2)	Causality Factor (2)	Causality Factor (3)
$N = 1$	1.8000	1.783	2.790
$N = 2$	1.7028	1.838	3.019
$N = 3$	1.8721	1.888	3.262
$N = 4$	1.8344	1.977	2.788
$N = 5$	1.8540	2.018	2.880

Each of the intermodulation frequencies has been recorded inside the Gamry software and has been employed in empirical relations shown by Bosch. et al in their work. As can be seen in their work, there are causality factors (2) and (3) which serve as internal checks for the validity of the data. This helps in checking if the data is reliable and if at all could be used for further analysis. Causality factors are also calculated automatically in the software. The data obtained here (**Table 10**) are checked with the causality factors and are made sure that those data which satisfy with acceptable causality are chosen and included in this work. Usually the causality factors chosen as a standard for collecting data ranged from with +/- 0.5 from the ideal values of 2 and 3.

The exchange current density was measured using three very different electrochemical techniques at same operating and process conditions. It was observed that the values were close to each other and of the same order of magnitude and were of the same order of magnitude as shown in **Table 11**. It is well known from literature that EIS, LSV and LPR could be used for the calculation of exchange current. But in this work, we proposed the use of another powerful technique, EFM, in obtaining the value of the exchange current directly from in-situ testing. The advantage of EFM is that, it is a non-destructive technique and also is completed within a short period of time. One important aspect which is to be considered is that all the three tests have been performed using three different instruments from different suppliers. The instrument error should be present in all the three data sets, and that should be taken into account while doing the comparative analysis. The obtained values are compared with the values reported by other authors for solid oxide fuel cells with similar materials composition and operating temperature.

Table 11. Values of the exchange current density obtained from EIS, LSV, LPR & EFM.

Data Acquisition Points	i_o (mA/cm^2) EIS	i_o (mA/cm^2) LSV	i_o (mA/cm^2) LPR	i_o (mA/cm^2) EFM
$N = 1$	3.9591	2.287	2.287	1.8000
$N = 2$	3.7750	2.288	2.288	1.7028
$N = 3$	3.9090	2.357	2.357	1.8721
$N = 4$	3.7867	2.317	2.317	1.8344
$N = 5$	3.7743	2.258	2.258	1.8540

The exchange current density is a critical factor in determining the performance of a SOFC. It is a measure of the kinetics of the electrochemical charge transfer reaction. In this work, the operating conditions used were standard including the fuel. While carrying out the degradation analysis of fuel cell stacks under other hydrocarbon fuels and simulated reformate streams, it becomes useful to monitor the change of the exchange current density. This helps to judge how and to what extent the cell degradation is occurring with regards to change in electrochemical properties due to modification in the microstructure properties. In some cases, there are various inorganic impurities present in the other hydrocarbon fuel streams. This affects the fuel cell by reacting with the anode microstructure or by altering the shape and size of the active catalyst surface by reducing the amount of available triple phase sites for electrochemical reaction. In such instances, a direct change in the exchange current density is observed, which makes it even more imperative to measure them.

EFM has been used by many people in corrosion studies. In this work, it has been proposed for the first time to be used for solid oxide fuel cells. This provides an opportunity for researchers to measure electrochemical parameters and also gives a flexibility to use it along with impedance spectroscopy and linear sweep voltammetry to obtain values for exchange current. A direct estimation of the exchange current from the software after performing the tests gives a leverage to analyze the fuel cell performance instantly rather than collecting EIS data and perform theoretical analysis on the experimental results. This takes time before final calculations are completed. EFM also gives the values of the Tafel parameters (Tafel Slopes) and electrochemical transfer coefficients directly from the obtained data using the software. Even though this work does not deal with the above mentioned parameters, more theoretical and modeling work is being carried out in regards to analysis of the Tafel parameters which also provide very useful information on the kinetic performance of the solid oxide fuel cell.

2. Design of Fuel Processing Systems

2.1. Development of ADG Fuel Processor Concept (novel)

2.1.1. Evaluation of commercial sorbents for ADG

In this project, the recommended commercial adsorbents have been tested. The adsorbents include SulfaTrap^{TM}-R7 and SulfaTrap^{TM}-R8 from the TDA Research and the SulfaTreat from A Smith/Schlumberger Company. All the adsorbents are recommended by the corresponding companies, representing the best adsorbent for sulfur removal from biogas. The adsorbents were used as received without further pretreatment.

Figure 40 shows the breakthrough curves for H_2S removal from the simulated ADG gas containing 200 ppmv H_2S, 10 v% N_2, 40 v% CO_2, and 50 v% CH_4 over the commercial TDA SulfaTrap-R7, TDA SulfaTrap-R8 and Smith/Schlumberger SulfaTreat adsorbents at room temperature. Under current conditions, all the evaluated adsorbents can removal H_2S from the gas stream. The H_2S concentration in the effluent was below 60 ppbv over these three adsorbents before breakthrough. The TDA SulfaTrap-R7 exhibited the best performance for H_2S removal. It took about 4000 min (about 3 days) to break through, significantly longer than the other two adsorbents, as shown in **Figure 40**. The corresponding breakthrough capacity was about 38.9 mg-H_2S/g. The TDA SulfaTrap-R8 also showed good performance for H_2S removal. It took about 1700 min to break through. The corresponding breakthrough capacity was about 22.3 mg-H_2S/g. Compared to the TDA SulfaTrap-R7 and -R8 adsorbents, the sorption performance of the Smith/Schlumberger SulfaTreat adsorbent for H_2S removal at the same conditions was much worse. H_2S broke through in ca. 95 min. The calculated breakthrough capacity over this

adsorbent was only ca. 0.9 mg-H_2S/g, significantly lower than those of both TDA SulfaTrap-R7 and SulfaTrap-R8.

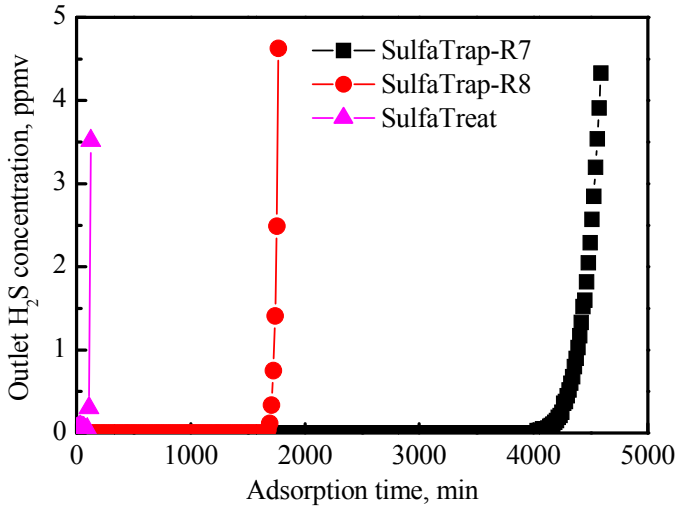

Figure 40. H_2S breakthrough curves for H_2S removal from the simulated ADG gas containing 200 ppmv H_2S, 10 v% N_2, 40 v% CO_2, and 50 v% CH_4 over the commercial TDA SulfaTrap-R7, TDA SulfaTrap-R8 and Smith/Schlumberger SulfaTreat adsorbent. Conditions: Volume of adsorbent bed, 1.9 ml; Temp, 25 °C; Pressure, 1 atm.; Flowrate, 50 ml/min (GHSV, ~1500 h^{-1}).

The adsorption performance of these three adsorbents for CO_2 capture has also been evaluated. The corresponding CO_2 breakthrough curves are presented in **Figure 41**, where C/C_o represents the ratio between the outlet CO_2 concentration and the initial one. As it can be seen, the outlet CO_2 concentration was close to the initial one. Furthermore, it almost reached the saturation point as soon as the model ADG gas was introduced. The results suggest that none of the adsorbents has the capability to remove CO_2 from ADG gas.

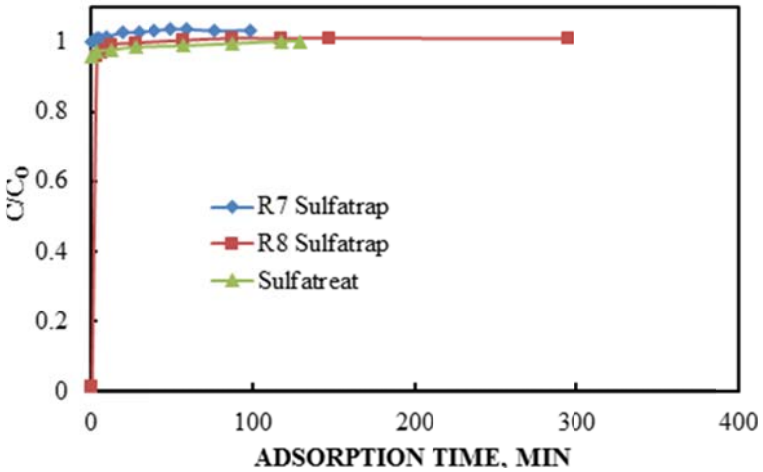

Figure 41. CO_2 breakthrough curves for CO_2 capture from the simulated ADG gas containing 200 ppmv H_2S, 10 v% N_2, 40 v% CO_2, 50 v% CH_4 over the commercial TDA SulfaTrap-R7, TDA SulfaTrap-R8 and Smith/Schlumberger SulfaTreat adsorbent. Conditions: Volume of adsorbent bed, 1.9 ml; Temp, 25 °C; Pressure, 1 atm.; Flowrate, 50 ml/min (GHSV, ~1500 h^{-1}).

Commercially available adsorbent, ZnO was also tested for ADG cleanup under different temperature, i.e., at room temperature (25 °C) and at 350 °C. The ZnO adsorbent (HTZ-5) was purchased from Haldor Topsoe. The detailed physical properties of the ZnO adsorbent are listed in **Table 12**. The adsorbent was used as received without further pretreatment.

Table 12. Typical physical parameters of ZnO oxide adsorbent, HTZ-5, Haldor Topsoe.

	HTZ-5
Shape	Extrudates
Size, diameter	4 mm
Length	4-8 mm
ZnO (wt%)	> 99
Al_2O_3 (wt%)	< 1

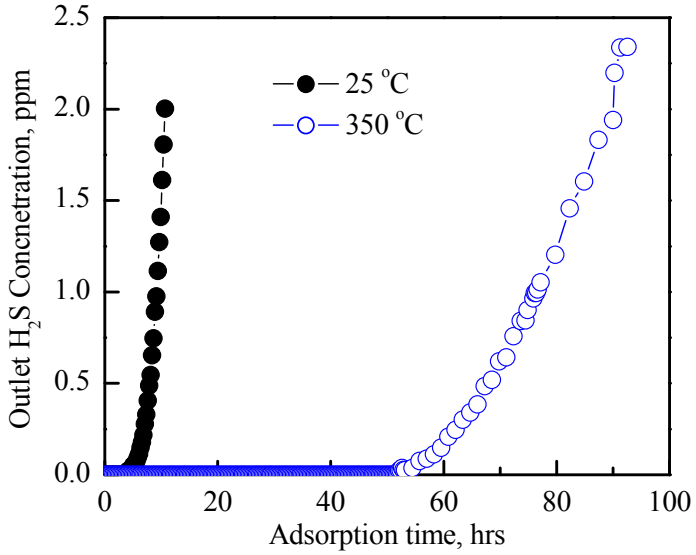

Figure 42. H_2S breakthrough curves for H_2S removal from the simulated ADG gas containing 200 ppmv H_2S- 10 v% N_2-40 v% CO_2-50 v% CH_4 over the commercial ZnO adsorbent at different adsorption temperatures. Conditions: Volume of adsorbent bed, 1.9 ml; Pressure, 1 atm.; Flowrate, 50 ml/min (GHSV, ~1500 h^{-1}).

Figure 42 shows the breakthrough curves for H_2S removal from the simulated ADG gas containing 200 ppmv H_2S- 10 v% N_2-40 v% CO_2-50 v% CH_4 over the commercial HTZ-5 ZnO adsorbent extrudates at room temperature (25 °C) and 350 °C. Under current conditions, the evaluated adsorbent can effectively remove H_2S from the gas stream. The H_2S concentration in the effluent was below 60 ppbv over these three adsorbents before breakthrough. However, the operation temperature can significantly affect the desulfurization performance of ZnO adsorbent. At room temperature, it took about 550 min to break through over the ZnO adsorbent. The corresponding adsorption capacity for H_2S was about 4.6 mg/g-A, still showing a good performance for ADG cleanup. As expected, raising the sorption temperature can result in the significant improvement in the sorption performance. As shown in **Figure 42**, at 350 °C, it took about 4600 min (or more than 3 days) to break through, significantly longer than the one obtained at room temperature. The corresponding breakthrough capacity was about 40.4 mg-H_2S/g-A, which is about one magnitude better than that at room temperature. The results confirm

that the conditions can greatly affect the performance of an adsorbent and the ZnO adsorbent prefers higher temperature for desulfurization. It demonstrates that commercial HTZ-5 ZnO adsorbent can effectively work for H_2S removal from ADG gas with very low H_2S concentration in the effluent before breakthrough, which is necessary for fuel cell applications.

In those experiments, the outlet CO_2 concentrations have also been tracked in the effluent by an on-line GC (SRI 8610C) with 5A and silica columns and a thermal conductive detector. No CO_2 adsorption was observed over the ZnO adsorbent, whether at 25 °C or at 350 °C, suggesting that ZnO adsorbent does not have the capability to remove CO_2 from ADG gas. It demonstrates that commercial HTZ-5 ZnO adsorbent can effectively work for H_2S removal from ADG gas with very low H_2S concentration in the effluent before breakthrough, which is necessary for fuel cell applications.

The H_2S adsorption performance of the commercial adsorbents for ADG is summarized in the **Table 13**. The results clearly show that at room temperature, the SulfaTrap-R7 adsorbent from TDA Research is the best adsorbent under the conditions studied in this project. The commercial ZnO adsorbent, HTZ-5 also exhibited an excellent capacity for H_2S removal but requires a higher operating temperature of 350 °C.

Table 13. H_2S adsorption performance of commercial adsorbents for ADG.

Adsorbent	Temp. °C	Cap(BT)*, LADG/g-sorb	Cap(BT)*, mg-H_2S/ml-sorb	Cap(BT)*, mg-H_2S/g-sorb
AC (EC)	25	0.25	0.015	0.07
HTZ-5 (ZnO)	25	16.5	4.0	4.6
	350	145.0	33.7	40.4
SulfaTreat	25	3.2	0.7	0.9
SulfaTrap-R8	25	79.6	12.5	22.3
SulfaTrap-R7	25	139.6	29.3	39.1

*Cap(BT) = Breakthrough Capacity at H_2S level of 100 ppb.

2.1.2. Novel Mesoporous Alumina Supported ZnO Adsorbents for ADG

Mesoporous alumina support was prepared via the cation-anion double hydrolysis method according the literature [23]. Typically, about 3.75 g of aluminum nitrate and 2.32 g of triblock copolymer Pluronic P123 ($EO_{20}PO_{70}EO_{20}$, MW=5800, Aldrich) were completely dissolved in 30 g of de-ionized water with stirring. At the same time, a 20 ml of solution containing 2.46 g of sodium aluminate was prepared and dropped into the aluminum nitrate solution under vigorous stirring. A white precipitate formed immediately. After further stirring at room temperature for 1 hr, the mixture was transferred into an autoclave and further treated to allow crystallization at 100 °C for 24 h. The resultant solid was recovered by filtration, washed with de-ionized water, dried at 100 °C overnight and finally calcined at 550 °C for 6 h with a heating rate of 2 °C/min.

The mesoporous alumina supported zinc oxide adsorbents were prepared by a wet impregnation method [24]. In a typical preparation, 300 mL of 2M potassium carbonate was added in 200 mL of 2M zinc nitrate solution with stirring. Then a calculated amount of mesoporous alumina was added in the suspension, and treated in an ultrasonic bath for 30 minutes. The mixture was then washed by 200 mL of 0.1M ammonia solution, and then by 100

mL of absolute ethanol. The filtrated solid was dried at 120 °C overnight and finally calcined at 250 °C for 3 h.

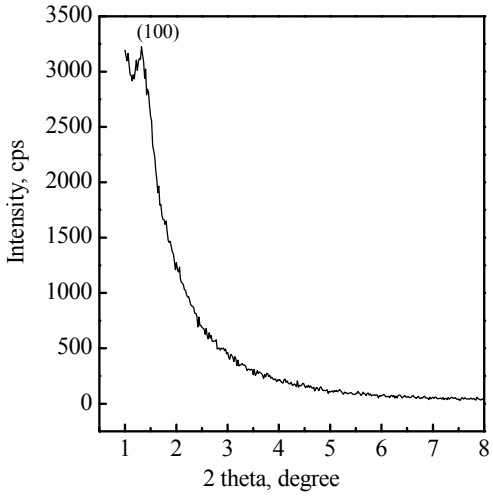

Figure 43. XRD profile of the synthesized mesoporous Al_2O_3 support.

The prepared mesoporous alumina has been characterized by x-ray diffraction (XRD) and N_2 adsorption-desorption method. **Figure 43** shows the XRD profile of the synthesized mesoporous alumina support at low angles. A characteristic peak was observed at $2\theta = 1.32^o$ in the diffraction of the synthesized Al_2O_3, indicating that the synthesized alumina has a typical mesoporous structure. It has been further confirmed by the N_2 adsorption-desorption characterization, as shown below.

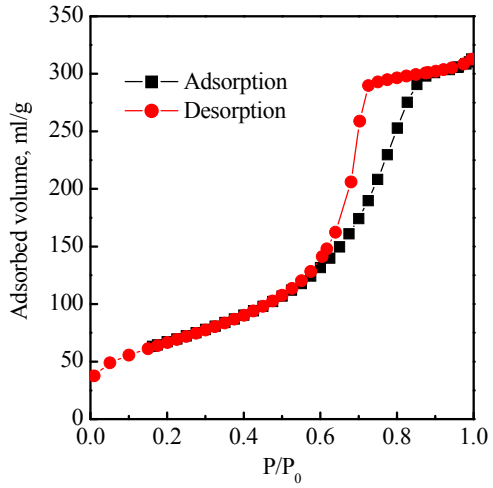

Figure 44. N_2 adsorption-desorption isotherm of mesoporous Al_2O_3.

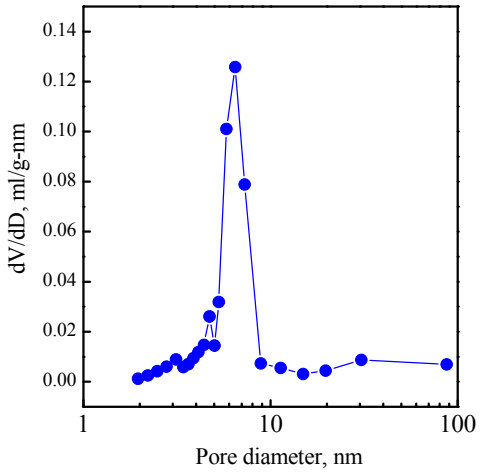

Figure 45. The pore size distribution calculated by BJH method.

Figure 44 shows the nitrogen adsorption-desorption isotherm for the synthesized alumina support. A typical type IV adsorption isotherm with a H1 hysteresis loop is obtained, indicating the uniform meso-structure of the synthesized Al_2O_3. On the basis of the nitrogen adsorption-

desorption isotherm, the surface area, pore volume and pore size of the mesoporous Al_2O_3 support can be calculated. **Figure 45** shows the pore size distribution curve calculated by BJH method. It shows that the material has a relative narrow distribution of the pore size, suggesting a uniform meso-structure. The mesoporous Al_2O_3 support synthesized in this period has a surface area of 244 m^2/g, a pore volume of 0.99 cm^3/g and a pore diameter of 6.5 nm. The surface area of the meso-Al_2O_3 support material is much higher than that of commercially available γ-Al_2O_3, whose surface area is about 150 m^2/g.

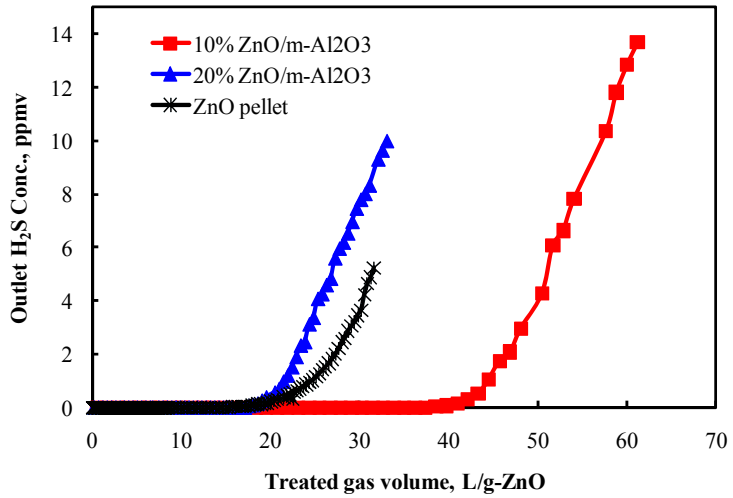

Figure 46. H_2S breakthrough curves for H_2S removal from the simulated ADG containing 200 ppmv H_2S- 10 v% N_2-40 v% CO_2-50 v% CH_4 over mesoporous alumina supported ZnO adsorbents at room temperature. Conditions: Volume of adsorbent bed, 2 ml; Pressure, 1 atm.; Flow-rate, 50 ml/min (GHSV, 1500 h^{-1}).

Figure 46 shows the breakthrough curves for H_2S removal from the simulated ADG gas containing 200 ppmv H_2S- 10 v% N_2-40 v% CO_2-50 v% CH_4 over the mesoporous Al_2O_3 supported ZnO adsorbents with different ZnO loadings at room temperature. For comparison, the commercial ZnO pellet adsorbent was also performed for the simulated ADG cleanup and the obtained breakthrough curve for H_2S removal is presented in Figure 8. At room temperature, the ZnO pellet shows a good performance for H_2S removal. It can treat about 24.7 L/g-ZnO of ADG before the outlet H_2S concentration is higher than 1 ppm. The corresponding adsorption capacity is 6.9 mg-H_2S/g-ZnO. When ZnO was loaded onto the mesoporous Al_2O_3 support at 10 wt%, the H_2S adsorption performance has been significantly improved. Before breakthrough at 1 ppmv, the treated ADG volume by 10 wt% ZnO/meso-Al_2O_3 adsorbent reaches as high as 44.5 L/g-ZnO, which is almost double of that of the commercial ZnO pellet. The corresponding H_2S adsorption capacity is also getting to 12.4 mg-H_2S/g-ZnO. The results suggest that using mesoporous alumina with high surface area as a support is beneficial to promote the performance of ZnO adsorbent for H_2S removal from ADG.

However, when ZnO loading increases to 20 wt%, the performance of ZnO/meso-Al_2O_3 adsorbent decreases much. Over the 20 wt% ZnO/meso-Al_2O_3 adsorbent, the treated ADG volume is about 21.5 L/g-ZnO before breakthrough with an adsorption capacity of 6.0 mg-H_2S/g-ZnO. The value is much lower than that for 10 wt% ZnO/meso-Al_2O_3, and even lower than that for the commercial ZnO pellet. Although there is no characterization data for the

mesoporous Al_2O_3 support ZnO adsorbents, generally lower loading gives better dispersion and smaller particles. Thus, the current results indicate that the H_2S adsorption capacity and ZnO usage for H_2S adsorption can be greatly promoted by loading onto a high surface area support with the improvement in the particle size and the dispersion of ZnO.

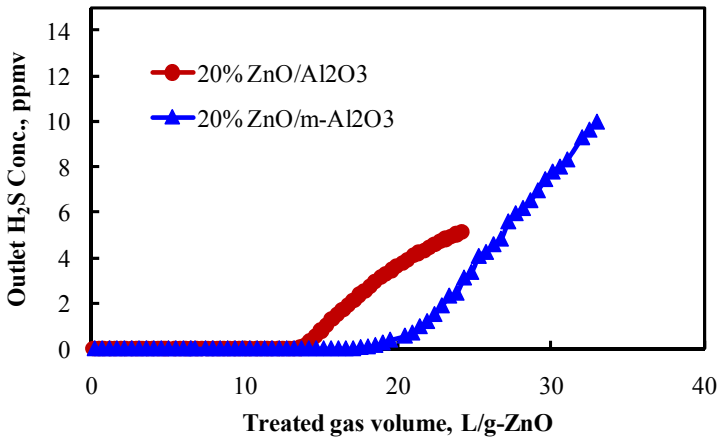

Figure 47. H_2S breakthrough curves for H_2S removal from the simulated ADG containing 200 ppmv H_2S- 10 v% N_2-40 v% CO_2-50 v% CH_4 over mesoporous alumina and commercial alumina supported ZnO adsorbents at room temperature. Conditions: Volume of adsorbent bed, 2 ml; Pressure, 1 atm.; Flow-rate, 50 ml/min (GHSV, ~1500 h^{-1}).

The beneficial effect on the adsorption performance of alumina supported ZnO adsorbents by using mesoporous alumina instead of commercial γ-Al_2O_3 has been investigated in this report period. **Figure 47** shows the breakthrough curves for H_2S removal from the simulated ADG gas containing 200 ppmv H_2S- 10 v% N_2-40 v% CO_2-50 v% CH_4 over the mesoporous Al_2O_3 and commercial γ-Al_2O_3 supported ZnO adsorbents at 20 wt% of ZnO loading. Compared to ZnO/meso-Al_2O_3, the treated ADG volume over the ZnO/γ-Al_2O_3 adsorbent is smaller, about 15.3 L/g-ZnO. The adsorption capacity is around 4.3 mg-H_2S/g-ZnO, lower than that of ZnO/meso-Al_2O_3 adsorbent (6.0 mg-H_2S/g-ZnO). The result exhibits that mesoporous alumina is a better support than commercial γ-Al_2O_3 for the preparation of supported ZnO adsorbents.

2.1.3. Novel metal oxide based adsorbents for sulfur removal from ADG

In this project, mesoporous titania-ceria metal oxide adsorbents were prepared via a urea precipitation/gelation according to the literature [25]. Prior to urea precipitation, aqueous solutions were prepared using cerium ammonium nitrate $(NH_4)_2Ce(NO_3)_6$ (Aldrich, 99.99%), titanium oxysulfate $TiOSO_4 \cdot xH_2SO_4 \cdot xH_2O$ (Aldrich, Ti: 18.5 wt %), and urea $CO(NH_2)_2$ (Aldrich 99+%). The total amount of cerium ammonium nitrate and titanium oxysulfate was 0.075 mol, but the Ti:Ce mole ratio was varied between 1:0 to 0:1. In a typical preparation, the prescribed amounts of cerium ammonium nitrate and titanium oxysulfate were dissolved in 200 mL of distilled water, respectively. Ammonium cerium nitrate aqueous solution was added to the titanium solution. The mixed aqueous solution was then added to 800 mL of aqueous solution containing 70 g of urea and stirred vigorously by a magnetic stirrer. The solution was heated to 90-95 °C and held there for 8 h, while the total liquid volume was kept at 1000 mL. The resulting precipitant was filtered and dried overnight in an oven at 110 °C. The dried precipitant was

crushed into powder and calcined in static air by heating at a rate of 1.5 °C/min from room temperature to 450 °C and kept at 450 °C for 6 h in a muffle furnace.

A series of TiO_2-CeO_2 mixed oxide adsorbents have been prepared with different Ti/Ce molar ratio including 9:1; 5:5 and 1:9 and evaluated for H_2S adsorption from model ADG steam containing 200 ppmv H_2S- 10 v% N_2-40 v% CO_2-50 v% CH_4 at room temperature. The obtained breakthrough curves and the calculated adsorption capacity are presented in **Figure 48** and **Table 14**, respectively.

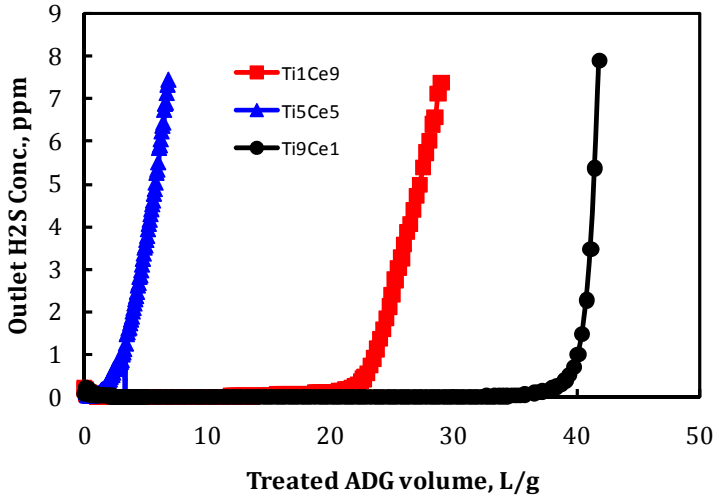

Figure 48. H_2S breakthrough curve for H_2S removal from the simulated ADG gas containing 200 ppmv H_2S- 10 v% N_2-40 v% CO_2-50 v% CH_4 over mesoporous TiO_2-CeO_2 mixed oxide adsorbent with different Ti/Ce molar ratio at room temperature. Conditions: volume of adsorbent bed, 2 ml; pressure, 1 atm.; flow-rate, 50 ml/min (GHSV, 1500 h^{-1}).

Table 14. The calculated adsorption capacity for TiO_2-CeO_2 material with different Ti/Ce ratio.

Sample	Temp., °C	Breakthrough Capacity, L-ADG/g	Breakthrough Capacity, mg-H_2S/g
$Ti_{0.9}Ce_{0.1}O_2$	25	40.5	11.3
$Ti_{0.5}Ce_{0.5}O_2$	25	3.2	0.9
$Ti_{0.1}Ce_{0.9}O_2$	25	23.7	6.6

The $Ti_{0.9}Ce_{0.1}O_2$ adsorbent showed the best adsorption capacity for H_2S adsorption for the model ADG at the studied conditions. It can treat about 40.5 L/g of ADG, corresponding to an adsorption capacity of 11.3 mg-H_2S/g-adsorbent. With the decrease of Ti/Ce ratio from 9 to 1, i.e., $Ti_{0.5}Ce_{0.5}O_2$ adsorbent, the adsorption performance of formed material dropped significantly, being 0.9 mg-H_2S/g-adsorbent, which is only 8% of that for the $Ti_{0.9}Ce_{0.1}O_2$ adsorbent. Interestingly, with the further decrease of the Ti/Ce ratio to 1/9, i.e., the adsorption performance increased again. The adsorption capacity was about 6.6 mg-H_2S/g-adsorbent over the $Ti_{0.1}Ce_{0.9}O_2$ adsorbent. The change in the adsorption capacity of the titania-ceria mixed oxide based adsorbents with the Ti/Ce ratio may suggest the adsorption sites over titania-ceria mixed oxide adsorbents may vary with the change of Ti/Ce ratio. So does the textural structure of titania-ceria mixed adsorbents.

Figure 49 shows the regenerability of $Ti_{0.9}Ce_{0.1}O_2$ adsorbent for H_2S removal from model ADG stream at room temperature. In each run, the spent adsorbent was regenerated using air flow at 350 °C for 2 hrs. After cooling to room temperature, the evaluation experiment was conducted at the same conditions.

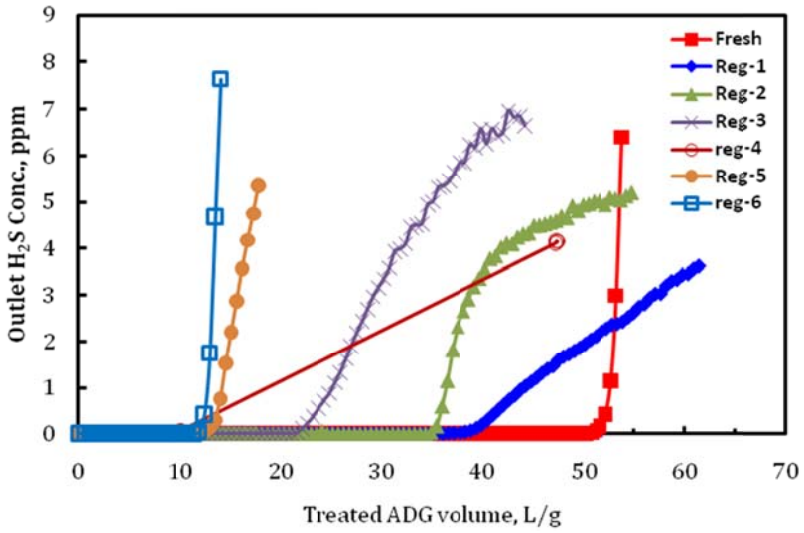

Figure 49. H_2S breakthrough curve for H_2S removal from the simulated ADG gas containing 200 ppmv H_2S-10 v% N_2-40 v% CO_2-50 v% CH_4 over mesoporous TiO_2-CeO_2 mixed oxide adsorbent with a Ti/Ce molar ratio of 9:1 at room temperature. Conditions: Volume of adsorbent bed, 2 ml; Pressure, 1 atm.; Flow-rate, 50 ml/min (GHSV, 1500 h^{-1}); The spent adsorbent was regenerated at 350 °C for 2 hrs.

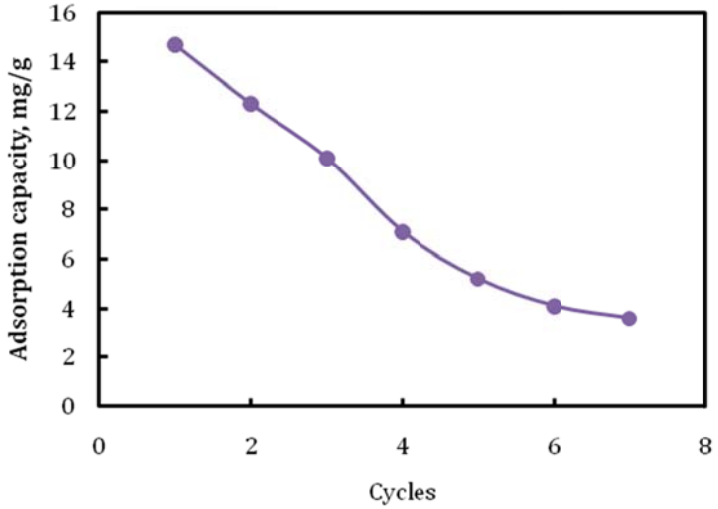

Figure 50. Adsorption capacity of $Ti_{0.9}Ce_{0.1}O_2$ adsorbent for H_2S removal from the simulated ADG gas containing 200 ppmv H_2S- 10 v% N_2-40 v% CO_2-50 v% CH_4 as a function of regeneration cycles. Adsorption conditions: Volume of adsorbent bed, 2 ml; Pressure, 1 atm.; Flow-rate, 50 ml/min (GHSV, 1500 h^{-1}). The spent adsorbent was regenerated at 350 °C in air for 2 hrs.

As it can be seen from the Figure, the fresh adsorbent showed a good performance of H_2S removal from model ADG stream at room temperature. It treated about 50 L of ADG per gram of adsorbent before H_2S broke through. After regeneration, the adsorption capacity decreased with the increase of regeneration time gradually. It was about 40 and 36 L of ADG per gram of adsorbent being treated before H_2S broke through for the first and second cycle of regeneration, respectively. After that, a quick drop in the adsorption capacity was observed. It was 20 and 10 L of ADG being cleaned over every gram of regenerated adsorbent, much lower than that of the fresh adsorbent. Promisingly, for 4^{th} to 6^{th} cycle of regeneration test, the decrease in the adsorption capacity became less.

To clearly show the trend of adsorption capacity of $Ti_{0.9}Ce_{0.1}O_2$ adsorbent with the regeneration cycles, the adsorption capacity as a function of regeneration cycles has been plotted and presented in **Figure 50**. Obviously, the $Ti_{0.9}Ce_{0.1}O_2$ adsorbent cannot be fully regenerated under current conditions. The adsorption capacity for H_2S decreased with the increase of regeneration cycles. After 6 cycles, the adsorption capacity was about 4.1 mg-H_2S/g-adsorbent, about 28% of that for the fresh adsorbent. Interestingly, the adsorption capacity did not change a lot, indicating that the adsorbent may be able to be regenerated at this level.

To further improve the H_2S adsorption performance of Ti-Ce adsorbent, copper incorporated Ti-Ce-O adsorbent has been prepared as the same procedure for the preparation of Ti-Ce-O by a co-precipitation method. The molar ratio of the prepared Cu-Ti-Ce-O adsorbent is 1:9:1 for Cu:Ti:Ce. The Cu-Ti-Ce-O adsorbent has been evaluated for H_2S removal from the simulated ADG containing 200 ppmv H_2S-10% N_2-40% CO_2-50% CH_4 at room temperature and 1 atm. The obtained H_2S breakthrough curve is presented in **Figure 51**. For comparison, those H_2S breakthrough curves obtained over Ti-Ce-O adsorbent, SulfurTrap R7 and SulfaTreat adsorbents are also presented.

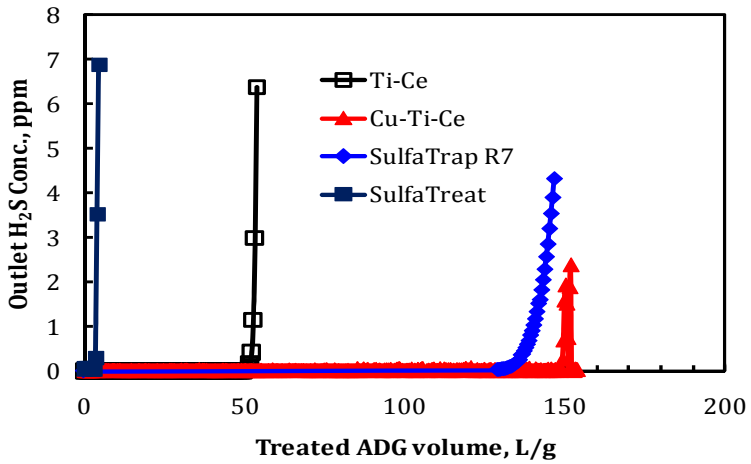

Figure 51. H_2S breakthrough curve over Cu-Ti-Ce mixed oxide adsorbent at room temperature. Conditions: Gas, 200 ppmv H_2S- 10 v% N_2-40 v% CO_2-50 v% CH_4; Volume of adsorbent bed, 2 ml; pressure, 1 atm.; flow-rate, 50 ml/min (GHSV, 1500 h^{-1}).

As it can be seen, Cu-Ti-Ce-O adsorbent exhibited very good performance for ADG cleanup. It can treat about 150 L-ADG/g before H_2S broke through. The corresponding adsorption capacity is 41.7 mg-H_2S/g, better than the best commercial adsorbent, SulfaTrap R7, tested in this project, which can treat about 139 L-ADG/g with an adsorption capacity of 39.1

mg-H_2S/g. The current result shows that the Cu-Ti-Ce-O adsorbent is more promising for ADG cleanup. More detailed study on this material will be carried out.

For comparison, the copper incorporated Ti-Ce-O adsorbent has also prepared by wet impregnation method and evaluated for H_2S adsorption from model ADG steam containing 200 ppmv H_2S- 10 v% N_2-40 v% CO_2-50 v% CH_4 at room temperature. As shown in **Table 15**, for the Cu-containing Ti-Ce-O adsorbents, different preparation method may generate the different status of copper particles with different physical and chemical properties, thus may result in different adsorption performance.

Table 15. The adsorption capacity of different adsorbents.

Sample	Temp., °C	Breakthrough Capacity, L-ADG/g	Breakthrough Capacity, mg-H_2S/g
Ti-Ce	25	40.5	11.3
Cu-Ti-Ce (7)	25	149.5	41.7
Cu-Ti-Ce (10)	25	120	33.4
Cu-Ti-Ce*	25	178.2	49.7
10% CuO/Ti-Ce*	25	136.2	38.0
SulfaTrap R7	25	139	39.1
SulfaTreat	25	3.2	0.9

Conditions: Gas, 200 ppmv H_2S- 10 v% N_2-40 v% CO_2-50 v% CH_4; Volume of adsorbent bed, 2 ml; pressure, 1 atm.; flow-rate, 50 ml/min (GHSV, 1500 h^{-1}). * Flow-rate, 200 ml.min (GHSV, 5454 h^{-1}).

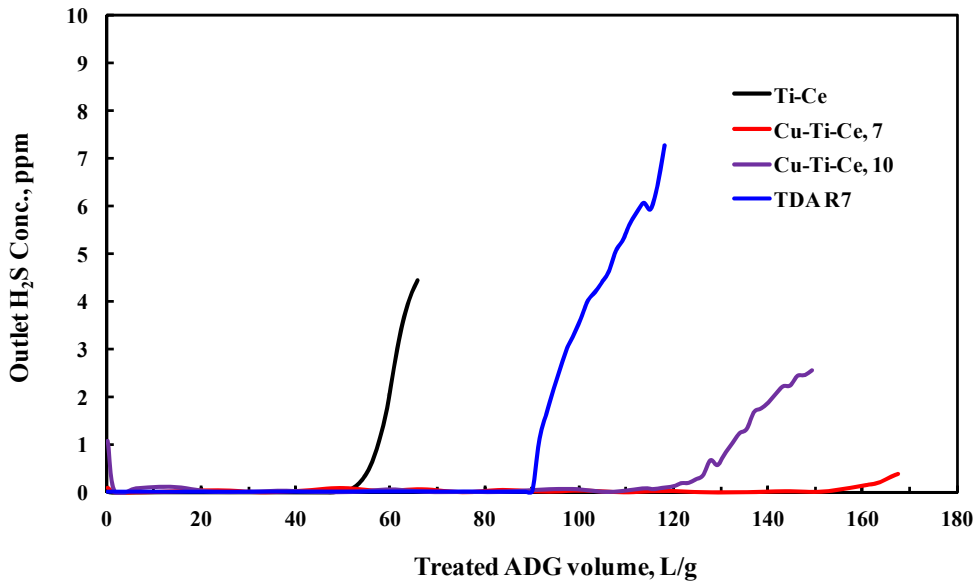

Figure 52. H_2S breakthrough curves over Ti-Ce, Cu-Ti-Ce-(7), Cu-Ti-Ce-(10) and TDA SulfurTrap R7 adsorbents at room temperature.

Additionally, during the preparation of Cu-Ti-Ce-O, the pH value was controlled to 7 and 10. The prepared Cu-Ti-Ce-(7) and Cu-Ti-Ce-(10) adsorbents have been evaluated for H_2S removal from the simulated ADG containing 200 ppmv H_2S-10% N_2-40% CO_2-50% CH_4 at room temperature and 1 atm. The obtained H_2S breakthrough curve is presented in **Figure 52**.

For comparison, those H_2S breakthrough curves obtained over Ti-Ce adsorbent and TDA SulfurTrap-R7 adsorbents are also presented. The obtained adsorption capacity is also listed in **Table 15**. Over the Cu-Ti-Ce-(7) adsorbent, about 150 L-ADG/g can cleaned before H_2S broke through. The corresponding adsorption capacity is 41.7 mg-H_2S/g. When, the Cu-Ti-Ce adsorbent was prepared at pH=10, the adsorption capacity for H_2S showed worse. The amount of ADG treated over Cu-Ti-Ce-(10) adsorbent was about 120 L-ADG/g (or 33.4 mg-H_2S/g), much lower than that of Cu-Ti-Ce-(7) adsorbent. It suggests that the preparation condition can affect the adsorption performance of the Cu-Ti-Ce adsorbent. It should be highlighted that both adsorbents exhibited much higher sulfur adsorption capacity than the best commercial adsorbent, TDA SulfaTrap R7, which can treat about 90 L-ADG/g with an adsorption capacity of 25.0 mg-H_2S/g at the studied conditions in this work.

To better understand the difference in the adsorption performance of Cu-Ti-Ce-O adsorbents for H_2S removal, the following characterizations have been performed. **Figure 53** shows the nitrogen adsorption-desorption isotherms for Ti-Ce, fresh Cu-Ti-Ce (7), spent Cu-Ti-Ce (7) and 10% CuO/Ti-Ce adsorbents. A typical type-IV adsorption isotherm with a H1 hysteresis loop was obtained over all Ti-Ce based adsorbents, indicating the Ti-Ce-based metal oxide adsorbents have a uniform meso-structure prepared by co-precipitation method. After 10 wt% CuO was impregnated to Ti-Ce adsorbent, the S-shape adsorption isotherm was still observed suggesting the meso-structure was preserved. For the sample of spent Cu-Ti-Ce (7), after ADG cleanup, the N_2 isotherm still showed a similar shape to that of the fresh one, suggesting the purification process did not destroy the pore structure.

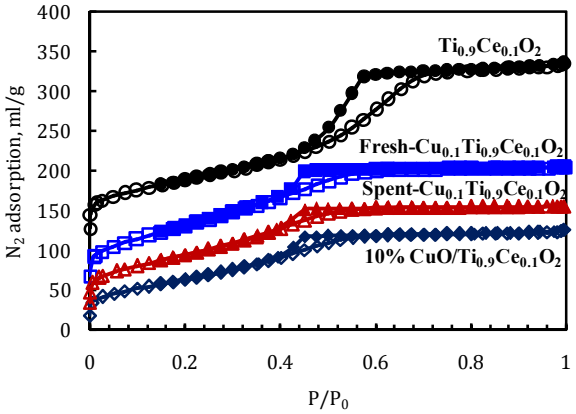

Figure 53. N_2 adsorption isotherms obtained at -196 °C.

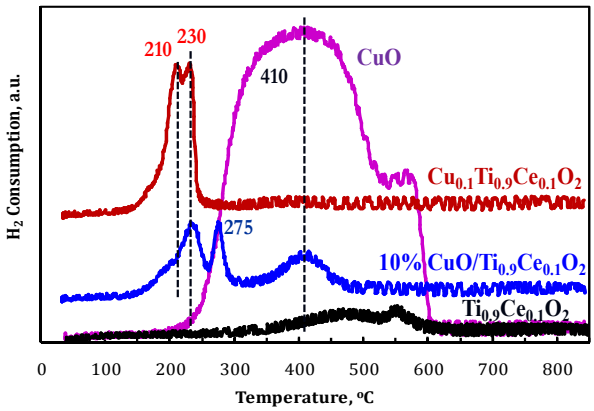

Figure 54. H_2-TPR Profiles.

Table 16. The porous properties of Ti-Ce oxide-based adsorbents.

Sample	BET Surface Area, m^2/g	Pore Volume, ml/g	Pore Diameter, nm
Ti-Ce	280	0.35	4.3
Cu-Ti-Ce (7)	331	0.26	3.7
Cu-Ti-Ce (10)	212	0.24	3.7
10% CuO/Ti-Ce	230	0.19	3.6
Spent Cu-Ti-Ce (7)	269	0.21	3.4

On the basis of the nitrogen adsorption-desorption isotherms, the BET surface area, pore volume and pore size of Ti-Ce based metal oxide adsorbents can be calculated, which are listed

in **Table 16**. All the Ti-Ce based adsorbents showed a narrow pore distribution in the range of 3-5 nm, which hints the uniform pore structure of the prepared materials. The Ti-Ce (9:1) adsorbent has a surface area of 280 m^2/g, a pore volume of 0.35 ml/g and a pore size peaked at 4.3 nm. After 10 wt% CuO loading by impregnation, the surface area, pore volume and pore size decreased to 230 m^2/g, 0.19 ml/g, and 3.6 nm, respectively, suggesting that the loaded CuO may located inside the pore channels of Ti-Ce support [26,27]. For the sample of Cu-Ti-Ce (7) prepared by co-precipitation method, it showed a higher surface area, but lower pore volume and smaller pore diameter compared to Ti-Ce (9:1) material, being 331 m^2/g, 0.26 ml/g and 3.7 nm, respectively. After ADG cleanup, the surface area decreased a lot, being 269 m^2/g, while there was only a slight change in pore volume and pore diameter as shown in **Table 16**. It may suggest that surface copper species are mainly responsible for sulfur removal in ADG stream. The current result reveals that high surface area is beneficial to the Ti-Ce based adsorbents for ADG cleanup and may be more important than pore volume and pore size. When the pH value was adjusted to 10, the resultant Cu-Ti-Ce-(10) adsorbent also showed very similar data in texture properties: a surface area of 212 m^2/g, a pore volume of 0.24 ml/g and a pore size of 3.7 nm. The current result clearly reveals that the final pH value for material preparation does not affect the texture properties of the Cu-Ti-Ce adsorbent. There must be other reasons causing the great change in sulfur adsorption capacity of the Cu-Ti-Ce adsorbent obtained at different pH value.

The redox property of Ti-Ce-O based adsorbents has been examined by H_2-TPR technique and the results are shown in **Figure 54**. For comparison, the H_2-TPR profile of a commercial copper oxide powder purchased from Aldrich is also presented. As it can be seen, the Ti-Ce (9:1) adsorbent showed a wide and weak reduction peak ranged from 300 to 600 °C, which may mainly relate to the partial reduction of CeO_2 in the mixed metal oxide [25]. The low reduction peak may be due to high oxygen deficiency in the material [25]. The bulk CuO gave a wide reduction peak from 200 to 600 °C with centered at about 410 °C, as shown in Figure 4. After loading 10 wt% CuO over Ti-Ce (9:1) material, there are three main reduction peaks located at 230, 275 and 410 °C, respectively, suggesting three different types of copper oxide species. The bulk-like copper oxide may contribute to the reduction peak at 410 °C, while the reduction occurred at 230 °C may be attributed to those CuO species located inside the pores. The reduction peak at 275 °C can be tentatively attributed to those small CuO particles located over the external surface of Ti-Ce support. Over Cu-Ti-Ce (1:9:1) adsorbent prepared by co-precipitation method, only two strong reduction peaks are observed at 210 and 230 °C. It may suggest that CuO species over Cu-Ti-Ce (1:9:1) adsorbent are only located inside the pores and the two reduction peaks can be attributed to the reduction of CuO to Cu_2O and the further reduction of Cu_2O to Cu, respectively. The current H_2-TPR results clearly show that CuO species in Cu-Ti-Ce (1:9:1) adsorbent is easier to reduce than those in 10% CuO/Ti-Ce (9:1) adsorbent, which may be a reason that the Cu-Ti-Ce (1:9:1) adsorbent gave a better performance of sulfur removal.

We have further examined the redox property of Ti-Ce-O adsorbents prepared at different pH value by H_2-TPR technique and the results are shown in **Figure 55**. As seen, the Ti-Ce adsorbent showed a wide and weak reduction peak ranged from 400 to 650 °C, which may mainly relate to the partial reduction of CeO_2 in the mixed metal oxide [25]. The low reduction peak may be due to high oxygen deficiency in the material [25]. Over Cu-Ti-Ce adsorbent prepared by co-precipitation method, only two strong reduction peaks are observed at 189 and 216 °C. It may suggest that CuO species over Cu-Ti-Ce adsorbent are only located inside the pores and the two reduction peaks can be attributed to the reduction of CuO to Cu_2O and the

further reduction of Cu_2O to Cu, respectively. As shown in Figure 5, the Cu-Ti-Ce-(7) and Cu-Ti-Ce-(10) adsorbents showed very similar H_2-TPR profiles, giving the same reduction peaks. It indicates that the final pH value in the material preparation does not change the redox property of Cu-Ti-Ce adsorbent. However, the peak area, which represents the hydrogen consumption for CuO reduction is different. The amount for Cu-Ti-Ce-(7) adsorbent was higher than that for Cu-Ti-Ce-(10) adsorbent. The area of reduction peak at the temperature range of 100-300 °C for the Cu-Ti-Ce-(10) adsorbent is about 80% of that for the Cu-Ti-Ce-(7) adsorbent, i.e., the CuO amount in the Cu-Ti-Ce-(10) adsorbent is about 80% of that in the Cu-Ti-Ce-(7) adsorbent. We have noticed that the adsorption capacity of the Cu-Ti-Ce-(10) adsorbent (120 L-ADG/g) is also about 80% of that for the Cu-Ti-Ce-(7) adsorbent (150 L-ADG/g). The H_2-TPR results support that the amount of CuO over the Cu-Ti-Ce adsorbent decreased with the increase in the pH value from 7 to 10 during co-precipitation. The current study also implies that the active component for sulfur adsorption over the Cu-Ti-Ce adsorbent is mainly the copper oxide species.

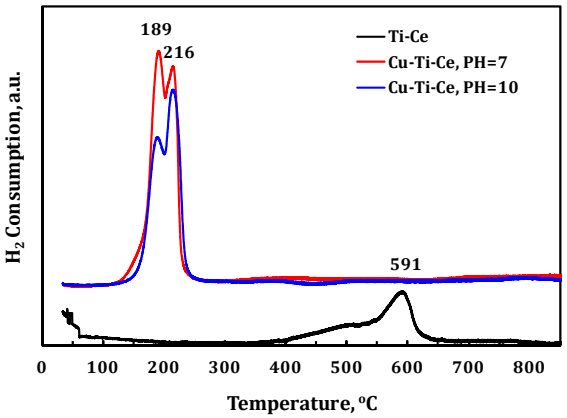

Figure 55. H_2-TPR Profiles.

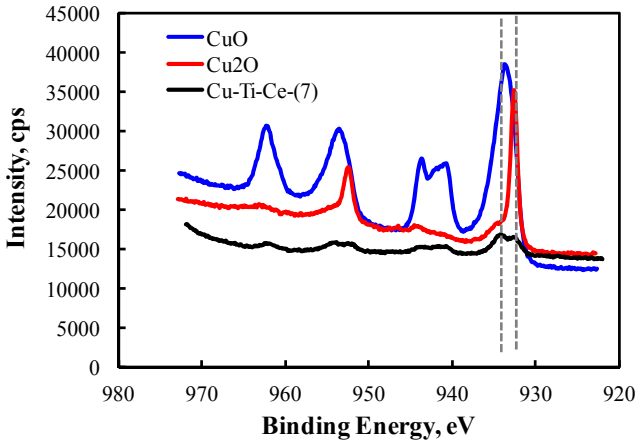

Figure 56. XPS Cu 2p spectra for standard CuO, Cu_2O samples and Cu-Ti-Ce-(7) adsorbent.

XPS analysis was conducted to understand the surface chemical state of Cu, Ti, Ce, and O in Cu-Ti-Ce-(7) oxides. Figure 8 shows the XPS Cu 2p1/2 and Cu 2p3/2 spectra of Cu-Ti-Ce-(7) mixed oxides prepared via co-precipitation at pH value of 7. For comparison and identification, the standard XPS Cu 2p spectra from CuO and Cu_2O were also collected and presented in **Figure 56**. As can be seen, the Cu 2p peaks for CuO sample was at 934, 942, 944, 954 and 962 eV. As for the Cu_2O sample, the typical Cu 2p peaks located at 933 and 952 eV. Over the Cu-Ti-Ce-(7) adsorbent, the XPS Cu 2p signal was much lower compared to the CuO and Cu_2O samples. The Cu 2p3/2 peaks at 933 and 934 eV were clearly observed, indicating that the chemical state of Cu in the Cu-Ti-Ce-(7) adsorbent may contain both Cu^{2+} and Cu^{+}, which may be the reason why the Cu-Ti-Ce-(7) adsorbent showed such a good performance for sulfur removal.

Figure 57 shows the XPS Ti 2p1/2 and Ti 2p3/2 spectra of the standard TiO_2 sample and the Cu-Ti-Ce-(7) mixed oxide adsorbent prepared via co-precipitation at pH value of 7. The standard TiO_2 sample gave the XPS Ti 2p peaks at 458.8 and 464.7 eV. Over the Cu-Ti-Ce-(7) adsorbent, the Ti 2p peaks located 458.4 and 464.2 eV, suggesting a clear red shift in binding energy for Ti in the Cu-Ti-Ce-(7) adsorbent compared to pure TiO_2 sample. This red shift in the

Ti 2p binding energy implies that the oxidation state of Ti in the Cu-Ti-Ce-(7) mixed oxide adosrbent was estimated as lower than 4+, probably being reduced by the co-existence of Ce in the bulk, as observed by Watanabe et al. [25].

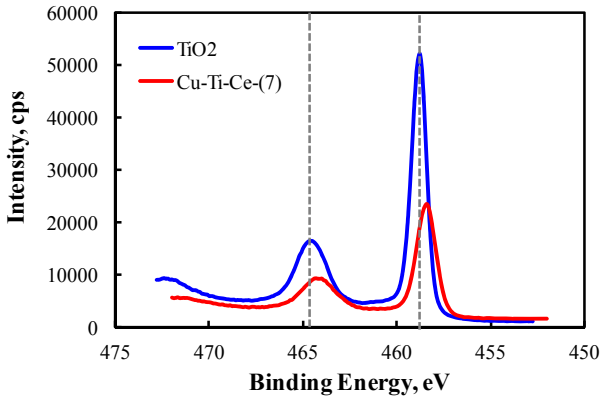

Figure 57. XPS Ti 2p spectra for the standard TiO_2 sample and the Cu-Ti-Ce-(7) adsorbent.

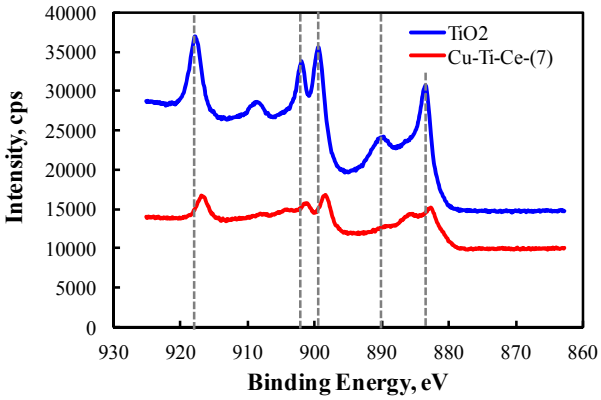

Figure 58. XPS Ce 3d spectra for the standard CeO_2 sample and the Cu-Ti-Ce-(7) adsorbent.

Figure 58 shows the XPS Ce 3d spectra of the standard CeO_2 sample and the Cu-Ti-Ce-(7) mixed oxide adsorbent prepared via co-precipitation at pH value of 7. Ce 3d spectrum of CeO_2 shows six peaks at 917.9, 908.5, 902.0, 899.5, 890.2, and 883.5 eV. These peaks represent the presence of Ce^{4+} [1]. The intensity of these six peaks decreased greatly over the Cu-Ti-Ce-(7) adsorbent. The peak intensity at 908.5 and 890.2 eV even vanished. In addition, the peak position for the other four peaks shifted to a lower binging energy, becoming 916.7, 901.4, 898.9 and 882.7 eV. These changes in the Ce 3d XPS spectra point to the increased Ce^{3+} concentration of total Ce in the Cu-Ti-Ce-(7) mixed oxide compared to the CeO_2 sample [25].

Figure 59 shows O 1s spectra of CuO, Cu_2O, TiO_2, CeO_2 and Cu-Ti-Ce-(7) mixed oxide adsorbent. Binding energy of O 1s for surface oxygen of these oxides was 529.6 eV for TiO_2, 529.0 eV for CeO_2, 529.7 eV for CuO and 530.6 eV with a shoulder at 531.6 eV for Cu_2O, respectively, suggesting that the binding energy for O 1s changes slightly with the adjacent metal element. As for the Cu-Ti-Ce-(7) adsorbent, the binding energy of O 1s for the surface oxygen was 529.9 eV, slightly higher than those for TiO_2 and CuO, close to the one for Cu_2O. No individual O 1s peak corresponding to these TiO_2, CeO_2, CuO and Cu_2O appears in the spectra of Cu-Ti-Ce-(7) mixed oxide. Such a binding energy of the O 1s for the Cu-Ti-Ce-(7) adsorbent may suggest that Cu, Ti and Ce chemically interact with one aother in the CuO-TiO_2-CeO_2 mixed oxide. In other words, the mixed oxides are not mixtures of these three different oxides but rather a uniform solid solution in which Cu, Ti and Ce have chemical interactions, which may reduce the chemical state of these elements.

Consequently, the XPS analysis on Cu, Ti, Ce and O elements over the Cu-Ti-Ce-(7) adsorbent showed that the introduction of CuO, TiO_2 into CeO_2 can cause the partial reduction of all these three metal oxides which may induce the formation of oxygen vacancy on the surface. As observed over Ti-Ce series adsorbents for desulfurization of organic sulfur compounds from liquid hydrocarbon fuels, the oxygen vacancy played a critical role for sulfur removal from the simulated ADG gas stream under room temperature and atmospheric pressure [25]. Further XPS analysis on the Cu-Ti-Ce adsorbents prepared via wet impregnation, incipient wet impregnation,

co-precipitation at pH value of 10 and physically mixing of CuO oxide and the prepared Ti-Ce material is need to clarified the effect of preparation method on their desulfurization performance for H_2S removal from the anaerobic digest gas.

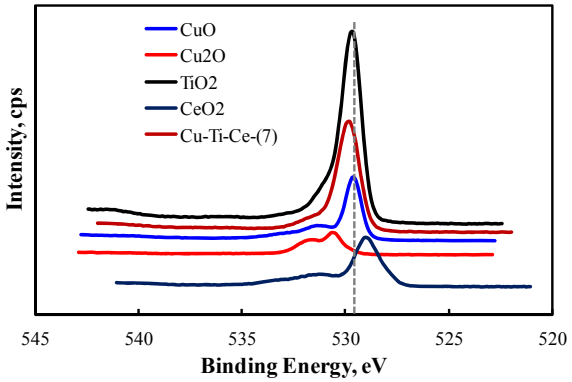

Figure 59. XPS O 1s spectra for CuO, Cu_2O, TiO_2, CeO_2 and the Cu-Ti-Ce-(7) adsorbent.

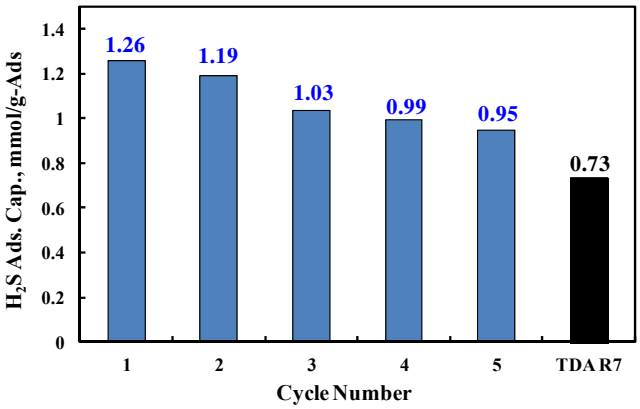

Figure 60. H_2S adsorption capacity as a function of regeneration cycle number over the CuO-TiO_2-CeO_2 (7) adsorbent. H_2S adsorption and adsorbent regeneration was performed at room temperature and 350 °C, respectively.

The prepared CuO-TiO_2-CeO_2 (7) adsorbent has been evaluated for H_2S removal from the simulated ADG containing 200 ppmv H_2S-10% N_2-40% CO_2-50% CH_4 at room temperature and 1 atm. The spent adsorbent was then regenerated in situ with flowing air (50 ml/min) at 350 °C for 30 min. The adsorption-regeneration has been carried out for 5 cycles. **Figure 60** shows the calculated adsorption capacity as a function of regeneration cycle number over the CuO-TiO_2-CeO_2 (1:9:1) adsorbent. For comparison, the adsorption capacity obtained over the fresh TDA SulfaTrap R7 adsorbent is also presented. As seen, with the increase of regeneration cycle number, the adsorption capacity decreases. It was about 1.26 mmol-H_2S/g-Ads (or 42.8 mg-H_2S/g-Ads) for the fresh CuO-TiO_2-CeO_2 (1:9:1) adsorbent. After 1st regeneration, the adsorption capacity slightly dropped to 1.19 mmol-H_2S/g-Ads, about 94% recovered. Then the adsorption capacity decreased gradually to 1.03, 0.99 and 0.95 mmol-H_2S/g-Ads for the 2nd, 3rd and 4th regeneration, showing a recovery of 82%, 78% and 75%, respectively. The decreasing trend suggests that the adsorption capacity of CuO-TiO_2-CeO_2 (1:9:1) adsorbent can be partially recovered. It is worth mentioning that the regenerated adsorbent still shows a high capacity for H_2S removal. Compared to the fresh TDA SulfaTrap R7 adsorbent, which has a capacity of 0.73 mmol-H_2S/g-Ads, the regenerated CuO-TiO_2-CeO_2 (1:9:1) adsorbent showed much higher capacity. Even after 5 adsorption-regeneration cycles, the obtained capacity still reached 0.95 mmol-H_2S/g-Ads, about 30% higher than that for the fresh TDA SulfaTrap R7 adsorbent. The current results strongly imply that the developed CuO-TiO_2-CeO_2 (1:9:1) adsorbent in this project is promising for H_2S removal from biogas.

In order to better understand the role of Cu in the Cu-Ti-Ce-O adsorbent, the prepared Cu-Ti and Cu-Ce and Cu/Ti-Ce(P-M) adsorbents have been prepared and evaluated for H_2S removal from the simulated ADG containing 200 ppmv H_2S-10% N_2-40% CO_2-50% CH_4 at room temperature and 1 atm. The obtained H_2S breakthrough curve is presented in **Figure 61**.

For comparison, those H_2S breakthrough curves obtained over Ti-Ce, Cu-Ti-Ce-(7) adsorbent and TDA SulfurTrap R7 adsorbents are also presented. The obtained adsorption capacity is listed in **Table 17.**

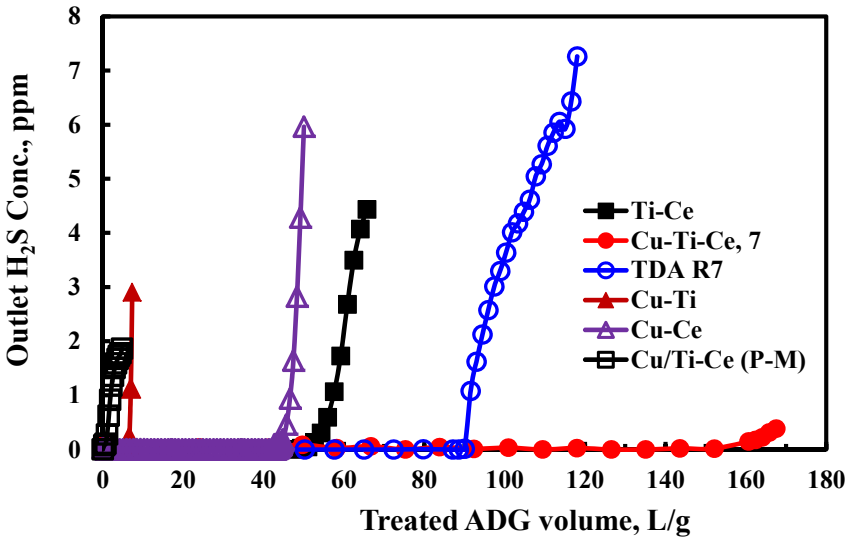

Figure 61. H_2S Breakthrough Curves over Ti-Ce, Cu-Ti, Cu-Ce, Cu/Ti-Ce (P-M), Cu-Ti-Ce-(7), and TDA SulfurTrap R7 Adsorbents at Room Temperature.

Table 17. The Adsorption Capacity of Different Adsorbents.

Sample	Temp., °C	Breakthrough Capacity, L-ADG/g	Breakthrough Capacity, mg-H_2S/g
Ti-Ce	25	52	14.4
Cu-Ti	25	6.3	1.8
Cu-Ce	25	44.3	12.3
Cu/Ti-Ce (P-M)	25	0.8	0.2
Cu-Ti-Ce-(7)	25	150	41.7
TDA SulfaTrap R7	25	90	25.0

Conditions: Gas, 200 ppmv H_2S- 10 v% N_2-40 v% CO_2-50 v% CH_4; Volume of adsorbent bed, 2 ml; pressure, 1 atm.; flow-rate, 200 ml.min (GHSV, 5454 h^{-1}).

As seen, Cu-Ce adsorbent can treat about 44 L-ADG/g (or 12.3 mg-H_2S/g) before breakthrough. Compared to the Ti-Ce adsorbent which has a breakthrough capacity of 52 L-ADG/g (or 14.4 mg-H_2S/g), it is slightly lower. However, over the Cu-Ti adsorption, the adsorption performance for H_2S removal from the simulated ADG stream is much worse. It can only treat about 6.3 L-ADG/g (or 1.8 mg-H_2S/g), which is significantly lower than that of Cu-Ce and Ti-Ce, about 7 and 9 times lower. The results may suggest that the Ti-Ce composition may be more crucial for achieving a good adsorbent with high performance for H_2S adsorption from the model ADG stream under the studied conditions.

With the addition of copper, the adsorption performance was improved significantly. Over the Cu-Ti-Ce-(7) adsorbent, about 150 L-ADG/g can cleaned before H_2S broke through. The corresponding adsorption capacity is 41.7 mg-H_2S/g. However, when, the Cu-Ti-Ce adsorbent was prepared by physical mixing method, i.e., the Cu/Ti-Ce (P-M) adsorbent, the adsorption capacity for H_2S showed significantly worse. The amount of ADG treated over Cu/Ti-

Ce (P-M) adsorbent was only about 0.8 L-ADG/g (or 0.2 mg-H_2S/g), more than two order of magnitude lower that of Cu-Ti-Ce-(7) adsorbent. The best commercial adsorbent, TDA SulfaTrap R7, can treat about 90 L-ADG/g (or 25.0 mg-H_2S/g) at the studied conditions in this work. In our previous report, we have showed that the Cu-Ti-Ce adsorbents prepared via co-precipitation at pH=10, via wet impregnation method and via incipient wet impregnation method exhibited great difference in the breakthrough capacity for H_2S removal from ADG stream. It supports that the preparation condition can greatly affect the adsorption performance of the Cu-Ti-Ce adsorbent. Among the prepared Cu-Ti-Ce samples, the one prepared via co-precipitation at pH value of 7 showed the best, while the one prepared by physically mixing copper oxide with Ti-Ce mixed oxide gave the worst performance for H_2S.

The adsorbents including TiO_2-CeO_2, CuO-TiO_2, CuO-CeO_2 and CuO/TiO_2-CeO_2-(p) were characterized by nitrogen physisorption for their porous properties including surface area, pore volume and pore diameter. **Figure 62** shows the nitrogen adsorption-desorption isotherms for TiO_2-CeO_2, CuO-TiO_2, CuO-CeO_2 and CuO/TiO_2-CeO_2-(p) adsorbents. The result for the CuO-TiO_2-CeO_2 adsorbent prepared by co-impregnation method with pH value at 7 is also presented for comparison. As can be seen, the typical type-IV adsorption isotherm with a H1 hysteresis loop was obtained over the TiO_2-CeO_2, CuO-TiO_2 and CuO-TiO_2-CeO_2 adsorbents, indicating these adsorbents have a uniform meso-structure prepared by co-precipitation method. The CuO/TiO_2-CeO_2-(p) adsorbent prepared by physical mixing of CuO and TiO_2-CeO_2 also gave a type-IV isotherm with a H1 hysteresis loop, suggesting that the meso-structure of TiO_2-CeO_2 is pertained. Over the CuO-CeO_2 adsorbent, although a hysteresis loop can be observed, it is locating at lower P/P_0 value and show much smaller, compared to other adsorbents.

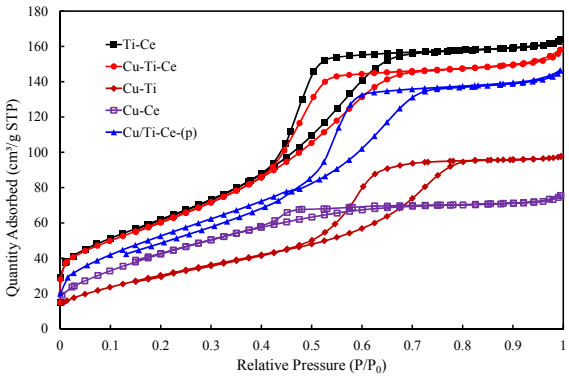

Figure 62. N_2 adsorption isotherms obtained at -196 °C.

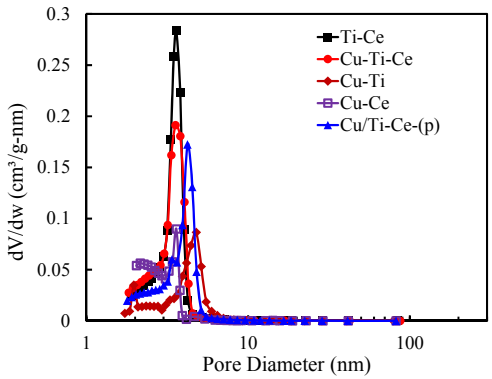

Figure 63. Pore size distribution calculated by BJH method from N_2 desorption branch.

On the basis of the nitrogen adsorption-desorption isotherms, the BET surface area, pore volume and pore size of these adsorbents can be calculated, which are listed in **Table 18**. The pore size distribution calculated by BJH method from the N_2 desorption branch is presented in **Figure 63**. All the adsorbents showed a narrow pore distribution in the range of 3-5 nm, which hints the uniform pore structure of the materials prepared in this work. The TiO_2-CeO_2 adsorbent has a surface area of 223 m^2/g, a pore volume of 0.25 ml/g and a pore size peaked at 3.6 nm as shown in Table 2. For the sample of CuO-TiO_2-CeO_2 prepared by co-precipitation method, it showed a surface area of 218 m^2/g, a pore volume of 0.24 ml/g and a pore size peaked at 3.6 nm. After TiO_2-CeO_2 was physically mixed with commercial CuO, the formed CuO/TiO_2-CeO_2-(p) adsorbent gave a surface area of 193 m^2/g, a pore volume of 0.23 ml/g and a pore size peaked at

4.2 nm. Both the surface area and pore volume were slightly smaller than those for the TiO_2-CeO_2 adsorbent and CuO-TiO_2-CeO_2 adsorbents. As for the Cu-TiO_2 and CuO-CeO_2 adsorbent, the obtained surface areas were even smaller compared to Ti-Ce based adsorbents. The surface area was 113 and 158 m^2/g, and pore volume was 0.16 and 0.12 ml/g, respectively, for the Cu-TiO_2 and CuO-CeO_2 adsorbent. It is expected higher surface area may give a higher adsorption capacity, which will be examined in the next report period for H_2 removal from a simulated ADG.

Table 18. The porous properties obtained from the nitrogen isotherm for the adsorbents.

Sample	BET Surface Area, m^2/g	Pore Volume, ml/g	Pore Diameter, nm
TiO_2-CeO_2	223	0.25	3.6
CuO-TiO_2-CeO_2	218	0.24	3.6
CuO-TiO_2	113	0.16	4.5
CuO-CeO_2	158	0.12	3.9
CuO/TiO_2-CeO_2-(p)	193	0.23	4.2

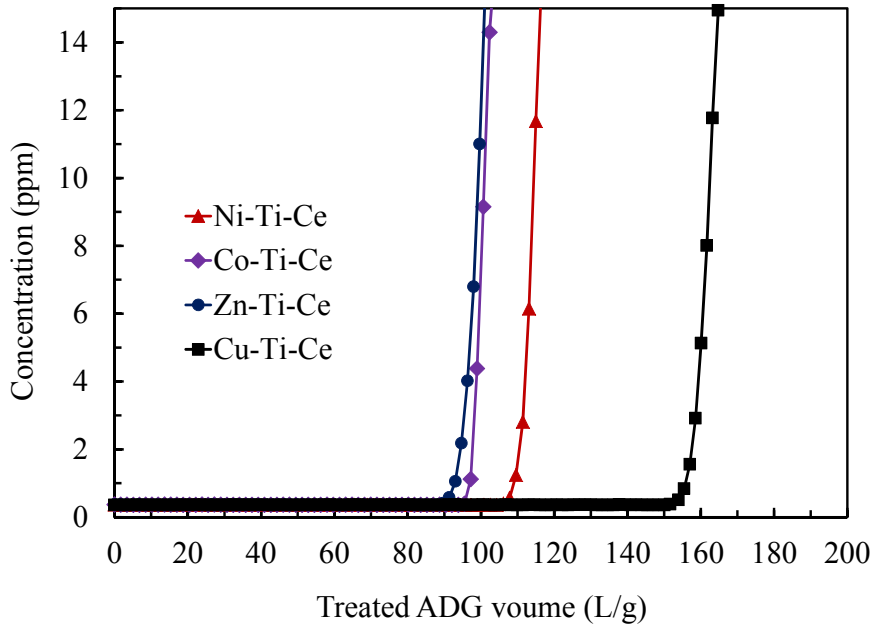

Figure 64. H_2S Breakthrough Curves over Ni-Ti-Ce-O, Co-Ti-Ce-O, Zn-Ti-Ce-O, and Cu-Ti-Ce-O Adsorbents for H_2S Adsorption from a Model ADG Containing 200 ppmv H_2S-10% N_2-40% CO_2-50% CH_4 at Room Temperature and a Flow Rate of 0.2 L/min.

Beside the Cu-Ti-Ce adsorbent, we have studied some other trinary metal oxides adsorbents including Ni-Ti-Ce-O, Co-Ti-Ce-O and Zn-Ti-Ce-O adsorbents for H_2S removal from the simulated ADG stream with the composition of 200 ppmv H_2S-10% N_2-40% CO_2-50% CH_4 at room temperature and atmospheric pressure. The obtained H_2S breakthrough curves are presented in **Figure 64**. The obtained adsorption breakthrough capacities calculated from breakthrough curves are listed in **Table 19**. For comparison, the obtained results for the Cu-Ti-Ce-O adsorbent are also presented. As it can be seen, over all the trinary metal oxides adsorbents studied in this work, before breakthrough, H_2S was completely captured by the adsorbents and

the outlet H_2S concentration was below the detection limit of the analyzer, i.e., < 10 ppbv. That is, more than 99% of H_2S was removed. It suggests that all the trinary metal oxides adsorbents have high affinity to H_2S, though the breakthrough time is different over these adsorbents with different transition metal oxides incorporated. For example, it took about 7 hours of adsorption to break through for the Zn-Ti-Ce-O adsorbent, while about 9 hours of adsorption was needed to break through for the Ni-Ti-Ce-O adsorbent. In other words, for the Zn-Ti-Ce-O adsorbent, every gram of the adsorbent can treat about 88.6 liter of raw ADG with 200 ppmv H_2S to be less than 10 ppbv. The corresponding breakthrough capacity was 24.6 mg-H_2S/g-adsorbent. Furthermore, the breakthrough curve quickly jumps after breakthrough, which implies that the adsorption kinetics over these trinary metal oxides adsorbents is fast.

Table 19. The H_2S adsorption breakthrough capacity for different adsorbents.

Sample	Temp., °C	Breakthrough Capacity, L-ADG/g	Breakthrough Capacity, mg-H_2S/g
Ni-Ti-Ce-O	25	111.4	31.0
Co-Ti-Ce-O	25	91.0	25.3
Zn-Ti-Ce-O	25	88.6	24.6
Cu-Ti-Ce-O	25	150	41.7
TDA SulfaTrap R7	25	90	25.0

Conditions: Gas, 200 ppmv H_2S- 10 v% N_2-40 v% CO_2-50 v% CH_4; Volume of adsorbent bed, 2 ml; pressure, 1 atm.; flow-rate, 200 ml.min (GHSV, 5454 h^{-1}).

As seen, the H_2S adsorption performance of the trinary metal oxides adsorbent is closely related to the type of transition metal oxide that was incorporated into the trinary metal oxides adsorbent. The Ni-Ti-Ce-O adsorbent can treat about 111.4 L-ADG/g-sorb (or 31.0 mg-H_2S/g-sorb) before breakthrough. Using the cobalt oxide instead of NiO, the adsorption capacity of the Co-Ti-Ce-O adsorbent is lower. It can treat about 91.0 L-ADG/g-sorb (or 25.3 mg-H_2S/g-sorb) before breakthrough. The adsorption capacity is even less when zinc oxide is used. The breakthrough capacity of the Zn-Ti-Ce-O adsorbent is about 88.6 L-ADG/g-sorb (or 24.6 mg-H_2S/g-sorb). Among the trinary metal oxides adsorbents tested in this project, the Cu-Ti-Ce-O shows the best performance for H_2S removal from the simulated ADG with 200 ppm H_2S at room temperature. The current results further support that the adsorption performance of M-Ti-Ce-O adsorbent varies with the composition of the transition metal oxide. The intimate interactions between the three components of MO_x, TiO_2 and CeO_2 play a critical role for the superior adsorption performance of the M-Ti-Ce-O adsorbent for H_2S. So far, the Cu-Ti-Ce-O adsorbent is the best for deep desulfurization of ADG for fuel cells under room temperature. Nonetheless, all the trinary metal oxides adsorbents developed in this period exhibit either comparable H_2S removal capacity to the commercial adsorbent, TDA SulfaTrap R7 adsorbent, or even better.

In order to understand the effect of porous properties on the sulfur adsorption performance, we have conducted the N_2 physisorption characterization in this period. **Figure 65** shows the nitrogen adsorption-desorption isotherms for the Ni-Ti-Ce-O, Co-Ti-Ce-O, Zn-Ti-Ce-O, and Cu-Ti-Ce-O adsorbents obtained at -196 °C. A typical type-IV adsorption isotherm with a H1 hysteresis loop was obtained over all these adsorbents, indicating the metal oxides adsorbents have a uniform meso-structure prepared by co-precipitation method. However, the hysteresis loop for the Co-Ti-Ce-O and Zn-Ti-Ce-O adsorbents located at a higher P/P_0 value, compared to

the Ni-Ti-Ce-O and Cu-Ti-Ce-O adsorbents, suggesting a larger pore diameter for the Co-Ti-Ce-O and Zn-Ti-Ce-O adsorbents. The Ni-Ti-Ce-O and Cu-Ti-Ce-O adsorbents have the same position for the hysteresis loop, implying a similar pore structure of these two adsorbents despite different metal oxide was incorporated into the framework of the meso-structure.

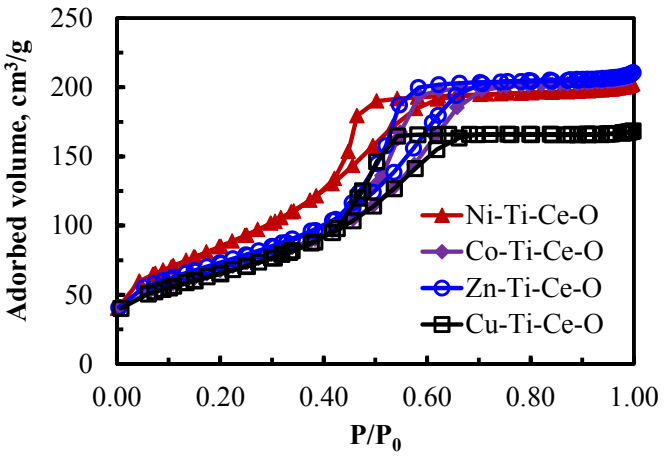

Figure 65. N_2 Adsorption Isotherms for Ni-Ti-Ce-O, Co-Ti-Ce-O, Zn-Ti-Ce-O, and Cu-Ti-Ce-O Adsorbents Obtained at -196 °C.

Table 20. The porous properties of the trinary Ni-Ti-Ce-O, Co-Ti-Ce-O, Zn-Ti-Ce-O and Cu-Ti-Ce-O adsorbents.

Sample	BET Surface Area, m^2/g	Pore Volume, ml/g	Pore Diameter, nm
Ni-Ti-Ce-O	314	0.38	3.70
Co-Ti-Ce-O	245	0.39	4.56
Zn-Ti-Ce-O	263	0.39	4.41
Cu-Ti-Ce-O	237	0.32	4.02

On the basis of the nitrogen adsorption-desorption isotherms, the BET surface area, pore volume and pore size of the Ni-Ti-Ce-O, Co-Ti-Ce-O, Zn-Ti-Ce-O, and Cu-Ti-Ce-O adsorbents can be calculated, which are listed in **Table 20**. All the adsorbents showed a narrow pore distribution in the range of 2-7 nm, which hints the uniform pore structure of the adsorbent materials prepared. The Ni-Ti-Ce-O adsorbent has a BET surface area of 314 m^2/g, a pore volume of 0.38 ml/g and a pore size peaked at 3.70 nm. For the sample of Co-Ti-Ce-O, it showed a BET surface area of 245 m^2/g, a pore volume of 0.39 ml/g and a pore size peaked at 4.56 nm. When the ZnO was incorporated in the Ti-Ce-O, the Zn-Ti-Ce-O adsorbent showed a higher BET surface area of 263 m^2/g, but a similar pore volume of 0.39 ml/g and a pore size of 4.41 nm. All these trinary metal oxides adsorbents showed higher BET surface area, larger pore volume and pore diameter than the Cu-Ti-Ce-O adsorbent, which has the value of 237 m^2/g, 0.32 ml/g and 4.02 nm for the BET surface area, larger pore volume and pore diameter, respectively. Considering that the Cu-Ti-Ce-O adsorbent exhibits a much better adsorption capacity than any these Ni-Ti-Ce-O, Co-Ti-Ce-O, and Zn-Ti-Ce-O adsorbent, it should be concluded that the chemical composition of the trinary metal oxides adsorbent is more important than the porous properties of the adsorbent.

2.1.4. Novel MBS sorbents for ADG cleanup

2.1.4.1 PEI-based MBS sorbents

We also have developed the novel molecular basket sorbent by loading 50 wt% of polyethylenimine (PEI) on mesoporous molecular sieve SBA-15 support (termed as PEI-50/SBA-15) for ADG cleanup. **Figure 66** shows the breakthrough curves for CO_2 and H_2S removal from the simulated ADG gas containing 200 ppmv H_2S- 10 v% N_2-40 v% CO_2-50 v% CH_4 over the novel PEI-50/SBA-15 molecular basket adsorbent at room temperature (25 °C).

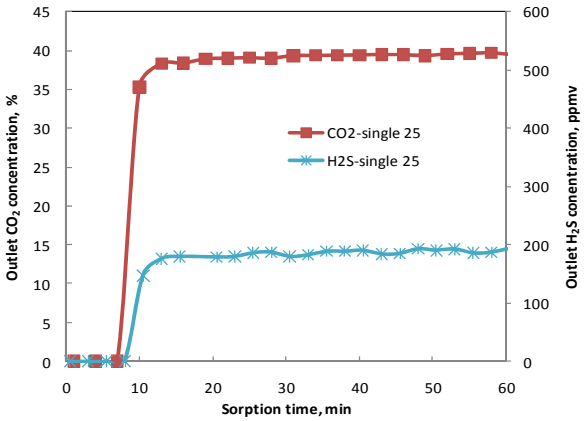

Figure 66. CO_2 and H_2S breakthrough curves for CO_2 and H_2S removal from the simulated ADG gas containing 200 ppmv H_2S- 10 v% N_2-40 v% CO_2-50 v% CH_4 over PEI-50/SBA-15 adsorbent at room temperature. Conditions: Volume of adsorbent bed, 21.4 ml; Weight, 4.6 g; Pressure, 1 atm.; Flow-rate, 50 ml/min (GHSV, ~140 h^{-1}).

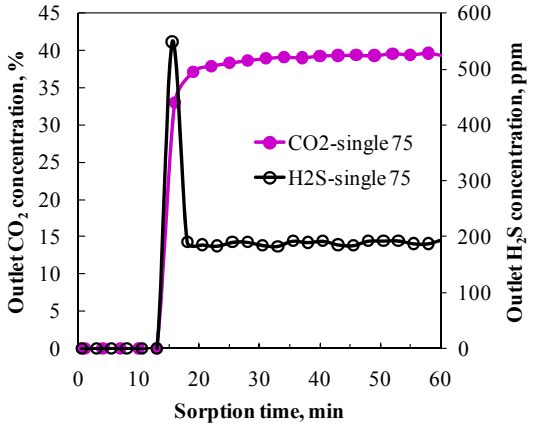

Figure 67. CO_2 and H_2S breakthrough curves for CO_2 and H_2S removal from the simulated ADG gas containing 200 ppmv H_2S- 10 v% N_2-40 v% CO_2-50 v% CH_4 over PEI-50/SBA-15 adsorbent at 75 °C. Conditions: Volume of adsorbent bed, 21.4 ml; Weight, 4.6 g; Pressure, 1 atm.; Flow-rate, 50 ml/min (GHSV, ~140 h^{-1}).

At room temperature, the molecular basket sorbent, PEI-50/SBA-15 can effectively remove H_2S as well as CO_2 from the ADG gas stream, which is significantly different from other studied commercial adsorbents in this project. Those commercial adsorbents can only work for H_2S removal and do not have affinity to CO_2. Before breakthrough, both CO_2 and H_2S concentrations in the effluent were below the detector limitation of the analyzer, i.e., CO_2 concentration below 500 ppmv and H_2S concentration below 60 ppbv. Unlike other commercial adsorbents, it can also be observed that the breakthrough curve quickly reached the saturation point after the breakthrough point, indicating the very fast sorption kinetics over the PEI-50/SBA-15 sorbent.

In our previous study, it was found that the best sorption performance can be obtained at 75 °C for CO_2 capture. Thus, we have also investigated the cleanup performance of MBS at 75 °C. **Figure 67** shows the breakthrough curves for CO_2 and H_2S removal from the simulated ADG gas containing 200 ppmv H_2S- 10 v% N_2-40 v% CO_2-50 v% CH_4 over the novel PEI-50/SBA-15 molecular basket adsorbent at 75 °C. It can be seen that before breakthrough, both CO_2 and H_2S concentrations in the effluent were below the detector limitation of the analyzer, i.e., CO_2 concentration below 500 ppmv and H_2S concentration below 60 ppbv, even at higher

temperature, as observed at room temperature. In addition, unlike other commercial adsorbents, the breakthrough curves for both CO_2 and H_2S quickly reached the saturation point after the breakthrough point, indicating the very fast sorption kinetics over the PEI-50/SBA-15 sorbent. From the breakthrough curves, it should be pointed out that when CO_2 broke through, the outlet H_2S concentration became significantly higher, reaching 560 ppmv, far from its initial concentration, which was about 200 ppmv. Then, the H_2S concentration fell back to its feeding concentration. The phenomenon strongly suggests that the sorption of CO_2 over the MBS is stronger and can significantly affect the sorption H_2S. Additionally, there is a competition sorption between CO_2 and H_2S in the MBS sorbent and the part of ad sorbed H_2S was kicked out of the sorption sites by CO_2, which resulted in a high peak in the H_2S breakthrough curve shown in **Figure 67**.

Table 21. Sorption capacities of PEI-50/SBA-15 for CO_2 and H_2S separation at room temperature.

Temp, °C		Breakthrough Capacity, mg/g	Saturation Capacity, mg/g
25	CO_2	54.9	77.5
	H_2S	0.024	0.029
75	CO_2	102.0	127.7
	H_2S	0.039	0.039

Based on the breakthrough curves, the corresponding sorption capacity including breakthrough capacity and saturation capacity can be calculated. The computed capacities are presented in **Table 21**. The PEI-50/SBA-15 sorbent showed high sorption capacity for CO_2 capacity. The sorption capacity reached 54.9 mg-CO_2/g-S and 77.5 mg-CO_2/g-S for breakthrough capacity and saturation capacity, respectively. However, for H_2S removal, the sorption capacity of PEI-50/SBA-15 sorbent was low. It was only 0.024 mg-H_2S/g-S and 0.029 mg-H_2S/g-S for breakthrough capacity and saturation capacity, respectively. When the sorption temperature was raised to 75 °C, the PEI-50/SBA-15 sorbent showed high sorption capacity for CO_2 capacity. The sorption capacity reached 102.0 mg-CO_2/g-S and 127.7 mg-CO_2/g-S for breakthrough capacity and saturation capacity, respectively. The adsorption capacity for H2S was also increased slightly compared to that at 25 °C. the sorption capacity of PEI-50/SBA-15 sorbent for H_2S removal was 0.039 mg-H_2S/g-S and 0.039 mg-H_2S/g-S for breakthrough capacity and saturation capacity, respectively. The value is significantly lower than those of the tested commercial adsorbents such as SulfaTrap and ZnO adsorbents.

The prepared PEI/SBA-15 sorbents have been characterized by SEM and TGA methods. **Figure 68** shows the SEM images of SBA-15 and PEI/SBA-15 sorbents. As it can be seen, the road-like morphology stacked into tower-like arrays was observed over the calcined SBA-15, which was composed of small SBA-15 particles (**Figure 68a**). The size of most particles was below 1 μm. After PEI loading, the morphology of the formed materials changed significantly. For the sample with 30 wt% PEI loading, it can be seen that the shape was almost the same as that of pure SBA-15, except some parts of particles were separately dispersed (**Figure 68b**). However, for PEI-50/SBA-15, highly dispersed particles were observed. The average particle size was still below 1 μm (**Figure 68c**). No agglomerates or larger clusters were observed in PEI-50/SBA-15, suggesting that the loaded PEI was completely filled into the pore channels of SBA-15, which is consistent with the results from XRD and N_2 adsorption-desorption. Furthermore, the sorbent particles became highly dispersed after the 50 wt% loading of PEI,

which may benefit the CO_2 sorption. With continuous increasing PEI loading to 65 wt%, the particles agglomerated and the spherical balls with the diameter up to 20 mm was recognized (**Figure 68d**), strongly indicating that a significant amount of PEI exists on the external surface of the particles and/or fill in the gaps between the small particles, leading to the agglomeration. The SEM images clearly indicate that the introduced PEI is located inside the pore channels of SBA-15 when the PEI loading is 50 % or less, while the excessive PEI is coated on the external surface of the particles when the PEI loading is higher than 50 %, which is in accord with the conclusions from both the XRD and N_2 adsorption-desorption characterizations.

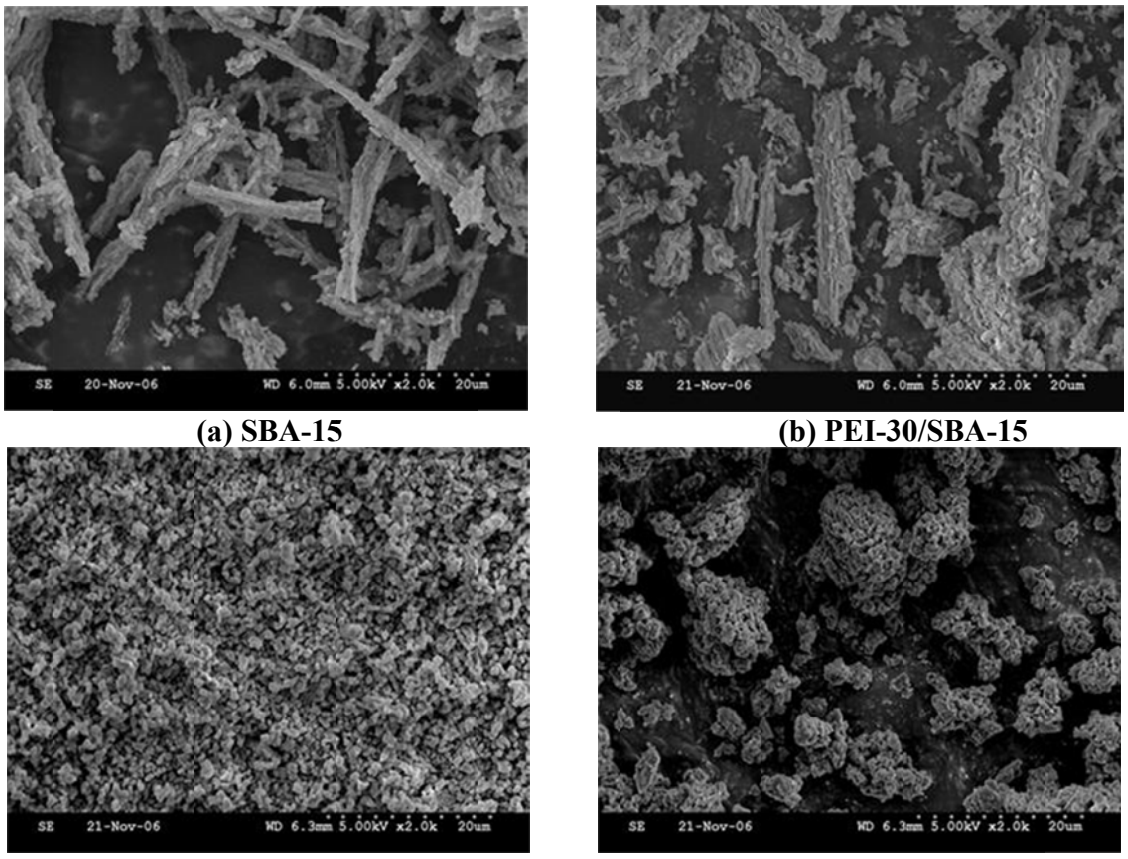

(a) SBA-15 **(b) PEI-30/SBA-15**

(c) PEI-50/SBA-15 **(d) PEI-65/SBA-15**

Figure 68. SEM images of (a) SBA-15, (b) PEI-30/SBA-15, (c) PEI-50/SBA-15 and (d) PEI-65/SBA-15.

The thermo-chemical properties of SBA-15, PEI and PEI-loaded SBA-15 samples were studied by TGA. **Figure 69** shows the thermal gravimetric and the differential thermal gravimetric analysis profiles of SBA-15 samples with different PEI-loading amounts. For comparison, the results from pure PEI are also presented. There was about 7 % of weight loss observed over pure SBA-15 before 100 °C, probably due to the desorption of the adsorbed moisture and/or other gases like CO_2, suggesting the SBA-15 prepared in this work has a potential to adsorb the moisture and/or other gases at room temperature. Almost no weight loss was observed when the temperature was higher than 100 °C, until 600 °C. For the pure PEI, the weight loss was 2 % when the temperature was increased to 100 °C, and then decomposition started at above 150 °C with a sharp weight loss appearing at about 200 °C. When the

temperature was higher than 300 °C, the rate of weight loss decreased, indicating a different decomposition process. At 600 °C, decomposition of PEI was almost complete.

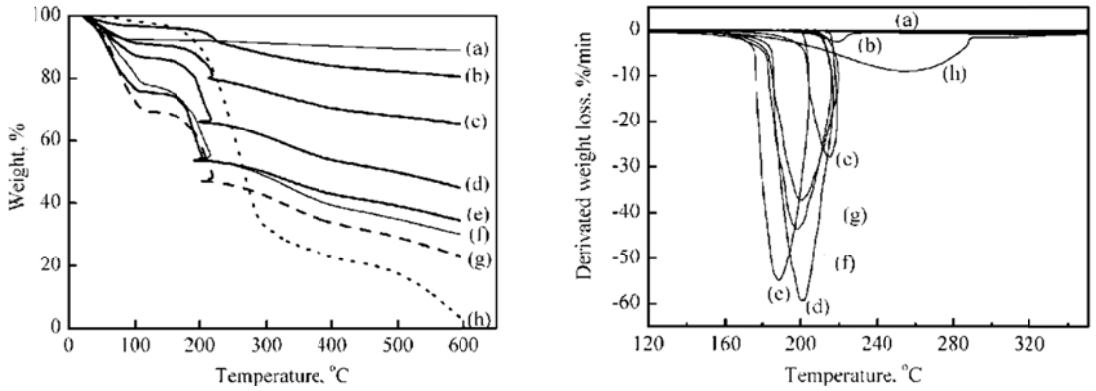

(A) **(B)**

Figure 69. (A) TGA and (B) DTGA profiles for (a) SBA-15, (b) PEI-15/SBA-15, (c) PEI-30/SBA-15, (d) PEI-50/SBA-15, (e) PEI-60/SBA-15, (f) PEI-65/SBA-15, (g) PEI-70/SBA-15 and (h) pure PEI.

After PEI was loaded into SBA-15, the sharp weight loss occurred at lower temperatures, as shown in **Figure 69B**, suggesting that the decomposition temperature of PEI decreased. In addition, the temperature range for the decomposition of loaded PEI was significantly narrower than that for the pure PEI. This change can be attributed to the uniform dispersion of PEI into the meso-channels of SBA-15. For PEI-15/SBA-15, the decomposition peak temperature was 220 °C. With increasing the PEI loading amount, the peak temperature progressively shifted to 215 °C for PEI-30/SBA-15, to 200 °C for PEI-50/SBA-15 and even to 188 °C for PEI-60/SBA-15. The interaction between the loaded PEI and the surface silanol groups of SBA-15 has been identified in our early *in-situ* FTIR study, which may greatly improve the thermal stability of loaded PEI in SBA-15. Thus, lower PEI loading exhibited higher decomposition temperature. With the increase of PEI loading, the interaction between PEI and the SBA-15 surface becomes weaker, and thus, the highly dispersed PEI decomposition temperature decreased. However, for PEI-65/SBA-15 and PEI-70/SBA-15 samples, the peak temperatures shifted back to higher temperatures (about 198 °C and 200 °C, respectively). This change indicates that for PEI-65/SBA-15 and PEI-70/SBA-15 samples, the excessive amount of the loaded PEI was coated on the external surface of SBA-15 particles, leading the agglomeration of the particles. It enhances the barrier of the decomposed product diffusion and heat transfer, and as a result, the decomposition peak temperature increased. Consequently, the TGA and differential-TGA (DTGA) results are consistent with the conclusion obtained from other characterization techniques.

2.1.4.2 Other amine-based MBS sorbents

Other amine based MBS sorbents have also been investigated in this project, including Polyallylamine (PA), polyethyleimine (PEI) and N, N, N′, N′-Tetramethyl-1,6-hexanediamine (TMHDA), (3-aminopropyl) trimethoxysilane (APTMS, Aldrich), [3-(methylamino) propyl] trimethoxysilane (MAPTMS) and [3-(diethylamino) propyl] trimethoxysilane (DEAPTMS), the molecular structure of which is depicted in **Figure 70**, were used as typical primary, secondary

and tertiary amine compounds to study the effect of amine structure on the sorption performance for H_2S sorption over amine based MBS.

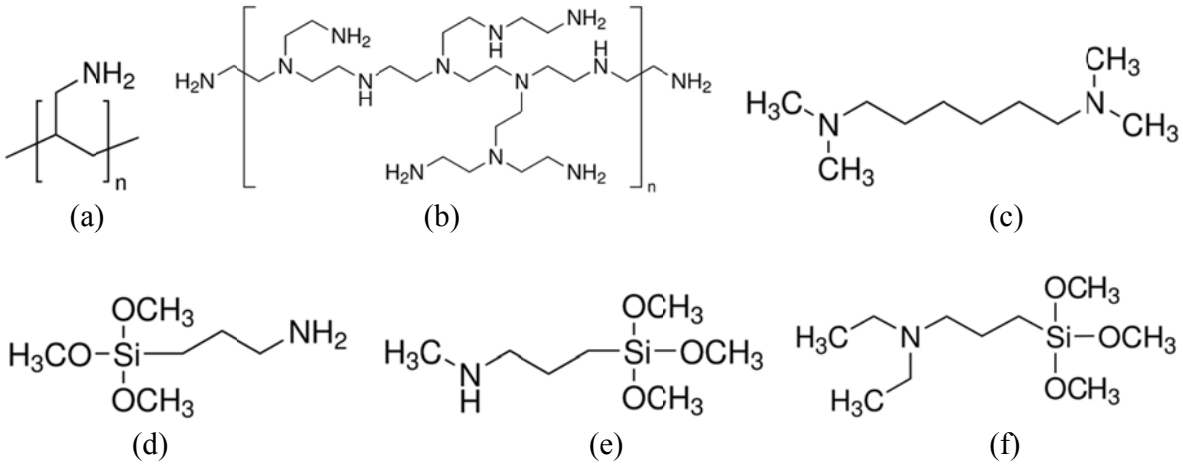

Figure 70. The molecular structure of (a) polyallylamine (PA), (b) polyethyleimine (PEI), (c) N, N, N′, N′-Tetramethyl-1,6-hexanediamine (TMHDA), (d) (3-aminopropyl) trimethoxysilane (APTMS) (RH_2N-), (e) [3-(methylamino) propyl] trimethoxysilane (MAPTMS) (R_2HN-) and (f) [3-(diethylamino) propyl] trimethoxysilane (DEAPTMS) (R_3N-).

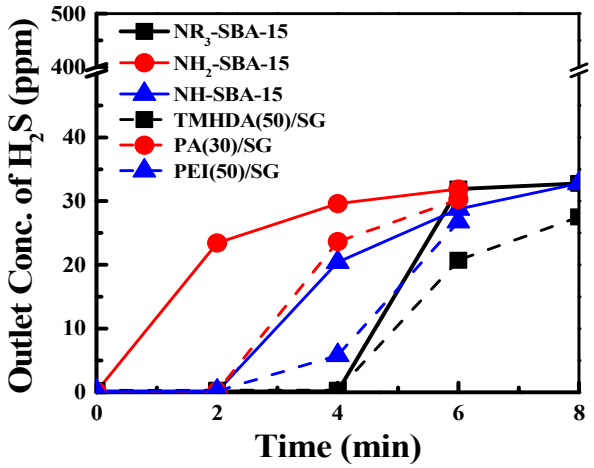

Figure 71. H_2S sorption breakthrough curves on the different amine sorbents for H_2S sorption from the gas stream from the gas stream with the presence of CO_2.

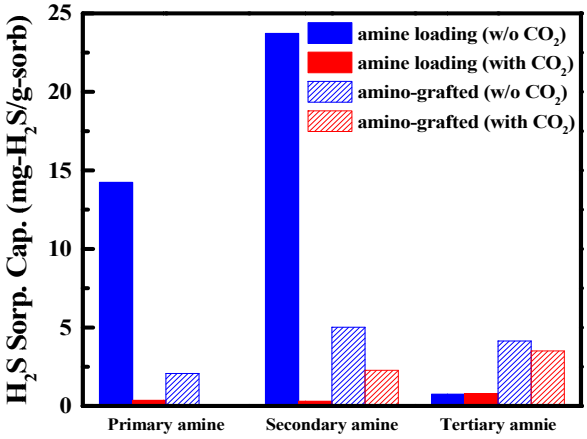

Figure 72. Effect of amine structure on the H_2S sorption capacity of the different amine based sorbents for H_2S sorption from the gas stream with and without the presence of CO_2.

The prepared MBS materials have been evaluated for H2S removal with and without the presence of CO_2 for ADG cleanup. The obtained breakthrough curves for H_2S sorption with the presence of CO_2 are all presented in **Figure 71**. It is clear that tertiary amine groups were better for H_2S sorption with CO_2 in both amine-impregnated sorbents and amino-grafted sorbents, which implies that tertiary amine group is more promising for H_2S removal in the gas stream with the presence of high concentration CO_2 such as biogas if the appropriate tertiary amine structure can be designed and synthesized.

Table 22 and **Figure 72** present the H_2S sorption capacities of the amino-grafted and amine-impregnated sorbents with different amine structure for H_2S sorption from the gas stream with and without the presence of CO_2. Comparing with two tertiary amine functionalized sorbents, the amino-grafted sorbent, NR_3-SBA-15, has a higher H_2S sorption capacity than THMDA(50)/SG. One possible reason is that the steric hindrance of THMDA polymer impedes the sorption of H_2S molecules over amine groups. Another reason is because of the support as SBA-15 has more advantages than silica gel including higher surface area and uniform pore structure. The H_2S sorption capacities on primary and secondary amino-grafted sorbents, however, are much lower than those of the primary and secondary amine-impregnated sorbents, which is not as expected.

Table 22. H_2S sorption capacities of the amino-grafted and amine-impregnated sorbents for H_2S sorption from the gas stream with and without the presence of CO_2.

Sorbent	H_2S sorption capacity, mg-H_2S/g-sorb	
	without CO_2	with CO_2
NR_3-SBA-15	4.14	3.51
NH_2-SBA-15	2.07	0
NH-SBA-15	5.07	2.28
THMDA(50)/SG	0.75	0.79
PA(30)/SG	14.24	0.36
PEI(50)/SG	23.72	0.30

Considering that under dry conditions, the tertiary amine does not react with CO_2 but still can work with H_2S molecules as follows:

$$CO_2 + R_3\text{-}N \neq \quad (3)$$

$$H_2S + 2R_3\text{-}N = R_3\text{-}N\text{-}HSH\text{-}N\text{-}R_3 \quad (4)$$

It is projected that the use of tertiary amine may eliminate the negative effect of CO_2 on H_2S sorption. Thus, we have further investigated the effect of CO_2 presence on the H_2S sorption performance of the TMHDA based adsorbents.

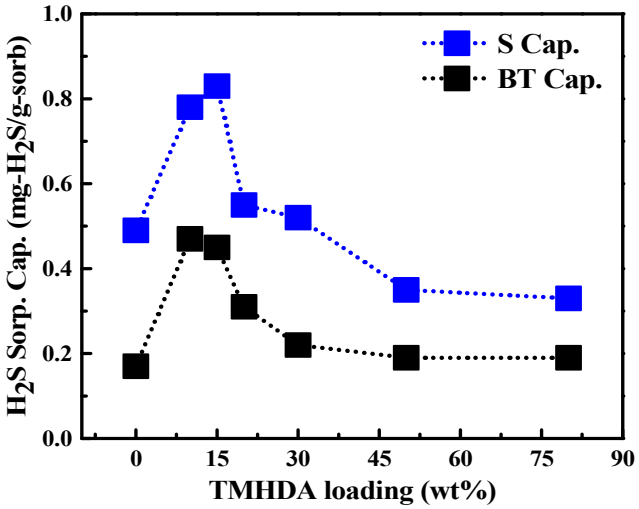

Figure 73. H_2S sorption capacity on different weight percentage of TMHDA loading on SBA-15. Conditions: *T*, 25 °C; Feed-gas, 500 ppm H_2S-CO_2-N_2; Flow rate, 15 ml/min.

First, we examined the effect of TMHDA loading on the H2S sorption capacity of TMHDA/SBA-15 sorbents and found that the sorption capacity decreased with the increase of TMHDA loading amount. However, the sorption capacity increased again when the TMHDA loading amount was increased to 80 wt%. To confirm the result, the 80 wt% THMDA loaded sample was re-examined. In addition, to identify the optimum TMHDA loading, the loading amount of THMDA was further lowered to 10 wt% in this report period. The prepared sorbents were evaluated for H_2S sorption from the simulated biogas containing 500 ppmv H_2S-10% CO_2 in N_2 at 25 °C. **Figure 73** shows the H_2S breakthrough and saturation sorption capacity of TMHDA/SBA-15 sorbents as a function of TMHDA loading amount. The obtained saturation and breakthrough capacity over TMHDA/SBA-15 adsorbents with different TMHDA loadings for H_2S adsorption with the presence of 10% CO_2 are listed in **Table 23**.

Table 23. H_2S breakthrough and saturation sorption capacities of TMHDA/SBA-15 adsorbents with different TMHDA loadings for H_2S sorption from the gas stream with the presence of 10 v% CO_2 at room temperature and atmospheric pressure.

Sample	S Cap. (mg-H_2S/g-sorb)	BT Cap. (mg-H_2S/g-sorb)
SBA-15	0.49	0.17
TMHDA(10)/SBA-15	0.78	0.47
TMHDA(15)/SBA-15	0.83	0.45
TMHDA(20)/SBA-15	0.55	0.31
TMHDA(30)/SBA-15	0.52	0.22
TMHDA(50)/SBA-15	0.35	0.19
TMHDA(80)/SBA-15	0.33	0.19

As can be seen from the figure, the H_2S sorption capacity was increased with the increase of TMHDA loading up to 15wt%. SBA-15 alone showed a lower capacity for H_2S sorption. The saturation and breakthrough capacity was 0.49 and 0.17 mg-H_2S/g-sorb, respectively. When 10 wt% TMHDA was loaded, the sorption was increased. It was 0.78 and 0.47 mg-H_2S/g-sorb for the saturation and breakthrough capacity, respectively. Increasing TMHDA amount to 15 wt%, the saturation and breakthrough capacity was also increased to 0.83 and 0.45 mg-H_2S/g-sorb, respectively. However, further increasing the TMHDA amount, both the saturation and breakthrough capacities decreased, gradually. The TMHDA(50)/SBA-15 and TMHDA(80)/SBA-15 sorbents showed the saturation capacity of 0.35 and 0.33 mg-H_2S/g-sorb, respectively, which are even less than that of SBA-15 alone. It may be because the pore channels of SBA-15 were blocked by TMHDA at higher TMHDA loadings, resulting in the decrease in the H_2S sorption capacity. The maximum H_2S sorption capacity was obtained over the TMHDA(15)/SBA-15 sample, suggesting that the optimum TMHDA loading over SBA-15 for H_2S sorption from biogas at °C was about 15 wt%.

Second, the effect of the gas hourly space velocity (GHSV) on the H_2S sorption capacity of the optimum sorbent, TMHDA(15)/SBA-15 was studied by changing the gas flow rate. The GHSV studied was 377, 628 and 1004 h^{-1}, respectively. The obtained H_2S saturation sorption capacity as a function of GHSV is presented in **Figure 74**. Obviously, the increase of the GHSV results in the decrease of the H_2S sorption capacity. At higher GHSV, that is higher flow rate, the residence time is much shorter, i.e., a shorter contact time. As a consequence, the sorption

capacity is lower. The result suggests that lower GHSV is preferred in order to get a higher H_2S sorption capacity over the TMHDA(15)/SBA-15 sorbent.

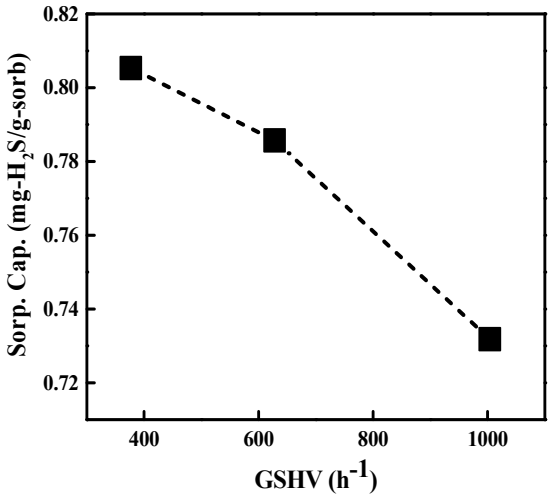

Figure 74. H_2S sorption capacity of TMHDA(15)/SBA-15 at different gas hourly space velocity (GHSV). Conditions: *T*, 25 °C; Feed-gas, 500 ppm H_2S-10 vol%CO_2-N_2.

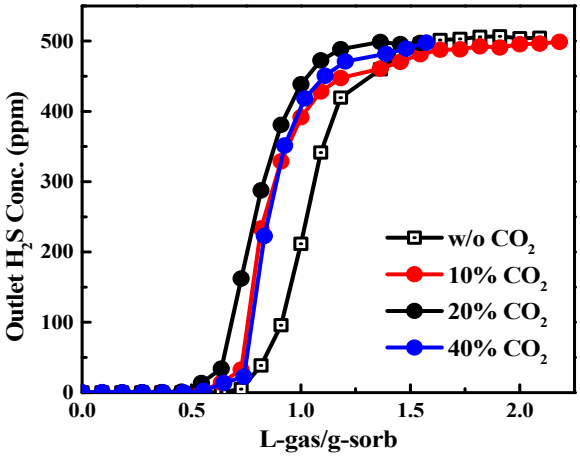

Figure 75. H_2S sorption breakthrough curve on TMHDA(15)/SBA-15 with different CO_2 inlet concentration. Conditions: *T*, 25 °C; Feed-gas, 500 ppm H_2S-CO_2-N_2; Flow rate, 15 ml/min.

Third, the effect of CO_2 concentration on the H_2S sorption capacity of TMHDA(15)/SBA-15 was examined as biogas normally contains up to 40-60 vol% CO_2, which may significantly affect the sorption performance of TMHDA/SBA-15 sorbent for H_2S. **Figure 75** shows the H_2S breakthrough curves on the TMHDA(15)/SBA-15 sorbent at different inlet concentration of CO_2. Compared to the case with the presence of CO_2, H_2S broke through slightly later and it took a little longer time to reach the saturation when CO_2 was not present. It can also be seen that the H_2S breakthrough curves were not almost overlapped for the CO_2 feed concentration of 10, 20 and 40 vol%. The breakthrough point was almost the same. This result indicates that the inlet CO_2 concentration (up to 40 vol%) does not significantly influence the H_2S sorption performance of TMHDA(15)/SBA-15 sorbent. Thus, TMHDA(15)/SBA-15 can be feasible for H_2S sorption from biogas.

Fourth, the effect of inlet H_2S concentration on the H_2S sorption capacity of TMHDA(15)/SBA-15 was investigated at 25 °C. The obtained H_2S saturation sorption capacity was plotted in **Figure 76** as a function of inlet H_2S concentration. The H_2S saturation capacity increased with the increase of the inlet H_2S concentration, but not a linear relationship. The trend shown in **Figure 76** may suggest that the H_2S sorption over TMHDA(15)/SBA-15 sorbent may obey the Langmuir sorption mechanism, thus could be described by the Langmuir equation and isotherm.

The equation of Langmuir isotherm is presented in Equation (1), in which, *Ce* and *q* are the inlet concentration of H_2S in the gas stream and the H_2S saturation capacity at equilibrium, respectively. *K* is the adsorption equilibrium constant and q_m is the maximum adsorption saturation capacity of the sorbent. If H_2S obey the Langmuir isotherm, a plot of $1/q$ versus $1/C_e$ will be a straight line, as described as Equation (2).

$$q = \frac{Kq_mC_e}{1+KC_e} \cdots\cdots (1)$$

$$\frac{1}{q} = \frac{1}{Kq_mC_e} + \frac{1}{q_m} \cdots\cdots (2)$$

On basis of the data in **Figure 76**, the $1/q$ value as a function of $1/C_e$ was plotted as shown in **Figure 77**. A good linear relation between $1/q$ and $1/C_e$ was obtained with R^2 value of 0.9949 at 25 °C, suggesting that H_2S sorption over TMHDA(15)/SBA-15 obeys the Langmuir adsorption mechanism. The q_m and K values can be estimated by linear regression which were 0.046 mmol-H_2S/g-sorb and 0.002, respectively.

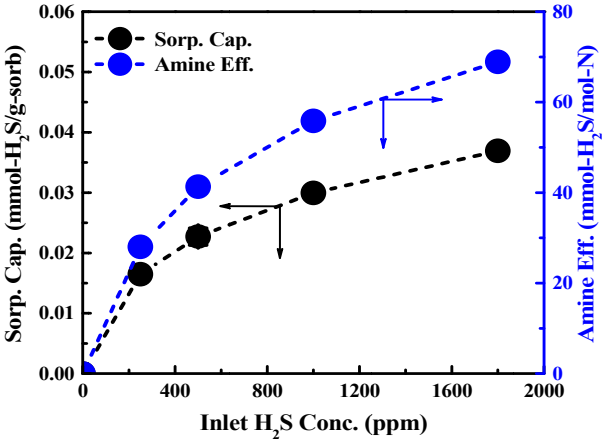

Figure 76. H_2S sorption capacity on TMHDA(15)/SBA-15 with different inlet H_2S concentration. Conditions: *T*, 25 °C; Feed-gas, H_2S- 10 vol%CO_2-N_2; Flow rate, 15 ml/min.

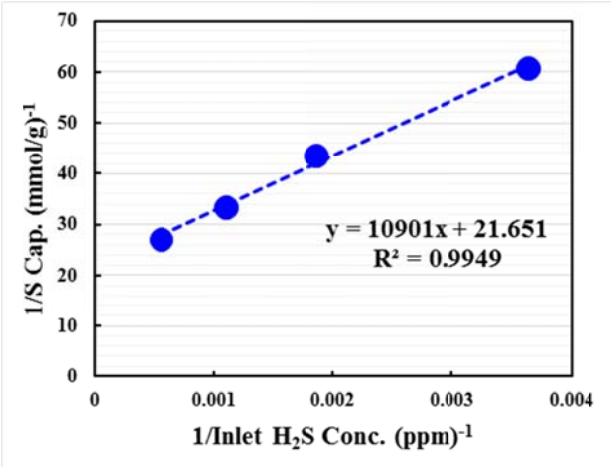

Figure 77. Plot of 1/q versus $1/C_e$ for TMHDA(15)/SBA-15 at 25 °C.

Fifth, the effect of support was also examined. We prepared a new molecular basket sorbent using a coal-derived carbon black, C5 as the support with loading 15 wt% TMHDA. The prepared TMHDA(15)/C5 sorbent was evaluated for H_2S sorption from the simulated biogas with 500 ppm H_2S in N_2 with and without the presence of 10 vol% CO_2 at 25 °C. The obtained breakthrough curves are shown in **Figure 78**. Based on the breakthrough curves, the corresponding breakthrough capacities were calculated and the values are presented in **Figure 79**. For comparison, the H_2S breakthrough curves obtained over the C5 support under the same conditions and the calculated breakthrough capacities are also presented in **Figures 78 and 79**, respectively. Without the presence of CO_2, C5 showed a breakthrough capacity of 0.94 mg-H_2S/g-sorb. After 15 wt% TMHDA loading, the breakthrough capacity became 0.84 mg-H_2S/g-sorb. However, after breakthrough, the increase of the outlet H_2S concentration with time on stream was slower than that of C5 support, showing that the loading of TMHDA into C5 support promotes the H_2S sorption performance of C5 support.

Unlike that the sorption capacity decreased with the presence of CO_2 as observed on SBA-15 based molecular basket sorbents, over both the C5 support and TMHDA(15)/C5 sorbent, the sorption capacity for H_2S actually increased greatly with the presence of 10 vol%

CO_2. Over C5 support, H_2S breakthrough capacity increased to 2.27 mg-H_2S/g-sorb with the presence of 10 vol% CO_2 from 0.94 mg-H_2S/g-sorb without CO_2. As for the TMHDA(15)/C5 sorbent, the breakthrough capacity even increased to 4.32 mg-H_2S/g-sorb, an increase of 400% compared that without CO_2 presence. The results suggest that the presence of CO_2 promotes H2S sorption over C5 and TMHDA(15)/C5 sorbents. More work need to conduct to fully understand the promotion effect of CO_2 on H_2S sorption over the C5 and TMHDA(15)/C5 sorbents.

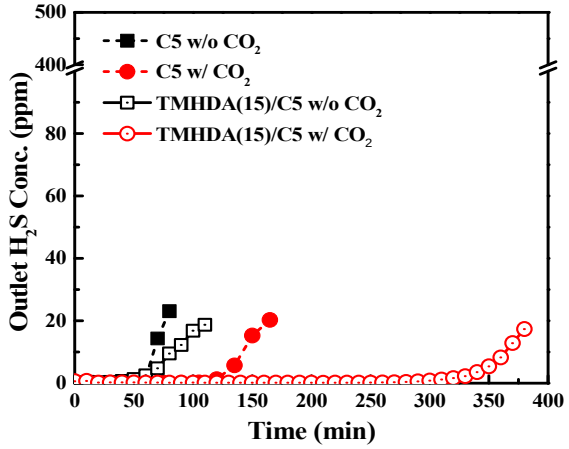

Figure 78. H_2S breakthrough curves on C5 and TMHDA(15)/C5 with and without CO_2. Conditions: *T*, 25 °C; Feed-gas, 500 ppm H_2S-10 vol% CO_2-N_2; Flow rate, 15 ml/min.

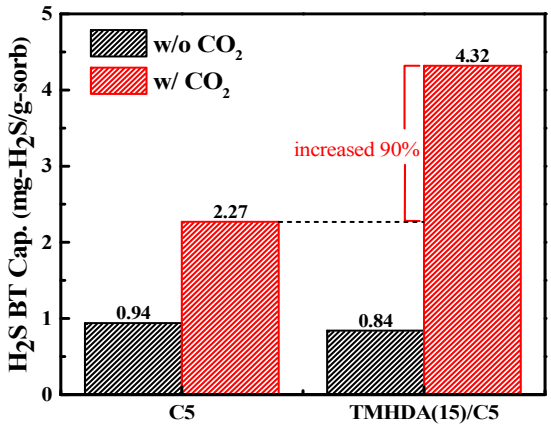

Figure 79. H_2S breakthrough capacities on C5 and TMHDA(15)/C5 with and without CO_2. Conditions: *T*, 25 °C; Feed-gas, 500 ppm H_2S-10 vol% CO_2-N_2; Flow rate, 15 ml/min.

Compared to the C5 support, the TMHDA loaded sorbent, TMHDA(15)/C5 exhibited a significantly higher breakthrough capacity. It is about 90% increase in the H_2S sorption breakthrough capacity. It may be attributed to the fact that the amine compound, TMHDA could provide more basic active sites for the H_2S sorption on the surface of the sorbent.

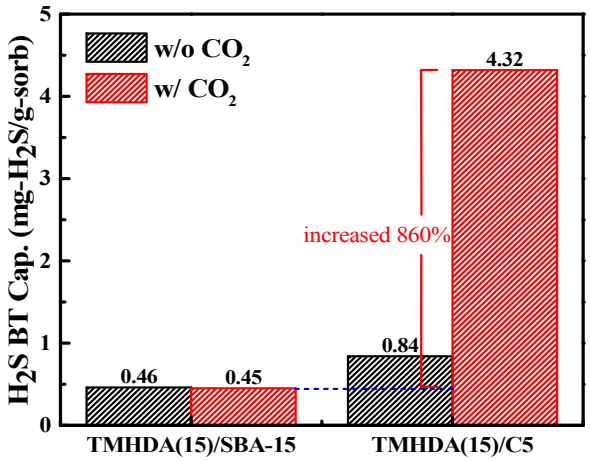

Figure 80. H_2S breakthrough capacities compared with SBA-15 and C5 as a support with and without the presence of CO_2. Conditions: *T*, 25 °C; Feed-gas, 500 ppm H_2S-(10 vol% CO_2)-N_2; Flow rate, 15 ml/min.

The obtained H_2S sorption capacity of TMHDA(15)/C5 was further compared to that of TMHDA(15)/SBA-15 sorbent, which is shown in **Figure 80**. The TMHDA(15)/C5 sorbent showed a much higher H_2S breakthrough capacity (4.32 mg-H_2S/g-sorb) than the TMHDA(15)/SBA-15 sorbent, the H_2S breakthrough capacity of which was only 0.45 mg-H_2S/g-sorb. One possible reason is that C5 itself may be a good sorbent which can adsorb a certain amount of H_2S while SBA-15 alone is hardly able to adsorb H_2S or CO_2. Moreover, the abundant carboxyl and hydroxyl groups on the carbon surface could enhance the loading and dispersion of TMHDA which may further improve H_2S sorption performance. The current result indicates that the TMHDA(15)/SBA-15 sorbent is a better option than the TMHDA(15)/SBA-15 sorbent for H_2S sorption from biogas.

2.1.5. Adsorbents for ammonia removal

In this project, we have also developed a new type solid adsorbent for ammonia removal on the basis of the "molecular basket" concept, using mesoporous molecular sieve, SBA-15 as the support and the poly(acrylic acid-co-maleic acid) (50 wt% solution in water, average M_w 3000, purchased from Aldrich) as the active phase which provide numerous NH_3-affinity sites for ammonia adsorption. The polymer was loaded via wet impregnation method. The polymer loading amount was 15, 25 and 30 wt%. The prepared MBS has been termed as PAM-15/SBA-15, PAM-25/SBA-15 and PAM-30/SBA-15. After drying in the vacuum oven at 100 °C for overnight, the PAM/SBA-15 adsorbents were evaluated for ammonia adsorption by NH_3-TPD method.

The NH_3-adsorption was performed on the Micromeritics AutoChem 2910. About 200 mg of NH_3-MBS adsorbent was loaded into a quartz U-tube reactor. As demonstrated in **Figure 81**, before ammonia adsorption, the PAM/SBA-15 sorbent was pretreated at 100 °C for 30 minutes. The adsorption was carried at 40 °C with a model gas of NH_3 in He. The ammonia concentration in the model gas was 2 vol%. The desorption was carried out by raising temperature from 40 to 110 °C and hold at 100 °C for another 20 minutes with pure He as a purge gas. The released ammonia gas was recorded on-line by GC.

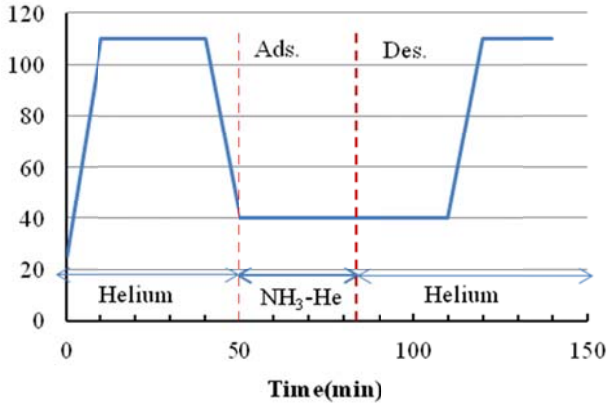

Figure 81. The procedure for ammonia adsorption and desorption over the PAM/SBA-15 sorbents via ammonia temperature-programmed desorption method.

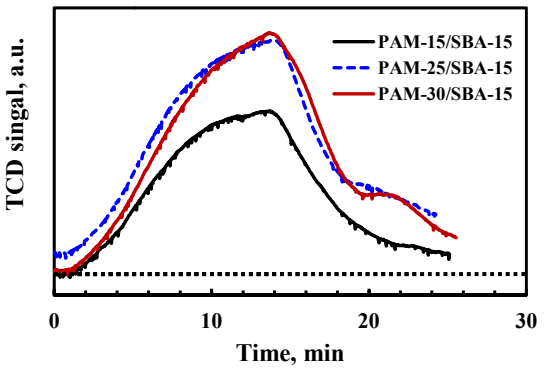

Figure 82. Ammonia-TPD profile as a function of time over the PAM-15/SBA-15, PAM-25/SBA-15 and PAM-30/SBA-15 adsorbents. The ammonia adsorption was conducted at 40 °C with 2 v% NH_3 in Helium under a flow rate of 100 ml/min.

The NH_3-TPD profiles for the PAM-15/SBA-15, PAM-25/SBA-15 and PAM-30/SBA-15 adsorbents are presented in **Figure 82**. As can be seen, all the adsorbents can adsorb ammonia from the gas stream containing 2 v% NH_3 at the temperature of 40 °C. With the increase of temperature under helium flow, the adsorbed ammonia can be desorbed. The desorption can be completed at 100 °C. In addition, with increasing the PAM loading amount, the TCD signal becomes stronger, indicating more ammonia being released. In other words, the adsorbent with higher PAM loading shows higher adsorption capacity for ammonia. Besides, a secondary desorption peak located at the desorption time of about 20 minutes can be observed over the sample with higher PAM loadings, especially for the PAM-30/SBA-15 sorbent. It may suggest that secondary adsorption sites may exist over the PAM-30/SBA-15 sorbent and increase with the increase of PAM loading amount.

On the basis of the desorption curve, the corresponding adsorption capacity of the adsorbent can be calculated, which is about 3.36 mmol-NH_3/g-sorbent (i.e., 5.7 wt%), 4.21 mmol-NH_3/g-sorbent (i.e., 7.1 wt%), and 3.96 mmol-NH_3/g-sorbent (i.e., 6.7 wt%) for the PAM-15/SBA-15, PAM-25/SBA-15 and PAM-30/SBA-15 adsorbents, respectively. **Figure 83** shows the ammonia adsorption capacity as a function of PAM loading over the PAM/SBA-15 adsorbents measured by NH_3-TPD. Clearly, increasing the PAM loading amount from 15 to 25 wt%, the ammonia adsorption capacity increased. The ammonia uptake over the PAM-25/SBA-15 adsorbent is about 25% higher than that for the PAM-15/SBA-15 adsorbent. However, further increasing PAM loading to 30 wt%, a decrease in ammonia adsorption capacity was observed, though the drop was not much, only about 6%. In this study, 25 wt% of PAM loading is the optimized amount for PAM/SBA-15 adsorbent for ammonia adsorption.

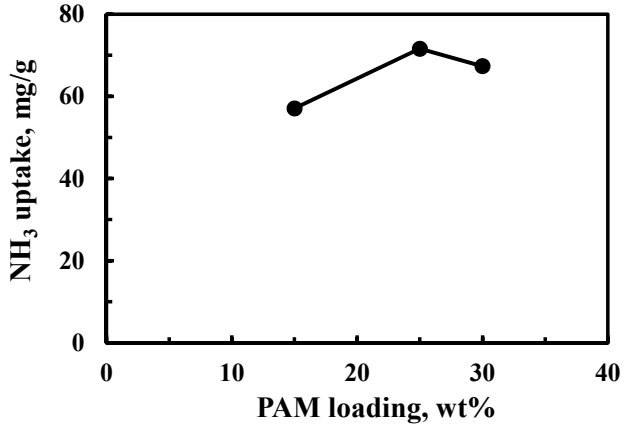

Figure 83. Ammonia adsorption capacity as a function of PAM loading over the PAM/SBA-15 adsorbents measured by NH_3-TPD method.

Although SBA-15 based molecular basket sorbent (MBS) showed a good performance for ammonia adsorption and was able to reduce the ammonia level to the point required for fuel cell applications, the support, mesoporous SBA-15 is not commercially available and the preparation cost is very high, thus the use of SBA-15 may not be practical for the project. Thus, a serial of NH_3-MBS materials for ammonia removal on the basis of the "molecular basket" concept using some commercially available silica support including fumed silica (FS, Cab-O-Sil M-5, Aldrich), silica-gel A (SG-A, Merck grade 10180), silica-gel B (SG-B, Davisil grade 644), silica-gel C (SG-C, Merck grade 7734). The porous properties of these silica supports are listed

in **Table 24**. The polymer was loaded via wet impregnation method. The polymer loading amount was 15, 30, and 50 wt%. The prepared MBS has been termed as PAM(*x*)/*y*, where *x* represents the loaded polymer amount in weight percentage of the total adsorbent and *y* represents the used support. After drying in the vacuum oven at 100 °C for overnight, the adsorbents were evaluated for ammonia adsorption by NH_3-TPD method.

Table 24. The porous properties of commercially available silica supports.

Sample	BET Surface Area, m^2/g	Pore Volume, ml/g	Pore Diameter, nm
FS	214	0.55	14.0
SG-A	750	0.68	4.0
SG-B	300	1.15	15.0
SG-C	550	0.80	6.0

Table 25 shows the ammonia adsorption capacity of the NH_3-MBS adsorbents with 30 wt% PAM polymer loading for ammonia adsorption from a model gas contain 2 v% NH_3 in He at 40 °C measured by TPD method. It can be seen that the adsorption capacity varies with the support used. Among the tested samples, the PAM(30)/SG-B showed highest capacity for NH_3 adsorption, being about 33.3 mg-NH_3/g-sorb. The adsorption capacity of PAM(30)/SG-A was similar to that of PAM(30)/FS, being 29.4 and 25.2 mg-NH_3/g-sorb, respectively, slightly lower than that of PAM(30)/SG-B. When SG-C was used as the support, the adsorption capacity for NH_3 was much lower, being only about 13.7 mg-NH_3/g-sorb, which is less than half of that obtained over the PAM(30)/SG-B adsorbent.

Table 25. The NH_3 adsorption capacity of different NH_3-MBS with 30 wt% PAM polymer loading measured by TPD method.

Sample	Capacity, mg-NH_3/g-sorb
PAM(30)/FS	25.2
PAM(30)/SG-A	29.4
PAM(30)/SG-B	33.3
PAM(30)/SG-C	13.7

Thus, SG-B was chosen as the best silica support for the further study. A series of PAM/SG-B adsorbents have been prepared by loading different amount of PAM onto the SG-B support, including PAM(15)/SG-B, PAM(30)/SG-B and PAM(50)/SG-B adsorbents. The adsorbents were further evaluated for NH_3 adsorption from the gas stream containing 2 v% NH_3 at the temperature of 40 °C by TPD method. On the basis of the desorption curve, the corresponding adsorption capacity of the adsorbent can be calculated, which is about 7.9 mg-NH_3/g-sorb, 33.3 mg-NH_3/g-sorb, and 12.9 mg-NH_3/g-sorb for the PAM(15)/SG-B, PAM(30)/SG-B and PAM(50)/SG-B adsorbents, respectively. **Figure 84** shows the ammonia adsorption capacity as a function of PAM loading over the PAM/SG-B adsorbents measured by NH_3-TPD. Clearly, increasing the PAM loading amount from 15 to 30 wt%, the ammonia adsorption capacity increased. The ammonia uptake over the PAM(30)/SB-G adsorbent is about 3 times higher than that for the PAM(15)/SG-B adsorbent. However, further increasing PAM loading to 50 wt%, a decrease in ammonia adsorption capacity was observed. About 2.5 times drop in the adsorption capacity was observed over the PAM(50)/SG-B adsorbent, compared to that for the PAM(30)/SB-G adsorbent. In this study, 30 wt% of PAM loading is the optimized

amount for PAM/SB-G adsorbent for ammonia adsorption under the conditions studied in this work.

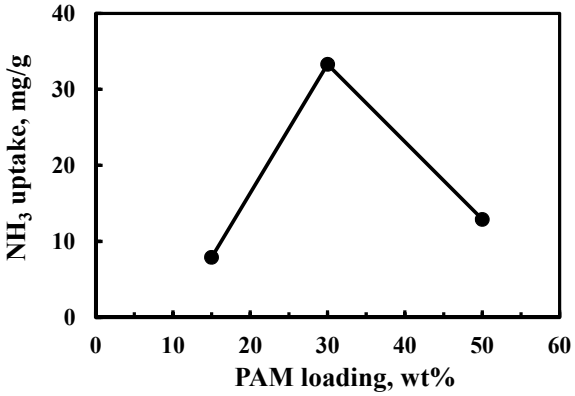

Figure 84. Ammonia adsorption capacity as a function of PAM loading amount over the PAM/SG-B adsorbent measured by NH_3-TPD method.

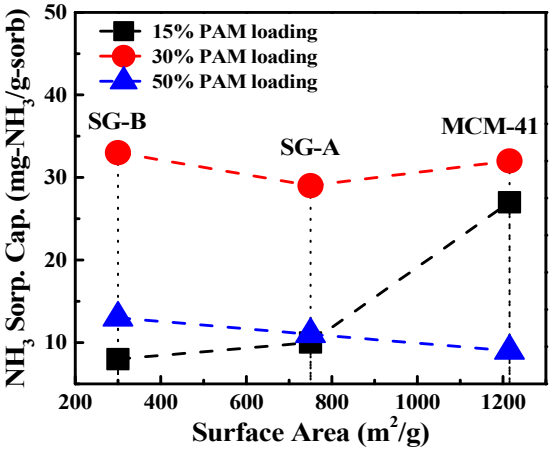

Figure 85. NH_3 sorption capacity as a function of the surface area of the supporting materials at the PAM loading of 15, 30 and 50 wt%.

As shown above, the measured NH_3 sorption capacities of the supported PAM sorbents were quite different with the PAM loading amount and the supporting material used including silica gel, MCM-41 and SBA-15. Since the pore properties of the supports are also quite different, it is important to identify the relationship between the NH_3 sorption capacity and the pore properties of the supporting materials including the surface area, pore volume and pore size. Thus, the relationship between the pore properties of the support and the NH_3 sorption capacity of the supported PAM sorbents over different supports has been examined in this report period.

Figure 85 shows the relationship of the NH_3 sorption capacity versus the values of the surface area of the supports with different PAM loadings including 15, 30 and 50 wt%. It can be seen that with 15 wt% PAM loading, the NH_3 sorption capacity increased with the increase of the surface area of the support. Higher surface area benefits the dispersion of loaded PAM polymer over the support, so that more sorption sites could be exposed for NH_3 sorption. As a result, a higher sorption capacity could be achieved with higher surface area. However, no obvious relationship between the NH_3 sorption capacity and the surface area of the support was observed at PAM loading of 30 and 50 wt%. It suggests that at the PAM loading higher than 30 wt%, the surface area is not a determined factor any more for the NH_3 sorption capacity of the supported PAM sorbents, due likely to the promotion in polymer dispersion is limited at high PAM loadings.

Figure 86 shows the relationship of the NH_3 sorption capacity versus the pore volume of the support with different PAM loadings including 15, 30 and 50 wt%. In this case, there is no relationship between the NH_3 sorption capacity and the pore volume over the 15 wt% PAM loaded sorbents. It may imply that the pore volume of the support does not influence the NH_3 sorption when the PAM loading is only 15 wt%. On the contrary, a good relationship between the NH_3 sorption capacity and the pore volume can be obtained over the 30 and 50 wt% PAM loaded sorbents. Over both sorbents, the measured NH_3 sorption capacity increased with the increase of the pore volume of the supporting material, indicating that the pore volume of the

support plays a vital role in determining the NH_3 sorption capacity of the supported PAM sorbents with PAM loading higher than 30 wt%. The higher the pore volume is, the more the PAM amount can be loaded inside pore channels. Consequently, a higher sorption capacity could be attained.

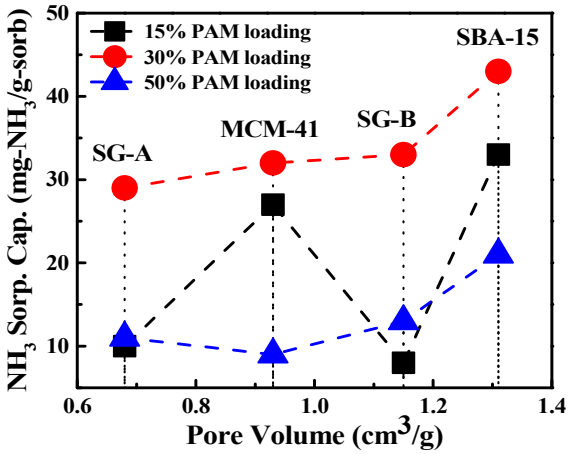

Figure 86. NH_3 sorption capacity as a function of the pore volume of the supporting materials at the PAM loading of 15, 30 and 50 wt%.

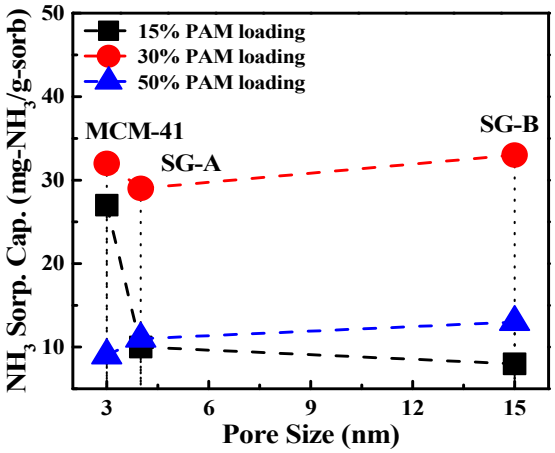

Figure 87. NH_3 sorption capacity as a function of the pore size of the supporting materials at the PAM loading of 15, 30 and 50 wt%.

Figure 87 shows the relationship of the NH_3 sorption capacity versus the pore size of the support with different PAM loadings including 15, 30 and 50 wt%. It can be seen that with 15 and 30 wt% PAM loading, there is no obvious relationship between the NH_3 sorption capacity and the pore size of the support over the supported PAM sorbents. It may imply that the pore size of the support is large enough to accommodate PAM loading and does not influence the NH_3 sorption when the PAM loading is below 30 wt%. When PAM loading is increased to 50 wt%, however, a slight increase in the measured NH_3 sorption capacity is observed with the increase of the pore size of the supporting material, indicating that the pore size of the support is also important in determining the NH_3 sorption capacity of the supported PAM sorbents at PAM loading of 50 wt% or higher. At low PAM loadings such 15 and 30 wt%, about 3 nm of pore size is large enough for PAM diffusion toward pore channels, thus exhibiting no influence. However, at high PAM loading, e.g. 50 wt%, the pore size could limit the diffusion of PAM inside pores. With a larger pore size, more PAM could easily diffuse inside and be accommodated within pores, showing a higher NH_3 sorption capacity.

In summary, the above results indicate that 1) the pore properties of the supporting material associated with PAM loadings has a profound impact on the NH_3 sorption capacity of the supported PAM sorbents; 2) at 15 wt% of PAM loadings, the NH_3 sorption capacity is mainly affected by the surface area of the support, while the pore volume and pore size has no or little influence on the sorption capacity; and 3) The promotion effect of the pore volume is observed over the supported PAM sorbents with 30 and 50 wt% PAM loading. While the pore size exhibits the influence on the sorption capacity only when the PAM loading is 50 wt% or higher.

2.1.6. Adsorbents for siloxane removal

In this project, siloxane compounds are also targeted contaminants to be removed. Among siloxanes detected in biogases, the linear hexamethyldisiloxane (L2), and the cyclic trimeric hexamethylcyclotrisiloxane (D3) and tetrameric octamethylcyclotetrasiloxane (D4) are usually the most abundant [28]. It is suggested in literature that compared to activated carbon, silica gel is more promising for siloxane removal in terms of adsorption capacity and regenerability [29]. Thus, we have purchased commercial silica gel samples testing for siloxane removal, which will be used as a baseline for this project. Two type of silica gel samples with different pore diameter and particle size were obtained from Sigma-Aldrich, i.e., 10 nm & 70-230 meshes and 6 nm & 230-400 meshes, which is termed as Silica Gel-10 and Silica Gel-6, respectively. Considering that MCM-41 and SBA-15 are typical silica-based mesoporous molecular sieves with high surface area, larger pore volume and pore diameter, they may be better for siloxane adsorption compared to silica gel material. Therefore, in this period, both silica gel samples, MCM-41 and SBA-15 adsorbents have been examined for siloxane removal. For a quick screening, a larger siloxane concentration (about 0.305 mg/mL) was applied and the hexamethyldisiloxane was used as the model siloxane compound.

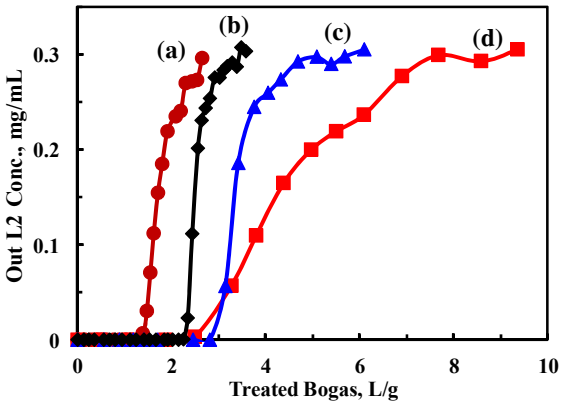

Figure 88. Breakthrough curves of hexamethyldisiloxane (L2) over the (a) silica gel (10 nm & 70-230 mesh), (b) silica gel (6 nm & 230-400 mesh), (c) MCM-41 and (d) SBA-15 at room temperature from a model gas containing 0.305 mg/mL of L2 in nitrogen.

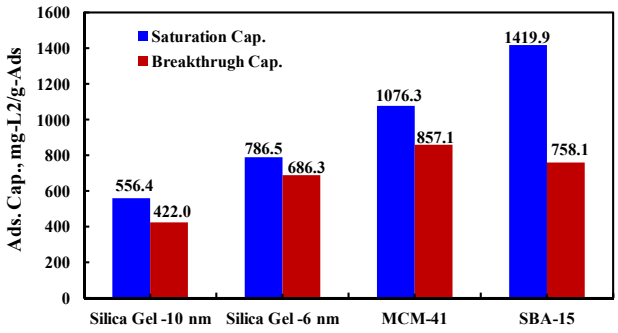

Figure 89. Breakthrough and saturation capacity of hexamethyldisiloxane (L2) over the adsorbents at room temperature from a model gas containing 0.305 mg/mL of L2 in nitrogen.

Figure 88 shows the breakthrough curves of L2 over the silica gel (pore size of 10 and 6 nm,), MCM-41 and SBA-15 adsorbents. As it can be seen, the silica gel adsorbent exhibited a good performance for L2 siloxane removal at room temperature, which is in agreement with that reported in literature [29]. In addition, the silica gel samples showed a different adsorption capacity. Over the Silica Gel-10 adsorbent, about 1.38 L/g of biogas could be treated before the L2 siloxane could be detected in the effluent. The treated biogas amount was about 2.25 L/g over the Silica Gel-6 adsorbent before breakthrough, which is about 63.5% higher than that for the Silica Gel-10 adsorbent. Compared to silica gel samples, the prepared MCM-41 and SBA-15 showed a better performance for L2 siloxane removal. Before breakthrough, the treated model biogas volume was 2.81 and 2.49 L/g over the MCM-41 and SBA-15 adsorbent, respectively.

On the basis of breakthrough curves, the corresponding breakthrough capacity and saturation capacity of the adsorbents studied in this work can be calculated. The results are presented in **Figure 89**. Over the silica gel samples, the saturation capacity and breakthrough capacity of 556.4 and 422.0 mg-L2/g for the Silica Gel-10 sample and 786.5 and 686.3 mg-L2/g for the Silica Gel-6 sample, respectively. Among the four adsorbents, The MCM-41 showed the highest breakthrough capacity of 857.1 mg-L2/g with a good saturation capacity of 1076.3 mg-L2/g. The highest saturation capacity was obtained over the SBA-15 adsorbent, which was 1419.9 mg-L2/g, about 80.5% increase of that for the Silica Gel-6 sample. The current results indicate that MCM-41 and SBA-15 are better than silica gel for siloxane removal at room temperature.

Based on literature [28], the cyclic siloxane should also be studied. Thus we also used the cyclic tetrameric octamethylcyclotetrasiloxane (D4) as the model siloxane compound, which was purchase from Sigma-Aldrich. A model gas containing N_2 saturated at room temperature with D4 (molecular weight, 296.6; melting point, 17.5 °C; boiling point, 172 °C; vapor pressure at 25 °C, 140 Pa [30]) by a bubbler was used for this ICP-MS calibration. Two N_2 gas lines controlled by the mass flow controllers are set up to adjust and obtain the desired D4 concentration for the calibration curve measurement: one is for D4 bubbling (containing about 1382 ppm D4) and the other is to dilute the stream containing D4. The mixture gas was monitored on-line by the GC-ICP-MS.

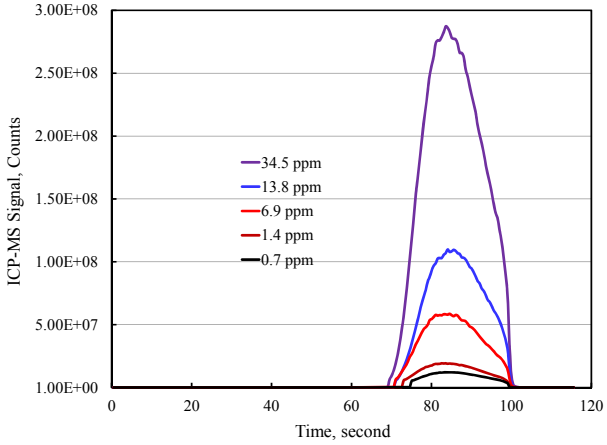

Figure 90. Real-time ICP-MS Signal for D4 at Different Concentrations.

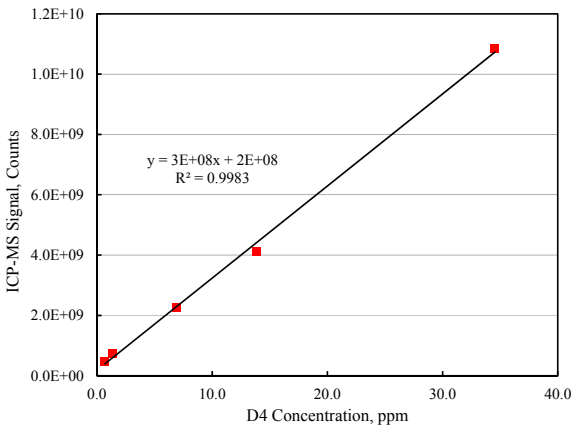

Figure 91. Calibration Curve of D4 for the ICP-MS.

The calibration of the ICP-MS for D4 silxoane was carried out for the concentrations ranging from 0.7 to 34.5 ppm. **Figure 90** shows the ICP-MS signal at different concentration of D4 and **Figure 91** shows the typical calibration curve for D4 siloxane. The calibration curve gives a good linearity with high R^2 value. The minimum concentration of siloxane was 0.7 ppm due to the limitation of the mass flow controller. The detecting limit for ICP-MS is much lower.

Figure 92 shows the breakthrough curve of 20 ppm D4 siloxane adsorption on the silica gel adsorbent at room temperature and atmospheric pressure. We selected a commercial silica gel as an adsorbent to removal siloxane from the model ADG. A high-purity grade silica gel (Merk Grade 10184) with pore size of 10 and 6 nm, particle size at 70-230 mesh and a surface area of 300 m^2/g was used. The ADG gas flowrate was about 200 mL/min. **Figure 93** shows the ICP-

MS signal for the outlet concentrations of D4 siloxane under different time on stream during the adsorption of D4 siloxane over silica gel.

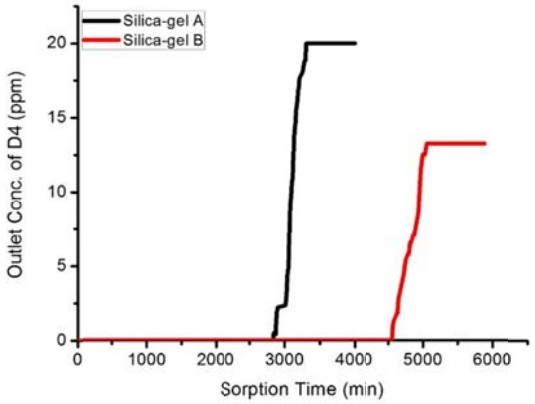

Figure 92. Breakthrough curve of 20 ppm D4 siloxane on the Merk silica gel with pore size of (A) 10 and (B) nm at room temperature and atmospheric pressure under the ADG gas flowrate of 200 mL/min with a GHSV of 5000 h^{-1}.

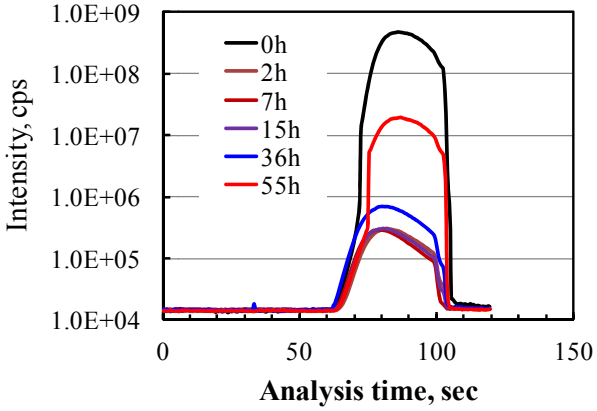

Figure 93. The real-time ICP-MS signal for the outlet D4 siloxane concentration under different time on stream during the adsorption of D4 siloxane over silica gel.

As can be seen, both the silica gel adsorbents showed a good performance for D4 siloxane removal from the model ADG gas under the conditions studied. Before breakthrough point that was designated at 100 ppb, the D4 siloxane can be completely removed and the outlet D4 concentration was only about couple of ppb. Over the silica gel sample with pore size of 10 nm, the outlet D4 siloxane concentration reached the breakthrough point after about 47 hrs of adsorption. It means about 567 L/g-A of biogas could be treated before breakthrough, which is corresponding to a breakthrough capacity of 135 mg-D4/g-A. . This result shows that silica gel is able to deeply remove siloxane down to ppb level and is more promising for cleanup of siloxane in ADG gas. The literature also reported a good performance of silica gel adsorbent for siloxane removal [29]. As for the silica gel sample with pore size of 6 nm, the adsorption performance is even better. It took about 76 hrs to break through. That is, about 910 L/g-A of biogas could be treated before breakthrough, corresponding to a breakthrough capacity of 217 mg-D4/g-A. It is about 60% higher than that for the one with pore size of 10 nm. It demonstrates that the pore size of silica gel can significantly affect the adsorption performance for siloxane. Suitable pore size is required for silica gel adsorbent to achieve high capacity for siloxane removal under the conditions studied.

2.1.7. Conceptual Process Design for ADG Fuel Processor

As shown in our previous quarterly reports, we have developed two types of solid sorbents, i.e., mixed metal oxides adsorbents and H_2S-molecular basket sorbents (H_2S-MBS), for deep desulfurization of the anaerobic digest gas (ADG) from 200-500 ppmv to around 10 ppbv with a good regenerability. We have also developed a new type solid sorbent for deep removal of ammonia from biogas stream, so-called NH_3-MBS using acidic polymer for NH_3 adsorption. Furthermore, we have investigated silica based adsorbents for siloxane removal and identified that mesoporpous silica is more effective for siloxane adsorption. On the basis of the adsorption

performance for deep desulfurization, NH_3 removal and siloxane adsorption, we subsequently propose a conceptual process of ADG fuel processor for use in the solid oxide fuel cell system, which is illustrated in the **Figure 94**.

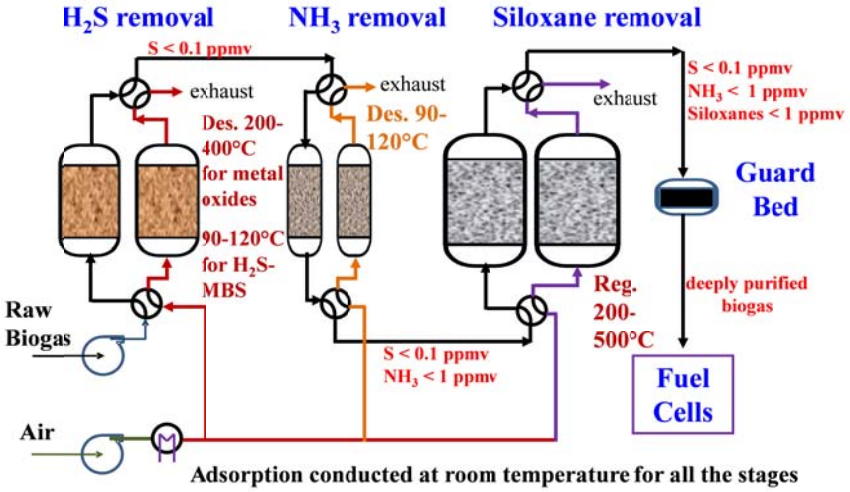

Figure 94. The conceptual design of the ADG processor utilizing the developed air-regenerable mixed metal oxides sdsorbent or H_2S-MBS for deep desulfurization and NH_3-MBS for NH_3 removal and mesoporous silica for siloxane removal with a activated carbon based guard bed to removal all other trace contaminants for SOFCs.

In this conceptual design of the ADG fuel processor, it involves three stages, i.e., the deep desulfurization stage, the NH_3 sorption stage and silocane removal stage, and an additional guard-bed for better performance of SOFC stacks. The air-regenerable mixed metal oxides adsorbent or low-temperature regenerable H_2S-MBS for deep desulfurization of ADG fuel down to below 10 ppbv, specific designed NH_3-MBS for deep removal of NH_3 to below 1 ppmv and high affinity mesoporous silica for siloxane removal developed in this project are applied in the these three stages, respectively.

In the desulfurization stage, the pressurized ADG fuel gas is introduced into the adsorption column, which is loaded with the air regeneration mixed metal oxide adsorbent or low-temperature regenerable H_2S-MBS. The adsorptive desulfurization is performed at room temperature. After desulfurization, the sulfur-free ADG fuel gas is then delivered to the ammonia adsorption stage. At the same time, the air flow is pumped to the adsorbent regeneration chamber, which is operated at a temperature of 200-400 °C when the mixed metal oxides adsorbent is applied or maintained at a temperature of 90-120 °C when the H_2S-MBS is packed. The fresh mixed metal oxides adsorbent or H_2S-MBS is first operated in the desulfurization chamber. After certain time of operation (on the basis of adsorbent performance for sulfur removal at 10 ppbv level), the spent adsorbent is then switched to the regeneration chamber, where the spent mixed metal oxides adsorbent will be completely regenerated by air at 200-400 °C. In the case of H_2S-MBS is used, the regeneration temperature is around 90-120 °C. The adsorption capacity for sulfur will be fully recovered. The regenerated adsorbent is then switched back to the desulfurization chamber for further cycles. In that way, the desulfurization adsorbent can be continuously operated on site for a long time. No manually operation is needed for the desulfurization stage until the adsorbent material has to be replaced.

It should be pointed out that if CO_2 removal is not required, the mixed metal oxides adsorbent and the H_2S-MBS using tertiary amine will be a good option for deep desulfurization of ADG fuel gas. However, if the partial and/or full removal of CO_2 is required as well as the removal of H_2S, the task-specific H_2S-MBS materials loaded with primary and/or secondary amine compounds such as polyethylenimine are recommended.

Similarly to the deep desulfurization stage, the NH_3 adsorption and siloxane removal stages can be operation in the same way. The regeneration of NH-MBS will be performed at 90-120 °C. While a much higher temperature is required to recover the adsorption capacity of mesoporous silica for siloxane as high temperature is needed to fully convert siloxane to silica under air flow. The upgraded ADG fuel gas will then pass through a short guard-bed packed with activated carbon to removal other in-significant trace contaminants. The deep cleaned ADG fuel gas will supply to the SOFC stack, which provides the power for various usages.

It should be pointed out that the energy required for the regeneration of solid adsorbents for the three stages in the ADG fuel processor is self-supported in this design by incorporating a secondary battery. The battery is initially charged ex-situ and provides the power for the starting of the processor. When the processor is under running condition, the battery can be fully charged by the SOFC stack and continuously supply the energy needed for the adsorbent regeneration chamber and other parts.

2.2. Commercial Diesel Fuel Processor

2.2.1. Desulfurization of Diesel Fuel

2.2.1.1. Supported-Ni adsorbent

In this project, we have developed the mesoprous molecular seive supported nickel adsorbents for deep desulfurization of commercial diesel fuel containing 15 ppmw sulfur. The molecular sieve, SBA-15 was synthesized according to the procedure reported by Wang et al. [27,31], who modified the method initially reported by Zhao et al. in 1998 [32]. Typically, a homogeneous mixture, which was composed of triblock copolymer Pluronic of P123 (EO20PO70EO20, MW=5800, Aldrich) and tetraethyl orthosilicate (TEOS) in hydrochloric acid, was stirred at 40 ºC for 20 h, and then further treated at 100 ºC for 24 h. The solid product was filtered and washed with plenty of water, dried in an oven at 100 ºC, and subsequently calcined at 550 ºC for 6 h under an air flow (100 ml/min).

The SBA-15-supported nickel sorbent were prepared by an incipient wetness impregnation (IWI) method. The desired amount of $Ni(NO_3)_2.6H_2O$ was dissolved in tetrahydrofuran (THF), and the solution was slowly added into the support material at room temperature under the mechanical stir without or with ultrasonic aid in a VWR-Model 75T ultrasonic bath. For the ultrasonic aid case, after adding the solution, the mixture was kept in the ultrasonic bath for 3 h at room temperature. The mixture was then dried in an oven at 100 ºC overnight. The dried samples were then reduced in a fixed-bed reactor under a pure hydrogen gas flow at 550 ºC for 4 h.

Evaluation of the ADS performance of sorbents was conducted in a fixed-bed flow sorption system with a stainless steel column (4.6 mm I.D. x 150 mm length). About 0.8-1.1 g (depending on the packing density of the sorbent) of the dried sorbent (before reduction) was packed into a stainless steel column, and then was reduced *in situ* under a pure hydrogen flow at 550˚C for 4 h. When the temperature of the column was decreased to the room temperature under the hydrogen flow, the column was disconnected to the system and sealed quickly. After weighting the sealed column to estimate the weight of the reduced nickel-based sorbent by

difference, the column was reconnected into the system for the subsequent desulfurization test. A commercial ULSD (or a model fuel) was fed into the column from the bottom by a HPLC pump. The adsorption conditions were controlled at 200 ˚C and a liquid hourly speed velocity (LHSV) of 4.8 h^{-1}. The effluent fuel from the top of the column was periodically sampled at an interval of 15-20 min for analysis. The ULSD with 15 ppmw total sulfur used in this study was from British Petroleum (BP).

Figure 95 shows the breakthrough curves of the ULSD over two Ni20/SBA-15 sorbents prepared by the IWI method with and without the ultrasonic aid. The breakthrough capacity of the Ni20/SBA-15 prepared by the IWI method without the ultrasonic aid was only 0.43 mg-S/g-sorb at a breakthrough sulfur level of 1 ppmw. This measured capacity is similar to that (0.47 mg-S/g-sorb) of the best Ni/SBA-15 sorbent reported by Park et al. for desulfurization of a ULSD with 11.7 ppmw sulfur. The shapes of the two breakthrough curves are also similar. The breakthrough capacity of the Ni20/SBA-15 prepared by the IWI method with the ultrasonic aid was increased to 0.98 mg-S/g-sorb, which is about two times higher than that of the Ni20/SBA-15 without the ultrasonic aid. In comparison with the previous sorbents prepared in the last period, the amount of the treated fuel per gram of sorbent at the breakthrough sulfur level of 2 ppmw increased significantly from less than 4 g-F/g-A to higher than 75 g-F/g-A, which increased by a factor of more than 18.

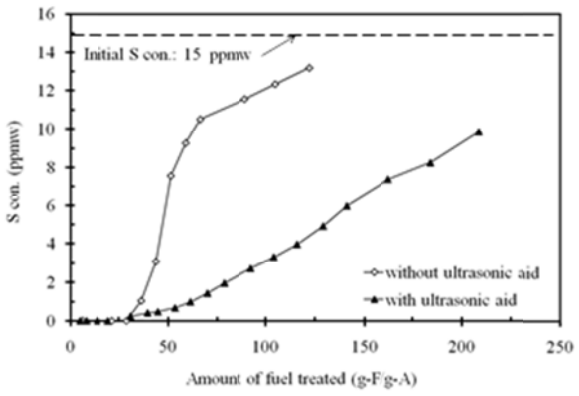

Figure 95. Breakthrough curves of ULSD over Ni20/SBA-15 sorbents prepared with and without ultrasonic aid. Sorption condition: 200 ˚C and 4.8 h^{-1} of LHSV.

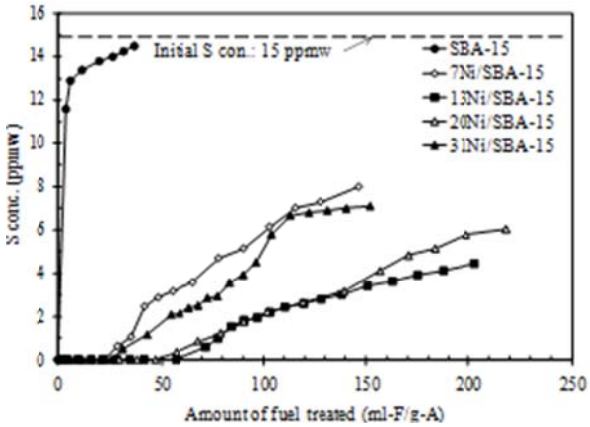

Figure 96. Breakthrough curves of ULSD over Ni/SBA-15 sorbents with different Ni-loading. Sorption condition: 200 ˚C and 4.8 h^{-1} of LHSV.

It is well known that the loading amount of nickel on the supports plays an important role in adsorption and heterogeneous catalysis. In order to examine the effect of the loading amount of nickel on the desulfurization performance, four Ni/SBA-15 sorbents with different nickel loading amounts of 7, 13, 20, and 31 wt % were prepared by using the IWI method with the ultrasonic aid. The ADS performance of the four Ni/SBA-15 sorbents as well as SBA-15 for the ULSD was evaluated in the flow sorption system at 200 °C and 4.8 h^{-1} of LHSV. The breakthrough curves are shown in **Figure 96**. SBA-15 shows almost no capacity for sulfur in comparison with Ni/SBA-15 sorbents, indicating that the nickel is a key component that interacts directly with the sulfur compounds. As it can be seen, the sorption capacities of 7Ni/SBA-15 and 31Ni/SBA-15 sorbents are much lower than those of 13Ni/SBA-15 and 20Ni/SBA-15

sorbents at a breakthrough sulfur level of 1 ppmw. The ADS capacity of the sorbents increases in the order of SBA-15 << Ni7/SBA-15 < Ni31/SBA-15 < Ni13/SBA-15 ≈ Ni20/SBA-15. The ADS capacity of 13Ni/SBA-15 and 20Ni/SBA-15 are 1.00 and 0.98 mg-S/g-sorb which are significantly higher than others.

Besides SBA-15, another mesoporous molecular sieve, MCM-48 which has a 3D pore structure was used as the supported for preparing the supported Ni adsorbent. The MCM-48-supported nickel sorbents with the nickel loading amount of 7, 13, 20, and 31 wt % were prepared by using the IWI method with the ultrasonic aid. Their sorption performances for desulfurization of the ULSD were evaluated in the flow sorption system at 200 °C and 4.8 h^{-1} of LHSV. The breakthrough curves for the four Ni/MCM-48 sorbents are shown in **Figure 97**. The Ni7/MCM-48, Ni13/MCM-48 and Ni31/MCM-48 showed the breakthrough capacity similar to the Ni/SBA-15 with the same nickel loading. Interestingly, it was found that Ni20/MCM-48 gave the highest breakthrough capacity of 2.1 mg-S/g-sorb among the sorbents prepared in this study, which is higher than that of Ni13/SBA-15, the best Ni/SBA-15 sorbent obtained in this study by a factor of 2. With increasing nickel loading, the measured breakthrough capacity increased at first, and then decreased after passing a maximum value. It seems that the continuous increase in the nickel loading may cause the agglomeration of the nickel particles and increase the nickel crystallite size, thus resulting in the decrease of the active surface nickel atoms. It should be mentioned that the best loading amount of nickel in this study was 13-20 wt% for SBA-15 and 20 wt % for MCM-48, while the best loading amount of nickel in the study by Park et al. is 30 wt% for both SBA-15 and KIT-6 [33]. The present study used the different diesel fuel and different sorbent preparation method, which may be the possible reasons. Further investigation is necessary to clarify it.

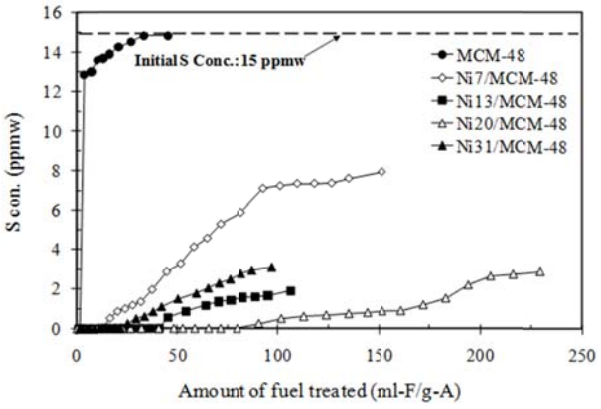

Figure 97. Breakthrough curves of ULSD over Ni/MCM-48 sorbents with different Ni-loading. Sorption condition: 200 ˚C and 4.8 h^{-1} of LHSV.

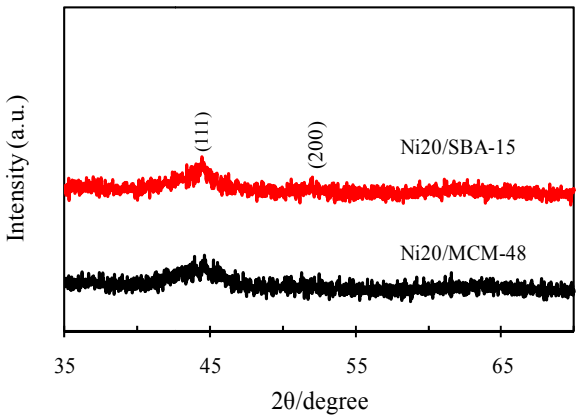

Figure 98. XRD patterns of the reduced Ni20/SBA-15 and Ni20/MCM-48 sorbents prepared by IWI with ultrasonic aid.

As shown in **Figure 96** and **97**, the desulfurization performance of Ni20/MCM-48 is about 2 times higher than that of Ni20/SBA-15, although both sorbent have the same nickel loading. The XRD pattern of the Ni20/MCM-48 is shown in **Figure 98** in comparison with that of Ni20/SBA-15. The peak for nickel (111) in Ni20/MCM-48 is broader than that in Ni20/SBA-15. According to the XRD patterns, the estimated nickel crystal size for the former is 2.4 nm and

for the latter is 3.3 nm. It is clear that the particle size of nickel crystallites in Ni20/MCM-48 is significantly less than that in Ni20/SBA-15. The further characterization of these two samples by the H_2 chemisorption shows that the nickel dispersion in Ni20/MCM-48 is about 35 %, which is significantly higher than that of 21 % in Ni20/SBA-15, which is consistent with the results from the XRD patterns. Comparison of Ni20/MCM-48 and Ni20/SBA-15 indicates that structure of the support material also plays an important role in determining the ADS performance of the nickel-based sorbents.

MCM-48 and Ni20/MCM-48 were also characterized by TEM. The TEM images are shown in **Figure 99**. **Figure 99a** confirms the three-dimensional branched network structure of the synthesized MCM-48. **Figure 99b** shows the uniform distribution of the nickel particles with an average particle size about 2.5 nm in Ni20/MCM-48, which is consistent with the crystal size (2.4 nm) based on the XRD analysis. Since the average pore size of MCM-48 is around 2.7 nm, the majority of the nickel particles should be in the MCM-48 channels, which results in the high dispersion of nickel on the MCM-48 surface. The three dimension pore structure, less pore size and higher surface area of MCM-48 may be the reasons why the performance of Ni20/MCM-48 is much better than that of Ni20/SBA-15, in which SBA-15 has with one dimension pore structure.

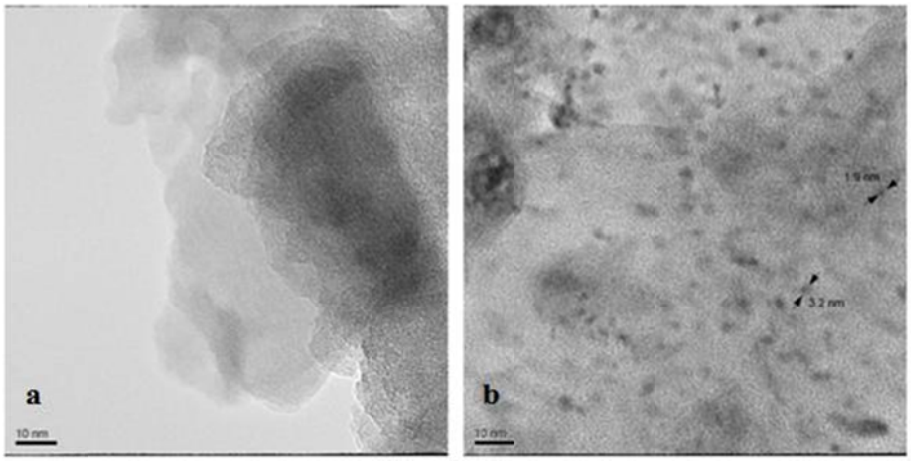

Figure 99. TEM images of MCM-48 (a) and the reduced Ni20/MCM-48 (b).

In order to clarify the desulfurization selectivity of Ni20/MCM-48 for various sulfur compounds in ULSD, the initial ULSD and the treated ULSD over Ni20/MCM-48 were analyzed by GC-PFPD. The sulfur compounds in the fuels were identified by comparison of the relative retention times with those reported in literature [34,35]. The GC-PFPD chromatograms of the initial ULSD and the treated ULSD with the assigned peaks are shown in Figure 12. The major sulfur compounds in initial ULSD with 14.5 ppmw sulfur are alkyl-DBTs with two alkyl substituent groups at the 4- and 6-positions, such as 4,6-DMDBT, 4-ethyl,6-methyl-dibenzothiophene (4-E,6-MDBT), 2,4,6-trimethyldibenzothiophene (2,4,6-TMDBT), 4,6-diethyldibenzothiophene (4,6-DEDBT) and 6-ethyl,2,4-methyldibenzothiophene (6-E,2,4-DMDBT). This type of the sulfur compounds have been reported to be the most refractory sulfur compounds [36], and thus, remained in the commercial ULSD even after deep HDS.

It can be seen from the GC-PFPD chromatogram (**Figure 100**) of the treated fuel corresponding to the collected sample at 107 mL-fuel/g-sorb, the first breakthrough sulfur compound was 4,6-DEDBT. By comparison of the GC-PFPD peak area of the sulfur compounds

in the treated and initial fuels, it appears that the desulfurization selectivity of Ni20/MCM-48 decreases in the order of 4-MDBT > 4,6-DMDBT ≈ 2,4,6-TMDBT > 4-E,6-MDBT ≈ 6-E,2,4-DMDBT, > 4,6-DEDBT. It indicates that the desulfurization selectivity is dependent not only on the number of the alkyl substituent groups at the 4- and 6-positions, but also on the size of the alkyl substituent groups at the 4- and 6-positions. The lowest selectivity for 4,6-DEDBT among all sulfur compounds in the ULSD can be ascribed to the two largest alkyl substituent groups (ethyl groups) at the 4- and 6-positions. This finding strongly suggests that the sorption of the sulfur compounds on the nickel-based adsorbents is directly through an interaction between the sulfur atom in alkyl DBTs and the exposed nickel atom, while both the number and the size of alkyl substituent groups at the 4- and 6-positons have a strongly steric hindrance toward such interaction. This steric hindrance increases the interaction distance between S atom and nickel sites, resulting in a weak interaction and a low selectivity for the alkyl DBTs with strong steric hindrance. Only highly active nickel sites, such as those at the edges and corners, may be able to interact with those sulfur compounds.

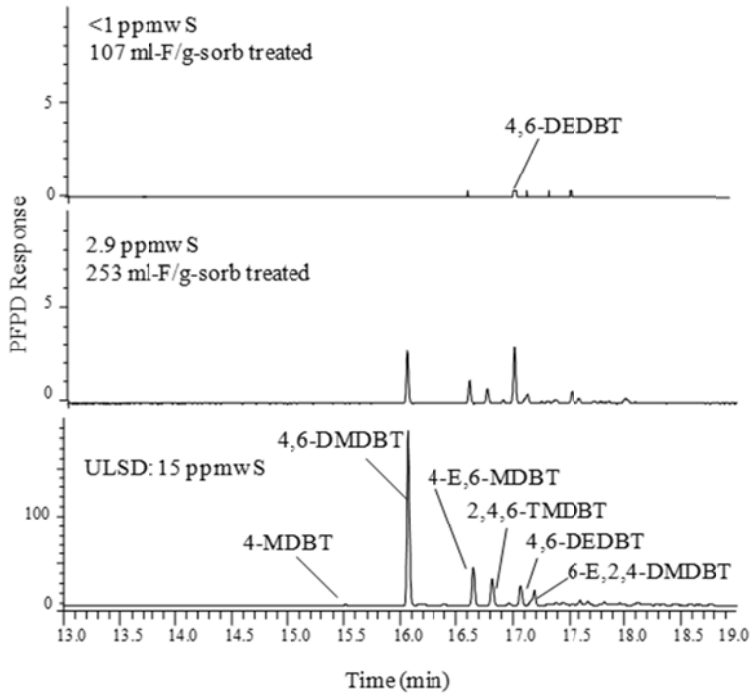

Figure 100. GC-PFPD chromatographs of the initial ULSD and desulfurized ULSD samples over Ni20/MCM-48 at 220 ˚C, 4.8 h^{-1} of LHSV.

In order to understand further how the alkyl DBTs with the two alkyl substituent groups at the 4- and 6-positions are removed from the ULSD by Ni20/MCM-48 adsorbent, ADS of a model fuel containing 9.12 mmol/L of 4,6-DMDBT in n-decane was performed over Ni20/MCM-48 at 220 °C and 4.8 h^{-1} of LHSV in the fixed-bed flow system. The products were identified by a combination of GC-MS and GC-FID analysis. The major products detected in the effluent are 3-MBP, 3,3'-DMBP and 3,4'-DMBP. The molar concentrations of the products and the reactant 4,6-DMDBT as a function of the effluent volume are shown in **Figure 101**. No sulfur compounds were detected when the effluent volume was less than 0.0195 L/g-sorb. The

breakthrough capacity for 4,6-DMDBT was about 0.18 mmol-S/g-sorb (or 5.8 mg-S/g-sorb), and the saturation capacity was about 0.28 mmol-S/g-sorb (or 8.8 mg-S/g-sorb). The total molar concentration of the alkyl biphenyls was less than 0.8 mmol/L, which is much lower than the molar concentration of 4,6-DMDBT in the initial fuel (9.12 mmol/L). In comparison of the total molar number of the alkyl biphenyls in the effluent and the total sorbed sulfur molar number, it is found that the total molar number of the alkyl biphenyls in the effluent is only 5.9 % of the total sorbed sulfur molar number, indicating that about 94% of the removed 4,6-DMDBT molecules or the formed intermediates from them still stay on the nickel surface. This value is much higher than that (33%) for the ADS of benzothiophene on a nickel-based sorbent at 25 °C, reported previously by Ma et al. [37].

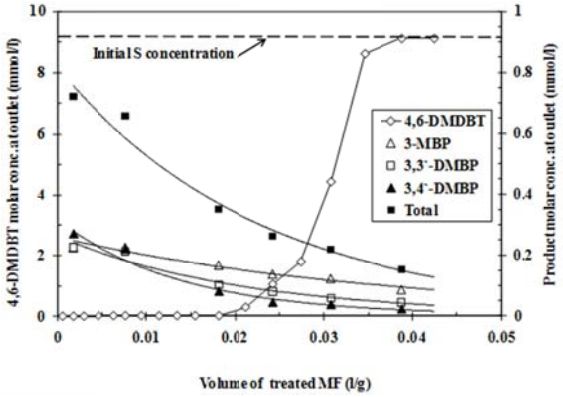

Figure 101. The molar concentrations of the formed products and reactant 4,6-DMDBT as a function of the effluent volume.

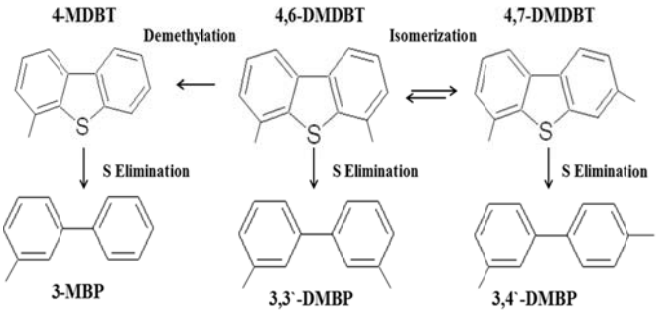

Figure 102. Desulfurization pathways of 4,6-DMDBT on Ni20/MCM-48.

This is also different from the results observed by Hu et al., who found that thiophene molecules interacted strongly with the metallic nickel on Raney Nickel surface at -100 °C, and formed the surface nickel sulfides and released all the hydrocarbon part at 220 °C [38]. A possible reason may be that no steric hindrance of the alkyl substituent groups in thiophene and benzothiophene allows a strong interaction between the sulfur and the exposed nickel, which facilitates the S-C bond scission and the release of the corresponding hydrocarbon. The results imply that the two methyl substituent groups at the 4- and 6-positions weaken remarkably the interaction between the sulfur atom and the exposed nickel atoms, resulting in the significant diminution of the S-C bond scission.

The presence of 3-MBP and 3,3`-DMBP and 3,4'-DMBP in the products implies that the sulfur atom in 4,6-DMDBT may be eliminated by three pathways, as shown in **Figure 102**: direct S elimination (DE) from 4,6-DMDBT, isomerization of 4,6-DMDBT to form 4,7-DMDBT followed by the S elimination from 4,7-DMDBT (IFE) and demethylation of 4,6-DMDBT to form 4-MDBT followed by the S elimination from 4-MDBT (DFE). The similar concentration of 3-MDBT, 3,3`-DMBP and 3,4'-DMBP was detected in the effluent when the treated volume of the model fuel was less than 0.01 L/g, indicating that the reaction rate for the three pathways was similar within this period of adsorption. After passing 0.01 L/g of the treated volume, the concentration of 3-MDBT was significantly higher than others, suggesting that the surface reaction through DFE became dominant.

By combination of the results of the ADS selectivity for the different sulfur compounds in the ULSD and the ADS of 4,6-DMDBT on Ni20/MCM-48, it is clear that the sulfur compounds are first adsorbed on the surface directly through an interaction between the sulfur atom in the compounds with the exposed nickel, and then, only a small part of the adsorbed sulfur compounds (~6 %) react further with the surface nickel through DE, IFE and DFE pathways to eliminate the sulfur atom by hydrogenolysis to form the surface nickel sulfide and release the corresponding hydrocarbon part from the surface to the liquid. It should be mentioned that the ADS was conducted in the absence of hydrogen gas. The required hydrogen for the formation of those hydrocarbons may come from the nickel surface or other hydrocarbons in the fuel. The results suggest that introducing hydrogen to the nickel surface should accelerate the hydrogenolysis of the adsorbed sulfur compounds and the release of the corresponding hydrocarbon part, and thus, providing more accessible nickel atoms to interact with other sulfur compounds, as also reported by Landau et al. [39].

In comparison of the ADS of ULSD and the model fuel on Ni20/MCM-48, the ADS breakthrough capacity of Ni20/MCM-48 for the model fuel is about 5.8 mg-S/g-sorb, which is about 3 times higher than that for ULSD. In addition of the higher sulfur concentration in the model fuel, there may be two other reasons: 1) ULSD contains more refractory sulfur compounds than the model fuel which contains 4,6-DMDBT only, such as 4-E,6-MDBT 6-E,2,4-DMDBT, and 4,6-DEDBT having larger size of the alkyl groups at the 4- and/or 6-positions; 2) ULSD contains 12 ppmw of nitrogen compounds, which is the same magnitude as the sulfur compounds, while the nickel-based sorbents usually have higher affinity to the nitrogen compounds than the sulfur compounds, as reported in our previous study [40].

2.2.1.2. Mixed-Metal-Oxides-based adsorbents

2.2.1.2.1 Multi-Mixed-Metal-Oxides-based adsorbents

In this project, more than 40 multi-mixed-metal oxides including: $Ti_{0.9}Ce_{0.1}O_2$, $Ti_{0.1}Ce_{0.9}O_2$, Al-Ti-Ce-O, Zr-Al-Ti-Ce-O, V-Al-Ti-Ce-O, Cu-Al-Ti-Ce-O, Zn-Al-Ti-Ce-O, Co-Al-Ti-Ce-O, Ni-Al-Ti-Ce-O, Mo-Al-Ti-Ce-O, Sm-Al-Ti-Ce-O, Mn-Al-Ti-Ce-O, Fe-Al-Ti-Ce-O, Cr-Al-Ti-Ce-O, W-Al-Ti-Ce-O, Pt-Al-Ti-Ce-O, etc., have been synthesized. The adsorption desulfurization activity of these metal oxides were tested using real diesel fuel with 15 ppmw sulfur in a batch system. The adsorption procedures for screening adsorbents are shown as follows: The adsorbents were dried at 110 ℃ for more than 10 hours before testing. About 0.5 g of the adsorbent and 5.0 g of the commercial diesel fuel were added into the test tube with a stirring bar. The tube was sealed with a cap, and set at room temperature, and the magnetic stirring was turn on. The adsorption time is 2 hours. After the adsorption experiment, the treated diesel fuel was separated from the adsorbent by centrifugation and moved into a small bottle for analysis.

The total sulfur concentrations in the diesel fuel were determined using an Antek 9000S total sulfur analyzer. The sulfur detection limit of the total sulfur analyzer in the normal working range is 0.5 ppmw sulfur. The sulfur contents after adsorption and the determined adsorption capacities of various adsorbents are shown in **Table 26**.The result indicated that the sulfur content in the fuel was able to be reduced to below 1 ppmw by using metal oxides Ti-Ce-Zr-O, Au-Al-Ti-Ce-O, Ti-Ce-Al-O and Pt-Al-Ti-Ce-O. The adsorption tests indicate that the sulfur content can be reduced to below 1 ppmw by using metal oxides Cu-Al-Ti-Ce-O, Mo-Al-Ti-Ce-O, Ni-Al-Ti-Ce-O, Fe-Al-Ti-Ce-O and Pt-Al-Ti-Ce-O in a batch adsorption system at room temperature under atmospheric pressure.

Table 26. Sulfur contents of the commercial diesel fuel after adsorption and the adsorption capacities of mixed-metal oxides in a batch system.

Adsorbent	Sulfur content after adsorption (ppm)	Sulfur capacity (mg-S/g-Ads.)
$Ti_{0.9}Ce_{0.1}O_2$	1.6	0.13
$Ti_{0.1}Ce_{0.9}O_2$	3.4	0.11
Al-Ti-Ce-O	2.5	0.12
Zr-Al-Ti-Ce-O	3.4	0.12
V-A-Ti-Ce-O	4.8	0.10
Cu-Al-Ti-Ce-O	0.0	0.15
Zn-Al-Ti-Ce-O	3.9	0.11
Co-Al-Ti-Ce-O	2.4	0.12
Ni-Al-Ti-Ce-O	0.8	0.14
Mo-Al-Ti-Ce-O	0.0	0.15
Sm-Al-Ti-Ce-O	2.6	0.12
Mn-Al-Ti-Ce-O	3.6	0.11
Fe-Al-Ti-Ce-O	0.8	0.14
Cr-Al-Ti-Ce-O	7.2	0.08
W-Al-Ti-Ce-O	2.5	0.12
Pt-Al-Ti-Ce-O	0.0	0.14

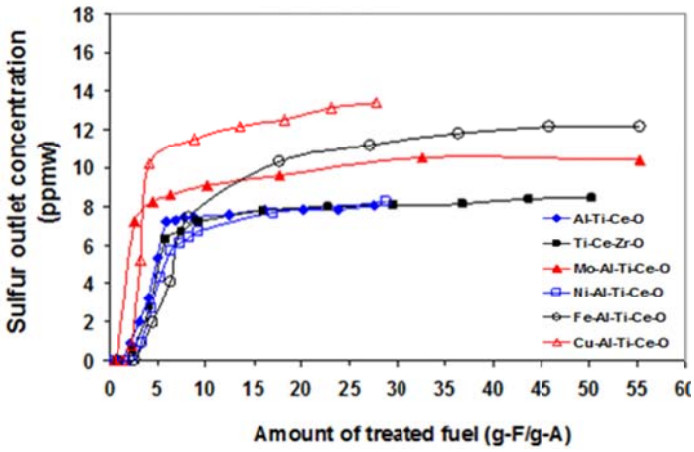

Figure 103. Breakthrough curves of commercial diesel fuel over mixed-metal oxides Al-Ti-Ce-O, Ti-Ce-Zr-O, Mo-Al-Ti-Ce-O, Ni-Al-Ti-Ce-O, Fe-Al-Ti-Ce-O and Cu-Al-Ti-Ce-O.

According to their adsorption performance in the batch tests, some representative mixed-metal oxides, which were able to reduce the sulfur content from 15 ppm to less than 1 ppmw in the batch system, were selected for further test in a fixed-bed flow system. The oxides selected for further evaluation are Al-Ti-Ce-O, Ti-Ce-Zr-O, Mo-Al-Ti-Ce-O, Ni-Al-Ti-Ce-O, Fe-Al-Ti-Ce-O and Cu-Al-Ti-Ce-O. The breakthrough curves of commercial diesel fuel over mixed-metal oxides are shown in **Figure 103**. The results show that the amount of treated fuel is lower than 5 gram fuel per gram adsorbent when the outlet sulfur content is 1 ppmw. It indicates that the adsorptive desulfurization (ADS) performance of these mixed-metal oxides is poor, although

these adsorbents were found good for ADS of jet fuels in our previous study. One of the probable reasons may be due to strong steric hindrance of alkyl groups in the sulfur compounds existing in the ultralow sulfur diesel, such as 4,6-dimethyldibenzothiophene.

2.2.1.2.2 Multi-layer adsorption process using multi-mixed-metal-oxides adsorbent

As shown above, the adsorptive desulfurization activities of the multi-mixed metal oxides were not good for desulfurization of a commercial diesel fuel with 15 ppmw sulfur. In order to increase the adsorption capacity of metal oxides, the multi-layer adsorption method was used. With the integration of activated carbon as the guarded-bed may benefit the adsorptive desulfurization process for diesel fuel. Consequently, about 40 activated carbons provided by different companies were first tested and screened for desulfurization of low sulfur diesel fuel in a batch system. The weight ratio of the diesel fuel to activated carbon was 25/1. The adsorption tests were conducted at the room temperature under atmospheric pressure. The total sulfur concentration in the diesel fuel was determined by an ANTEK 9000NS total sulfur analyzer. The sulfur detection limit of the total sulfur analyzer is 0.5 ppmw. The activated carbon was pretreated at 120 °C in a vacuum oven for 6 hours before adsorption test. The results are listed in **Table 27**.

Table 27. Sulfur content in commercial diesel fuel after 2-hours adsorption over different activated carbons in a batch system at room temperature.

Activated carbon	1#	2#	3#	4#	5#	6#	7#	8#	9#	10#
Sulfur content after adsorption	11.8	9.6	11.2	11.1	12.1	11.4	11.8	14.9	22.3	9.4
Activated carbon	11#	12#	13#	14#	15#	16#	17#	18#	19#	20#
Sulfur content after adsorption	6.1	12.5	11.4	7.9	10.6	11.6	11.1	8.8	10.8	11.6
Activated carbon	21#	22#	23#	24#	25#	26#	27#	28#	29#	30#
Sulfur content after adsorption	8.1	8.7	17.4	12.1	12.0	10.4	14.0	10.6	9.4	10.8
Activated carbon	31#	32#	33#	34#	35#	36#	37#	38#	39#	40#
Sulfur content after adsorption	10.1	7.8	10.7	19.6	14.6	10.2	11.1	17.4	11.2	13.9

It can be seen from **Table 27** that sulfur cannot be sufficiently removed from the fuel by these tested activated carbons. Some samples even got higher final sulfur concentration after adsorption than the initial sulfur content in the starting fuel, probably resulting from more fuel being adsorbed than sulfur over those carbon samples. The best was achieved on the activated carbon sample #11 with the sulfur content down to ca. 6 ppmw after 2-hrs adsorption. The results strongly suggest that activated carbon is not an efficient adsorbent for sulfur removal from a commercial diesel fuel and only activated carbon alone can not work well for deep ADS of the commercial diesel fuel.

Based on the batch adsorption results, six activated carbons with better adsorption performance were selected and tested in a fixed-bed flow system. The activated carbon was packed in a standard stainless steel column (4.6 mm I.D. and 150 mm Length). The packed columns were placed in a multi-channel convection oven. Before adsorptive desulfurization, the adsorbent bed was pretreated with Argon at a flow rate of 60 mL/min at ambient pressure, heated

to 300 °C at a temperature ramp of 10 °C/min, and kept at this temperature for 2 hours. After pretreatment, the oven temperature was then decreased to room temperature. In the adsorptive desulfurization, the argon gas flow was stopped, the commercial diesel fuel was sent into the adsorbent column by a HPLC pump, flowed up through the adsorbent bed at a liquid hourly space velocity (LHSV) of 4.8 h^{-1}. The effluent from the top of the column was collected periodically for analysis. The breakthrough curves of commercial diesel fuel over six selected activated carbons are shown in **Figure 104**.

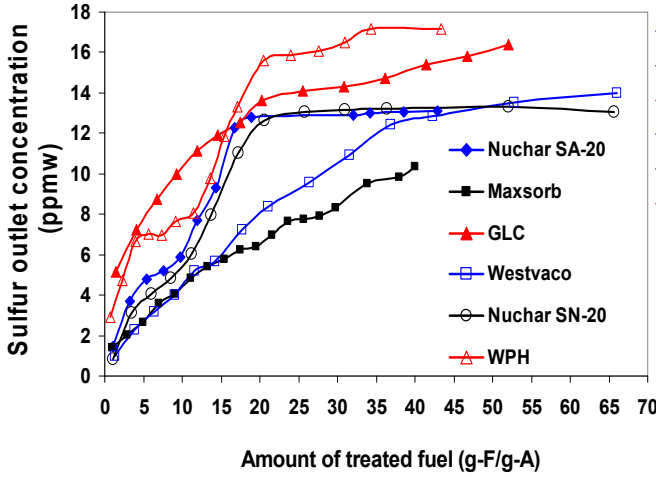

Figure 104. Breakthrough curves of commercial diesel fuel over six different activated carbon adsorbents in a fixed-bed flow system.

Like the metal oxides, the outlet sulfur content increased gradually over the activated carbon adsorbents with the increase of the treated fuels. However, none of them can reduce the sulfur below 1 ppmw. It indicates that the ADS performance of these activated carbon adsorbents is poor, although some activated carbons worked well for ADS of jet fuels in our previous study. The desulfurization performance of the studied samples decreased as follows: Maxsorb > Westvaco > Nuchar SN-20 > Nuchar SA-20 > GLC > WPH. Combined with the previous data using metal oxides as adsorbents for ADS of commercial diesel fuel, it suggests that high performance can not be achieved if only one adsorption column is used. It will be a good option that a multi-column desulfurization process is applied for ADS of diesel fuel by using our developed adsorbents. Accordingly, the best activated carbon sample, Maxsorb was selected as one of the adsorbents for the multi-column tests.

In the multi-column test, the bentonite was used in the first layer as a guard bed. The activated carbon, Maxsorb was used in the second layer as another guard bed. The third layer can be changed by different adsorbents. Multi-mixed-metal oxide M-Al-Ti-Ce-O was used in the third layer in this experiment. Bentonite and activated carbon were pretreated in argon flow at 300 ^{o}C for 2 hours, while M-Al-Ti-Ce-O was pretreated in air at 300 ^{o}C for 2 hours before adsorption tests. **Figure 105** shows the ADS results of the single layer, two layers and three layers with Bentonite, Maxsorb activated carbon and Al-Ti-Ce-O adsorbent. Bentonite alone has not apparent function in ADS of commercial diesel fuel. Moreover, the adsorption performance of Al-Ti-Ce-O adsorbent does not increase (even worse) if only the Bentonite was used as the guard bed. If activated carbon Maxsorb was used as the guard bed, the adsorption capacity of Al-Ti-Ce-O increased. The treated fuel was 6.8 g-F/g-A when the outlet sulfur content was 1ppm,

which was 2 times higher than that obtained on the Al-Ti-Ce-O adsorbent alone (2.3 g-F/g-A). The sulfur adsorption capacity of Al-Ti-Ce-O by using activated carbon as the guard bed is 0.1 mg-S/g-A. In the three layers process with Al-Ti-Ce-O as the adsorbent and both the Bentonite and activated carbons as the guard beds, similar result to the two-layers process with Al-Ti-Ce-O as the adsorbent and the activated carbons as the guard bed is obtained, as expected.

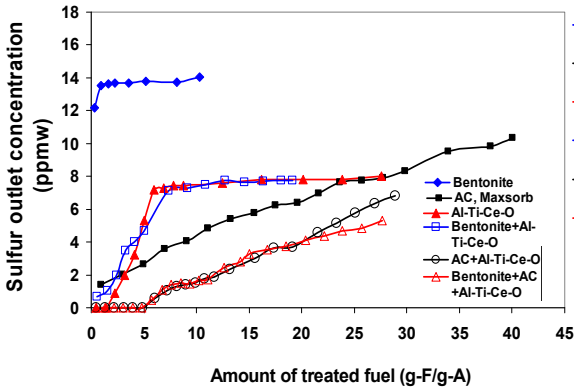

Figure 105. Breakthrough curves of commercial diesel fuel over Bentonite, Activated carbon Maxsorb, Al-Ti-Ce-O adsorbents in the single layer, two layers and three layers processes.

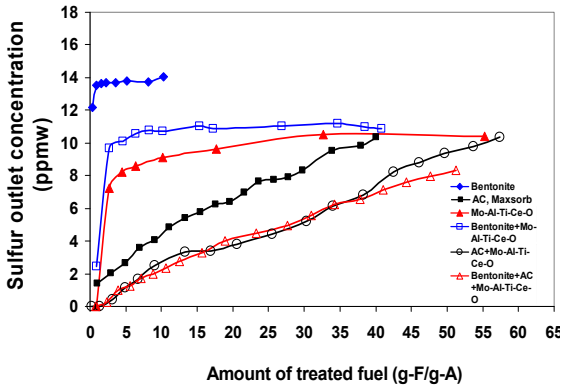

Figure 106. Breakthrough curves of commercial diesel fuel over Bentonite, Activated carbon Maxsorb, Mo-Al-Ti-Ce-O adsorbents in the single layer, two layers and three layers processes.

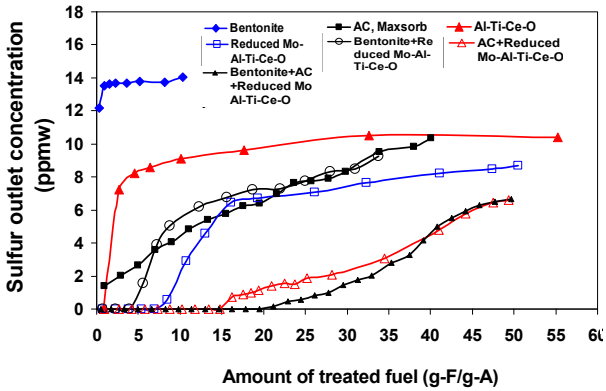

Figure 107. Breakthrough curves of commercial diesel fuel over Bentonite, Activated carbon Maxsorb, reduced Mo-Al-Ti-Ce-O adsorbents in the single layer, two layers and three layers processes.

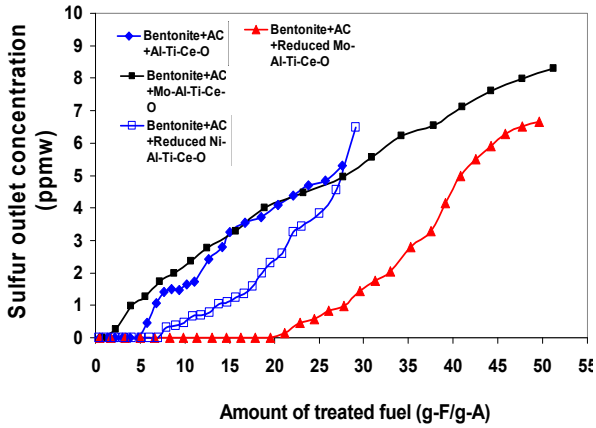

Figure 108. Breakthrough curves of commercial diesel fuel over three layer adsorption method.

The similar adsorption step and method were applied for Mo-Al-Ti-Ce-O, which is shown in **Figure 106**. The bentonite bed has no apparent helping in sulfur adsorption since the breakthrough curves are similar to those obtained from the two layers and three layers adsorption tests. The treated fuel was 6.3 g-F/g-A at 1 ppmw of the outlet sulfur content when the activated carbon was used as the guard bed. It is about 5 times higher than that obtained on Mo-Al-Ti-Ce-O adsorbent alone (1 g-F/g-A). The corresponding sulfur adsorption capacity was 0.1 mg-S/g-A.

Compared to Mo-Al-Ti-Ce-O adsorbent, the reduced Mo-Al-Ti-Ce-O adsorbent showed better adsorption performance and higher sulfur uptake than the origin one. Therefore, the reduced Mo-Al-Ti-Ce-O was also investigated. The adsorption results are displayed in **Figure 107**. Like Al-Ti-Ce-O and Mo-Al-Ti-Ce-O adsorbents, when the bentonite and the activated carbon were as the guard beds in the three-layer adsorption process, the adsorption performance of the reduced Mo-Al-Ti-Ce-O adsorbent also increased significantly. The treated fuel was 27.8 g-F/g-A at 1 ppmw of the outlet sulfur content. It is about 2 times higher than that obtained on reduced Mo-Al-Ti-Ce-O adsorbent alone (9 g-F/g-A). The corresponding sulfur capacity was 0.4 mg-S/g-A for this multi-layer adsorption test.

Additionally, multi-mixed-metal oxide Ni-Al-Ti-Ce-O was reduced in hydrogen and the ADS was conducted by the multi-layer method as that for Al-Ti-Ce-O, Mo-Al-Ti-Ce-O and reduced Mo-Al-Ti-Ce-O adsorbents. The result obtained from adsorption by three-layer process with the bentonite in the first layer, activated carbon in the second layer and the reduced Ni-Al-Ti-Ce-O in the third layer is shown in **Figure 108**. For comparison, the results obtained over the metal oxides Al-Ti-Ce-O and Mo-Al-Ti-Ce-O, reduced Mo-Al-Ti-Ce-O with the same three-layer process are presented. With the reduced Ni-Al-Ti-Ce-O adsorbent in the process, about 13.8 g-F/g-A of fuel can be treated with the outlet sulfur content below 1 ppmw. The corresponding sulfur capacity is 0.2 mg-S/g-A. As displayed in Figure 10, the reduced Mo-Al-Ce-Ti-O adsorption using the multi-layer adsorption method has the best performance for ADS of commercial diesel fuel. The desulfurization performance of the studied samples decreased as follows: reduced Mo-Al-Ce-Ti-O (27.8 g-F/g-A) > reduced Ni-Al-Ce-Ti-O (13.8 g-F/g-A) > Al-Ce-Ti-O (6.8 g-F/g-A) > Mo-Al-Ce-Ti-O (6.3 g-F/g-A).

2.2.1.2.3 Supported mixed-metal-oxides adsorbent

Different supports, including Na-Y zeolite, γ-Al_2O_3, bentonite, fumed silica, SBA-15, MCM-41 and MCM-48 were either purchased from Aldrich or synthesized in our lab and used as the support without further treatment. The support, SBA-15, MCM-41 and MCM-48 was prepared by the hydrothermal synthesis method. The surface area, pore volume and pore size of different support materials have been examined and the data are presented in **Table 28**. For comparison, the data for Ti-Ce-Al-O mixed metal oxide adsorbents are also listed. Fumed silica, EH-5 has a surface area of 315 m^2/g which is slightly larger than that of Ti-Ce-Al-O material (280 m^2/g), a pore volume of 0.70 cc/g and a pore size of 11.1 nm. Other mesoporous silica shows much higher surface area, 950 m^2/g for SBA-15, 1229 m^2/g for MCM-41 and 1281 m^2/g for MCM-48. It should also be noted that both SBA-15 and MCM-41 have a one dimensional pore structure, while it is a three-dimensional pore structure in MCM-48.

Figure 109 shows the effect of the supports on adsorption capacity of TiO_2-CeO_2 oxides for ADS of ULSD. From Figure 10, it can be seen that the positive effect of the supports follows the order of MCM-48 > MCM-41 > SBA-15 > Fumed Silica > Bentonite > γ -Al_2O_3 > Na-Y.

Figure 110 shows the effect of supports on the breakthrough capacity of TiO_2-CeO_2 oxides for ADS of ULSD. It can be seen that using Na-Y, γ-Al_2O_3 and Bentonite as support of TiO_2-CeO_2 oxides showed negative effect on ADS. The low ADS breakthrough capacity of Na-Y with high surface area and micro porosity may be due to the large size of 4,6-DMDBT molecule with dimension of 1.0 nm*0.63 nm, which limits diffusion of 4,6-DMDBT through the narrow micropore channel of Na-Y. The lower breakthough capacity mesoporous γ-Al_2O_3 and Bentonite could be possibly due to 1) a strong interaction between TiO_2-CeO_2 oxides and alumina support, thus supported TiO_2-CeO_2 oxides had less activity to O_2 in air for peroxide

generation; 2) low surface area of the two supports, resulting in the bigger particle size of TiO_2-CeO_2 oxides with lower activity.

Table 28. Physical properties of different supports.

Support	Composition	Pore size (nm)	Surface Area (m^2/g)	Provider	Commercial ID
Zeolite NaY	Si-Al-O/Na+	micro	900	Aldrich	Linde LZ-Y52
γ-Al_2O_3	Al-O	5.8	~200	SASOL	Puralox
Bentonite	Si-Al-O/Na+	meso	300-400	Alfa Aesar	-
Fumed silica	SiO2	11.1	315	CABOT	EH-5
SBA-15	SiO2	6.6	950	*	-
MCM-41	SiO2	2.74	1229	*	-
MCM-48	SiO2	2.36	1281	*	-
Ti-Ce-Al-O**	-	4.7	280	*	-

*prepared by hydrothermal method in the lab;
**as non-supported TiO_2-CeO_2 oxides.
***Experiment Condition: batch adsorption system; fuel of ULSD-BP; sorbent-to-fuel ratio of 0.1g:2g; adsorption T of 25 °C.

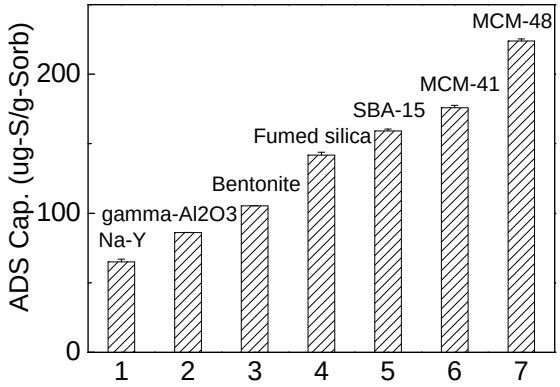

Figure 109. Effect of Support on Adsorption Capacity of TiO_2-CeO_2 Oxides for ADS of ULSD in Batch Adsorption System.

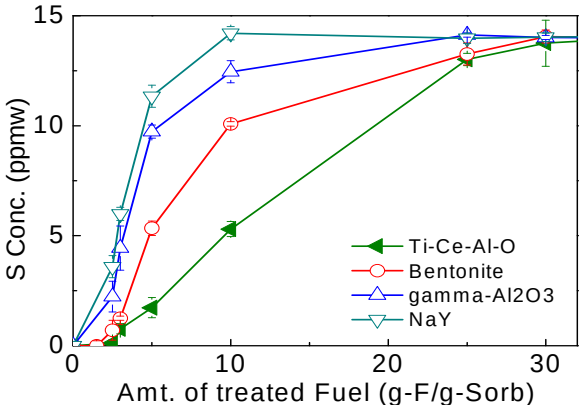

Figure 110. Mass-based Breakthrough Curves for ADS of ULSD over Three Supported TiO_2-CeO_2 Oxides.

Figure 111 and **Figure 112** show the effect of the mesopore molecular sieve supports on the breakthrough capacity of TiO_2-CeO_2 oxides for ADS of ULSD. It was found that using fumed silica, SBA-15, MCM-41 or MCM-48 as a support of TiO_2-CeO_2 oxides gave a positive effect on ADS. The positive effect can be contributed to high surface area of the support, which results in the smaller particle size of TiO_2-CeO_2 oxides with higher activity. However, by correlating the surface area with the ADS breakthrough capacity, as shown in **Figure 113**, it was found that the slope of the mesopore-molecular sieve-supported TiO_2-CeO_2 oxides is higher than that of the unsupported Ti-Ce-Al-O, suggesting that the mesopore molecular sieve supports play an important role in ADS.

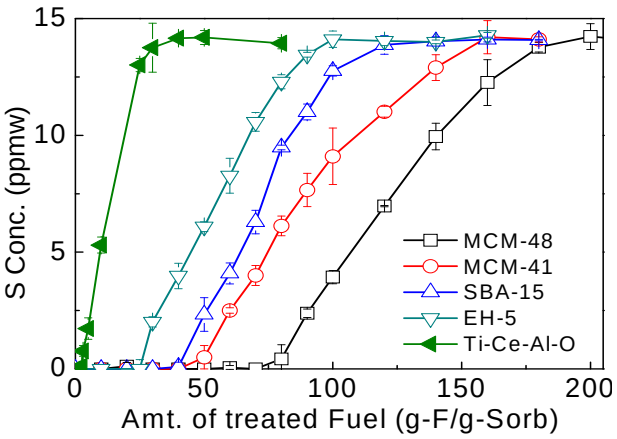

Figure 111. Mass-based breakthrough curves for ADS of ULSD over four mesopore-molecular-sieve-supported TiO_2-CeO_2 oxides.

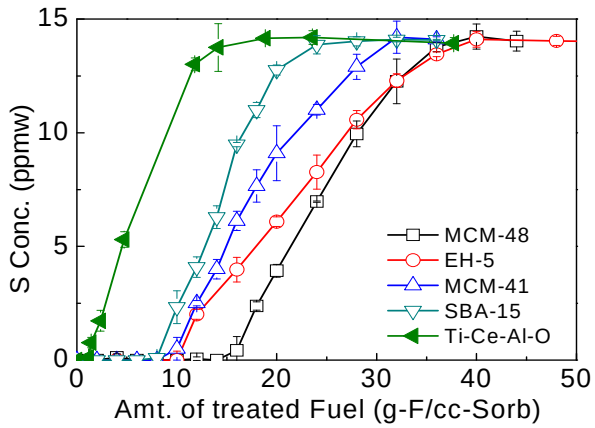

Figure 112. Volume-based breakthrough curves for ADS of ULSD over four supported TiO_2- CeO_2 oxides.

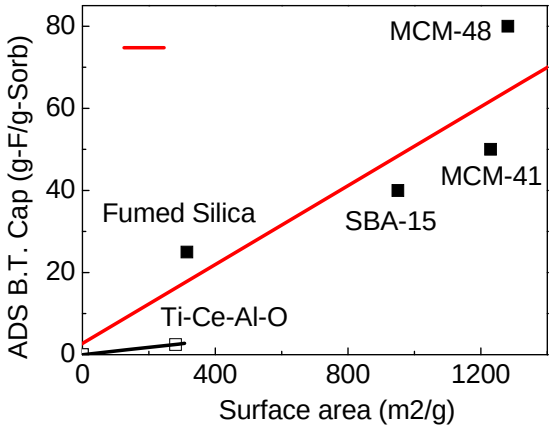

Figure 113. Correlation between surface area and ADS breakthrough capacity of the supported TiO_2-CeO_2 oxides.

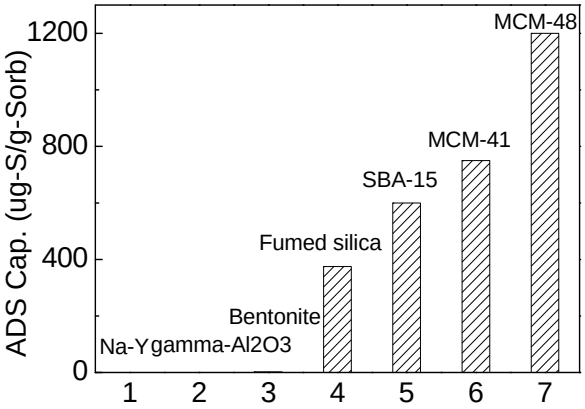

Figure 114. Effect of support of TiO_2-CeO_2 oxides on ADS capacity from ULSD in the flow system.

On the basis of the sorbent mass, as shown in **Figure 111**, it can be seen that the ADS breakthrough capacity decreases in the order of MCM-48 > MCM-41 > SBA-15 > EH-5, while on the basis of the sorbent volume, as shown in Figure 4, it can be seen that the ADS breakthrough capacity decreases in the order of MCM-48 > MCM-41 = EH-5 > SBA-15. The change of the order for EH-5 is due to the higher packing density of EH-5 in comparison with MCM-48, MCM-41 and SBA-15.

In summary, **Figure 114** shows the breakthrough capacity for ADS of ULSD over the seven supported TiO_2-CeO_2 oxides in flow system. It can be seen that the ADS breakthrough capacity follows the order of MCM-48 > MCM-41 > SBA-15 > Fumed Silica > unsupported TiO_2-CeO_2 oxides > Bentonite > γ-Al_2O_3 > NaY. The order obtained in the flow system is in good accordance with the order obtained in the batch system, as shown in **Figure 109**.

To further enhance the adsorption performance, the activated carbon was applied as a guard-bed as described previously. **Figure 115** shows the ADS breakthrough curves of ULSD

over the AC, Ti-Ce-O/EH-5, and AC+Ti-Ce-O/EH-5. It can be seen from **Figure 115** that the ADS capacity of AC+Ti-Ce-O/EH-5 tripled the ADS capacity of Ti-Ce-O/EH-5, and 12 times higher htan that of AC alone. Results suggest that there is a synergetic effect between AC and Ti-Ce-O/EH-5 for ADS of ULSD.

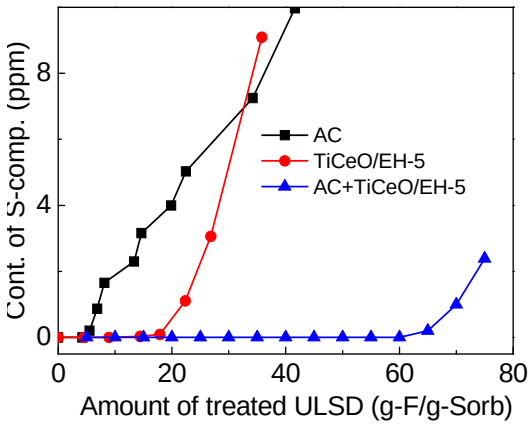

Figure 115. Breakthrough curves for ADS of ULSD over the AC, Ti-Ce-O/EH-5, and AC+Ti-Ce-O/EH-5 (Only weight of Ti-Ce-O/EH-5 was used for calculation of ADS capacity of (AC+ Ti-Ce-O/EH-5).

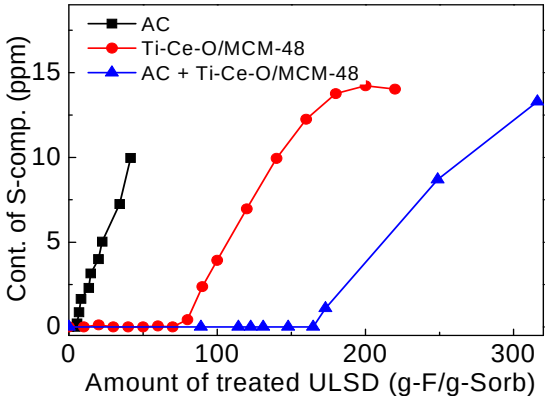

Figure 116. Breakthrough curves of sulfur compounds from ULSD over the AC, Ti-Ce-O/MCM-48, and AC followed with Ti-Ce-O/MCM-48 (Only weight of Ti-Ce-O/MCM-48 was used for calculation of ADS capacity of (AC+ Ti-Ce-O/MCM-48) due to low ADS capacity of AC alone.

Figure 116 shows the breakthrough curves of ULSD over the AC, Ti-Ce-O/MCM-48, and AC+Ti-Ce-O/MCM-48. It can be seen that the ADS capacity of AC+Ti-Ce-O/ MCM-48 can reach 165 g-F/g-sorb, which was double of the ADS capacity of Ti-Ce-O/MCM-48, and 32 times higher than that AC alone. A synergetic effect between AC and Ti-Ce-O/MCM-48 was also found for ADS of ULSD over AC+Ti-Ce-O/ MCM-48.

The present results clearly indicate that AC as a guarded bed can significantly increase the ADS capacity of the supported Ti-Ce-O. The results suggested that due to the complex composition of diesel fuel, there are competitive adsorption between sulfur compounds and certain types of compounds in the diesel on the active sites at the supported Ti-Ce-O. While using a guarded bed with ACMB-1, ACMB-1 can selectively or more preferentially adsorb and remove the certain types of competitive compounds before the feed contacts with the supported Ti-Ce-O. Therefore, more active sites on the supported Ti-Ce-O can be used for ADS, resulting in improvement of the ADS capacity.

In order to further understand the fundament of the competitive adsorption over the supported Ti-Ce-O for better design of functional sorbent/layered sorbents, adsorptive selectivity of the supported Ti-Ce-O adsorbents for different components in diesel fuel needs to be investigated in detail. Thus a model diesel fuel was prepared for this purpose. **Figure 117** shows the breakthrough curves for sulfur compounds over Ti-Ce-O mixed metal oxides from ULSD and MDF. Ti-Ce-O mixed metal oxides showed a breakthrough capacity of 57 g-F/g-sorb from MDF containing 15 ppw sulfur, which is around 20 times higher than that from the real ULSD. **Figure 118** shows the breakthrough curves for sulfur compounds over MCM-48 supported Ti-Ce-O mixed metal oxides adsorbent from ULSD and MDF. Similarly, over MCM-48 supported

Ti-Ce-O mixed metal oxides adsorbent, the obtained breakthrough capacity from MDF was about 1024 g-F/g-sorb, around 10 times higher than that from the real ULSD.

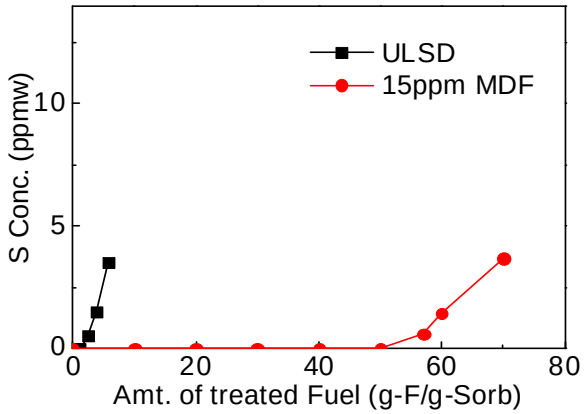

Figure 117. Breakthrough curves for sulfur compounds over Ti-Ce-O mixed metal oxides from ULSD and MDF at 25 °C and 9.6 h^{-1} LHSV.

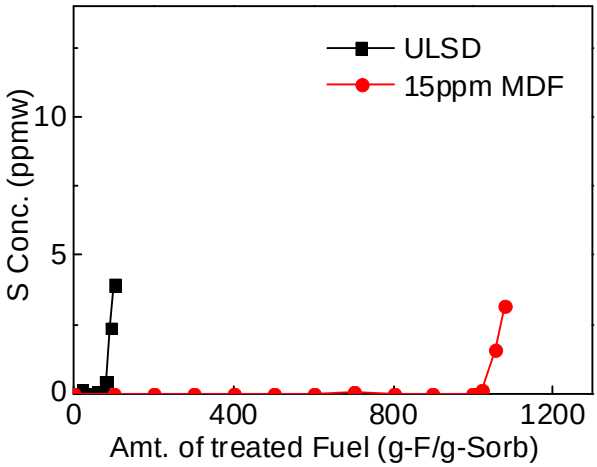

Figure 118. Breakthrough curves for sulfur compounds over MCM-48 supported Ti-Ce-O adsorbent from ULSD and 15 ppmw MDF at 25 °C and 9.6 h^{-1} LHSV.

Compared to the prepared MDF, the real ULSD is comprised of complex components. Diesel fuels consist mainly of saturated and aromatic hydrocarbons. Aromatic hydrocarbons include mono-aromatics, such as alkylated benzenes, and polycyclic aromatic hydrocarbons (PAHs), such as naphthalenes, fluorenes, and phenanthrenes. Formulated diesel fuels also contain additives introduced at very small proportion to improve performance, enhance its desirable characteristics and to reduce the undesirable ones, such as anti-oxidant stabilizers, cold flow improvers and cetane number improvers. Additionally, trace amount of nitrogen compounds and moisture is normally present in the commercial diesel fuels.

Since real diesel fuel is such a multi-component mixture, selective removal of trace sulfur compounds in ppmw scale from diesel fuel is a complex process and can be affected by other components. In terms of molecular interactions, not only the affinity between the adsorbate molecules and the adsorbent surface, but also the affinity between the solvent molecules and the adsorbent surface, and the affinity between the molecules of the solution components both in the surface layer and in the bulk phase can affect the adsorption from solution. Thus, the nature of solvent components can greatly influence the adsorption of the adsorbate molecules. If the affinity between the solvent molecules and the adsorbent surface is not negligible, the concentrations of these solvent components can also influence the adsorption of the adsorbate molecules, such as sulfur. Therefore, the presence of aromatic hydrocarbons in significant quantities, and trace amounts of hetero-atom compounds, especially nitrogen compounds in ULSD may have a significant impact on its deep ADS.

On the contrary, the MDF used in this project has a simple formula including only decane, hexadecane, tert-butylbenzene, and 4,6-DMDBT, the ADS capacities obtained from the MDF over Ti-Ce-O and MCM-48 supported Ti-Ce-O mixed metal oxides adsorbents were much higher than those from real ULSD, as shown in **Figures 117** and **118**, suggesting that critical inhibiting or competitive components for ADS are present in real ULSD. Our results from last

quarterly report showed that using AC as a guarded bed could greatly improve the ADS capacity of MCM-48 supported Ti-Ce-O adsorbent. A possible explanation is that some inhibiting or competitive compounds for ADS are present in ULSD, which is consistent with the results shown in **Figures 117** and **118**.

As shown in above that the addition of silver oxide could greatly improve the adsorption capacity of the Ti-Ce-O adsorbent, it thus was prepared and evaluated for ADS of ULSD. **Figure 119** shows breakthrough curves of sulfur compounds in ULSD over MCM-48 supported Ag_2O, Ti-Ag-O, Ti-Ce-O, and Ti-Ce-Ag-O adsorbents. It broke through immediately after the fuel was introduced over Ag_2O/MCM-48, suggesting that Ag_2O alone does not show good ability for sulfur removal from ULSD. Using Ag_2O to replace CeO_2, the resulting Ti-Ag-O/MCM-48 showed worse ADS performance from sulfur removal from ULSD than the Ti-Ce-O/MCM-48. However, when Ag_2O was added to Ti-Ce-O, the ADS performance of Ti-Ce-O/MCM-48 was improved, from 80 to being 95 g-F/g-sorb over the Ti-Ce-Ag-O/MCM-48. The sulfur breakthrough capacity decreased as following order of Ti-Ce-Ag-O/MCM-48 > Ti-Ce-O/MCM-48 > Ti-Ag-O/MCM-48 > Ag_2O/MCM-48. The present results indicate that the addition of Ag_2O may play an important role in improving the ADS performance of Ti-Ce-O/MCM-48 adsorbent.

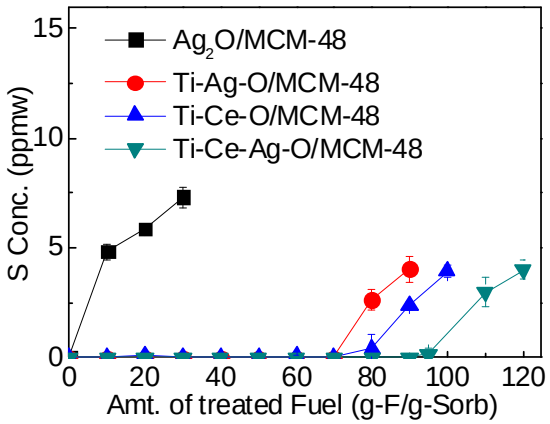

Figure 119. Breakthrough curves for sulfur compounds in ULSD over four supported metal oxides at 25 °C and 9.6 h^{-1} LHSV.

2.2.1.2.4 Air-promoted desulfurization over mixed-metal-oxides adsorbent

Figure 120 shows breakthrough curves of total sulfur compounds over TiO_2-CeO_2 mixed oxide adsorbent from ULSD with and without in-situ air flowing. Clearly, with in-situ air flowing, ADS breakthrough capacity increased significantly from 2.5 g-F/g-sorb to 22.5 g-F/g-sorb, suggesting in-situ air promoted significantly the ADS performance of TiO_2-CeO_2 mixed oxides for ULSD. In order to understand the promotion effect of in-situ air, we have studied the adsorbed sulfur species over the TiO_2-CeO_2 mixed oxide adsorbent by washing the spent TiO_2-CeO_2 sorbent with a solvent of acetone, which was conducted at 25 °C. The sulfur species in the eluent were analyzed by GC-SCD, which is shown in **Figure 121**. The GC-SCD spectrum of ULSD is also presented for comparison.

In the acetone solvent after washing the spent TiO_2-CeO_2 sorbent, along with very small amount of original sulfur species in ULSD at the retention time range of 15.9-17.2 min, some new sulfur species at the retention time range of 17.6-19.0 min with relatively high concentration were detected, suggesting the formation of new sulfur species by introducing in-situ air during ADS. Compared to our previous results and the literature [41], these new sulfur species can be

assigned to sulfone species, indicating the oxidation of original sulfur species in ULSD during the ADS process with in-situ air flowing. **Figure 122** shows dipole magnitude and electrostatic potential on electron density for dibenzothiophene (DBT) and dioxodibenzothiophnene ($DBTO_2$) [42]. It can be seen that $DBTO_2$ has much higher dipole magnitude and electrostatic potential than DBT, which indicates that $DBTO_2$ is more prone to be adsorbed on a surface. Thus, the current results show that the addition of in-situ air flowing could promote the oxidation of sulfur compounds in ULSD which is prone to be adsorbed over TiO_2-CeO_2 sorbent. Consequently, higher adsorption capacity can be obtained, as shown in **Figure 120**.

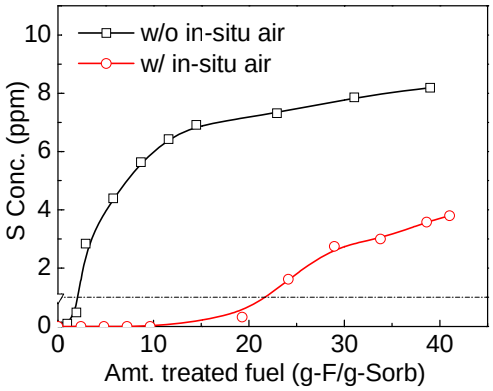

Figure 120. Breakthrough curves for sulfur compounds from ULSD over TiO_2-CeO_2 mixed oxides with and without in-situ air. Conditions: LHSV: 4.8 h^{-1}; Air Flow-rate 10 ml/min; T: 25 °C.

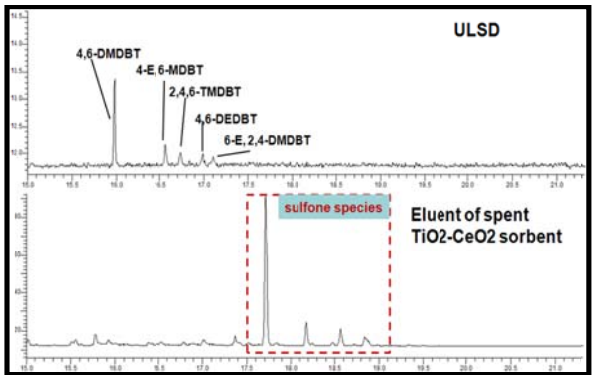

Figure 121. GC-PFPD spectrums of ULSD and eluent of spent TiO_2-CeO_2 adsorbent. Solvent used to wash the spent sorbent: Acetone; Washing Temp: 25 °C.

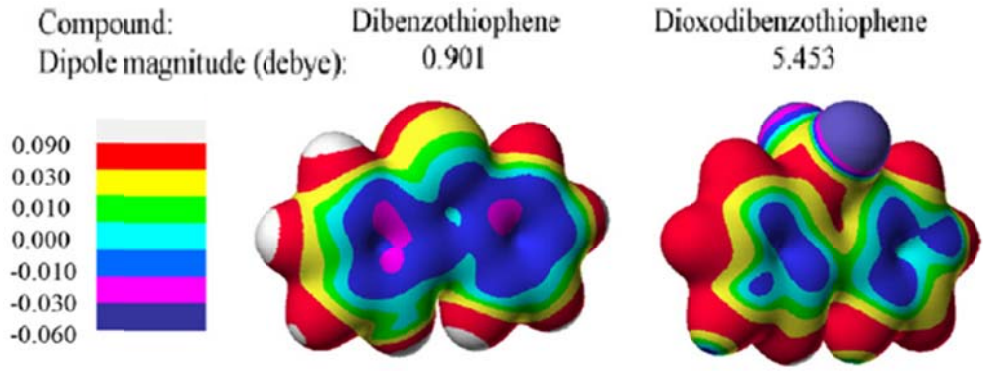

Figure 122. Dipole magnitude and electrostatic potential on electron density for DBT and DBT sulfone.

It has been demonstrated that the MCM-48 supported TiO_2-CeO_2 adsorbent has a better performance than unsupported TiO_2-CeO_2 adsorbent for sulfur removal from ULSD at room temperature. Therefore, we also compared the ADS performance of TiO_2-CeO_2 adsorbent with air flowing with that of MCM-48 supported TiO_2-CeO_2 adsorbent on the basis of adsorbent weight and volume, which is shown in **Figure 123**. At a weight base, the MCM-48 supported TiO_2-CeO_2 adsorbent showed much higher adsorption capacity than pure TiO_2-CeO_2 adsorbent, which is about 3 times. If considering the volume based capacity, the adsorption capacity of pure

TiO_2-CeO_2 adsorbent is about 71% of that for TiO_2-CeO_2/MCM-48 adsorbent. The comparison shows that even promoted by in-situ air flowing, the adsorption performance of TiO_2-CeO_2 adsorbent is still worse than that of MCM-48 supported TiO_2-CeO_2 adsorbent, demonstrating that applying a mesoporous support with high surface area and uniform pore structure is a more efficient way to improve the adsorption capacity of TiO_2-CeO_2 mixed oxide adsorbent.

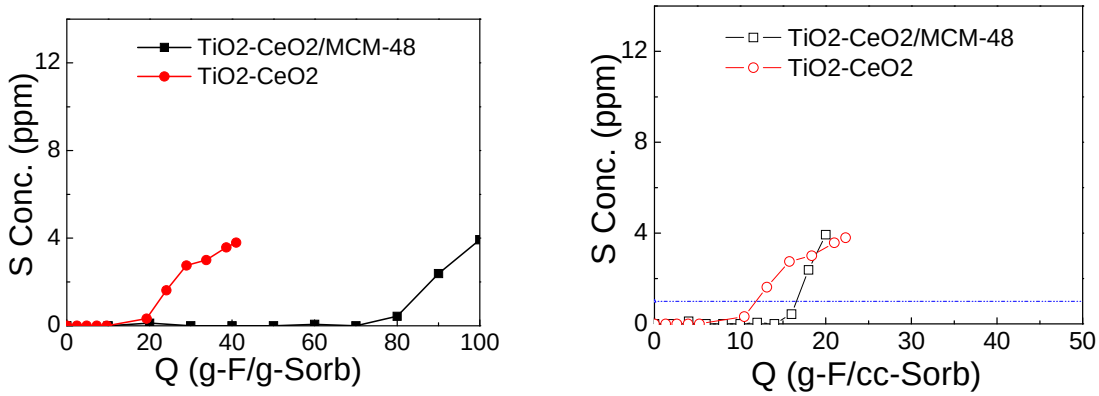

Figure 123. Breakthrough Curves of Total Sulfur Compounds over TiO_2-CeO_2 Adsorbent with Air Flow and TiO_2-CeO_2/MCM-48 Adsorbent without Air Flow from ULSD on the Basis of a) Adsorbent Weight and b) Adsorbent Volume. Conditions: LHSV, 4.8 h^{-1}; T, 25 °C; air flow, 10cc/min.

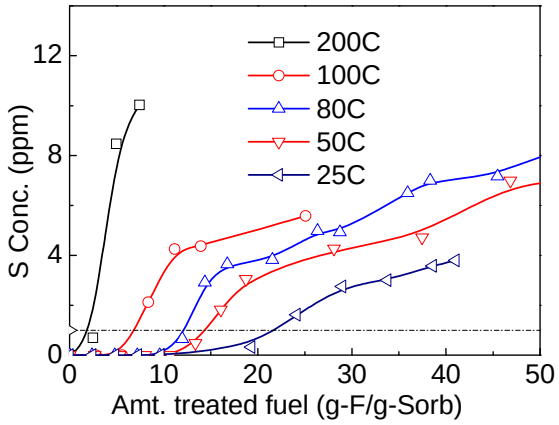

Figure 124. Breakthrough Curves for Sulfur Compounds from ULSD over TiO_2-CeO_2 Mixed Oxides with in-situ Air at Different Temperatures. Conditions: LHSV: 4.8 h^{-1}; Air Flow-rate: 10 cc/min.

Figure 124 shows breakthrough curves of total sulfur compounds from ULSD over TiO_2-CeO_2 adsorbent at different temperatures with in-situ air flowing. With the increase of adsorption temperature, the ADS performance of TiO_2-CeO_2 sorbent decreased. At 25 °C, the breakthrough capacity was about 22.5 g-F/g-sorb. It became 14, 12, 6 and 2 g-F/g-sorb for the adsorption temperature of 50, 80, 100 and 200 °C, respectively. As discussed above, the addition of air flow could promote the oxidation of sulfur compounds in ULSD and thus promotes the adsorption capacity of TiO_2-CeO_2 adsorbent. At higher temperature, however, the desorption of adsorbed

sulfur and sulfone compounds on the surface is preferred, resulting in the decrease of the breakthrough capacity. It should also be noted that at 80 °C or above, no sulfones were detected in treated fuel, implying less or no oxidation of sulfur occurred at higher temperatures even with air flowing. Knowing that many aromatics and other hydrocarbons exist in ULSD which can be also oxidized under air at high temperature, the decrease in adsorption capacity for sulfur compounds may be due to the competitive oxidation of hydrocarbons and consequent adsorption of hydrocarbon oxides rendered by air at high temperature (>80 °C) over TiO_2-CeO_2 adsorbent.

Figure 125 shows the breakthrough curves of different compounds in MDF over TiO_2-CeO_2 mixed oxides. The corresponding adsorption selectivity factors and adsorption capacity for different compounds were calculated. The results are listed in **Table 29** and **Table 30**, respectively. It can be seen that the overall adsorption selectivity follows the order: indole > $DBTO_2$ > DBT > MDBT > BT > DMDBT > Phe > Flu ~ MNap > Nap. This selectivity order further explained the promoting effect of in-situ air on ADS. We have shown in previous quarterly report that in-situ air promoted the formation of sulfone species over TiO_2-CeO_2 adsorbents. Here we present that the TiO_2-CeO_2 adsorbent showed higher adsorption selectivity to sulfone compound, compared to the other sulfur compounds. It may be due to much higher dipole moment of sulfone compounds.

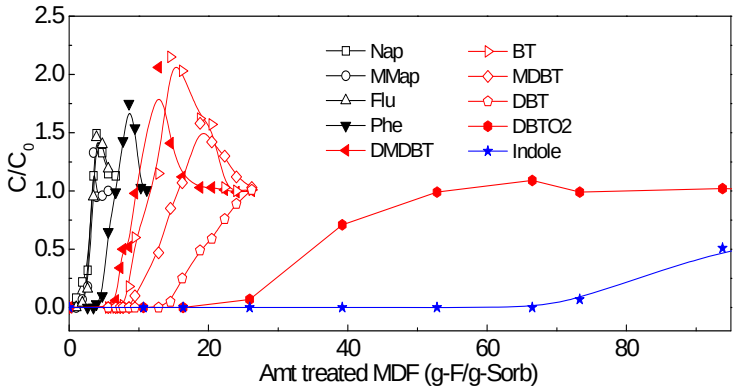

Figure 125. Breakthrough curves of different compounds in MDF over TiO_2-CeO_2 mixed oxides at 25 °C and 9.6 h^{-1} of LHSV.

Table 29. Adsorption selectivity factor relative to Naphthalene for each compound in MDF over TiO_2-CeO_2 metal oxides.

	Nap	Flu	MNap	Phe	DMDBT	BT	MDBT	DBT	$DBTO_2$	Indole
TiO_2-CeO_2	1	1.88	1.88	4.76	6.68	7.74	9.44	11.14	25.90	73.31

Table 30. Adsorption capacities (mmol/g) for each compound in MDF over TiO_2-CeO_2 metal oxides.

TiO_2-CeO_2	Nap	Flu	MNap	Phe	DMDBT	BT	MDBT	DBT	$DBTO_2$	Indole
Breakthrough	0.003	0.006	0.006	0.015	0.021	0.024	0.030	0.035	0.081	0.229
Saturation	0.008	0.009	0.009	0.017	0.025	0.030	0.043	0.060	0.149	>0.312
Net	0.005	0.007	0.007	0.012	0.014	0.018	0.030	0.060	0.149	>0.312

It can also be observed that nitrogen compound, indole showed quite high adsorption selectivity, suggesting nitrogen compounds in fuel could be competitively adsorbed on TiO_2-

CeO_2 adsorbent as well as sulfur compounds including sulfones. The competitive adsorption of nitrogen compounds may inhibit ADS over the TiO_2-CeO_2 adsorbent. In addition, all the sulfur compounds showed higher adsorption selectivity than aromatic hydrocarbons, suggesting TiO_2-CeO_2 adsorbent has higher affinity to sulfur rather than the aromatic pi-system of aromatic compounds. Therefore, the adsorption mode of sulfur compounds over TiO_2-CeO_2 adsorbent is most probably through sulfur atom. It is further supported by the presence of steric hindrance for the adsorption of sulfur compounds over TiO_2-CeO_2 adsorbent, as evidenced by the selectivity and capacity order of DBT > MDBT > DMDBT shown in **Table 29** and **Table 30**.

Figure 126 shows the breakthrough capacity of TiO_2, CeO_2, and TiO_2-CeO_2 adsorbents for sulfur adsorption from ULSD with and without in-situ air at the sulfur level of 1 ppmw and 4 ppmw. It can be seen that the introduction of in-situ air showed no effect on ADS capacity of CeO_2, but a little promotion effect on ADS capacity of TiO_2. By doping Ce into TiO_2, however, the effect of in-situ air on ADS is much more significant. The adsorption capacity in the presence of air was about 8-11 times of that without in-situ air. It strongly suggests that the addition of CeO_2 to TiO_2 shows a synergetic effect on the ADS of ULSD, especially when air is present. The result may also imply that specific sites on TiO_2, rather than on CeO_2 could play an important role in the ADS of diesel fuel with the presence of air over the TiO_2-CeO_2 adsorbent. However, more studies and detailed characterizations would be necessary to clarify the exact role of CeO_2 in the TiO_2-CeO_2 mixed oxides adsorbent.

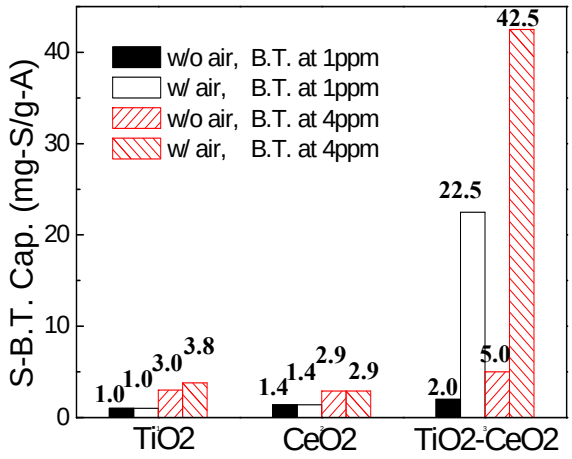

Figure 126. Breakthrough capacity of TiO_2, CeO_2, and TiO_2-CeO_2 adsorbents for sulfur adsorption from ULSD with and without in-situ air at the sulfur level of 1 ppmw and 4 ppmw.

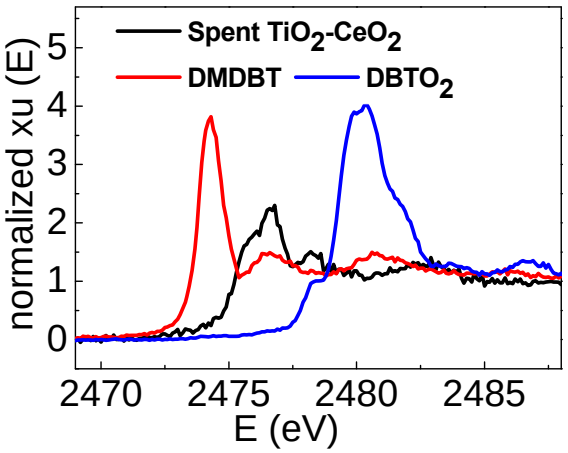

Figure 127. Sulfur-XANES spectra of the spent TiO_2-CeO_2 adsorbent, the standard 4,6-DMDBT and standard DBT sulfone ($DBTO_2$).

In order to better understand the air-promoted ADS process over the TiO_2-CeO_2 adsorbent, the spent TiO_2-CeO_2 adsorbent was analyzed by sulfur-XANES to identify the sulfur species, which may shed light on the air-promoted ADS mechanism over the TiO_2-CeO_2 adsorbent. **Figure 127** shows the S-XANES spectrum of the spent TiO_2-CeO_2 adsorbent. For comparison, the S-XANES spectra of 4,6-DMDBT and $DBTO_2$ are also presented. The major sulfur species on the spent TiO_2-CeO_2 mixed oxides adsorbent showed a higher oxidation state than initial sulfur species, suggesting the oxidation of sulfur species happened on TiO_2-CeO_2

mixed oxides adsorbent with air feeding. By comparison with standard 4,6-DMDBT and $DBTO_2$ samples, the sulfur species did not have a high oxidation state as $DBTO_2$, but an oxidation state in between 4,6-DMDBT and $DBTO_2$. It was suggested by literature [43] that sulfoxides have an oxidation state in between sulfide and sulfone. Therefore, the new sulfur species may be sulfoxides over the spent TiO_2-CeO_2 adsorbent in this work. It may be concluded that by introducing air during ADS over the TiO_2-CeO_2 mixed oxides adsorbent, the initial sulfur compounds was in-situ chemically transformed to sulfoxide species and adsorbed over the TiO_2-CeO_2 mixed oxides adsorbent.

It is worth mentioning here that oxidative desulfurization (ODS) has recently been extensively studied in the field of desulfurization. In most cases of ODS studies, active oxidants including hydrogen peroxide, organic peroxides, ozone, are used for ODS in the presence of various catalysts at non-ambient conditions. Here, to the best of our knowledge, this is the first report using air as an oxidant for chemical oxidation of sulfur compounds in fuel to oxidized sulfur species over an active surface under ambient conditions.

As shown in **Figure 126**, doping Ce into TiO_2 shows a significantly synergistic effect on ADS. To investigate the effect of Ce dopant on the structure of TiO_2-CeO_2 sorbent for ADS, in this report period, Ce K-edge XANES were studied. **Figure 128** shows Ce-XANES spectra of TiO_2-CeO_2 adsorbent at different X-ray exposure times. It can be seen that with longer exposure times, the Ce K-edge XANES spectra shifted left to lower binding energy. The result suggests that X-ray itself for XANES characterization can reduce Ce^{4+} to Ce^{3+} with longer exposure due to the instability of electronic structure of cerium in TiO_2-CeO_2 structure.

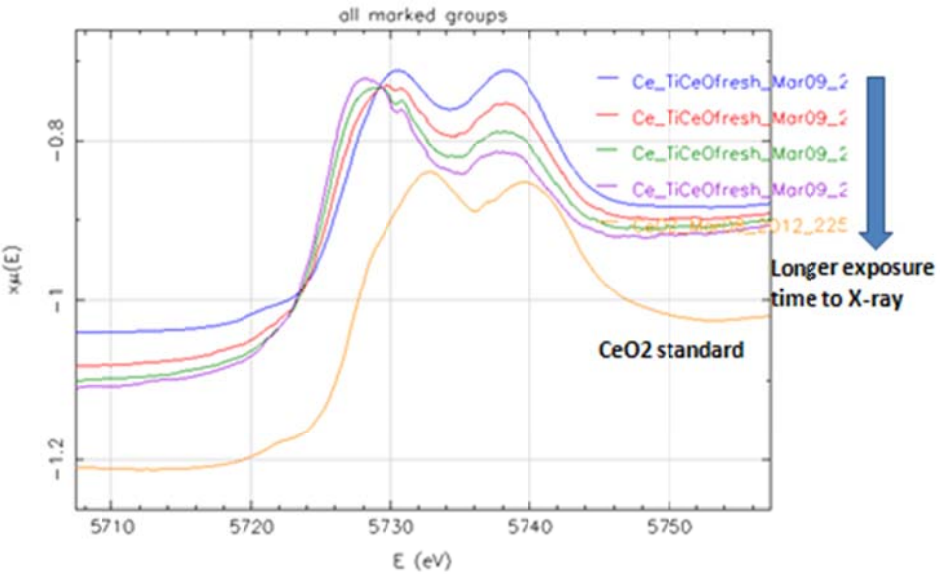

Figure 128. Ce-XANES spectra of TiO_2-CeO_2 adsorbent at different X-ray exposure times.

It is projected that in the Ce doped TiO_2 adsorbent, the Ti and Ce metal cations can influence each other which may result in the shift of their valence to a lower value. Accompanying the reduction of Ti^{4+} to Ti^{3+} and Ce^{4+} to Ce^{3+} in the $Ti_{0.9}Ce_{0.1}O_2$ sample, the oxygen vacancy sites can form on its surface, and the concentration of reduced center sites can be proportional to that of the oxygen vacancies formed [44]. It was reported that oxygen vacancy sites can act as the anchoring sites for O_2 molecules [45] to generate active oxygen species, such

as superoxides (O_2^-) on its surface, which may serve as the active sites for oxidation reactions [44,46]. In such cases, the active oxygen species activated in oxygen vacancy sites can be the key chemical species for various reactions.

To investigate the active oxygen species on the $Ti_{0.9}Ce_{0.1}O_2$ adsorbent under air flow at room temperature, infrared spectroscopy was used due to its capability for the identification of the active oxygen species in-situ [47]. **Figure 129** shows the diffuse reflectance infrared Fourier transform spectroscopy (DRIFTS) profiles of $Ti_{0.9}Ce_{0.1}O_2$ in comparison to the single TiO_2 and CeO_2, with air flowing in-situ at 25 °C. A moderate band appears at around 1126 cm^{-1}, which can be assigned to superoxide species, O_2^-, based on the theoretic calculation in the references [48,49], supporting the formation of superoxide species in the mixed $Ti_{0.9}Ce_{0.1}O_2$ oxides sample. Because of the presence of trivalent Ti and Ce in the mixed $Ti_{0.9}Ce_{0.1}O_2$ metal oxides adsorbent, the oxygen-vacancy sites can form near the trivalent Ti and Ce which may be able to accommodate and activate oxygen from air at room temperature. The accommodated or activated oxygen species can further serve as the active species [50,51] and contribute to sulfur oxidation to sulfoxides. The IR absorption band located at ca. 1650 cm^{-1} can be attributed to the bending vibrations of hydroxyl group [49].

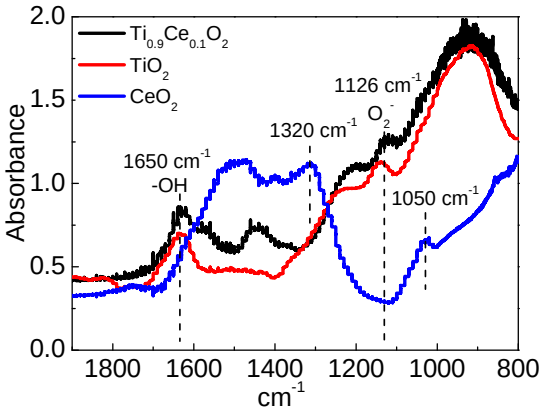

Figure 129. DRIFTS Profiles of TiO_2, CeO_2, and $Ti_{0.9}Ce_{0.1}O_2$ Under an Air Flow Rate of 50 ml/min at 25 °C.

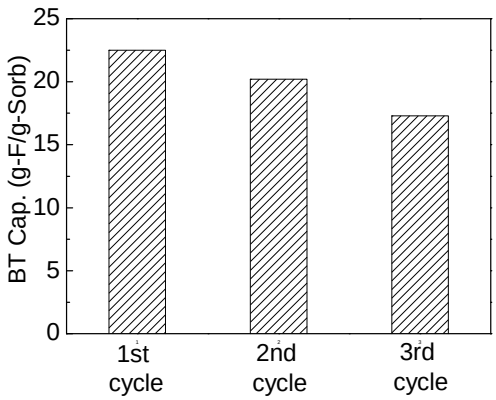

Figure 130. Break-through Capacity of the $Ti_{0.9}Ce_{0.1}O_2$ Adsorbent in the First Three Regeneration Cycles by Oxidative Air Treatment at 400 °C.

Different from the mixed $Ti_{0.9}Ce_{0.1}O_2$ metal oxides sample, there was no clear peak related to peroxide species at around 1100-1200 cm^{-1} [47,52] observed on CeO_2 under air flow, suggesting no superoxide species formed on CeO_2 itself. This may be due to a low concentration of the reduced Ce metal ions, or a high vacancy formation energy, or a high peroxide formation energy, etc. It should be mentioned that although active oxygen species were not identified in our lab-prepared CeO_2, it can be generated under certain conditions as reported in literatures [47] since the population and the state of each oxygen species varies on the basis of temperature, pressure, pretreatment history, and defect density, etc. [53]. The IR spectra of CeO_2 show the absorption bands at around 1050 and 1320 cm^{-1}, which are the characteristic vibrations of CeO_2 [54]. For the single TiO_2, superoxide species with the absorption bands at around 1126 cm^{-1} can be detected with air flowing in-situ at room temperature, as shown in Figure 8 (red line). The theoretic calculation showed that the superoxide species formed on the $Ti_{0.9}Ce_{0.1}O_2$ adsorbent are more active than those on TiO_2 for sulfur oxidation. Therefore, it is likely that more energy is

required for the dissociation of superoxide species formed in TiO_2 to chemically oxidize organosulfur compounds to sulfoxides. The results may further suggest that both oxygen activation on the vacancy sites for the formation of superoxide species and the dissociation of the activated superoxide species are important for air-promoted ADS over the metal oxides adsorbents.

The regenerability of the adsorbent is also important for the project. Thus, the spent $Ti_{0.9}Ce_{0.1}O_2$ adsorbent was regenerated by air at 400 °C. The adsorption performance of the regenerated adsorbent was examined. The breakthrough capacity for each cycle is shown in **Figure 130**. The regenerated $Ti_{0.9}Ce_{0.1}O_2$ adsorbent showed a comparable ADS performance after 3 cycles, indicating that the adsorption capacity can be recovered by air oxidation. However, the adsorption capacity dropped gradually with the cycles of regeneration, hinting that the adsorption capacity cannot be fully recovered and a loss of active sites may occur during the regeneration of the $Ti_{0.9}Ce_{0.1}O_2$ adsorbent via air treatment.

To understand the reason why the adsorptive capacity of the $Ti_{0.9}Ce_{0.1}O_2$ adsorbent decreased with the regeneration cycles, the fresh and regenerated $Ti_{0.9}Ce_{0.1}O_2$ adsorbents have been characterized by XANES technique. **Figure 131** shows Ti $L_{2,3}$-edge XANES spectra of the fresh and regenerated $Ti_{0.9}Ce_{0.1}O_2$ (from the 3rd cycle) adsorbents. The calculated percentage of Ti^{3+} and Ti^{4+} in the adsorbent is listed in **Table 31**. As can be seen, the amount of Ti^{3+} in the $Ti_{0.9}Ce_{0.1}O_2$ adsorbent decreased after regeneration. The percentage of Ti^{3+} ion in the regenerated $Ti_{0.9}Ce_{0.1}O_2$ adsorbent was about 42.7%, much lower than that of the fresh one, which was about 60.2%.

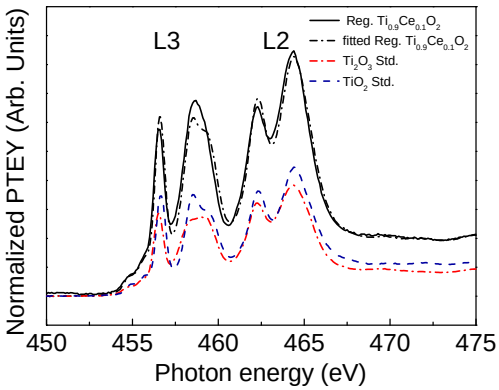

Figure 131. Ti $L_{2,3}$-edge XANES spectrum of regenerated $Ti_{0.9}Ce_{0.1}O_2$ (from the 3rd cycle), and linearly fitted spectrum with standard Ti_2O_3 and anatase TiO_2.

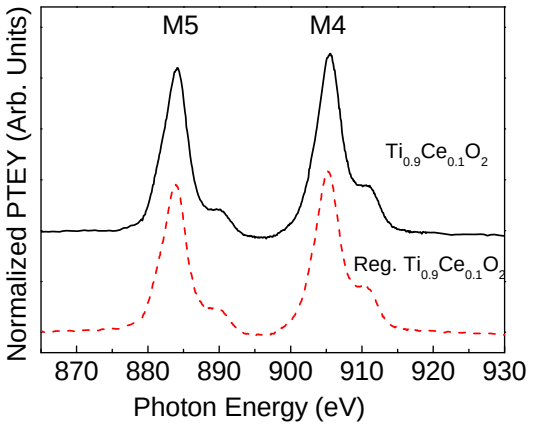

Figure 132. Ce $M_{4,5}$-edge XANES spectra of the fresh and the regenerated $Ti_{0.9}Ce_{0.1}O_2$ (from the 3rd cycle).

Table 31. The percentage of Ti^{3+} and Ti^{4+} in the fresh and regenerated $Ti_{0.9}Ce_{0.1}O_2$ (from the 3rd cycle) adsorbent calculated from the Ti $L_{2,3}$-edge XANES spectra.

	$Ti_{0.9}Ce_{0.1}O_2$	Reg. $Ti_{0.9}Ce_{0.1}O_2$
Reference spectrum	Abundance (%)	Abundance (%)
Ti^{3+} (Ti_2O_3)	60.2	42.7
Ti^{4+} (anatase TiO_2)	39.8	57.3

Figure 132 shows the Ce $M_{4,5}$-edge XANES spectra of the regenerated $Ti_{0.9}Ce_{0.1}O_2$ (from the 3rd cycle) in comparison with the fresh $Ti_{0.9}Ce_{0.1}O_2$. The M5/M4 ratio which represents the ratio of Ce^{3+}/Ce^{4+} is computed and listed in **Table 32**. The M5/M4 ratio in the regenerated $Ti_{0.9}Ce_{0.1}O_2$ (from the 3rd cycle) adsorbent was 0.868, while it was 0.889 over the fresh $Ti_{0.9}Ce_{0.1}O_2$ adsorbent. It implies a decrease in the amount of Ce^{3+} after regeneration.

Table 32. M5/M4 ratio in the fresh and the regenerated $Ti_{0.9}Ce_{0.1}O_2$ (from the 3rd cycle) calculated from Ce $M_{4,5}$-edge XANES spectra.

	$Ti_{0.9}Ce_{0.1}O_2$	Reg. $Ti_{0.9}Ce_{0.1}O_2$
M5/M4 ratio	0.889	0.868

As shown above, both the reduced centers of Ti^{3+} and Ce^{3+} on the surface of the $Ti_{0.9}Ce_{0.1}O_2$ adsorbent decreased after regeneration. Consequently, less active oxygen-vacancy sites would be available for oxygen activation and dissociation for sulfur oxidation, resulting in a lower adsorption capacity after regeneration. This is in good agreement with the adsorption performance of the regenerated adsorbent with cycles as shown in Figure 9. It reveals that the reduced centers of Ti^{3+} and Ce^{3+} on the $Ti_{0.9}Ce_{0.1}O_2$ surface may be critical for air-promoted ADS process. The loss of active sites on the $Ti_{0.9}Ce_{0.1}O_2$ surface may be due to the thermal instability of these Ti^{3+} and Ce^{3+} sites, or the blocking effect of some active sites by stubborn residues on the spent $Ti_{0.9}Ce_{0.1}O_2$ adsorbent that cannot be removed in air regeneration process. To clearly clarify the degradation mechanism, however, more work is needed. The understanding of the degradation mechanism is crucial for finding a more efficient regeneration method and better operating conditions. Moreover, from the perspective of the design of new metal-oxide based adsorbents for ADS, it is highly desirable if the regenerability could be taken into account initially in the design of an integrated adsorbent formula.

2.2.2. Reforming of Commercial Diesel Fuel

2.2.2.1. Method for fuel-steam mixing and preheating

As suggested in our statement of work and the reported literature review on diesel reforming, the homogeneous mixing and proper preheating of diesel fuel and steam are of vital importance to prevent fuel decomposition before the catalyst bed, thus significantly reducing the carbon formation which may block the reactor and the whole process. In our previous studies, we have proposed a new design of a mixer for the pre-mixing of jet fuel and steam to minimize the coke formation prior to the pre-reforming [55], as shown in **Figure 133**. In this design, the fuel should be kept at lower temperatures (below 150 °C) before fuel meets steam, i.e., rather than allowing the fuel to evaporate itself at the wick, the steam should serve to vaporize the fuel, which can thus result in more homogeneous pre-mixing on the basis of the results we found in examining the effects of using wick mixer for feed introduction on carbon formation at different temperatures. To improve the pre-mixing of jet fuel and steam, a wick material (quartz fiber) was added into the stainless steel tube between the outlet of fuel line and the inlet of reactor (the pre-mixing zone) to prevent the formation of droplets at the end of fuel line, which could lead to un-stable flow and poor mixing of jet fuel and steam.

This design was examined for diesel fuel. Although diesel fuel has higher boiling points (160 ~ 380 °C) and higher viscosity than jet fuels, the current fuel-steam mixing and preheating design was successfully applied for diesel steam reforming process. No carbon formation was

observed in the wick and on the wall of the reaction tube, indicating that such a design is applicable to diesel steam reforming in this project.

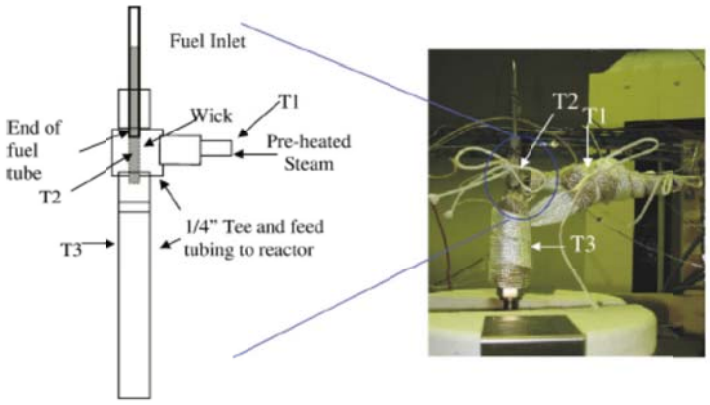

Figure 133. Schematic of the pre-heater of the reformer system used to vaporize and mix fuel and steam. T1 (300-400 °C), T2 (< 150°C) and T3 (< 350°C, until fuel is properly mixed) indicate the temperatures of the steam, fuel evaporation, and mixing zones, respectively (Ref. [55]).

2.2.2.2. Steam reforming catalysts

2.2.2.2.1 Ni catalysts

Figure 134 shows the hydrogen production as a function of reaction time (or time on stream, TOS) in steam reforming of commercial diesel with 15 ppmw sulfur over the K-modified Ni catalysts at 800 °C. 10Ni/A catalyst showed high initial activity for diesel steam reforming. The Hydrogen yield was about 0.17 mol/g_{fuel}-min. However, the activity of 10Ni/A catalyst decreased with the increase of reaction time. The hydrogen production decreased down to 0.12 mol/g_{fuel}-min after 80 hrs of reforming. After about 80 of TOS, a great drop was observed in 10 hrs for 10Ni/A catalyst, which was probably induced by accumulated carbon deposition, as indicated in **Figure 136**. The hydrogen production was only about 0.03 mol/g_{fuel}-min after 150 hrs of diesel reforming. With the addition of K, almost the same initial hydrogen production was attained over the 10Ni1K/A and 10Ni5K/A catalysts as that over the 10Ni/A catalyst, suggesting that the addition of K does not impair the activity of the Ni catalyst. Furthermore, the deactivation over the K-modified Ni catalysts was much less than the Ni catalyst, especially over the 10Ni5K/A catalyst. After 150 hr of diesel reforming, the hydrogen production over the 10Ni5K/A catalyst could still be maintained at relatively high level (0.10 mol/g_{fuel}-min), compared to the 10Ni1K/A and 10Ni/A catalyst. The results in **Figure 134** also present that 5 wt% K addition can more notably enhance the resistance of Ni catalyst to sulfur poisoning and/or carbon deposition than 1 wt% K.

Due to the significant improvement in the performance of Ni catalyst with the addition of K, it is worth measuring the reducibility of Ni catalyst with the presence of potassium. Thus, in this report, these catalysts have been characterized by hydrogen temperature programmed reduction (H_2-TPR) method. **Figure 135** shows the H_2-TPR profiles of 10Ni/Al, 10Ni1K/Al and 10Ni1K/Al catalysts. The 10Ni/Al catalyst exhibits a small and broad peak between 400 and 850°C, which can be attributed to the reduction of NiO in intimate interaction with the Al_2O_3 support. With 1 wt% of K addition, the obtained TPR profile of the 10Ni1K/A catalyst was similar to that of 10Ni/A catalyst, except that the intensity was slightly higher than that of

10Ni/A catalyst, especially for the peak at around 700 °C. It suggests the reducibility of Ni has been changed with the addition of only 1 wt% of K, although the change is not significant. However, when K loading was up to 5 wt%, the 10Ni5K/Al catalyst exhibited distinctly different H_2-TPR behavior from the 10Ni/Al sample. An intensive peak between 350 and 500 °C can be easily observed. Although it is difficult to tell what species is attributed to at current state, it is still clear that the reducibility of the NiO is greatly promoted due to the addition of K. In addition, the reduction peak at about 700 °C becomes sharper and wider. According to the literature, the reduction of NiO species interacting with alumina support occurs at about 550 °C, while the reduction of highly dispersed non-stoichiometric amorphous nickel aluminate spinels and diluted $NiAl_2O_4$-like phase happens at higher temperatures. The results suggest that after potassium addition, the amount of nickel aluminate species also increases in addition to the improvement in the Ni reducibility. Certainly, the likelihood of K_2O reduction in this temperature range may not be totally ruled out.

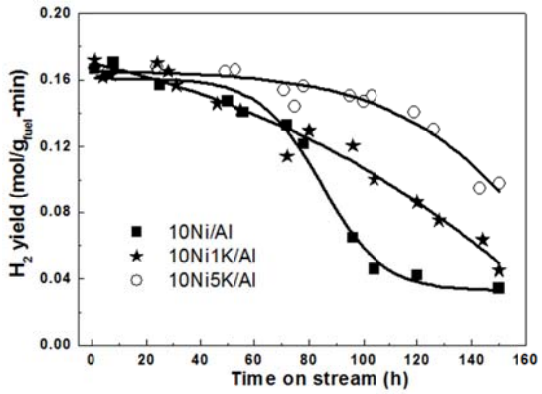

Figure 134. H_2 production for steam reforming of commercial diesel with 15 ppmw sulfur as a function of time on stream (TOS) over 10Ni/Al, 10Ni1K/Al, and 10Ni5K/Al catalysts. Reaction conditions: W_{cat}, 1.0 g; T, 800 °C; $WHSV$, ~5.1 h^{-1}.

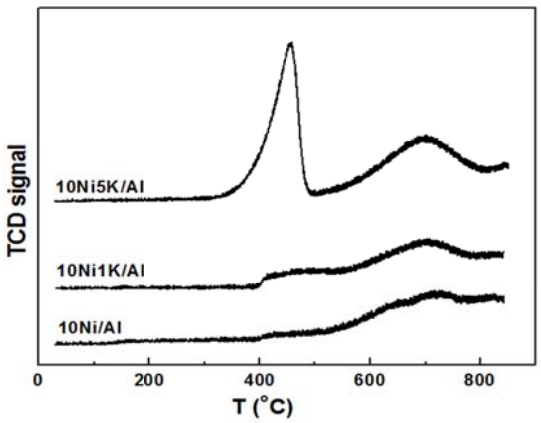

Figure 135. TPR profiles of Al_2O_3 supported 10wt% Ni (10Ni/Al), 10wt% Ni with 1 wt% K modified (10Ni1K/Al), and 10wt% Ni with 5 wt% K modified (10Ni5K/Al).

As shown earlier that the catalytic performance of Ni catalyst for steam reforming of commercial diesel fuel with 15 ppmw sulfur at 800 °C was notably enhanced with the addition of K, especially for the one with 5 wt% K loading. To understand the reason, we have carried the carbon deposit analysis on these spent catalysts. The results are presented in **Figure 136**. The amount of deposit carbon over the 10Ni/A catalyst after 150 hrs of the steam reforming was as high as 1.2 g/g-cat. After K addition, carbon deposition can be pronouncedly reduced. It was ca. 0.8 g/g-cat of carbon over the spent 10Ni1K/Al catalyst, which is about two-thirds of that over the spent 10Ni/A catalyst. When the K addition was increased to 5 wt%, the reduce of carbon deposit over the Ni catalyst became more significantly. The measured carbon amount over the spent 10Ni5K/A catalyst was ca. 0.2 g/g-cat, only about 17% of that over the spent 10Ni/A catalyst and 25% of that over the spent 10Ni5K catalyst. The reduced carbon deposit is probably because that the presence of K facilitates carbon gasification resulting in that the deposited carbon cannot significantly accumulate over the catalyst surface, as suggested by many researchers. The current study indicates that K addition is a promising method to improve the

catalytic performance of Ni catalyst for commercial diesel steam reforming at 800 °C by inhibiting the carbon deposition.

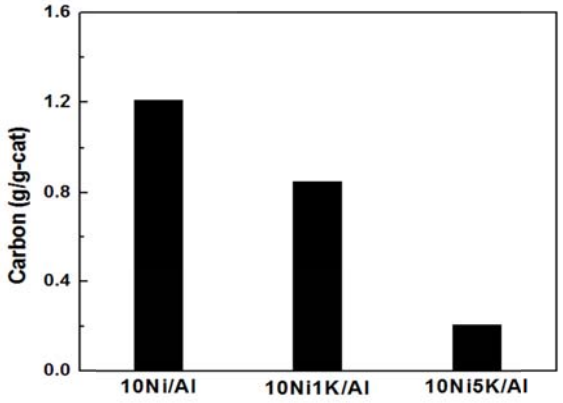

Figure 136. The carbon amounts over the spent catalysts after 150-h steam reforming of commercially available diesel with 15 ppmw sulfur at 800°C.

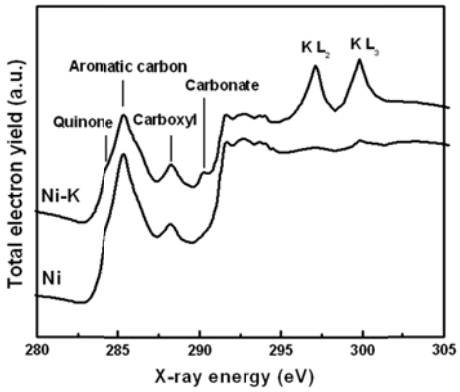

Figure 137. Carbon K-edge XANES spectra of the spent 10wt%Ni and 10wt%Ni-5wt%K catalysts supported on Al_2O_3 after steam reforming of commercial diesel with 15 ppmw sulfur at 800 ºC for 150 hrs.

In order to explore the effect of K modification on the carbon deposition, the spent 10wt% Ni/Al and 10wt% Ni-5wt% K/Al catalysts after steam reforming of commercial diesel with 15 ppm sulfur at 800 ºC for 150 hrs were characterized by carbon K-edge X-ray absorption near-edge structure (XANES) spectroscopy. The results are shown in **Figure 137**. Carbon K-edge XANES measurements were conducted at beam-line U4B of the National Synchrotron Light Source (NSLS), Brookhaven National Laboratory, Upton, NY. All the carbon spectra were collected in a total electron yield mode. A reference compound was always recorded simultaneously to provide energy alignment. All the XANES data were processed using Athena [56].

As shown in the **Figure 137**, both the catalysts exhibit a strong peak at 285.2 eV and a plateau starting around 291.5 eV, corresponding to π^* transition and σ^* exciton of aromatic carbons, respectively [57]. This demonstrates the accumulation of aromatic carbons on the used catalysts. Beside the aromatic peak at 285.2 eV, there is a shoulder peak at around 284.4 eV, which can be attributed to quinone-like hydrocarbons. They very likely came from the reaction between the deposited aromatic carbons and steam, which might be an initial step for the gasification of the aromatic carbons. In addition, a small peak associated with carboxyl (-COOH) appears at ca. 288.3 eV [58]. The formation of carboxyl is a result of carbon gasification as well. For the used K-modified Ni catalyst, two intensive peaks of K L_2 and K L_3 can be observed at 297.5 and 300.0 eV, confirming the presence of K in the catalyst. Moreover, Compared Ni/Al catalyst, an extra peak at 290.2 eV which can be attributed to carbonate (CO_3^{2-}) species is observed over the Ni-K/Al catalyst [57]. It suggests that the presence of K may be able to promote the formation of carbonate species. Carbonate (CO_3^{2-}) species are normally less stable than aromatic carbons, and can decompose at lower temperature, which can benefit the gasification process and thus reduce the carbon deposition. Consequently, we believe that the formation of carbonate (CO_3^{2-}) species due to the presence of K may be critical to significantly reduce carbon deposition on Ni catalyst during steam reforming of commercial diesel with 15 ppm sulfur at high temperature such as 800 ºC.

2.2.2.2.2 Ni-Co catalysts

The alumina-supported monometallic Ni and bimetallic Ni-Co catalysts were prepared via wet co-impregnation on the supports using a aqueous solution of $Ni(NO_3)_2$ or a mixed aqueous solution of $Ni(NO_3)_2$ and $Co(NO_3)_2$ for monometallic Ni and bimetallic Ni-Co catalysts, respectively. For the samples with potassium modification, the KNO_3 solution was used and mixed with the metal solution before all the components was impregnated on the desired support. Then the slurry was dried overnight at 100°C, followed by calcination at 550°C for 6 hrs. The prepared catalysts include 10Ni/Al, 10Ni5K/Al, 10Ni5Co/Al and 10Ni5Co5K/Al catalyst.

The prepared catalysts have been characterized by N_2-adsorption-desoption technique over a Quartchrome Autosorb-1 analyzer at the liquid-nitrogen temperature (-196 °C) to examine the BET (Brunauer-Emmett-Teller method) surface area and pore volume. Each sample was degassed by heating at 200 °C under vacuum prior to the measurement. The results are listed in **Table 33**. The commercial alumina support has a high surface area of 144 m^2/g. After 10 wt% of Ni addition, the surface area slightly decreased to about 121 m^2/g. The addition of Ni and Co resulted in higher decrease of the surface area than Ni alone. The addition of K also resulted in the further decrease of the surface area and pore volume.

Table 33. The textural properties of Alumina supported Ni and Ni-Co catalysts with or without K modification.

Catalysts	Surface area (m^2/g)	Pore volume (cm^3/g)
γ-Al_2O_3	144.4	0.81
10Ni/Al_2O_3	120.9	0.61
10Ni5Co/Al_2O_3	113.2	0.69
10Ni5K/Al_2O_3	104.4	0.58
10Ni5Co5K/Al_2O_3	98.6	0.54

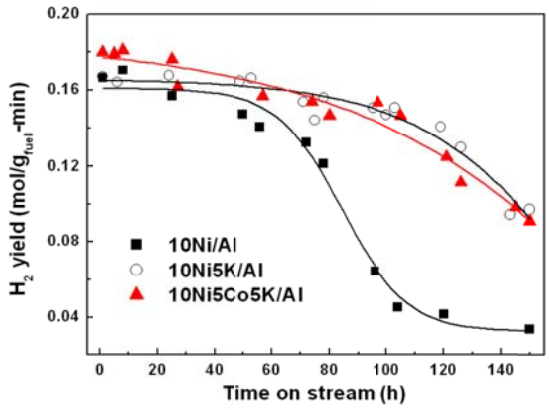

Figure 138. H_2 yields for 150 h steam reforming of commercially available diesel with 15 ppmw sulfur over Al_2O_3 supported 10wt% of Ni (10Ni/Al), 10wt% of Ni and 5 wt% of K (10Ni5K/Al), and 10wt% of Ni, 5wt% of Co and 5 wt% of K (10Ni5Co5K/Al). Reaction conditions: *W*: 1g, *T*: 800°C, WHSV: ~5.1 h^{-1}.

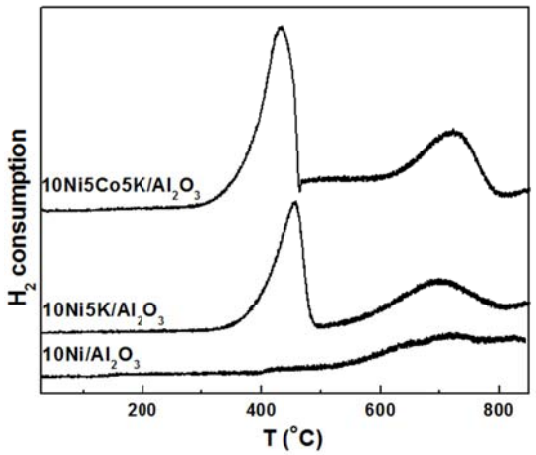

Figure 139. TPR profiles of Al_2O_3 supported 10wt% of Ni (10Ni/Al), 10wt% of Ni and 5 wt% of K (10Ni5K/Al), and 10wt% of Ni, 5wt% of Co and 5 wt% of K (10Ni5Co5K/Al).

Figure 138 shows the catalytic performances of the 10Ni/Al, 10Ni5K/Al and 10Ni5Co5K/Al catalysts for steam reforming of commercial diesel fuel with 15 ppmw sulfur at 800 °C and a WHSV of 5.1 h^{-1}. An on-line GC-TCD equipped with a Molecular Sieve 5A column and a silica gel column will be used for the analysis of gas products including H_2, CH_4, CO and CO_2 (and other light hydrocarbons if present) in the reformate gas. The liquid products were periodically collected by a condenser for the conversion calculation on the basis of the assumption that all of the remaining fuel in the liquid products is of the same composition as the initial fuel.

It can be seen that the initial H_2 yields for both 10Ni/Al and 10Ni5K/Al are ca. 0.16 mol/g_{fuel}-min (The theoretic H_2 yield should be between 0.22-0.23 mol/g_{fuel}-min). The reforming activity of 10Ni/Al was stable for 60 h, after which the H_2 yield gradually decreased, and finally reached ca. 0.04 mol/g_{fuel}-min after 150 h of TOS (time on stream). The significant deactivation of 10Ni/Al is most likely due to sulfur poisoning and carbon deposition. With the addition of K, although the 10Ni5K/Al catalyst still deactivated somehow, it became much slower comparing to the catalyst with Ni only. It is widely accepted that the presence of K can promote the gasification of coke on Ni catalyst. Thus, the better resistance of 10Ni5K/Al catalyst to the deactivation during steam reforming of commercial diesel could also be attributed to the role of K in effective gasification of carbon deposits over the Ni catalyst. With further Co addition (i.e., 10Ni5Co5K/Al catalyst), the initial H_2 yield could be apparently increased to ca. 0.18 mol/g_{fuel}-min, indicating that the presence of Co may promote the reforming efficiency of Ni catalyst. However, with the reaction preceding, the activity of 10Ni5Co5K/Al progressively declined and became very close to that of 10Ni5K/Al. According to the above facts, a little promotion effect of 5 wt% Co addition is observed for steam reforming of commercially available diesel with 15 ppmw sulfur over Al_2O_3 supported Ni catalyst at 800°C.

These catalysts have been characterized by hydrogen temperature programmed reduction (H_2-TPR) method to verify the roles of potassium and Co addition. **Figure 139** shows the H_2-TPR profiles of 10 wt% Ni/Al_2O_3 (10Ni/Al), 10 wt% Ni-5 wt% K/Al_2O_3 (10Ni5K/Al) and 10 wt% Ni-5 wt% Co-5 wt% K/Al_2O_3 (10Ni5Co5K/Al) catalysts. The 10Ni/Al catalyst exhibits a broad peak between 500 and 850°C, which can be attributed to the reduction of NiO in intimate interaction with the Al_2O_3 support. With the addition of K, the 10Ni5K/Al catalyst exhibited distinctly different H_2-TPR behavior from the 10Ni/Al sample. An intensive peak between 350 and 500 °C can be easily observed. Although it is difficult to tell what species is attributed to at current state, it is still clear that the reducibility of the NiO is greatly promoted due to the addition of K. In addition, the reduction peak at about 700 °C becomes sharper and wider. According to the literature, the reduction of NiO species interacting with alumina support occurs at about 550 °C, while the reduction of highly dispersed non-stoichiometric amorphous nickel aluminate spinels and diluted $NiAl_2O_4$-like phase happens at higher temperatures. The results suggest that after potassium addition, the amount of nickel aluminate species also increases in addition to the improvement in the Ni reducibility. With further addition of Co, the formed 10Ni5Co5K/Al catalyst showed similar H_2-TPR profile to the 10Ni5K/Al catalyst.

After reaction, the carbon deposit on the spent catalysts has been analyzed. **Figure 140** shows the amount of carbon deposited on the spent catalysts after 150-h steam reforming of commercially available diesel with 15 ppmw sulfur at 800°C. There is about 1.2 g/g-cat of carbon deposited on the 10Ni/Al catalyst. After K addition, carbon deposition is significantly reduced. It is only ca. 0.2 g/g-cat of carbon over the 10Ni5K/Al catalyst. It is probably because that the presence of K facilitates carbon gasification resulting in that the deposited carbon cannot

significantly accumulate over the catalyst surface, as suggested by many researchers. However, with further addition of Co into the 10Ni5K/Al catalyst, the deposit carbon amount increases slightly to 0.35 g/g-cat over the 10Ni5Co5K/Al catalyst. Since the presence of Co can also contribute to the formation of carbon deposit, the loading amount of K and Co may have to change and optimize in order to suppress the carbon deposition over the Ni and Co based catalyst with better catalytic performance for diesel steam reforming, which will be investigated in future. It should be mentioned that the Ni/Al and Ni-K/Al catalysts tested here are working as the baseline for the development Ni-Co-K based catalysts and other transition metal based reforming catalysts.

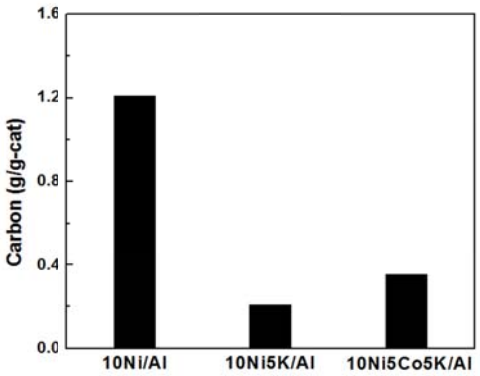

Figure 140. The carbon amounts over the spent catalysts after 150-h steam reforming of commercial diesel with 15 ppmw sulfur at 800 °C.

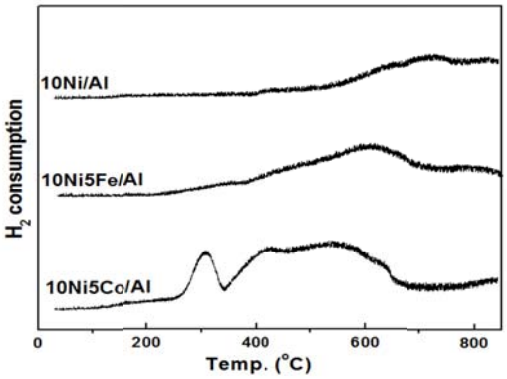

Figure 141. TPR profiles of Al_2O_3 supported 10wt% Ni (10Ni/Al), 10wt% Ni and 5 wt% Fe (10Ni5K/Al), and 10wt% Ni and 5 wt% Co (10Ni5Co/Al).

2.2.2.2.3 Ni-Fe catalysts

The influence of iron addition on alumina supported Ni catalysts in comparison with the cobalt addition has been studied. The alumina-supported monometallic Ni and bimetallic Ni-Co, Ni-Fe catalysts were prepared via wet co-impregnation on the alumina support using a aqueous solution of $Ni(NO_3)_2$ or a mixed aqueous solution of $Ni(NO_3)_2$ and $Co(NO_3)_2$ (or $Fe(NO_3)_3$) for monometallic Ni and bimetallic Ni-Co, Ni-Fe catalysts, respectively. Then the slurry was dried overnight at 100°C, followed by calcination at 550°C for 6 hrs. The prepared catalysts are termed as 10Ni/Al, 10Ni5Co/Al, 10Ni5Fe/Al and 10Ni5Fe5K/Al catalysts.

The prepared catalysts have been characterized by temperature programmed reduction to examine the reducibility of the loaded metals. The results are shown in **Figure 141**. The 10Ni/Al catalyst exhibits a broad peak between 500 and 850°C, which can be attributed to the reduction of NiO in intimate interaction with the Al_2O_3 support. As either Fe or Co is added into the Ni catalyst, the reduction behavior is changed significantly. With the addition of iron, the reduction of metals begins at about 250 °C with a maximum reduction temperature at ca. 620 °C. For the case of Co addition, a new, narrow reduction peak can be easily observed, which may be attributed to the reduction of cobalt oxide. Another major reduction ranges from 350 to 700 °C, whose temperature is much lower compared to Ni alone. In addition, the reduction peak area is much larger, indicating more Ni may be reduced in the bimetallic Ni-Co system. The results strongly suggest the interaction between Ni and the second metal Fe or Co. It also demonstrates that the interaction between Ni and other metal (Fe or Co) is able to alter the surface properties of Ni catalyst, causing the change of chemical properties of Ni catalyst.

Figure 142 shows the hydrogen production as a function of reaction time (or time on stream, TOS) in steam reforming of commercial diesel with 15 ppmw sulfur over the alumina supported Ni catalysts including 10Ni/Al, 10Ni5Co/Al, 10Ni5Fe/Al and 10Ni5Fe5K/Al at 800 °C. 10Ni/Al catalyst showed high initial activity for diesel steam reforming. The Hydrogen yield was about 0.17 mol/g_{fuel}-min. However, the activity of 10Ni/Al catalyst decreased with the increase of reaction time. The hydrogen production decreased down to 0.12 mol/g_{fuel}-min after 80 hrs of reforming. After about 80 of TOS, a great drop was observed in 10 hrs for 10Ni/Al catalyst, which was probably induced by accumulated carbon deposition and sulfur poisoning, as indicated in **Figure 143**. The hydrogen production was only about 0.03 mol/g_{fuel}-min after 150 hrs of diesel reforming. By adding Co as a secondary transition metal, the initial hydrogen production was much improved, reaching to about 0.22 mol/g_{fuel}-min. However, the activity of Ni-Co catalyst decreased very quickly. In about 60 hrs of reforming, only about 0.02 mol/g_{fuel}-min of the hydrogen yield could be attained. On the other side, when 5% of iron was added to the Ni catalyst, although the initial hydrogen production does not change much, the activity was much more stable than both Ni alone and the Ni-Co catalyst. During the 150 hrs of reforming, the hydrogen production rate dropped only about 0.04 mol/g_{fuel}-min. As high as 0.14 mol/g_{fuel}-min of hydrogen production could be maintained over the Ni-Fe catalyst, even after 150 hrs of reforming.

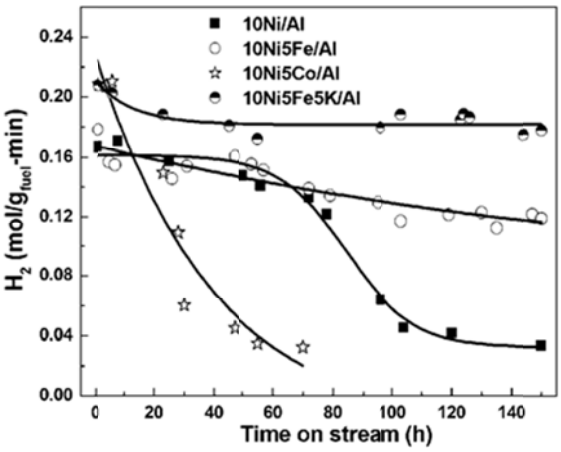

Figure 142. H_2 production for steam reforming of commercial diesel with 15 ppmw sulfur as a function of time on stream (TOS) over 10Ni/Al, 10Ni5Co/Al 10Ni5Fe/Al, and 10Ni5Fe5K/Al catalysts. Reaction conditions: W_{cat}, 1.0 g; T, 800 °C; S/C, 3.0; $WHSV$, ~5.1 h^{-1}.

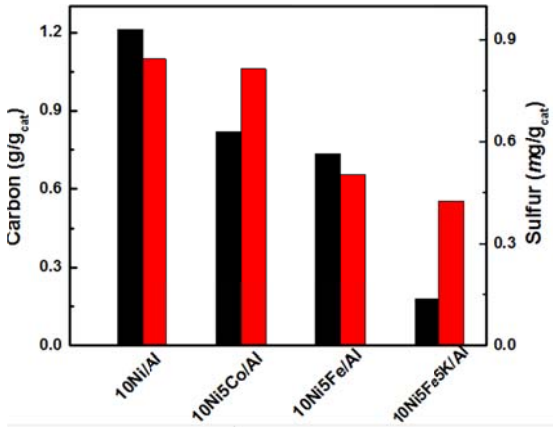

Figure 143. Carbon and sulfur contents in the used 10Ni, 10Ni-5Co, 10Ni-5Fe, and 10Ni-5Fe-5K catalysts after steam reforming of commercial diesel with 15 ppm sulfur at 800 ºC. All the catalysts were tested for 150 h on stream, except the Ni-Co catalyst (70 h on stream).

Based on the better performance, the Ni-Fe/Al catalyst was further modified by adding 5% of K to change the surface properties of the Ni-Fe/Al catalyst. As it can be seen from, the addition of K can only improve of the initial activity of the Ni-Fe/Al catalyst, but also the resistance of Ni-Fe/Al catalyst to carbon deposition and sulfur poisoning. The initial hydrogen production jumped from 0.18 mol/g_{fuel}-min without K addition to 0.21 mol/g_{fuel}-min with the K addition. Meanwhile, the hydrogen production can be maintained at about 0.19 mol/g_{fuel}-min level for a long term steam reforming, although a slight drop was observed at the beginning of

the reaction. The result indicates that the Ni-Fe/Al with K addition is more promising for steam reforming of commercial diesel at 800 °C so far.

To understand the reason, we have carried out a carbon and sulfur deposit analysis on these spent catalysts. The results are presented in **Figure 143**. The amount of carbon and sulfur deposited over the 10Ni/A1 catalyst after 150 hrs of the steam reforming was as high as 1.2 g/g-cat and 0.84 mg/g-cat, respectively. With the addition of Co, after 150 hrs of reforming, about of 0.85 g/g-cat of carbon was deposited and 0.82 mg/g-cat of deposit sulfur were detected. When comparing the reforming performance and carbon and sulfur deposition amount between Ni/Al and Ni-Co/Al catalyst, we probably can propose that after the addition of Co, the formed Ni-Co catalyst is more sensitive to the sulfur poisoning, which results in the quick drop in its reforming activity, as shown in **Figure 142**.

However, the addition of Fe to the Ni catalyst, the detected carbon and sulfur amount over the spent Ni-Fe/Al catalyst was lower, about 0.8 g/g-cat of deposit carbon and about 0.51 mg/g-cat of deposit sulfur. Thus, better reforming performance of Ni-Fe/Al catalyst may be attributed to its improved carbon and sulfur resistance. Interestingly, after further addition of K, carbon deposition can be pronouncedly reduced. It was 0.2 g/g-cat of carbon over the spent 10Ni5Fe5K/Al catalyst, which is about one-fourth of that over the spent 10Ni5Fe/Al catalyst, only one-sixth of that over the spent 10Ni/Al catalyst. The reduced carbon deposit is probably because that the presence of K facilitates carbon gasification resulting in that the deposited carbon cannot significantly accumulate over the catalyst surface, as suggested by many researchers. In addition, the residue sulfur was also slightly reduced, being 0.42 mg/g-cat on the spent 10Ni5Fe5K/Al. This current study confirms that K addition is a promising method to improve the catalytic performance of Ni-Fe catalyst for commercial diesel steam reforming at 800 °C by inhibiting the carbon deposition.

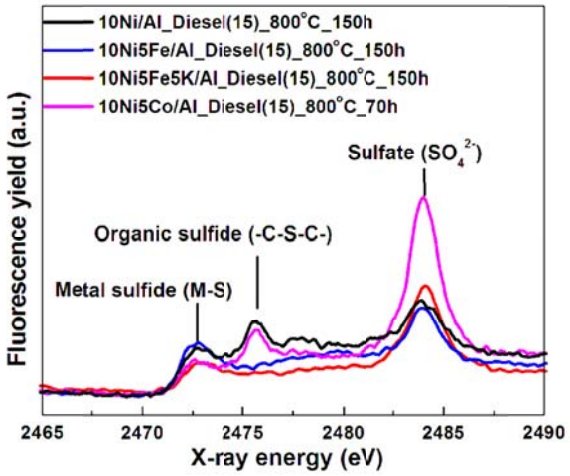

Figure 144. Sulfur K-edge XANE spectra of used 10Ni, 10Ni-5Fe, 10Ni-5Fe-5K, and 10Ni-5Co after steam reforming of commercial diesel with 15 ppm sulfur at 800 ºC. All the catalysts were tested for 150 h on stream, except the Ni-Co catalyst (70 h on stream).

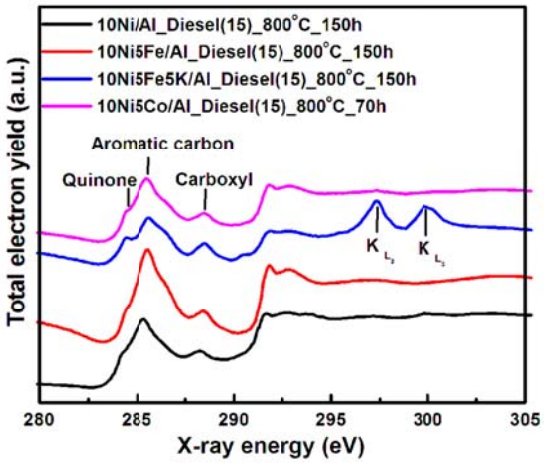

Figure 145. Carbon K-edge XANES spectra of used 10Ni, 10Ni-5Fe, 10Ni-5Fe-5K, and 10Ni-5Co after steam reforming of commercial diesel with 15 ppm sulfur at 800 ºC. All the catalysts were tested for 150 h on stream, except the Ni-Co catalyst (70 h on stream).

Figure 144 shows sulfur K-edge XANE spectra of the spent 10wt%Ni/Al_2O_3, 10wt%Ni-5wt%Fe/Al_2O_3, 10wt%Ni-5wt%Fe-5wt%K/Al_2O_3, and 10wt%Ni-5wt%Co/Al_2O_3 after steam reforming of commercial diesel with 15 ppm sulfur at 800 ºC. All the catalysts were tested for 150 h on steam, except the Ni-Co catalyst, which was run for 70 h on steam. Over the used Ni/Al_2O_3 catalyst, three XANES peaks can be identified, which can be attributed to metal sulfide (M-S) at 2472.1 eV, organic sulfide (-C-S-C-) at 2475.3 eV, and sulfate (SO_4^{2-}) at 2480.1 eV, respectively [59,60]. The same sulfur species can also be found over the used 10Ni-5Co/Al_2O_3 catalyst. However, only the peaks for metal sulfide and sulfate are observable over the 10Ni-5Fe/Al_2O_3 and 10Ni-5Fe-5K/Al_2O_3 catalysts. The absence of organic sulfides in the Fe-modified Ni catalysts suggests that the presence of Fe may hinder sulfur adsorption on reforming catalysts, which may explain the improved sulfur tolerance of Ni-Fe catalyst.

Figure 145 exhibits carbon K-edge XANE spectra of these used catalysts. The 10Ni/Al_2O_3 catalyst shows an intensive peak at 285.2 eV with a plateau starting at 291.5 eV, corresponding to π^* transition and σ^* excitation of aromatic carbon, respectively [61,62]. The observation of these two features at the same time suggests that the carbon depositing on the used Ni/Al_2O_3 catalyst are mainly graphite. Moreover, a weak peak can be identified at 288.3 eV, which may be caused by the formation of carboxyl groups (COOH) [62]. The existence of this peak may hint the reaction between the deposit carbon and steam (i.e., carbon gasification).

The carbon K-edge XANE spectrum of the used 10Ni-5Fe/Al_2O_3 catalyst is almost the same as that of the used 10Ni/Al_2O_3 catalyst, implying that the addition of iron does not significantly change the carbon structures. Compared to the 10Ni-5Fe/Al_2O_3 catalyst, further addition of K results in the decrease of the peak intensity for aromatic carbon species, and the increase of the peak intensity for quinone-like carbon species. It has been known that quinone-like carbon species are the intermediates of carbon gasification [63-65]. This result indicates that K modification can enhance the gasification of deposit carbon and therefore reduce the carbon accumulation on the 10Ni-5Fe-5K/Al reforming catalyst.

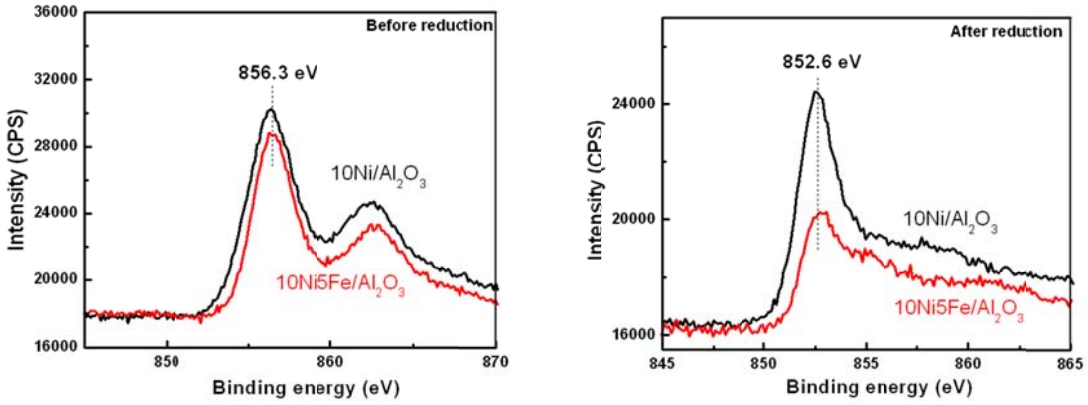

Figure 146. Ni 2p XPS Spectra of the 10wt% Ni/Al_2O_3 and 10wt% Ni-5wt% Fe/Al_2O_3Catalysts before (A) and after (B) H_2 Reduction (H_2 reduction conditions: 100 ml/min of 10%H_2/He, 800 ºC, 1 h).

We have also conducted XPS analysis on the Ni and Ni-Fe catalysts. **Figure 146** shows Ni 2p XPS spectra of the 10wt% Ni/Al_2O_3 and 10wt%Ni-5wt% Fe/Al_2O_3 catalysts before (A) and after (B) H_2 reduction at 800 ºC for 1h. Before reduction (Figure 15A), similar Ni 2p XPS spectra were observed over the 10 wt% Ni/Al_2O_3 and 10wt% Ni-5wt% Fe/Al_2O_3 catalysts, a

main peak at 856.3 eV with a satellite peak at about 862.7 eV, indicating only NiO exists on the both catalysts before reduction. No significant differences in peak shape and intensity are observed for the unreduced catalysts. After the reduction (Figure 16B), the Ni 2p XPS peak for both catalysts shifted down to 852.6 eV, suggesting the formation of metallic Ni. It is interesting to note that the peak intensity for the Ni-Fe/Al_2O_3 catalyst is obviously lower than that of the Ni/Al_2O_3 catalyst. One possible reason is that the added Fe may cover the Ni metal surface in the Ni-Fe/Al_2O_3 catalyst after reduction.

On the basis of XPS analysis, the surface chemical composition of the 10wt% Ni/Al_2O_3 and 10wt% Ni-5wt% Fe/Al_2O_3 catalysts before and after H_2 reduction can be calculated and the results are summarized in **Table 34**. It can be seen that the Ni/Fe molar ratio on the surface decreased from 1.5 for the unreduced Ni-Fe/Al_2O_3 catalyst to 0.8 for the reduced Ni-Fe/Al_2O_3 catalyst. In other words, after reduction, surface iron becomes even richer than that before reduction. The change may suggest that upon H_2 reduction, Fe may cover Ni metals, which further support the conclusion drawn from XPS spectra. Compared Ni/Al_2O_3 catalyst, the enhanced sulfur tolerance of the Ni-Fe/Al_2O_3 catalyst in steam reforming of commercial diesel fuel may likely be attributed to the iron protection on Ni from sulfur contacting by covering Ni surface.

Table 34. Surface chemical composition of the 10Ni and 10Ni-5Fe catalysts before and after H_2 reduction (H_2 reduction conditions: 100 ml/min of 10% H_2/He, 800 ºC, 1 h) by XPS.

Catalyst	Treatment	Element (wt%)					Ni/Fe
		Ni	Al	O	C	Fe	molar ratio
Ni/Al_2O_3	Unreduced	8.56	47.96	41.67	1.80	-	-
	H_2/800 ºC	4.30	53.84	42.66	-	-	-
Ni-Fe/Al_2O_3	Unreduced	8.66	43.41	40.91	1.40	5.62	1.47
	H_2/800 ºC	3.50	50.54	41.94	-	4.02	0.83

Figure 147 shows the Ni 2p XPS spectra of the used 10 wt% Ni/Al_2O_3 and 10 wt% Ni-5 wt% Fe/Al_2O_3 catalysts after steam reforming of commercial diesel with 15 ppmw sulfur at 800 ºC for 150 h. Both used catalysts show intensive peaks at ca. 586.4 eV, which can be attributed to the presence of Ni^{2+}. This result suggests that the surface of these used catalysts was oxidized during the storage under ambient conditions. However, there is a pronounced difference between the XPS spectra of the two used catalysts: an obvious shoulder at 583.5 eV, which can be likely associated with the formation of nickel carbide, is observed over the used Ni catalyst, but it is rather weak over the used Ni-Fe catalyst. The difference may imply the formation of nickel carbide over the Ni catalyst, while its formation was suppressed over the Ni-Fe catalyst. It is known that the formation of nickel carbide is detrimental to hydrocarbon reforming over Ni catalysts. Therefore, it appears that the addition of Fe inhibits the formation of nickel carbide, which should benefit steam reforming of commercial diesel over the Ni-Fe catalyst.

The surface elemental composition of the used 10 wt% Ni/Al_2O_3 and 10 wt% Ni-5 wt% Fe/Al_2O_3 catalysts after steam reforming of commercial diesel with 15 ppmw sulfur at 800 ºC for 150 h are summarized in **Table 35**. After the reaction, the concentration of surface Ni over the Ni catalyst was determined to be 3.88 wt%, which is much lower than the theoretical value (10 wt%). Over the Ni-Fe catalyst, the concentration of surface Ni was further decreased to 2.19 wt%. The weight ratio of surface Fe to surface Ni is 1.6 (3.61/2.19), which is about three times

higher than the theoretical Fe/Ni weight ratio, 0.5 for the 10 wt% Ni-5 wt% Fe/Al_2O_3 catalyst. This fact reveals that, after the reaction, Fe is prone to enrich on the surface compared to Ni, which may contribute to the better sulfur and carbon resistance of the Ni-Fe catalyst.

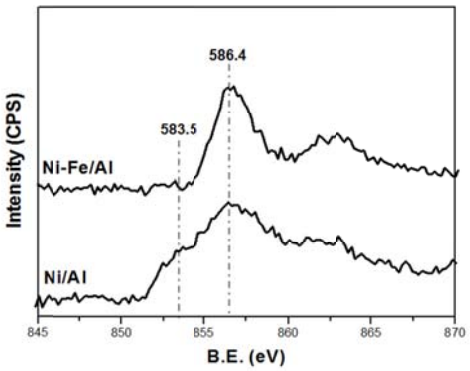

Figure 147. Ni 2p XPS spectra of the used 10 wt% Ni/Al_2O_3 and 10 wt% Ni-5 wt% Fe/Al_2O_3 catalysts after steam reforming of commercial diesel with 15 ppmw sulfur. Reforming conditions: 1 g of catalyst, 800 ºC, S/C = 3, and TOS = 150 h.

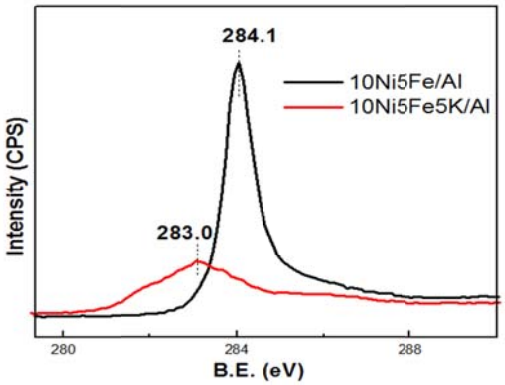

Figure 148. C1s XPS spectra of the used 10wt%Ni-5wt%Fe/Al_2O_3 and 10wt%Ni-5wt%Fe-5wt%K/Al_2O_3 catalysts after steam reforming of commercial diesel with 15 ppmw sulfur. Reforming conditions: 1 g of catalyst, 800 ºC, S/C = 3, and TOS = 150 h.

Table 35. Surface elemental composition of the used 10 wt% Ni/Al_2O_3 and 10 wt% Ni-5 wt% Fe/Al_2O_3 catalysts after steam reforming of commercial diesel with 15 ppmw sulfur at 800 ºC for 150 h.

Catalyst Sample	Element (wt%)					
	Ni	Fe	K	Al	O	C
Ni/Al	3.88	-	-	24.09	28.68	43.35
Ni-Fe/Al	2.19	3.61	-	23.84	25.67	44.69

XPS characterization was also carried out to study the effect of K modification on the carbon deposition over Al_2O_3 supported Ni-Fe catalyst after steam reforming of commercial diesel fuel containing 15 ppmw sulfur at 800 °C and a steam-to-carbon ratio of 3.0 for 150 hrs on stream. The result is presented in **Figure 148** and the surface elemental analysis on the 10Ni5Fe/Al and 10Ni5Fe5K/Al samples by XPS is listed in **Table 36**.

It can be seen that the C 1s peak for the used 10wt%Ni-5wt%Fe/Al_2O_3 is significantly stronger than that for the used 10wt%Ni-5wt%Fe-5wt%K/Al_2O_3, suggesting that the carbon deposition on the former is more severe compared to the latter. This is corroborated by the surface elemental analysis regarding the carbon deposition summarized in **Table 36**, which shows that the carbon amount is 44.69 and 17.20 wt% for the used 10wt%Ni-5wt%Fe/Al_2O_3 and 10wt%Ni-5wt%Fe-5wt%K/Al_2O_3 catalysts after 150 hrs of diesel steam reforming, respectively. Moreover, the C 1s peak positioned at 284.1 eV for 10wt%Ni-5wt%Fe/Al_2O_3, while that of 10wt%Ni-5wt%Fe-5wt%K/Al_2O_3 dramatically shifted to 283.0 eV. According to literature [4], the C 1s peak at 284.1 and 283.0 eV can be attributed to graphitic carbon and isolated carbon, respectively. Therefore, it is indicating that the addition of potassium not only suppresses the

carbon deposition over the catalyst surface, but also shifts the formation of graphitic carbon to isolated carbon on the surface of reforming catalyst during the diesel reforming.

Table 36. Surface elemental composition of the used 10wt%Ni-5wt%Fe/Al_2O_3 and 10wt%Ni-5wt%Fe-5wt%K/Al_2O_3 catalysts after steam reforming of commercial diesel with 15 ppmw sulfur at 800 ºC for 150 h.

Catalyst Sample	Element (wt%)					
	Ni	Fe	K	Al	O	C
Ni-Fe/Al	2.19	3.61	-	23.84	25.67	44.69
Ni-Fe-K/Al	4.52	5.72	1.13	32.50	38.93	17.20

2.2.3. Conceptual Process Design for Diesel Fuel Processor

As shown in our previous quarterly reports, we have developed an effective and efficient adsorbent material for deep desulfurization of commercial diesel fuel from 15 ppmw to below 1 ppm with a good regenerability at high temperature under air. In addition, the carbon-resistant and sulfur-tolerant reforming catalyst based on the transition metals has been developed and exhibited a good catalytic performance for steam reforming of commercial diesel fuel under the temperature of 800 °C and with the steam to fuel ratio of 3. On the basis of the adsorption performance for deep desulfurization and the catalytic performance for diesel steam reforming, we subsequently propose a conceptual process of diesel fuel processor for use in the solid oxide fuel cell system, which is illustrated in the **Figure 149**.

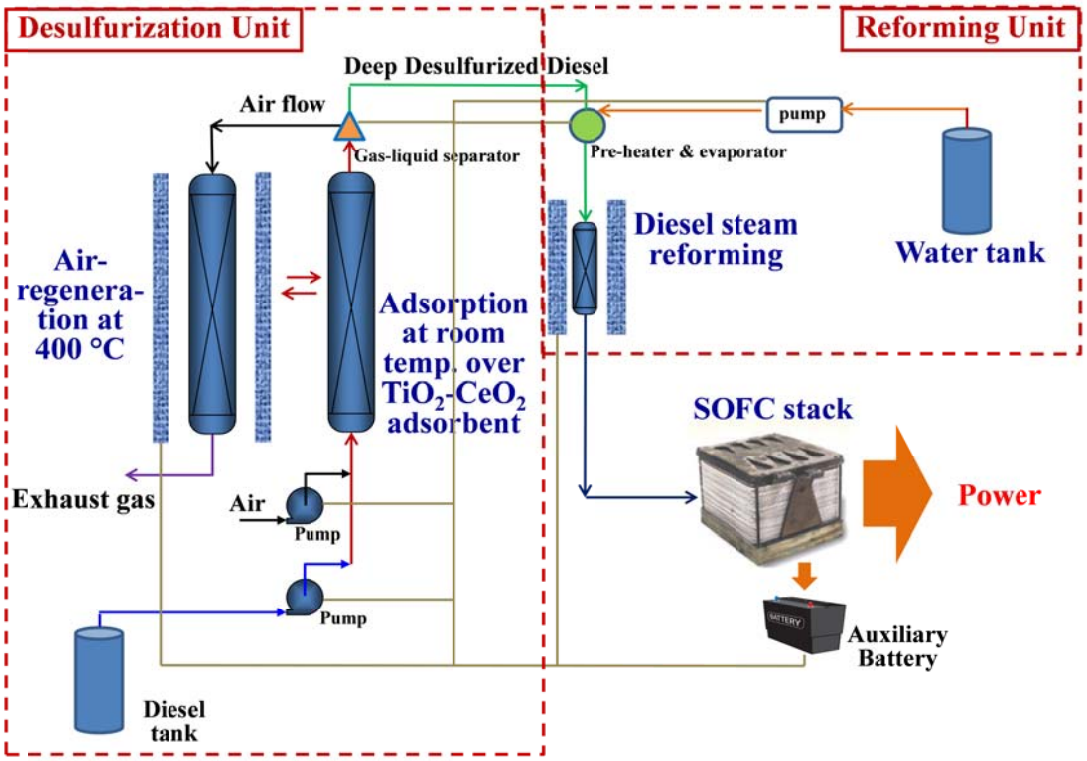

Figure 149. The conceptual design of the diesel fuel processor utilizing the developed air-regenerable TiO_2-CeO_2 mixed oxide adsorbent for deep desulfurization and the highly carbon-resistant and sulfur-tolerant Fe-Ni based catalyst for diesel steam reforming for SOFCs.

In this conceptual design,the diesel fuel processor involves two units, i.e., the desulfurization unit and the reforming unit. The air-regenerable TiO_2-CeO_2 mixed oxide adsorbent for deep desulfurization of diesel fuel down to below 1 ppm and the highly carbon-resistant and sulfur-tolerant Fe-Ni based catalyst for diesel steam reforming developed in this project are applied in the desulfurization unit and the reforming unit, respectively.

In the desulfurization unit, the diesel fuel is pumped into the adsorption column, which is loaded with the TiO_2-CeO_2 mixed oxide adsorbent with air flowing. The adsorptive desulfurization is performed at room temperature. After desulfurization, the products pass through a gas-liquid separation unit. The cleaned diesel fuel is then delivered to the reforming unit. At the same time, the air flow is circulated back to the adsorbent regeneration unit, which is operated at a temperature of 400 °C. The fresh TiO_2-CeO_2 mixed oxide adsorbent is first operated in the desulfurization chamber. After certain time of operation (on the basis of adsorbent performance for sulfur removal at 1 ppmw level), the spent adsorbent is then switched to the regeneration chamber, where the spent adsorbent will be completely regenerated by air at 400 °C and the adsorption capacity for sulfur will be fully recovered. The regenerated adsorbent is then switched back to the desulfurization chamber for further cycles. In that way, the TiO_2-CeO_2 mixed oxide adsorbent can be continuously operated on site for a long time. No manually operation is needed for the desulfurization unit until the adsorbent material has to be replaced.

The cleaned diesel fuel from the desulfurization unit normally contains sulfur content less than 1 ppmw and enters the reforming unit. At the preheater, the liquid diesel fuel is heated up and evaporated. At the same time, the diesel vapor is mixed with the steam, which is provided by a pump through a pre-installed water tank and generated in situ in the preheater. The pre-mixed diesel vapor and steam then reacts over the Fe-Ni based reforming catalyst at 800 °C, producing a hydrogen rich reformate gas with low sulfur for SOFC. The SOFC stack provides the power for various usages. The Fe-Ni catalyst is proven to be highly carbon-resistant and sulfur-tolerant, thus can be operated a long time before replacement. Consequently, in the processor, the reforming catalyst may be optimized so that it can be replaced during the schedule maintenance service.

It should be pointed out that the energy required for the adsorbent regeneration unit and the reforming reactor in the diesel fuel processor is self-supported in this design by incorporating a secondary battery. The battery is initially charged ex situ and provides the power for the starting of the processor. When the processor is under running condition, the battery can be fully charged by the SOFC stack and continuously supply the energy needed for the adsorbent regeneration chamber, the steam reforming reactor and other parts.

3. Design Test Platforms to Evaluate Fuel Processing Technology

3.1. Test on button cells

Based on the report provided by Delphi in regards to the work carried out on button cells, it was understood that it was quite similar to the experiments conducted at Penn State. The testing process was initiated with pure hydrogen to mainly check if the experiment rigs and other related electrochemical equipments were according to the specifications and requirements from Delphi. Earlier, the suggested process which was employed for constructing the Membrane Electrode Assembly (MEA) with the button cell, was according to PSU methodologies. But after Delphi provided assistance in a few of the accessories necessary for MEA preparation in a better and sophisticated way, the new recipe was also used at PSU. The simulated reformate composition was decided mutually by Delphi and PSU and initial testing was accomplished to

make sure we get cell performance at acceptable levels for long term testing. Delphi decided on the cell conditioning procedure before testing of the inorganic contaminants and the same process was accepted and followed at PSU. The initial concentration levels which were selected for the contaminants were as follows:

1. H_2S - 500 ppb 1 ppm 5 ppm
2. Siloxane - 20 ppm 50 ppm 100 ppm
3. Chlorine - 20 ppm 50 ppm 100 ppm
4. Ammonia - 20 ppm 50 ppm 100 ppm

Except siloxane the rest of the three contaminants were tested according to the pre-determined concentration levels. Upon recommendation of PSU based on the results obtained, it was concluded that the specified levels were too high for siloxane. The tests were conducted at Delphi too and was confirmed and a much lower concentration range was decided for siloxane by both parties. In terms of the electrochemical measurements, both groups have used Electrochemical Impedance Spectroscopy (EIS) and Polarization curves to understand the performance and degradation characteristics of the button cell. In addition to the above mentioned techniques, PSU has used a relatively new technique called Electrochemical Frequency Modulation (EFM) to understand more about the kinetics of the electrochemical reactions and its dependency and relation with the degradation dynamics for the button cells under varied operating conditions. The general conclusions until now are similar which both Delphi and PSU have obtained.

The evaluation of Delphi's fuel cell performance, subjected to four contaminants at varying levels of each contaminant

---

Experimental:

All SOFC's tested were Ni-YSZ anode supported cell formats. The anode side current collector is made from a Ni mesh with four platinum (Pt) wires attached. The cathode current collector is made from silver (Ag) mesh with four Pt wires attached. The samples were installed in an alumina tube with a glass seal to separate the anode and cathode gasses. Anode gas used to reduce and perform baseline test was comprised of 0.5LPM H_2 and 0.5LPM N_2, the cathode gas used was 0.25LPM of air. The sequence of operations was as follows:

- Seal the button cell in the test stand
- Reduce the anode in 50%H_2/50%N_2 for two hours at 750C
- Measure impedance at 700 mv and 800 mV, IV sweep from OCV to 0.6V.
- Soak in 50%H_2/50%N_2 for 24 hrs. @0.6A/cm^2
- Measure impedance at 700 mv and 800 mV, IV sweep from OCV to 0.6V.
- Soak in reformate (H_2 50%, CH_4 3%, CO_2 22%, N_2 20%, H_2O 5%) for 24 hrs. @0.6A/cm^2
- Add contaminant for up to 100 hours to stabilize
- Measure impedance at 700 mv and 800 mV, IV sweep to 0.4V
- End of test

Contaminants used:

- Sulfur: Introduced as H_2S gas with N_2 as its carrier gas.
- Ammonia: introduced as NH_3 gas with N_2 as its carrier gas.

- Halides: Tetrachloroethylene was introduced by bubbling N_2 through the liquid.
- Siloxanes: Decamethylcyclopentasiloxane was introduced by bubbling N_2 through the liquid.

Baseline Cell Testing

Figure 150 shows that the baseline cell exhibited very little degradation during soaking. After the cell was put on reformate, it had a 2% step reduction in power from 466 mW to 456 mW, which is common for the fuel cell due to the reduction in H_2. The graph of electrochemical impedance spectra in **Figure 151** indicates the polar resistance had increased very little. Some of the increase was caused by switching from $50H_2/50N_2$ to reformate.

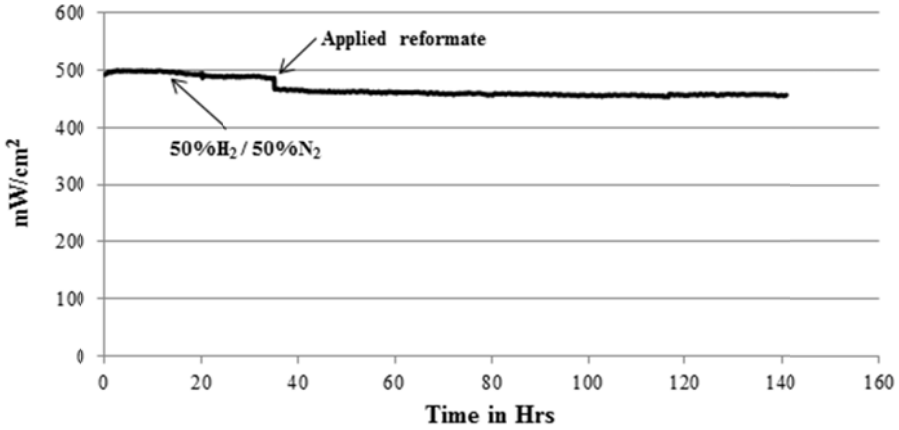

Figure 150. Baseline button cell performance during constant current soak.

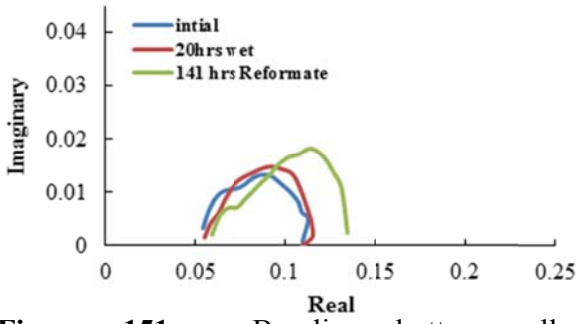

Figure 151. Baseline button cell electrochemical impedance at 800mV.

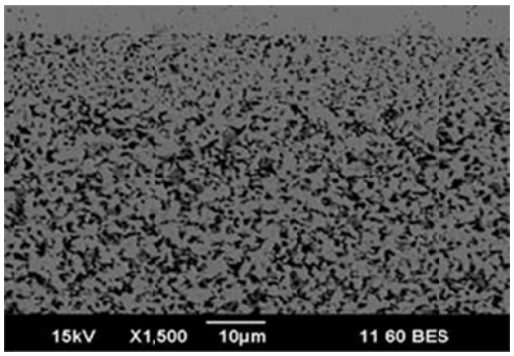

Figure 152. Baseline anode morphology.

SEM examination of the baseline bulk anode (**Figure 152**) showed no unusual morphology.

Sulfur contamination:

The graph in **Figure 153** shows the degradation of the cell due to H_2S poisoning. As the concentration of H_2S increases, the power decreases. This is due to the blockage of the active nickel sites in the anode layer and (potentially) the formation of nickel sulfides. The power outage, seen at 275 hours, shows that when the H_2S was stopped the cell power recovered to some degree. In **Figure 154**, the electrochemical impedance spectra show the polarization

resistance had increased as the H_2S concentrations increased. Also it can be seen that the Ohmic resistance had not increased significantly.

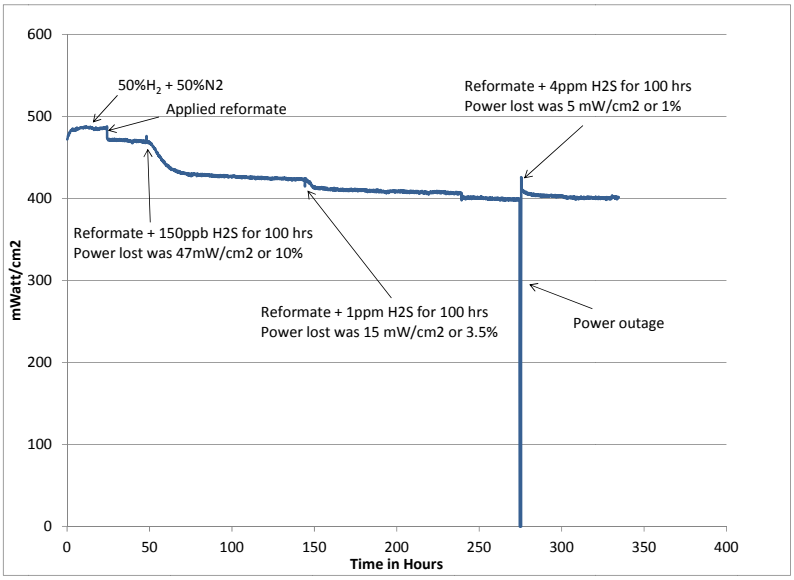

Figure 153. Cell power reduction with increasing H_2S concentration.

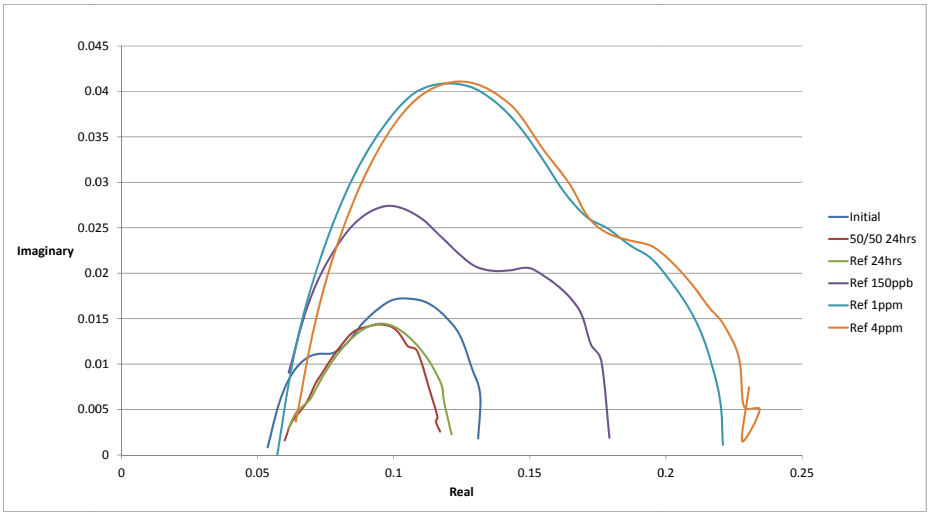

Figure 154. Electrochemical impedance spectra at 800mV with increasing H_2S concentration.

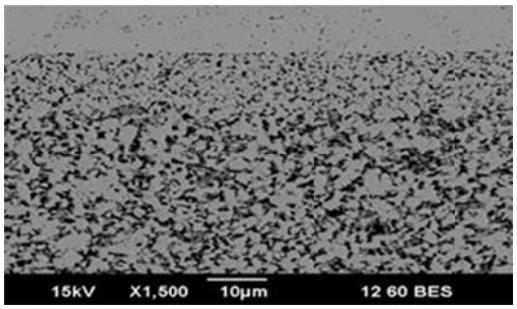

Figure 155. Anode morphology after H_2S exposure.

SEM examination (**Figure 155**) of the sulfur contaminated bulk anode showed no unusual morphology. Sulfur could not be detected by our SEM.

Ammonia contamination:

Figure 156 shows that up to 100 ppm of ammonia had very little effect on the cell power. Ammonia will convert to N_2 and H_2 when heated. The graph of electrochemical impedance spectra (**Figure 157**) shows that the polar resistance changes were relatively small.

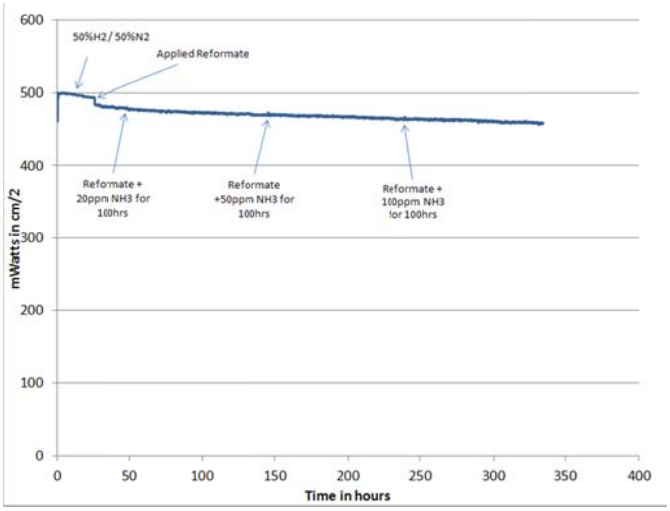

Figure 156. Cell power reduction with increasing ammonia concentration.

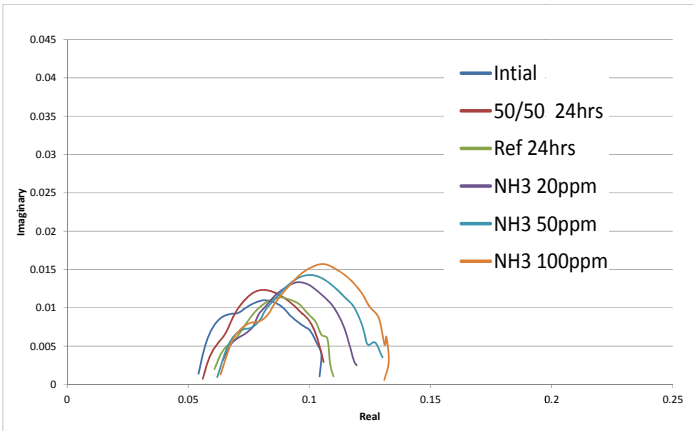

Figure 157. Electrochemical impedance with increasing ammonia concentration.

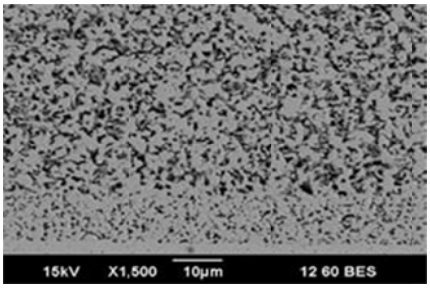

Figure 158. Anode morphology after exposure to ammonia.

SEM examination of the Ammonia contaminated bulk anode (**Figure 158**) showed no unusual morphology.

Halides

Figure 159 shows that tetrachloroethylene introduced to reformate at 100 ppm or less has very little effect on the cell. In the graph of **Figure 159** the electrochemical impedance spectra show that the polar resistance changes were also relatively small.

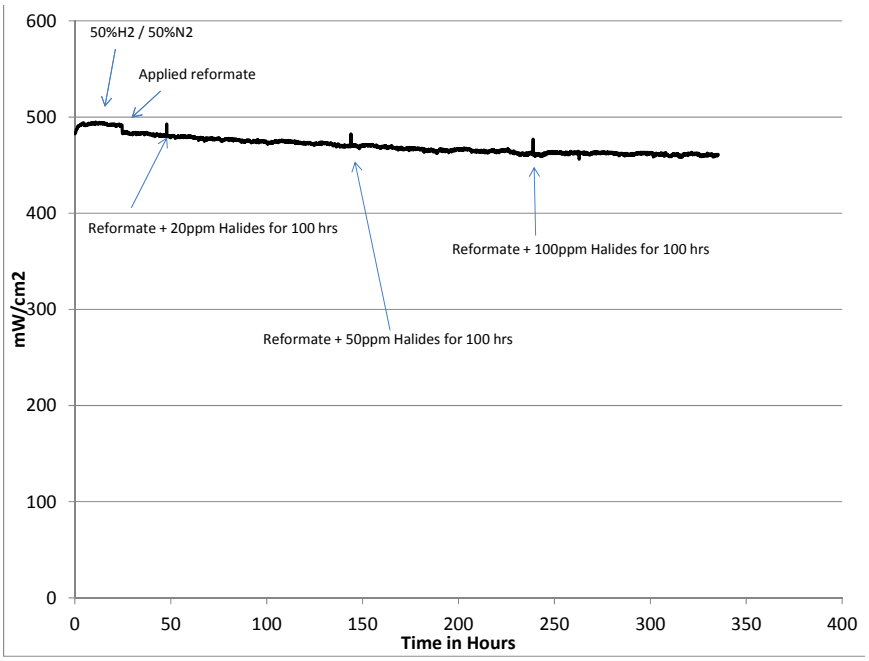

Figure 159. Cell power reduction with increasing tetrachloroethylene concentration.

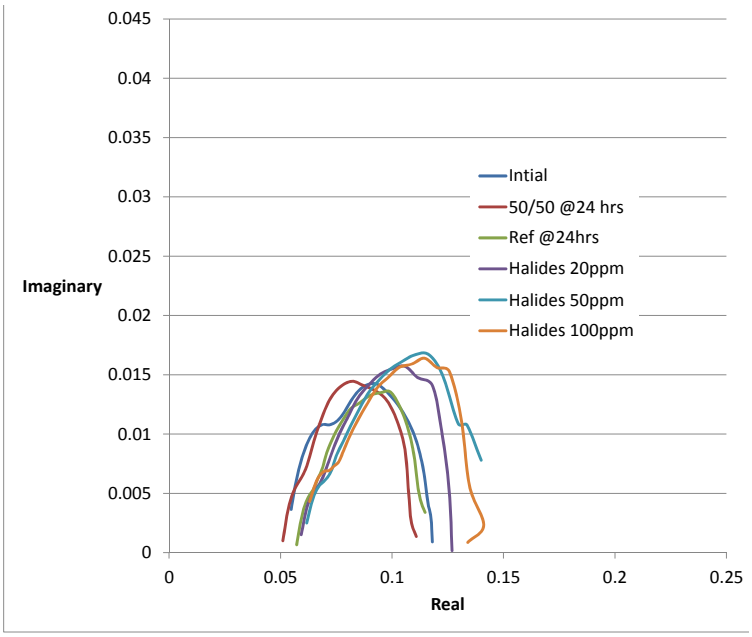

Figure 160. Electrochemical impedance with increasing tetrachloroethylene concentration.

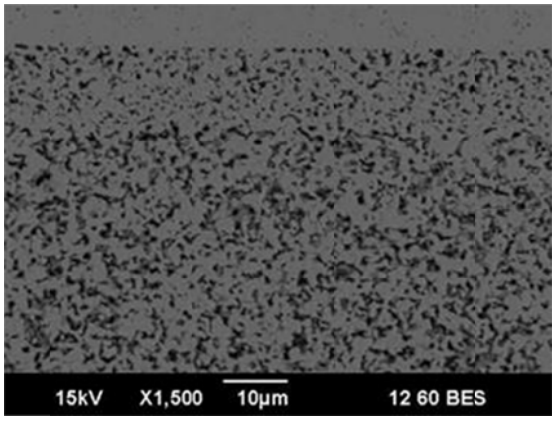

Figure 161. Anode morphology after exposure to tetrachloroethylene.

SEM examination of the tetrachloroethylene contaminated bulk anode (**Figure 161**) showed no unusual morphology.

Siloxanes:

Figure 162 shows that decamethylcyclopentasiloxane introduced to reformate at 1ppm or less has very little effect on the cell. Degradation increased when the concentration increased to the 2 ppm level, and more at the 3 ppm level. In the graph of the electrochemical impedance spectra (**Figure 163**), the polar resistance changes were small up to 2 ppm, with the 3 ppm level causing the most significant change compared to the baseline.

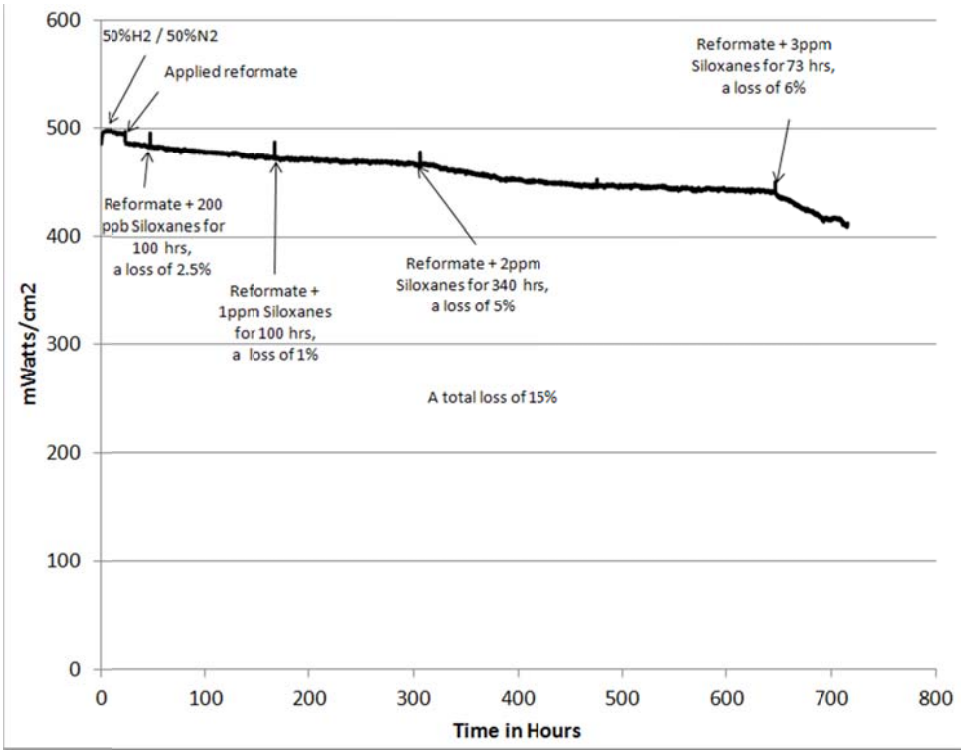

Figure 162. Cell power reduction with increasing decamethylcyclopentasiloxane concentration.

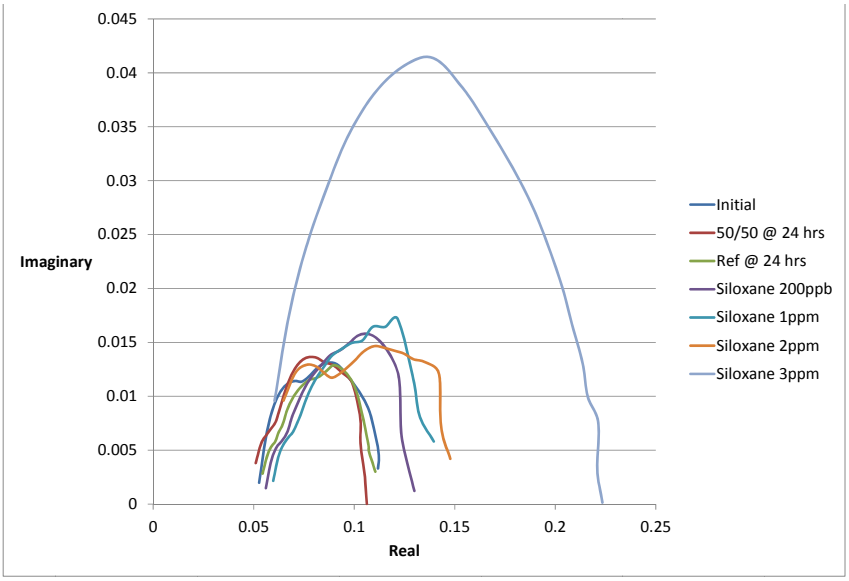

Figure 163. Electrochemical impedance spectra.

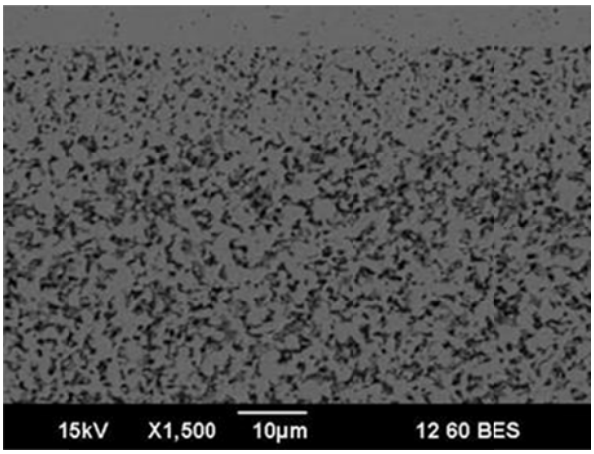

Figure 164. Anode morphology after exposure to decamethylcyclopentasiloxane.

SEM examination of the decamethylcyclopentasiloxane contaminated bulk anode (**Figure 164**) showed no unusual morphology.

Summary:

A 2.5 cm^2 SOFC button cell test platform was used to test four different contaminants with increasing concentrations. Sulfur, ammonia, halides, and siloxanes are contaminants typically found in biogas. Ammonia and the halide tested did not degrade the cell power of the button cell up to 100 ppm during the testing. Sulfur was found to degrade the cell but could be tolerated below the 200 ppb level. Sulfur is known to reduce the efficiency of the cell and over the long term may result in degraded performance, even at concentrations below 200 ppb. Siloxanes also could be tolerated in concentrations below 200 ppb. However, siloxanes also could deteriorate the cell further over the long term exposure. Post test SEM examination of the cells' bulk anodes showed no unusual morphology.

Recommendation:

It is recommended that sulfur and siloxanes be removed from the biogas fuel feed in order for the Delphi fuel cell stack to operate at its peak performance for extended periods.

3.2. Test on Delphi Gen 4 stack

Delphi also settled up and conducted the stack test using 5 different fuel compositions. Delphi built the Gen 4 solid oxide fuel cell stack, tested the stack under conditions agreed upon by Delphi and Penn State, and then correlated with/provided confirmation of the stack performance data generated by Penn State on commercial diesel fuel simulated reformate. Delphi first generate initial performance curves (IV curves) on a standard fuel composition (humidified 50% H_2-50% N_2) and constant current tests on the agreed upon fuel composition to correlate with Penn State testing, measure the fuel utilization of the stack, and characterize performance at conditions agreed upon between Penn State and Delphi. The testing was completed on 2 Gen 4 stacks and ran 1 hour constant current at each of the test points. Stack was run with constant fuel blend and internal temperature for each test point. The detailed test results are reported as follows.

Gen 4 Stack Test 1

Table 37 lists the each 5 testing conditions agreed upon between Penn State and Delphi performed for the first test on the Delphi Gen 4 stack. The obtained power density and mean voltage results are shown in **Figure 165-167**.

Table 37. The 5 testing conditions agreed upon between Penn State and Delphi performed for the first test on the Delphi Gen 4 stack.

	Fuel 1		Fuel 2		Fuel 3		Fuel 4		Fuel 5	
Gas	Gas %	SLPM	Gas %	SLPM	Gas %	SLPM	Gas %	SLPM	Gas %	SLPM
H2	48.5%	83.97	30.0%	43.18	40.0%	62.38	25.0%	38.17	10.0%	13.99
CO	0.0%	0.00	20.0%	28.79	10.0%	15.59	10.0%	15.27	10.0%	13.99
CH4	0.0%	0.00	0.0%	0.00	0.0%	0.00	5.0%	7.63	10.0%	13.99
CO2	0.0%	0.00	0.0%	0.00	25.0%	38.98	30.0%	45.80	30.0%	41.98
H2O	3.0%	5.19	50.0%	71.97	25.0%	38.98	30.0%	45.80	40.0%	55.98
N2	48.5%	83.97	0.0%	0.00	0.0%	0.00	30.0%	45.80	0.0%	41.98
Total	100.0%	173.13	100.0%	143.94	100.0%	155.94	100.0%	152.67	100.0%	139.95
Current	140.00		120.00		130.00		140.00		140.00	
Utilization	50.0%		50.0%		50.0%		50.0%		50.0%	
Time (hrs)	1.00		1.00		1.00		1.00		1.00	

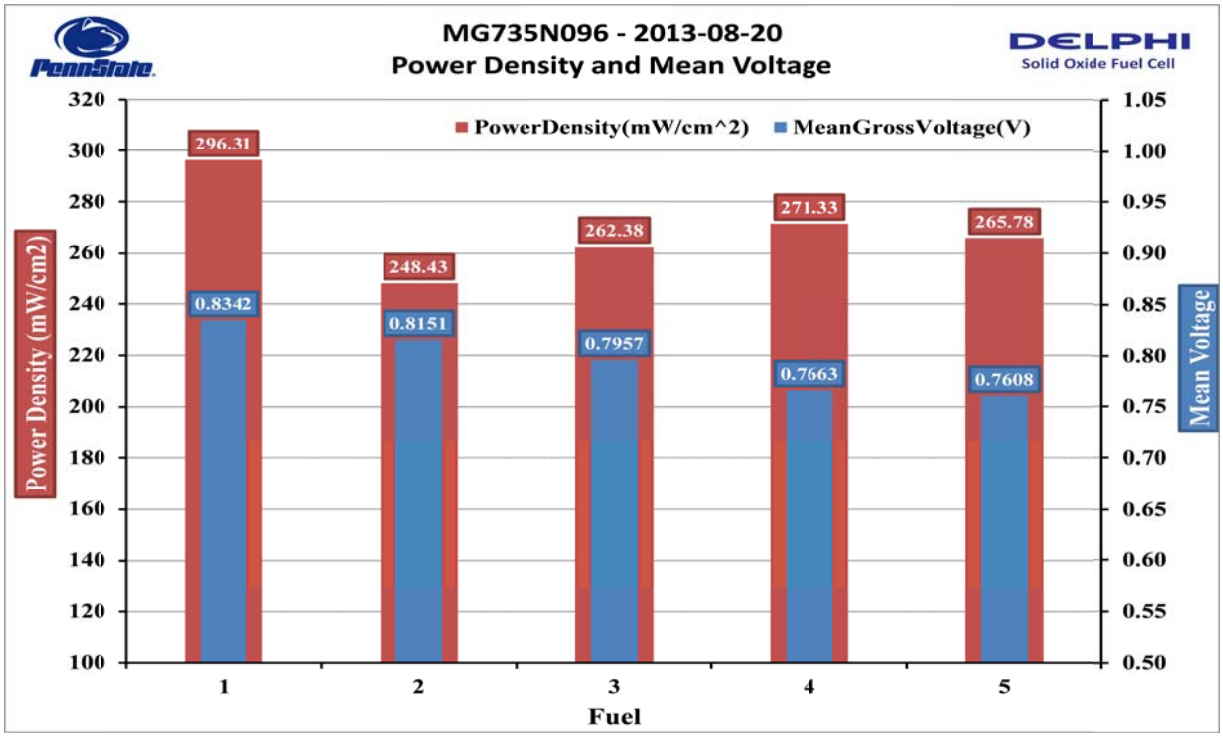

Figure 165. Summary of power density and mean voltage generated from the stack in the first test.

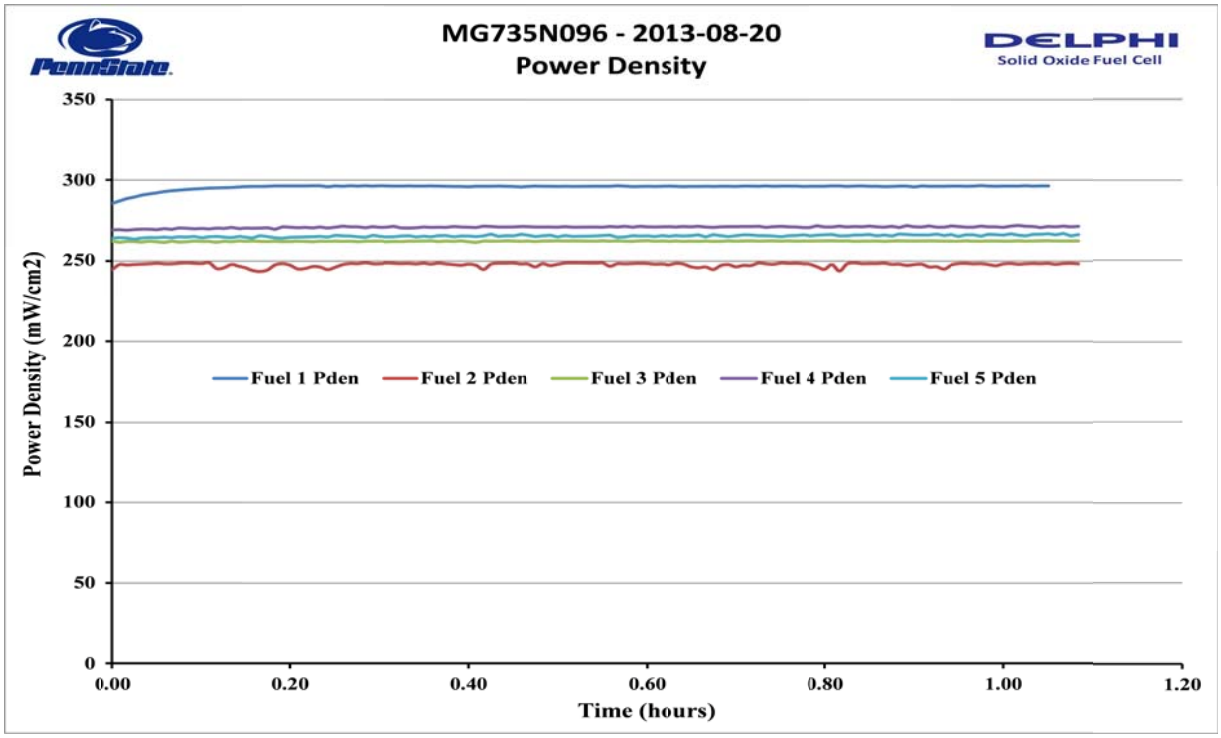

Figure 166. The power density as a function of run time generated from the stack in the first test.

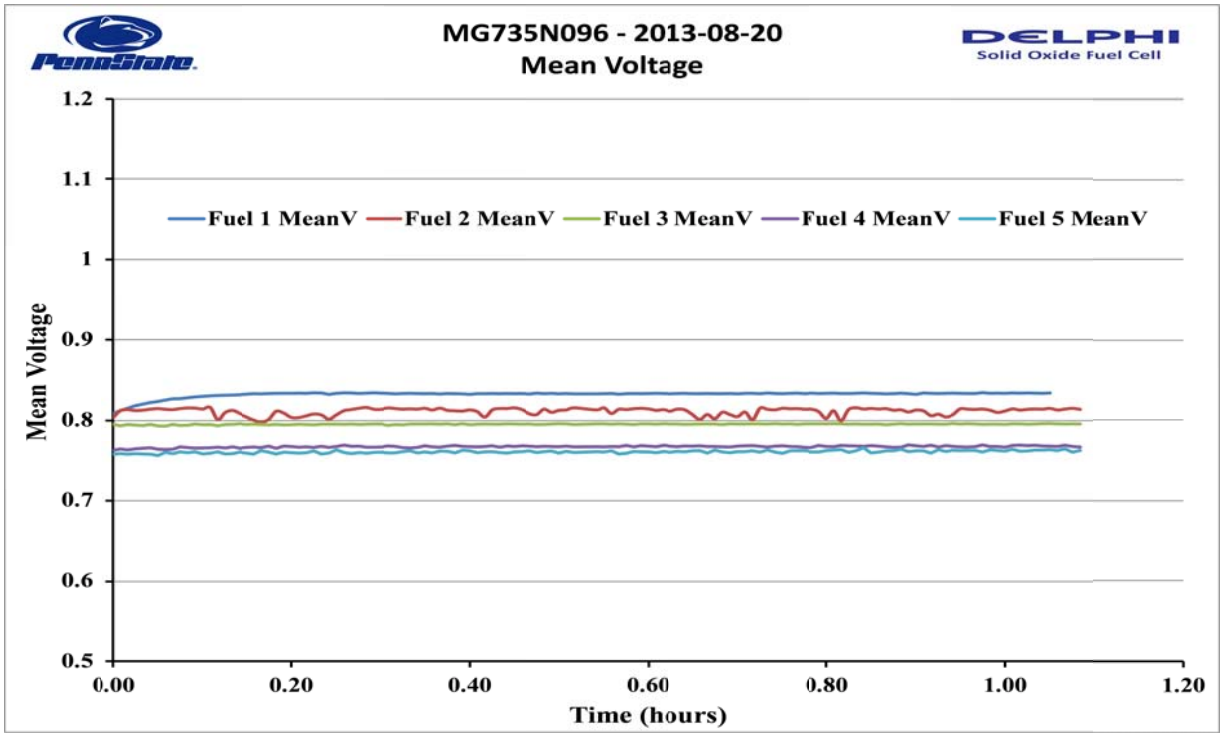

Figure 167. The mean voltage as a function of run time generated from the stack in the first test.

Gen 4 Stack Test 2

Table 38 lists the each 5 testing conditions agreed upon between Penn State and Delphi performed for the first test on the Delphi Gen 4 stack. The obtained power density and mean voltage results are shown in **Figure 168-171**.

Table 38. The 5 testing conditions agreed upon between Penn State and Delphi performed for the second test on the Delphi Gen 4 stack.

	Fuel 1		Fuel 2		Fuel 3		Fuel 4		Fuel 5	
Gas	Gas %	SLPM	Gas %	SLPM	Gas %	SLPM	Gas %	SLPM	Gas %	SLPM
H2	48.5%	63.01	30.0%	37.80	40.0%	50.40	25.0%	28.64	10.0%	10.50
CO	0.0%	0.00	20.0%	25.20	10.0%	12.60	10.0%	11.46	10.0%	10.50
CH4	0.0%	0.00	0.0%	0.00	0.0%	0.00	5.0%	5.73	10.0%	10.50
CO2	0.0%	0.00	0.0%	0.00	25.0%	31.50	30.0%	34.37	30.0%	31.50
H2O	3.0%	3.90	50.0%	63.01	25.0%	31.50	30.0%	34.37	40.0%	42.00
N2	48.5%	63.01	0.0%	0.00	0.0%	0.00	30.0%	0.00	0.0%	0.00
Total	100.0%	129.91	100.0%	126.01	100.0%	126.01	100.0%	114.56	100.0%	105.01
Current	140.00		140.00		140.00		140.00		140.00	
Utilization	50.0%		50.0%		50.0%		50.0%		50.0%	
Time (hrs)	1.00		1.00		1.00		1.00		1.00	
OCV (V)	1.080		0.956		0.975		0.988		0.973	

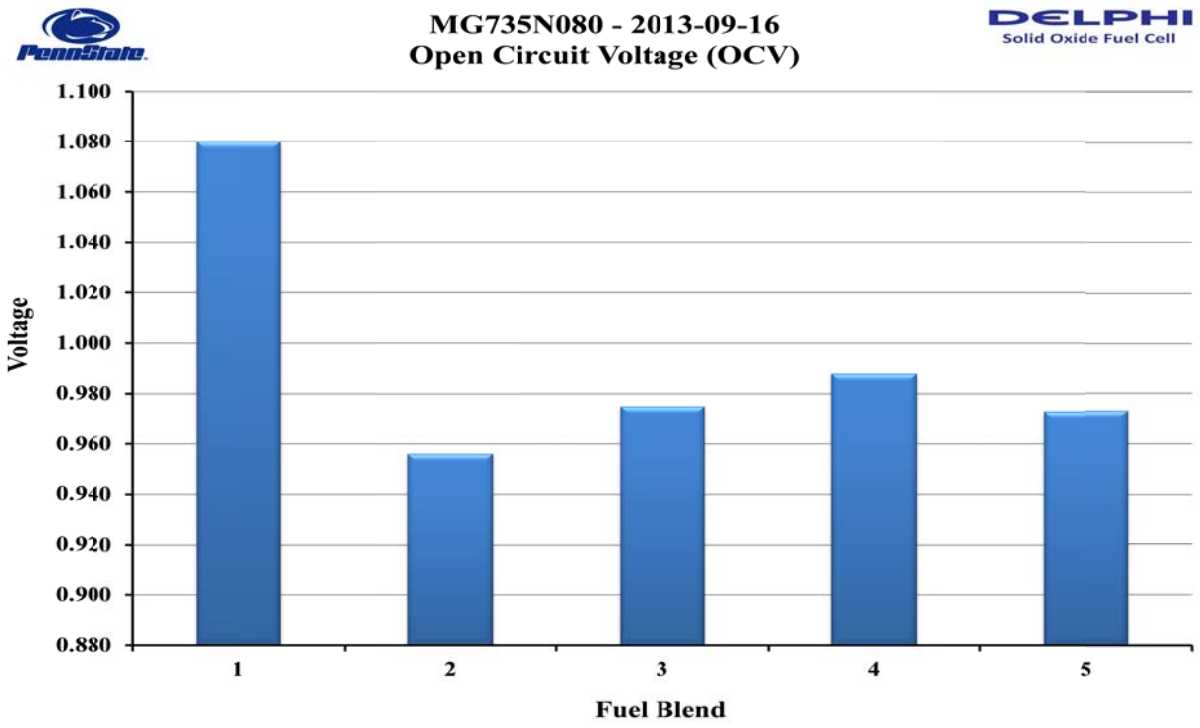

Figure 168. The open circuit voltage (OCV) results generated from the stack in the second test.

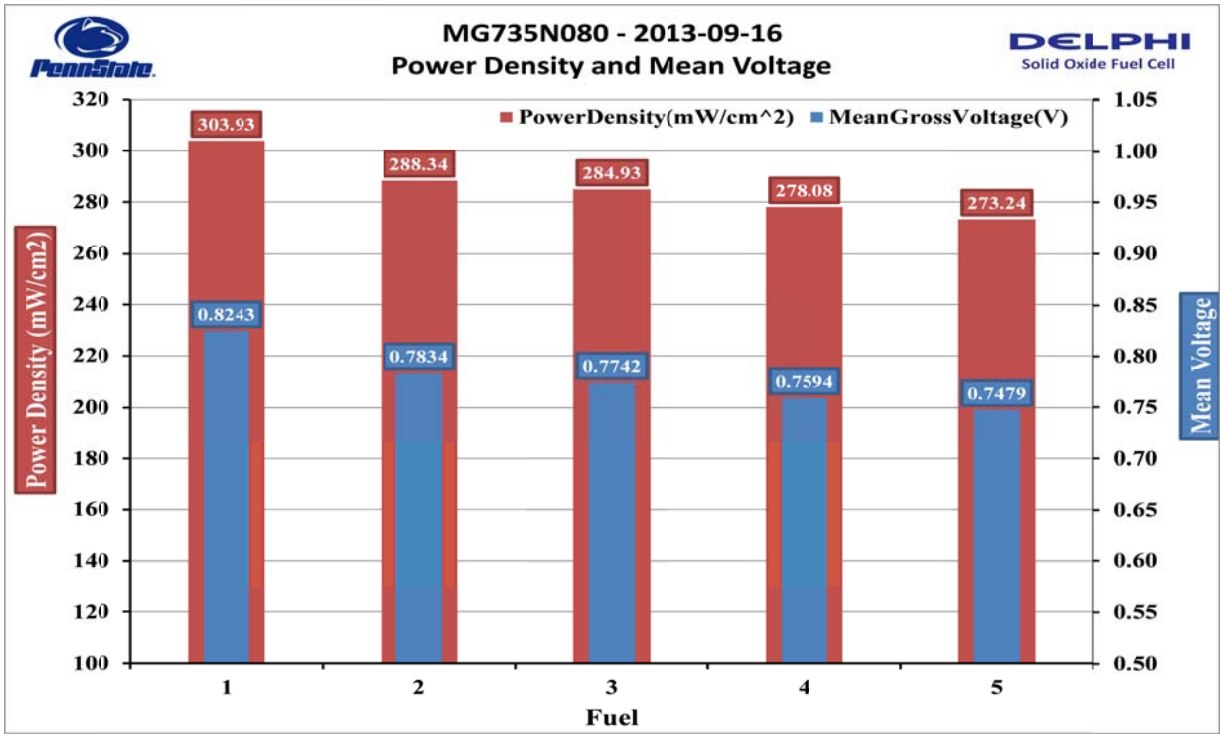

Figure 169. Summary of power density and mean voltage generated from the stack in the second test.

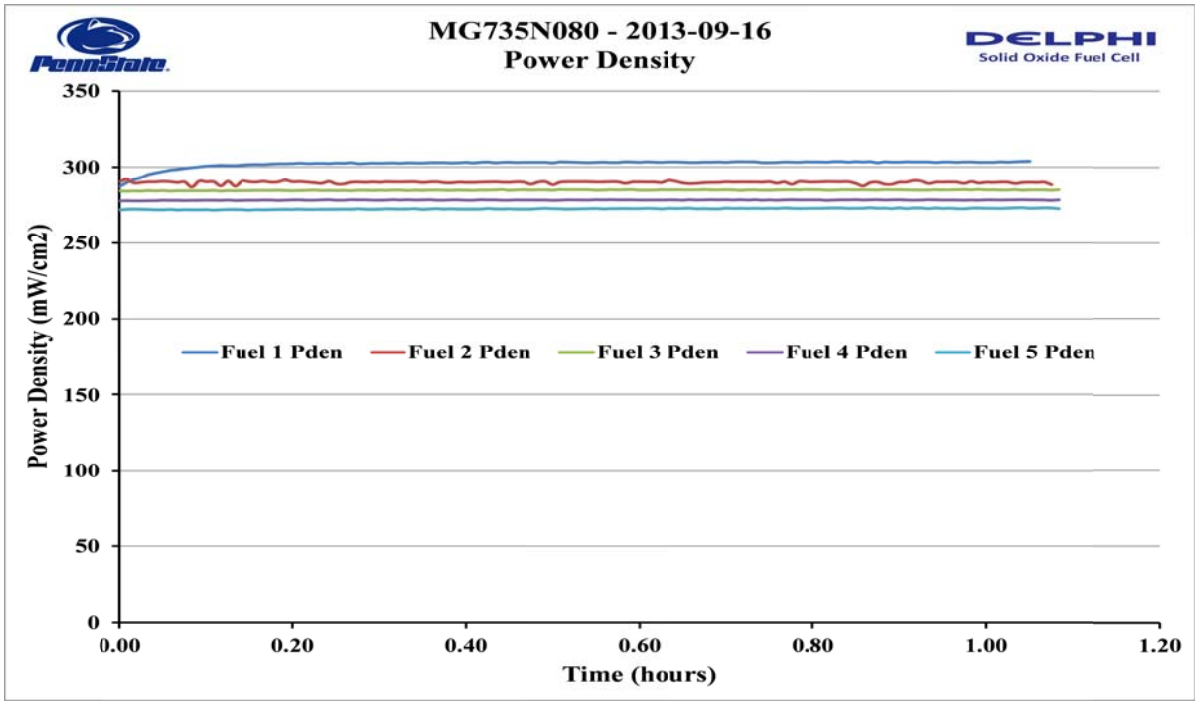

Figure 170. The power density as a function of run time generated from the stack in the second test.

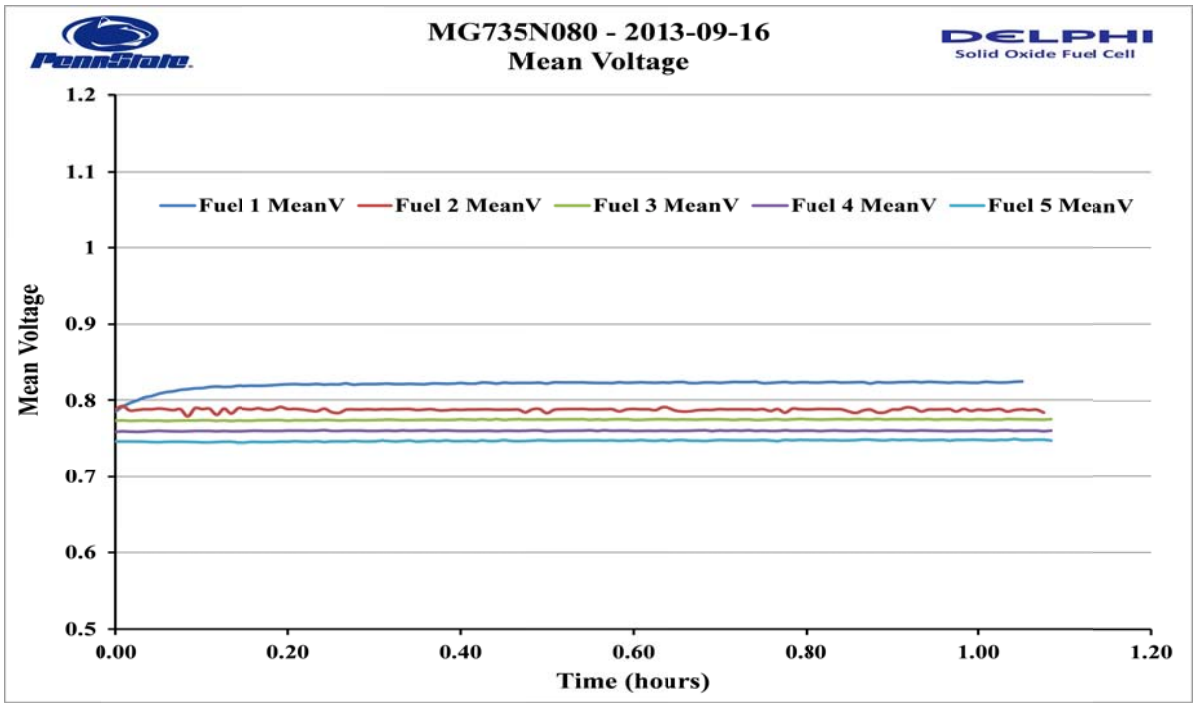

Figure 171. The mean voltage as a function of run time generated from the stack in the second test.

Gen 4 Stack Test Comparison

Table 39 compares the testing conditions conducted for 2 tests on the Delphi Gen 4 stack. During Test 1, the current had to be lowered for Fuel-2 and Fuel-3 due to higher internal temperature. Fuel-2 and Fuel-3 aren't compared due to the differences in the test conditions. **Figure 172-174** shows the comparison in power density and mean voltage for the two tests on the Gen 4 Stack with the fuel composition of Fuel-1, Fuel-4 and Fuel-5.

Table 39. The comparison of 5 testing conditions performed for the two tests on the Delphi Gen 4 stack.

Test 1 Points

	Fuel 1		Fuel 2		Fuel 3		Fuel 4		Fuel 5	
Gas	Gas %	SLPM	Gas %	SLPM	Gas %	SLPM	Gas %	SLPM	Gas %	SLPM
H2	48.5%	83.97	30.0%	43.18	40.0%	62.38	25.0%	38.17	10.0%	13.99
CO	0.0%	0.00	20.0%	28.79	10.0%	15.59	10.0%	15.27	10.0%	13.99
CH4	0.0%	0.00	0.0%	0.00	0.0%	0.00	5.0%	7.63	10.0%	13.99
CO2	0.0%	0.00	0.0%	0.00	25.0%	38.98	30.0%	45.80	30.0%	41.98
H2O	3.0%	5.19	50.0%	71.97	25.0%	38.98	30.0%	45.80	40.0%	55.98
N2	48.5%	83.97	0.0%	0.00	0.0%	0.00	30.0%	45.80	0.0%	41.98
Total	100.0%	173.13	100.0%	143.94	100.0%	155.94	100.0%	152.67	100.0%	139.95
Current	140.00		120.00		130.00		140.00		140.00	
Utilization	50.0%		50.0%		50.0%		50.0%		50.0%	
Time (hrs)	1.00		1.00		1.00		1.00		1.00	

Test 2 Points

	Fuel 1		Fuel 2		Fuel 3		Fuel 4		Fuel 5	
Gas	Gas %	SLPM	Gas %	SLPM	Gas %	SLPM	Gas %	SLPM	Gas %	SLPM
H2	48.5%	63.01	30.0%	37.80	40.0%	50.40	25.0%	28.64	10.0%	10.50
CO	0.0%	0.00	20.0%	25.20	10.0%	12.60	10.0%	11.46	10.0%	10.50
CH4	0.0%	0.00	0.0%	0.00	0.0%	0.00	5.0%	5.73	10.0%	10.50
CO2	0.0%	0.00	0.0%	0.00	25.0%	31.50	30.0%	34.37	30.0%	31.50
H2O	3.0%	3.90	50.0%	63.01	25.0%	31.50	30.0%	34.37	40.0%	42.00
N2	48.5%	63.01	0.0%	0.00	0.0%	0.00	30.0%	0.00	0.0%	0.00
Total	100.0%	129.91	100.0%	126.01	100.0%	126.01	100.0%	114.56	100.0%	105.01
Current	140.00		140.00		140.00		140.00		140.00	
Utilization	50.0%		50.0%		50.0%		50.0%		50.0%	
Time (hrs)	1.00		1.00		1.00		1.00		1.00	
OCV (V)	1.080		0.956		0.975		0.988		0.973	

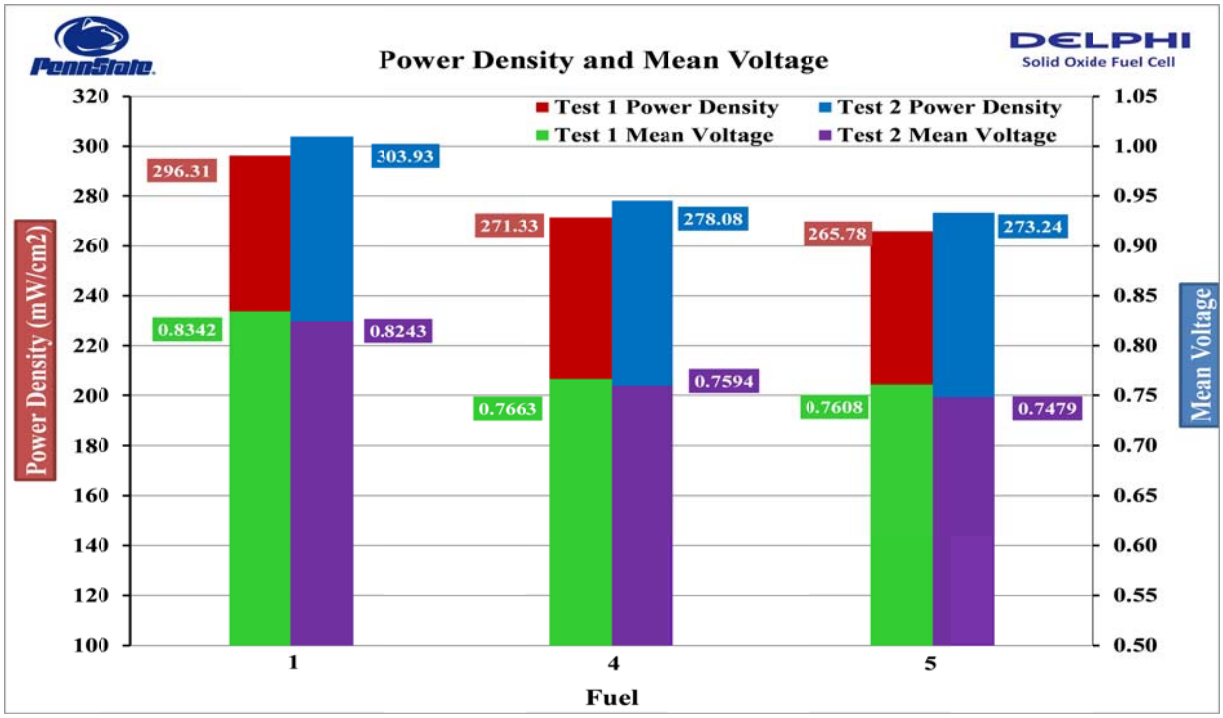

Figure 172. Comparison in power density and mean voltage for the two tests on Gen 4 Stack with the fuel composition of Fuel-1, Fuel-4 and Fuel-5.

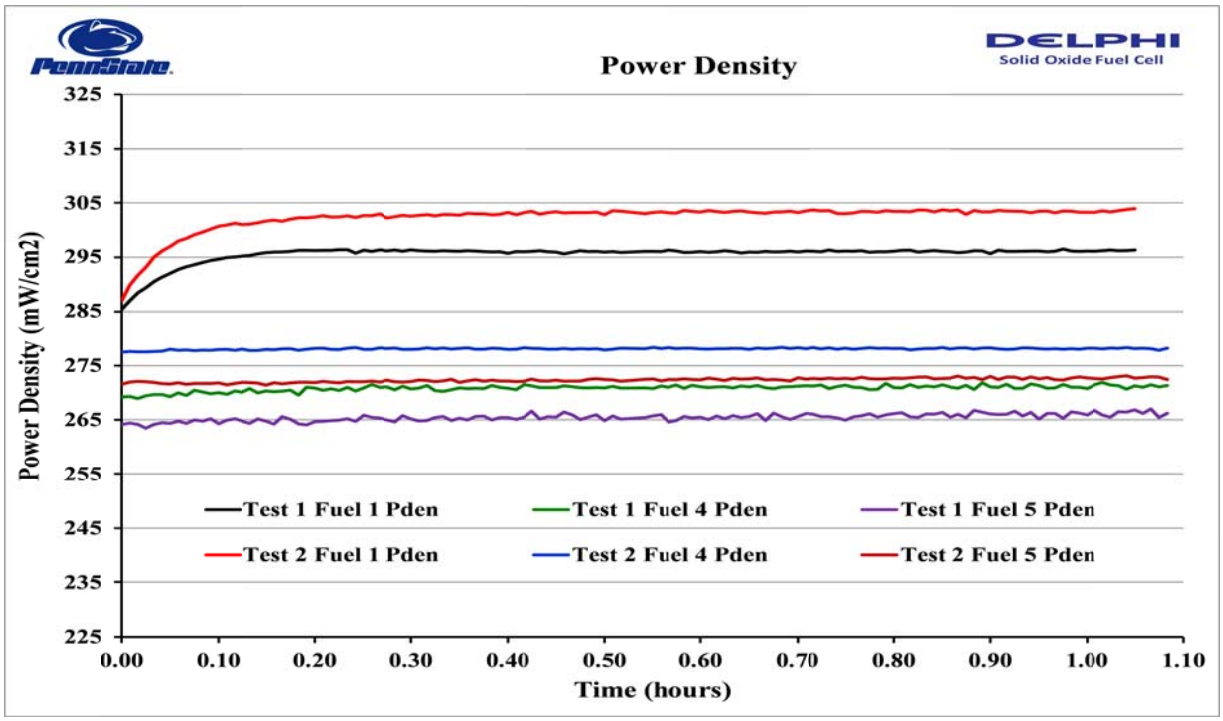

Figure 173. Comparison in power density as a function of run time for the two tests on Gen 4 Stack with the fuel composition of Fuel-1, Fuel-4 and Fuel-5.

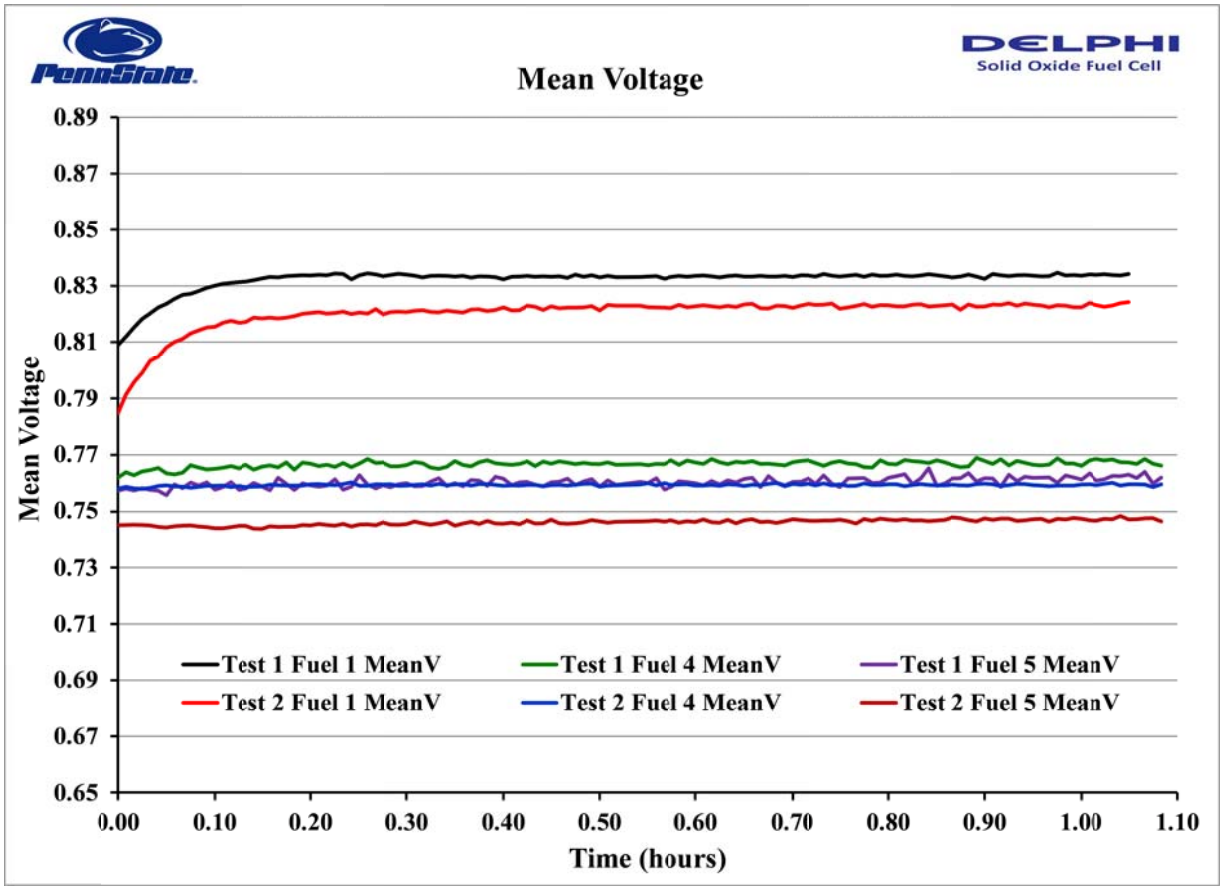

Figure 174. Comparison in mean voltage as a function of run time for the two tests on Gen 4 Stack with the fuel composition of Fuel-1, Fuel-4 and Fuel-5.

E. References

[1] Modern Aspects of Electrochemistry, B. E. Conway, J. Bockris, and R.E. White, Edts., Kluwer Academic/Plenum Publishers, New York, 1999, Vol. 32, p. 143-248.

[2] Electrochemical impedance spectroscopy theory, www.gamry.com.

[3] A.J.Bard, L.R. Faulkner, Electrochemical Methods, Fundamentals and Applications, John Wiley&Sons, Inc. 2001 2nd Ed.

[4] X. Yuan, H. Wang, J. C. Sun, J. Zhang, Int. J. Hydrogen Energy 32 (2007) 4365.

[5] Q.-A. Huang, R. Hui, B. Wang, J. Zhang, Electrochim. Acta, 52 (2007) 8144.

[6] A. Barbucci, M. Carpanese, A. Reverberi, G. Cerisola, M. Blanes, P. Luis Cabot, M. Viviani, A. Bertei, C. Nicolella, J. Appl. Electrochem., 38 (2008) 939.

[7] J.P. Trembly, R.S. Gemmena, and D.J. Bayless, J. Power Sources (2007) 171 818–825.

[8] J.R. Wilson, D.T. Schwartz, and S.B. Adler, Electrochim. Acta (2006) 151, 389–1402.

[9] D.Z. de Florio, R. Muccillo, V. Esposito, E. Di Bartolomeo, and E. Traversab, J. Electrochem. Soc. (2005) 152 A88.

[10] A. Hagen, R. Barfod, P.V. Hendriken, Y.-L. Liu, and S. Ramousse, J. Electrochem. Soc. (2006) 153, 6, A1165

[11] H. Zhu and R.J. Kee, J. Electrochem. Soc. (2006) 153, 9, A1765

[12] M.J.L. Østerrgard, and M. Mogensen, Electrochim. Acta, (1993) 38, 2015.

[13] M.J. Jørgensen, and M. Mogensen, J. Electrochem. Soc. (2001) 148, 5, A433.

[14] S. McIntosh, S.B. Adler, J.M. Vohs, and R.J. Gorte, Electrochem. Solid-State Lett. (2004) 7, 5, A111.

[15] E. P. Murray, T. Tsai, S.A. Barnett, Solid State Ionics (1998) 110, 235.

[16] Jiang, Y. and Virkar, A.V., J. Electrochem. Soc., 148 A706-A709 (2001).

[17] Saunders, G.J., Preece, J., and Kendall, K., J. Power Sources, 131, 23-26 (2004).

[18] Kendall, K., Slinn, M., and Preece, J., J. Power Sources, 157, 750-753 (2006).

[19] Gupta, G.K., Dean, A.M., Ahn, K., and Gorte, R.J., J. Power Sources, 158 497–503 (2006)

[20] A. Leonide, V. Sonn, A. Weber, and E. Ivers-Tiffee, J. Electrochem. Soc., 155, B36 (2008).

[21] V. Sonn., A. Leonide, and E. Ivers-Tiffee, J. Electrochem. Soc., 155, B675 (2008).

[22] S McIntosh, J.M. Vohs, and R.J. Gorte, J. Electrochem. Soc., 150 (10) A1305-A1312 (2003).

[23] Bai, P.; Wu, P.P.; Yan, Z.F.; Zhao, X.S. J. Mater. Chem. 2009, 19, 1554-1563.

[24] Wang, X.H.; Sun, T.H.; Yang, J.; Zhao, L.; Jia, J.P. Chem. Eng. J. 2008, 142, 48-55.

[25] Watanabe S; Ma, XL; Song CS. J. Phys. Chem. C 2009, 113, 14249-14257.

[26] Wang, X.; Ma, X.; Xu, X.; Sun, L.; Song, C.S. Top Catal 2008, 49, 108.

[27] Wang, X.X.; Ma, X.L.; Sun, L.; Song, C.S. Green Chem. 2007, 9, 695-702.

[28] T. Montanari, E. Finocchio, I. Bozzano, G. Garuti, A. Giordano, C. Pistarino, G. Busca, Chem. Eng. J., 2010, 165, 859-863.

[29] Ajhar, M.; Travesset, M.; Yuce, S.; Melin, T. Bioresource Technology, 2010, 101, 2913-2923.

[30] K. Oshita, Y. Ishihara, M. Takaoka, N. Takeda, T. Matsumoto, S. Morisawa, and A. Kitayama, Water Science & Technology 2010, 61(8), 2003-2012.

[31] X.X. Wang, Q.H. Zang, S.F. Yang, Y. Wang, J. Phys. Chem. B 109 (2005) 23500-23508.

[32] D. Zhao, J. Feng, Q. Huo, N. Melosh, G.H. Fredrickson, B.F. Chmelka, G.D. Stucky, Science 279 (1998) 548-552.

[33] J.G. Park, C.H. Ko, K.B. Yi, J. Park, S. Han, S. Cho, J. Kim. Appl. Catal. B: Environ. 81 (2008) 244-250.

[34] T. Schade, J.T. Andersson. *Energy & Fuels* 20 (2006) 1614-1620.
[35] T. Schade, J.T. Andersson. *Journal of Chromatography A* 1117 (2006) 206–213.
[36] X.L. Ma, K. Sakanishi, I. Mochida, Hydrodesulfurization reactivities of various sulfur compounds in diesel fuel. Ind. Eng. Chem. 33 (1994) 218–222
[37] X.L. Ma, M. Sprague, C.S. Song, Ind. Eng. Chem. Res. 44 (2005) 5768-5775
[38] H. Hu, M. Qiao, F. Xie, K. Fan, H. Lei, D. Tan, X. Bao, H. Lin, B. Zong, X. Zhang, *J. Phys. Chem. B* 109 (2005) 5186-5192.
[39] M.V. Landau, M. Herskowitz, R. Agnihotri, J.E. Kegerreis, *Ind. Eng. Chem. Res.* 47 (2008) 6904–6916.
[40] J.H. Kim, X.L. Ma, A. Zhou, C.S. Song, *Catal. Today* 111(1-2) (2006) 74-83
[41] Sundararaman R.; Ma, X.; Song, C. *Ind. Eng. Chem. Res.* ***2010***, *49,* 5561.
[42] Ma, X.; Zhou, A.; Song, C. *Catal. Today* ***2007****, 123,* 276.
[43] Jalilehvand, F. Sulfur: Not a silent element any more. *Chem. Soc. Rev.* ***2006****, 35*, 1256.
[44] N. J. Lawrence, J. R. Brewer, L. Wang, T. S. Wu, J. Wells-Kingsbury, M. M. Ihrig, G. H. Wang, Y. L. Soo, W. N. Mei and C. L. Cheung, *Nano Lett*, 2011, **11**, 2666-2671.
[45] H. Y. Kim, H. M. Lee and G. Henkelman, *J Am Chem Soc*, 2012, **134**, 1560-1570.
[46] J. Guzman, S. Carrettin and A. Corma, *J Am Chem Soc*, 2005, **127**, 3286-3287.
[47] L. Can, K. Domen, K. Maruya and T. Onishi, *J Am Chem Soc*, 1989, **111**, 7683-7687.
[48] G. Yang, L. J. Zhou, X. C. Liu, X. W. Han and X. H. Bao, *Catal Commun*, 2007, **8**, 1981-1984.
[49] M. Hussain, S. Bensaid, F. Geobaldo, G. Saracco and N. Russo, *Ind Eng Chem Res*, 2011, **50**, 2536-2543.
[50] F. M. F. Degroot, J. C. Fuggle, B. T. Thole and G. A. Sawatzky, *Phys Rev B*, 1990, **41**, 928-937.
[51] J. L. Maurice, G. Herranz, C. Colliex, I. Devos, C. Carretero, A. Barthelemy, K. Bouzehouane, S. Fusil, D. Imhoff, E. Jacquet, F. Jomard, D. Ballutaud and M. Basletic, *Epl-Europhys Lett*, 2008, **82**.
[52] M. Haneda, T. Mizushima and N. Kakuta, *J Chem Soc Faraday T*, 1995, **91**, 4459-4465.
[53] G. I. N. Waterhouse, G. A. Bowmaker and J. B. Metson, *Applied Surface Science*, 2003, **214**, 36-51.
[54] B. Yan and H. X. Zhu, *J Nanopart Res*, 2008, **10**, 1279-1285.
[55] J. Zheng, J.J. Strohm, C.S. Song, Fuel Proc. Technol. 89 (2008) 440-448.
[56] B. Ravel, M. Newville, J Synch. Rad. 12 (2005) 537.
[57] M. Schumacher, I. Christl, A.C. Scheinost, C. Jacobsen, R. Kretzschmar, Environ. Sci. Tech. 39 (2005) 9094.
[58] D.Zhou, R.A. Metzler, T. Tyliszczak, J.H. Guo, M. Abrecht, S.N. Coppersmith, P. Gilbert, J. Phys. Chem. B 112 (2008) 13128.
[59] H. Ota, T. Akai, H. Namita, S. Yamaguchi, and M. Nomura, J. Power Sources 119 (2003) 567-571.
[60] G.N. George, and M.L. Gorbaty, J. Am. Chem. Soc. 111 (1989) 3182-3186.
[61] A. Braun, F.E. Huggins, A. Kubatova, S. Wirick, M.M. Maricq, B.S. Mun, J.D. McDonald, K.E. Kelly, N. Shah, and G.P. Huffman, Environ. Sci. Tech. 42 (2008) 374-380.
[62] M. Schumacher, I. Christl, A.C. Scheinost, C. Jacobsen, and R. Kretzschmar, Environ. Sci. Tech. 39 (2005) 9094-9100.
[63] L.R. Radovic, J. Am. Chem. Soc. 131 (2009) 17166-17175.

[64] P.E. Fanning, and M.A. Vannice, Carbon 31 (1993) 721-730.
[65] Z.H. Zhu, J. Finnerty, G.Q. Lu, and R.T. Yang, Energy Fuels 16 (2002) 1359-1368

F. List of Publication

Refereed Journal Articles

1. J. Xiao, X.X. Wang, M. Fujii, Q.J. Yang, and C.S. Song. A Novel Approach for Ultra-Deep Adsorptive Desulfurization of Diesel Fuel over TiO_2-CeO_2/MCM-48 under Ambient Conditions. AIChE J., 2013, 59(5), 1441-1445.
2. J. Xiao, S. Sitamraju, Y.S. Chen, S. Watanabe, M. Fujii, M.J. Janik, and C.S. Song*. Air-promoted Adsorptive Desulfurization of Diesel Fuel over Ti-Ce Mixed Metal Oxides. AIChE Journal, 2015, 61 (2), 631-639, DOI: 10.1002/aic.14647.
3. K. T. Lee, E. Lee, C.S. Song, and M.J. Janik. Density Functional Theory Study of Propane Steam Reforming on Rh-Ni Bimetallic Surface: Sulfur Tolerance and Scaling/Brønsted-Evans-Polanyi Relations. Journal of Catalysis, 2014, 309, 248-259.
4. J. Xiao, S. Sitamraju, Y.S. Chen, M.J. Janik, and C.S. Song. Air-promoted Adsorptive Desulfurization (ADS) over $Ti_{0.9}Ce_{0.1}O_2$ Mixed Oxides from Diesel Fuel under Ambient Conditions. ChemCatChem, 2013, 5, 3582 – 3586.
5. K.T. Lee, C. S. Song, M. J. Janik. An ab initio Thermodynamics Examination of Sulfur Species Present on Rh, Ni, and Binary Rh-Ni Surfaces under Steam Reforming Reaction Conditions. Langmuir, 2012, 28(13), 5660-5668.
6. J. Xiao, C. S. Song, X. L. Ma and Z. Li. Effects of Aromatics, Diesel Additives, Nitrogen Compound, and Moisture on Adsorptive Desulfurization of Diesel Fuel over Activated Carbon. Industrial and Engineering Chemistry Research, 2012, 51 (8), 3436-3443.
7. C. Xie, Y. S. Chen, M. H. Engelhard, C. S. Song. Comparative Study on the Sulfur Tolerance and Carbon Resistance of Supported Noble Metal Catalysts in Steam Reforming of Liquid Hydrocarbon Fuel. ACS Catalysis. 2012, 2, 1127-1137.
8. J. H. Guo, M. J.Janik, C. S. Song. Density Functional Theory Study on the Role of Ceria Addition in TixCe1-xO2 Adsorbents for Thiophene Adsorption. J. Phys. Chem. C 2012, 3457-3466.
9. S. Sitamraju, M. J. Janik, C. S. Song. Selectivity of Adsorption of Thiophene and its Derivatives on Titania Anatase Surfaces: A Density Functional Theory Study. Topics in Catalysis, 2012, 55, 229-242.
10. C. Sentorun-Shalaby, S.K. Saha, X.L. Ma, C.S. Song. Mesoporous-molecular-sieve-supported nickel sorbents for adsorptive desulfurization of commercial ultra-low-sulfur diesel fuel. Appl. Catal. B: Environ 2011, 101, 718-726.
11. M. LaBarbera, M. Fedkin, X.X. Wang, C. Xie, C.S. Song, S. Lvov. Solid Oxide Fuel Cell Fueled by Diesel Reformate and Anaerobic Digester Gas. ECS Transactions 2011, 35(1), 2867-2872.
12. C. Xie, Y.S. Chen, Y. Li, X.X. Wang, C.S. Song. Influence of sulfur on the carbon deposition in steam reforming of liquid hydrocarbons over CeO_2-Al_2O_3 supported Ni and Rh catalysts. Applied Catalysis A: General 2011, 394, 32-40.
13. J. H. Guo, C. Xie, K. T. Lee, J.T. Miller, N. Guo, M.J. Janik, and C.S. Song. Improving the Carbon Resistance of Ni-Based Steam Reforming Catalyst by Alloying with Rh: A

Computational Study Coupled with Reforming Experiments and EXAFS Characterization. ACS Catalysis 2011, 1, 574-582.
14. C. Xie, Y.S. Chen, Y. Li, X.X. Wang, C.S. Song. Sulfur poisoning of CeO_2-Al_2O_3-supported mono- and bi-metallic Ni and Rh catalysts in steam reforming of liquid hydrocarbons at low and high temperatures. Applied Catalysis A: General 2010, 390, 210-218.
15. K. T. Lee, C. S. Song, M. J. Janik. Density functional theory study of sulfur tolerance of CO adsorption and dissociation on Rh-Ni binary metals. Applied Catalysis A: General 2010, 389, 122-130.
16. Y. S. Chen, C. Xie, Y. Li, C. S. Song, and T. B. Bolin. Sulfur Poisoning Mechanism of Steam Reforming Catalysts: an X-ray Adsorption near Edge Structure (XANES) Spectroscopic Study. Physical Chemistry Chemical Physics, Vo., 12, 2010, DE-b925910b, pp. 5707-5711
17. J. H. Guo, S. Watanabe, M. J. Janik, X.L. Ma, and C.S. Song. Density functional theory study on adsorption of thiophene on TiO_2 anatase (001) surfaces. Catalysis Today 2010, 149, 218-223.
18. Y. Li, X. X. Wang, C. Xie, C. S. Song. Influence of ceria and nickel addition to alumina-supported Rh catalyst for propane steam reforming at low temperatures. Applied Catalysis A: General, 2009, 357, 213-222.
19. X.L. Ma, X.X. Wang, C.S. Song. Molecular Basket Sorbents for Separation of CO_2 and H_2S from Various Gas Streams. Journal of the American Chemical Society 2009, 131, 5777-5783.
20. R. Sundararaman, and C. S. Song. Catalytic Oxidative Desulfurization of Diesel Fuels Using Air in a Two-Step Approach. Industrial and Engineering Chemistry Research, 2014, 53 (5), 1890–1899.
21. S. Sitamraju, M. J. Janik, C. S. Song. Active Sites on Ti-Ce Mixed Metal Oxides for Reactive Adsorption of Thiophene and Its Derivatives: A DFT Study. Submitted for publication, currently under revision after peer review.

Conference Papers - Non-refereed Publications

1. X.X. Wang, M. Fujii, C.S. Song. Development of solid adsorbents for biogas purification. *Preprints of Symposia – American Chemical Society, Division of Fuel Chemistry,* 57 (2), 2012, pp.
2. J. Xiao, X.X. Wang, Q.J. Yang, C.S. Song. Effect of Support for TiO_2-CeO_2 on Adsorptive Desulfurization (ADS) from Ultra-low Sulfur Diesel (ULSD) under Ambient Conditions. *Preprints of Symposia – American Chemical Society, Division of Fuel Chemistry,* 57 (2), 2012, pp.
3. J. Xiao, Q.J. Yang, X.X. Wang, C.S. Song. Air-promoted adsorptive desulfurization (ADS) over TiO_2-CeO_2 mixed oxides from ultra-low sulfur diesel (ULSD) under ambient conditions. *Preprints of Symposia – American Chemical Society, Division of Fuel Chemistry,* 57 (2), 2012, pp.

4. X.X. Wang, C. Xie, M. Labarbera, M. Fedkin, S. Lvov, C.S. Song. Steam reforming of liquid hydrocarbon fuels with online solid oxide fuel cell test. *Preprints of Symposia – American Chemical Society, Division of Fuel Chemistry,* 56 (1), 2011, pp.
5. C.S. Song, J.J. Strohm, J. Zheng, Y. Li, C. Xie, Y.S. Chen, X.X. Wang. Sulfur-tolerant and carbon-resistant bimetallic catalysts for steam reforming of liquid hydrocarbon fuels for fuel cells. *Preprints of Symposia – American Chemical Society, Division of Fuel Chemistry,* 56 (1), 2011, pp.
6. X.X. Wang, X.L. Ma, V. Schwartz, J.C. Clark, S.H. Overbury, X.C. Xu, C.S. Song. "CO_2 Capture over Molecular Basket Sorbent: Sorption Mechanism Study" *Preprints of Symposia – American Chemical Society, Division of Fuel Chemistry,* 56 (2), 2011, pp.
7. C. Xie, Y.S. Chen, Y. Li, X.X. Wang, C.S. Song. Steam reforming of liquid hydrocarbons over supported transition metal catalysts without and with potassium addition. *Preprints of Symposia – American Chemical Society, Division of Fuel Chemistry,* 54 (2), 2009, pp. 487-488.
8. C. Xie, Y.S. Chen, Y. Li, X.X. Wang, C.S. Song. Impact of sulfur poisoning on the carbon deposition over Rh and Ni catalysts in steam reforming of liquid hydrocarbons. *Preprints of Symposia – American Chemical Society, Division of Petroleum Chemistry,* 54 (1), 2009, pp. 11-12.
9. Lee, K. T., C. S. Song, M. J. Janik. Density Functional Theory Examination of Enhanced Sulfur Tolerance in Steam Reforming by Bimetallic Catalysts. Am. Chem. Soc. Div. Fuel Chem. Prep. 2012, 57(1), 979-880.

G. Appendix:

Siemens Energy Final Report "SOFC Operating on Alternative and Renewable Fuels"

SOFC Operating on Alternative and Renewable Fuels

Final Technical Progress Report

DOE Cooperative Agreement No. DE-NT0004396

Subaward No. 3763-SPGI-DOE-4396

Reporting Period:

October 1, 2009 to September 23, 2010

Prepared for

The Pennsylvania State University

by

Siemens Energy, Inc.
Stationary Fuel Cells Division
George Westinghouse Science & Technology Center
1310 Beulah Road
Pittsburgh, PA 15235-5098

Project Manager: Joseph F. Pierre

June 2011

DISCLAIMER

ACKNOWLEDGEMENT

This material is based upon work supported by the United States Department of Energy, National Energy Technology Laboratory under award Number DE-NT0004396.

A special note of thanks goes to Ms Heather Quendenfeld, Director, Power Systems Division, Mr. Joseph Stoffa, Program Manager, Mr. Travis Shultz, and Mr. Wayne Surdoval.

Task 1.0 – Project Management

The primary objective of this program was to complete the design and build of an advanced 25 kWe-class Solid Oxide Fuel Cell (SOFC) stack test article. The work described herein was intended to support the Siemens Energy DOE-sponsored Solid State Energy Conversion Alliance (SECA) Coal-based Systems Program (Contract number DE-FC26-05NT42613). The SECA Coal-based Systems Program was a three-phased program; Siemens Stationary Fuel Cells Division (SFC) successfully completed Phase I with the 5,000 hour test of a 10 kWe-class SOFC stack. The Phase I stack test, identified as POCD8R0, contained twenty-four 75 cm active length Delta8 scandia-stabilized zirconia cells. The successful completion of the 5,000 hr test enabled Siemens SFC to proceed into Phase II of the SECA Program.

The Phase II objective was the 5,000 hour test of a 25 kWe-class SOFC stack test article. This program supported that objective via the design, fabrication, and assembly of the stack test article, referenced in this report as POCD8R1. Testing of the POCD8R1 stack test article was funded by the SECA contract.

Due to unforeseen delays in the start of this program and to avoid delays in the Phase II POCD8R1 stack test, a number of critical path subtask level activities, particularly those under Tasks 7.1 and 7.2. were completed under the SECA contract.

The project was managed per with the Statement of Work (SOW) and the Project Management Plan. Relative to the POCD8R1 stack test article, all activities were completed in accordance with the overall SECA Program schedule and the stack test article was completed on-time and within budget.

The POCD8R1 stack test was initiated and ran for approximately 400 hrs before a cell failure aborted the test.

Other elements of this specific program, namely the preparation of the ring cell samples and the definition of the SOFC operational parameters were not completed.

Midway through the period of performance, Siemens decided to cease all SOFC-related activities and thus elected to fully terminate this program along with the DOE-funded SECA program. PSU subsequently issued to Siemens a stop-work order, effective September 23, 2010.

Figure 1 presents the program spending.

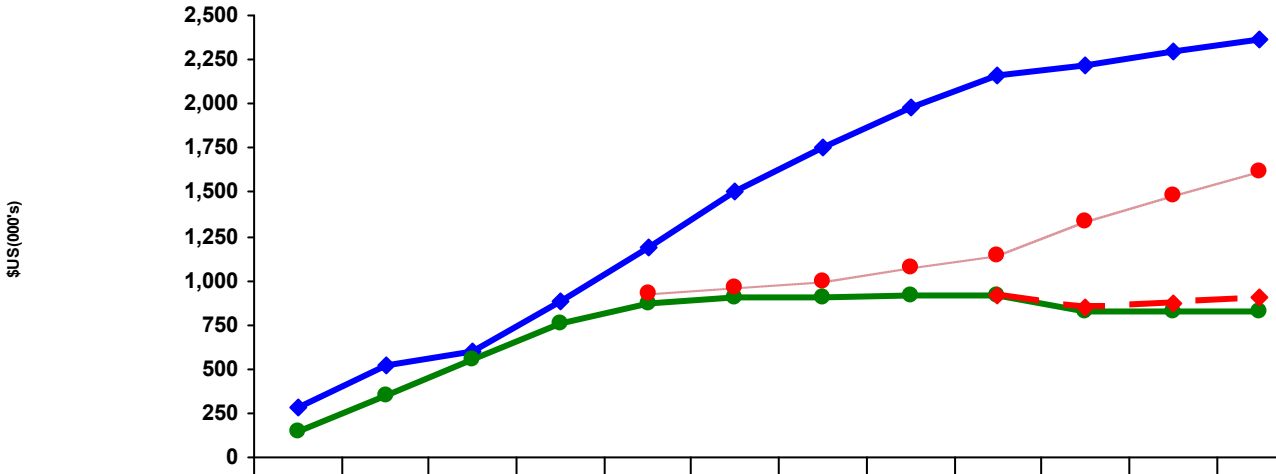

	Oct-09	Nov-09	Dec-09	Jan-10	Feb-10	Mar-10	Apr-10	May-10	Jun-10	Jul-10	Aug-10	Sep-10	
Baseline	$279	$523	$601	$883	$1,184	$1,500	$1,758	$1,975	$2,160	$2,221	$2,297	$2,364	
Actual DOE	$148	$354	$549	$762	$868	$901	$907	$911	$914	$828	$831	$831	
Forecast					$924	$957	$991	$1,074	$1,148	$1,337	$1,477	$1,618	
Revised Forecast									$921	$850	$870	$900	

Figure 1. – Program Spending

Task 2.0 – Research and Development for Alternative Fuel Processing

No work performed under this task.

Task 3.0 – Design Fuel Processing System

No work performed under this task.

Task 4.0 – Design SOFC Test Platform

No work performed under this task.

Task 5.0 – Build SOFC Test Platform

No work performed under this task.

Task 6.0 – SOFC Test Platform Installation and Testing

No work performed under this task.

Task 7.0 – POCD8R1 Stack Test Article

TASK 7.1 – POCD8R1 STACK TEST DESIGN & ANALYSIS

The objective of this task was to design and build the 25 kWe-class stack test article comprised of state-of-the-art Delta8 cells and incorporating design enhancements and cost reductions features relative to the POCD8R0 stack test article which was successfully tested in Phase I of the SECA Program.

TASK 7.1.1 – DEFINE OPTIMUM MODULE CONFIGURATION

The module configuration optimization analysis was completed under companion program DE-FC26-05NT42613.

TASK 7.1.2 – AIR DISTRIBUTION AND EXHAUST SYSTEM

The design of the spent fuel recirculator was determined to be satisfactory and thus no design work was required**.**

TASK 7.1.3 - FUEL DISTRIBUTION & RECIRCULATION SYSTEM

The design of the Fuel Distribution and Recirculation System was thoroughly analyzed to confirm there was adequate fuel distribution and fuel recirculation within the test article. The primary components evaluated included the fuel barrier, stack liner, and recirculation system. Upon analytical verification of component and system performance, the components were successfully fabricated and assembled into the stack test article.

Significant effort was expended to successfully fabricate the dies to form the thermal reliefs for fuel distribution components. The geometry of these thermal reliefs for these components was modified to reduce the cost from previous designs

In addition to defining forming methods, specific tooling and procedures required for assembly into the test article were defined and executed. This tooling permitted assembly options which reduced cost from prior fabrication and assembly methods.

Fuel Barrier

Cost reduction in the fuel barrier was achieved by reducing the depth of the fuel barrier relief and the spacing between the reliefs. Reductions in the amount of machining, size, and weight of the attachment components to the container for the foil were achieved. A forming die shape design was developed that minimized ‘springback’ from the relief, maintained the required flatness of the fuel barrier foil while allowing sufficient flexibility

to limit the thermal expansion loads. The net results was a design of the fuel barrier foil that was able to be fabricated from single commercially available width of foil material to essentially any practical length. Figure 2 shows the die used to form the fuel barrier assembly. The fuel barrier assembly is shown in Figure 3.

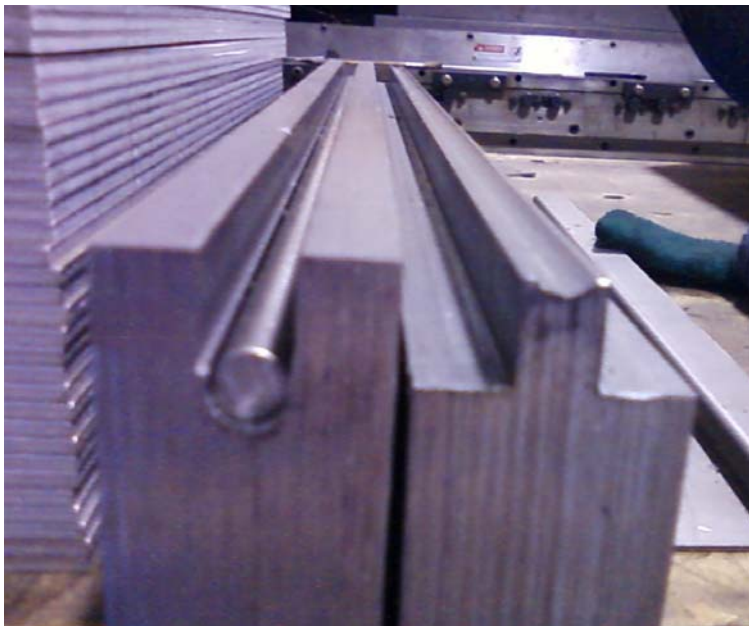

Figure 2 – Fuel Barrier Thermal Relief Forming Die

Figure 3 – Fuel Barrier Assembly

Stack Liner

The stack liner was fabricated by first seam welding commercially available foil material widths into larger single flat sheets of foil. The foil was then fed into a die to form a single thermal relief in the foil. The die employed in this process was designed as part of this activity and greatly simplified fabrication of the stack liner. This die and fabrication process permits stack liners to be fabricated using the same die for modules of different sizes. Previously, stack liners were fabricated by welding narrow panels bent on the edges to form the thermal relief. This approach was problematic due to the limited supply of material to form individual panels prior to welding. The newly developed forming process for the liner is significantly less expensive than the prior process in which each thermal relief was created by a weld seam due to less welding and less material waste. Simple methods to transport the large, thin foil sheets were defined. A portion of the fabricated stack liner is presented in Figure 4. A test piece used to establish and confirm the pleat spacing prior to liner fabrication is shown in Figure 5. The stack liner installed around the module can be seen in Figure 6.

Figure 4 - Stack Liner Fabrication

In addition to the forming methods, specific tooling and procedures required for assembly into the stack test article were defined, validated, and subsequently employed in the assembly of the POCD8R1 stack test article. The assembly of the fuel barrier required a special fixture to assure proper assembly into the module container. The fuel barrier was lowered into the container from the top after partial installation of the peripheral insulation located beneath the fuel barrier. Figure 7 shows the fuel barrier attached to the lifting fixture prior to installation into the module. Alignment of the attaching bolts and proper mating with the mounting to the inner wall of the container was critical. The assembly fixture successfully installed and located the fuel barrier

within the required tolerances. Prior units were assembled with an intermediate flange located at approximately mid-elevation of the container module. The lift fixture and assembly process developed for POCD8R1 eliminated the intermediate flange resulting in a substantial cost savings and establishes an assembly process that is applicable to larger units. Figure 8 shows the fuel barrier in the installed position.

Figure 5 - Liner Test Bends to Verify Pleat Spacing

Figure 6 – Stack Liner Installed Around the Fuel Cell Module

Figure 7 – Fuel Barrier and Lift Fixture

Figure 8 - Fuel Barrier in the Installed Position

Final installation of the remaining components of the Fuel Distribution and recirculation system was uneventful. Slight modifications to the stack liner were necessary to avoid interference with heater and instrumentation leads. Figure 9 shows the instrumentation leads crossing over the stack liner.

Figure 9 – Instrumentation Leads Crossing over the Stack Liner

In addition, the closed end bundle support plate which forms the top of the inlet fuel plenum was modified. The modification was necessary because the alignment of the closed end castings were out of position enough to prevent assembly of the top of the fuel plenum. Excessive force between the support pins and the closed end castings could apply unwanted axial load to the cells.

Figure 10 shows the test fit of the pins engaging the closed end castings on the ends of the fuel bundles. Ultimately, these pins were removed after the test fit. These pins are not necessary to react side loads on the bundles for a small stack that will not be transported and has limited horizontal thermal expansion. Modifications for larger stacks and those that will experience shipping loads will be necessary. There are several options available. The position of the closed end castings could be better controlled with a more precise fixture during stack assembly. The engagement of the support pin to the casting could be changed to permit more rotational freedom. The welded end of the support pin to the plate could be changed to a mechanical connection which would allow more movement to accommodate misalignment. Most likely a combination of these changes will be used in the design of larger units. Other approaches could be used depending on evaluation of function, ease of assembly, and cost.

Figure 11 shows the top of the fuel plenum in position prior to welding the container cover in place.

Figure 10 – Test Fit of Upper Positioning Plate

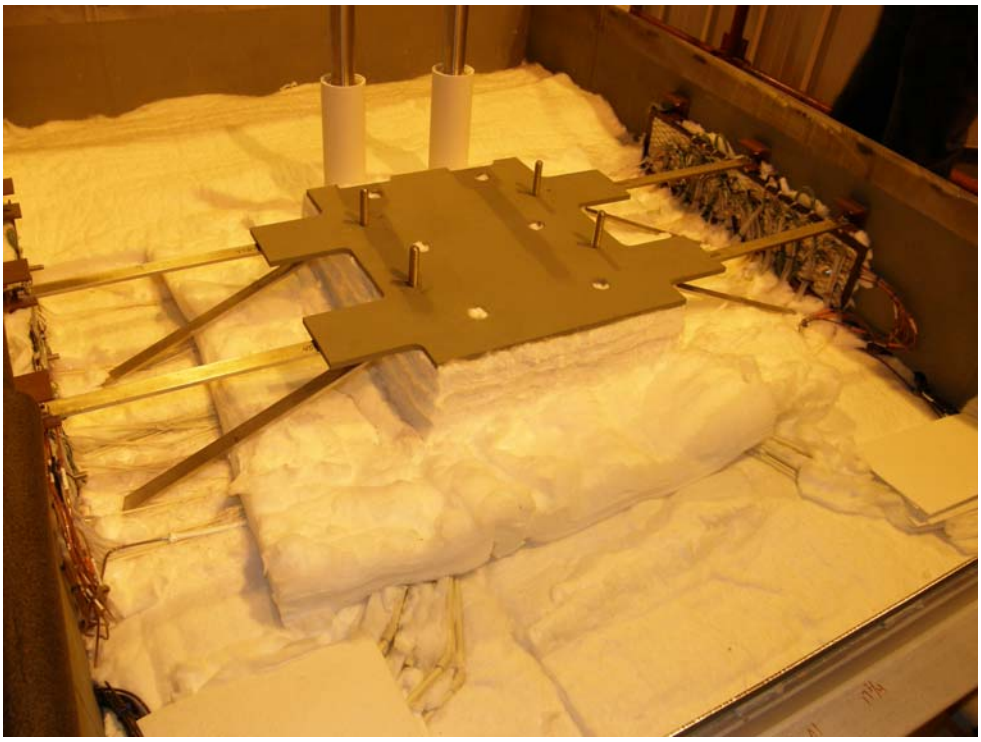

Figure 11 - Upper Positioning Plate Installed Prior to Welding Container Lid

TASK 7.1.4 – I&C SYSTEM

The design of the POCD8R1 stack test article was a scaled version of the atmospheric pressure advanced SOFC module (i.e a 250 kWe-class module). However this stack test article had significantly more instrumentation than would typically be found in a commercial module. Additional instrumentation was identified to verify analytical predictions for numerous critical components and various aspects of system performance.

Detailed designs, shown in Figure 12, that specified solder, flux, and shrink tubing were developed for the thermocouple lead terminations. Each termination was designed to accommodate the local maximum temperature and potentially moist environment.

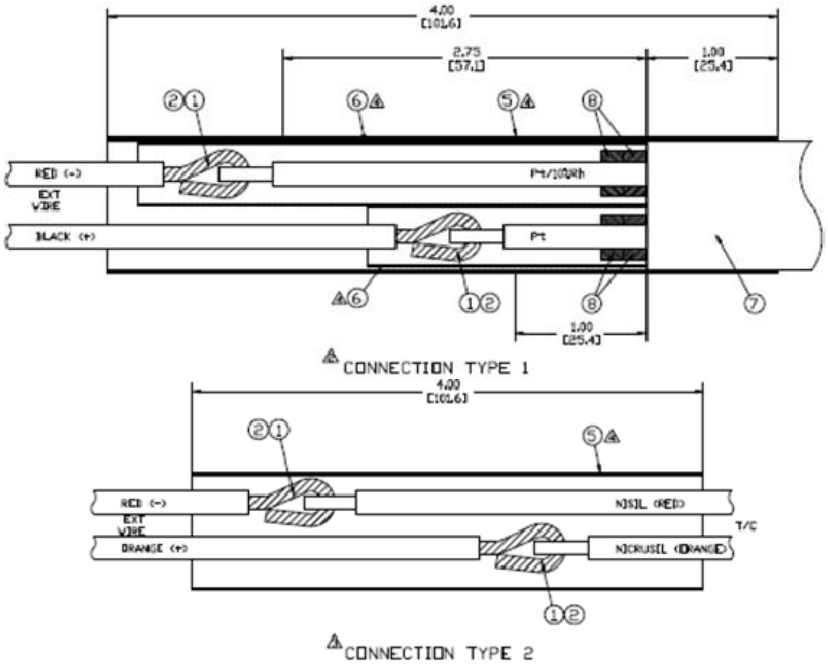

BILL OF MATERIAL

ITEM	PART NAME	SIZE REFERENCE INFORMATION
1	SOLDER	95% LEAD 3.2% TIN 1.8% SILVWR H/T PRT# 570-28R-20
2	FLUX	M-FLUX KIT PRT# M-FLUX-AR-KIT
3	SHRINK TUBING	CLEAR TEF .060 ID 2:1 SHRINKAGE PRT# TFM-004-6025-NAT
4	FEP TUBING	xxxx
5	SHRINK TUBING	CLEAR PTFE .25 OD 4:1 SHRINKAGE PRT# 75665K72
6	SHRINK TUBING	CLEAR PTFE .125 ID 2:1 SHRINKAGE PRT# TFM-016-6010-NAT
7	2-HOLE ALUMINA TUBING	.125 OD X .055 ID (TYPE S)
8	ALUMINA BEAD	.065 OD X .040 ID X .22 LONG
9	BUTT SPLICE	NYLON INSULATED DOUBLE CRIMP WIRE SIZE 12-10 AWG PRT# 7227K86
10	SHRINK TUBING	CLEAR PTFE .38 ID 4:1 SHRINKAGE PRT# 75665K74

Figure 12 – Thermocouple Lead Terminations

A significant effort was directed towards the finalization of the instrumentation routing that included the voltage taps, various thermocouple types, and gas sample tubes, as shown in Figure 13 The voltage taps and thermocouples required individualized implementation of various ceramic insulators including fish spine beads and various tubing types. The sensitivity of the terminations (shrink tubing and solder) to high temperatures required the terminations to be maintained at close proximity to the container wall. An expanded metal termination mount was developed to facilitate the anchoring of the terminations via the use of high temperature wire-ties, Figure 14.

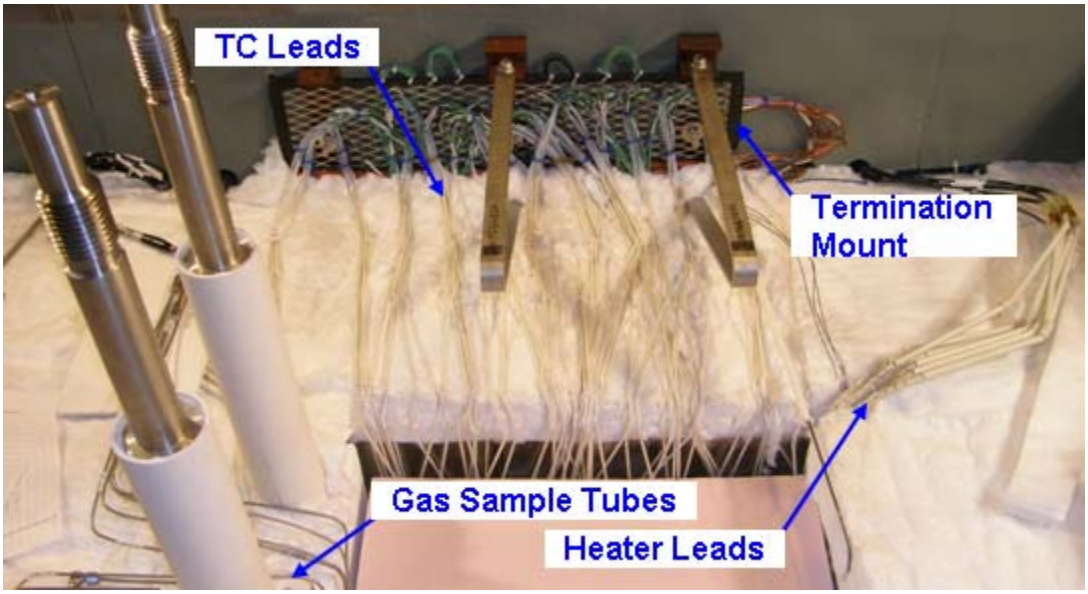

Figure 13 – Completed Instrumentation

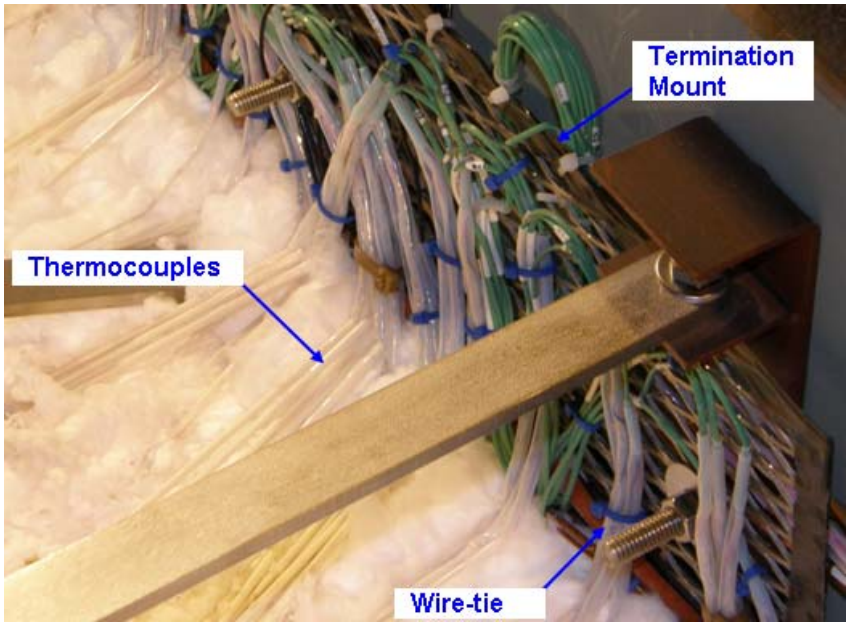

Figure 14 – Termination Mount

The finalization of the module instrumentation routing required that the appropriate feed-through type be specified for the voltage taps, various thermocouple types, and gas sample tubes. A schematic documenting the feed-through routing locations was created, Figure 15.

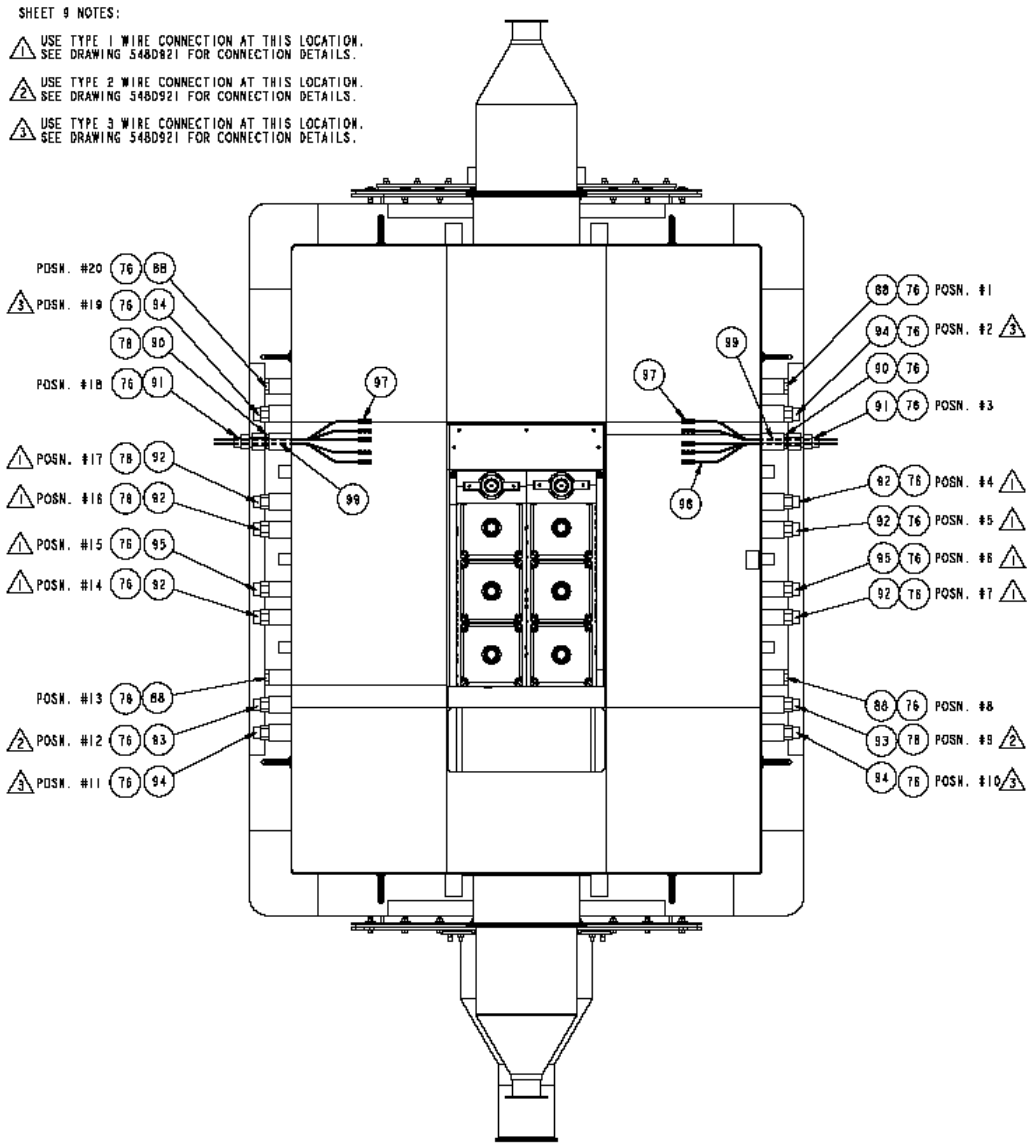

Figure 15 – Instrumentation Feed –through Schematic

Final hookup of all cell stack and balance-of-plant was successfully completed. Figure 16 shows the instrumentation feed-throughs and external wiring on the outside of the stack container.

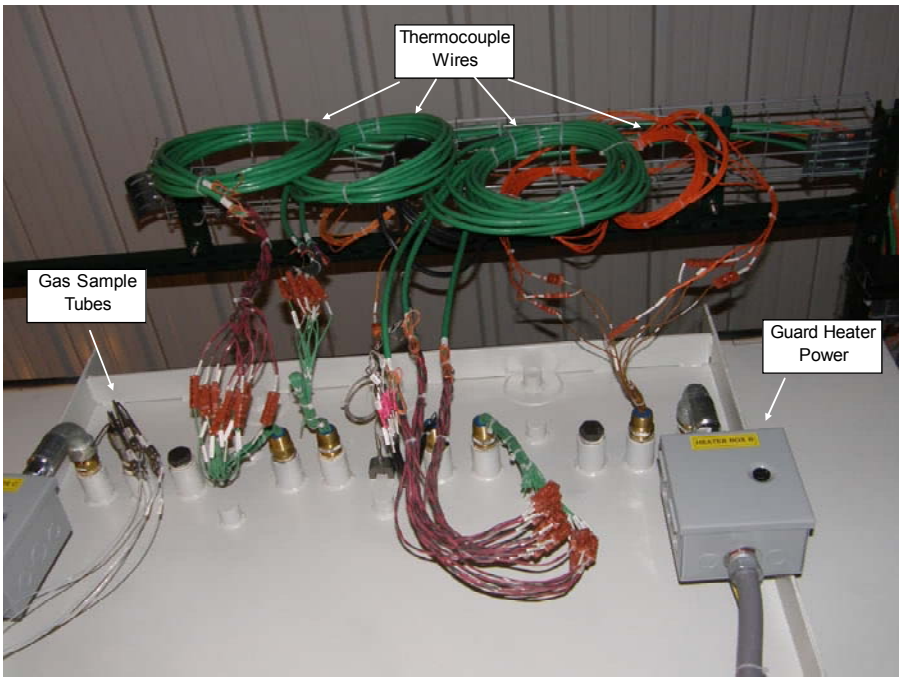

Figure 16 – Instrumentation Feed-throughs and External Wiring (pre-test)

During the startup, operation, and shutdown of the POCD8R1 stack test, only minor I&C-related operational difficulties were encountered. These were associated with a failed interface card in a datalogger. Of 148 data channels, there were no failures during the test, nor were there any instrumentation or guard heater failures experienced during operation.

Upon termination of the POCD8R1 stack test, the external instrumentation leads, guard heater power leads, and sample tubes were disconnected at the container fittings. All of these components were in excellent conditions with no signs of temperature effects or distress, as can be seen by comparing Figure 16 (post-test) with Figure 17 (pre-test). The power lead assemblies were disassembled and found to be in excellent condition (Figure 18). The peripheral insulation inside the container was damp from condensation. However, all internal instrumentation leads and guard heater power leads were in good condition with no evidence of shorting or overheating, Figure 19.

Based on post-test visual analysis it was determined that the I&C System functioned as designed.

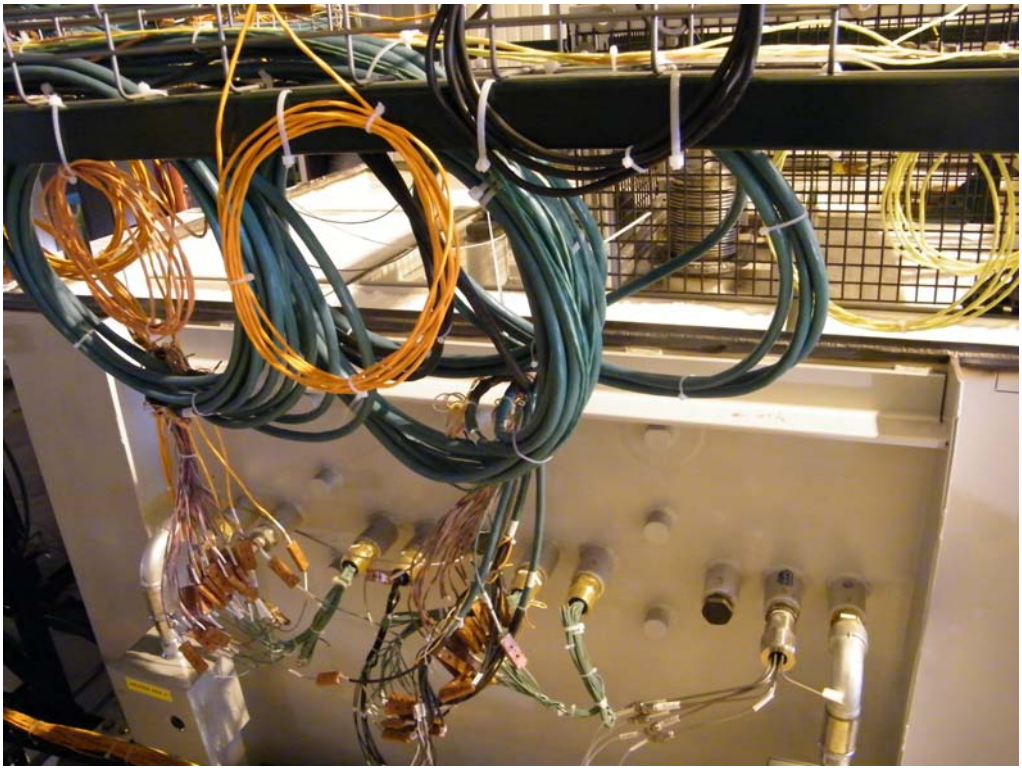

Figure 17 – Instrumentation Feed-throughs and External Wiring (post-test)

Figure 18 – Power Lead Seals

Figure 19 – Internal Instrumentation Leads

TASK 7.1.5 - CONTAINER AND THERMAL INSULATION

The purpose of this task was to design and procure the POCD8R1 container and internal insulation. A parallel effort, performed under companion program DE-FC26-05NT42613, was conducted on material characterization and testing to ensure that the selected materials were compatible with the metallic container, stacks internals, and the operating environment.

Module Container

The module container was fabricated, leak tested, and delivered. Execution of the low cost, light gage carbon steel design was successful. Minor difficulties were encountered maintaining the desired cavity tolerance at the top of the container, but this was resolved by addition of a stiffening rib. Although attachment of pipe couplings to the thin wall was no problem, welds attaching solid threaded bosses (used to attach internal support structures) were prone to cracking, or porosity. This could be reduced in future designs by adding weld material to both the inside and outside surfaces of the container wall. Figure 20 shows the module container after installation in the ventilation hood.

Thermal Insulation

The POCD8-R1 Test Article incorporated a thermal insulation package, installed between the inner walls of the rectangular container and the outer boundary of the cell stack liner. The insulation package was split into two regions: a high purity, in contact with the fuel inlet at the top and a low purity region around the stack and below the fuel

barrier in the stagnant area surrounding the air inlet and exhaust outlet, shown schematically in Figure 21.

Figure 20 – POCD8R1 Module Container in the Ventilation Hood

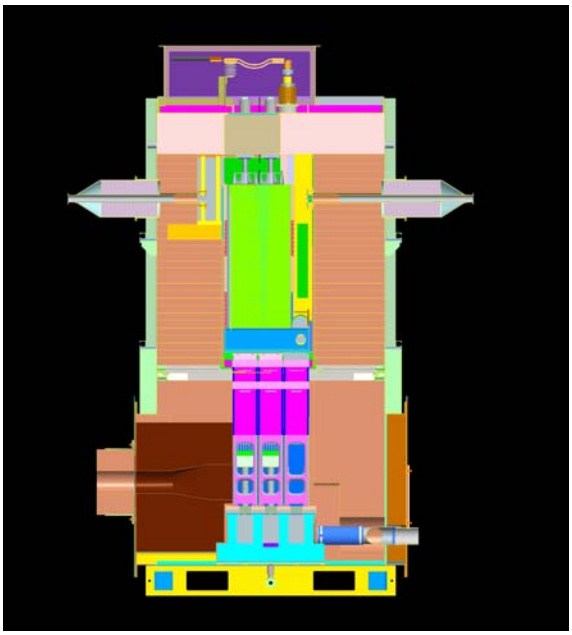

Figure 21 – Peripheral Insulation System

Specifically, the insulation package utilized a combination of 1) ceramic blankets, 2) bulk fibers as loose fill, and 3) special cast components (Bottom Exhaust Manifold, laminated boards, etc.). In addition, Nickel foils were placed at four elevations between blanket layers to create a high impedance path to fuel bypass and to limit free convection within the porous insulation. Finally, the whole insulation package rested on floor grating and screens to prevent direct contact with the wet container floor and prevent insulation damage from condensation.

Originally, the plan was to fill the container lower cavity, below the fuel barrier, with bulk fibers and to tamp down uniformly the loose fill to a nominal density of 8 pounds per cubic foot (pcf). However, once the stack was lowered in place, it become apparent that access for tamping was problematic from the top platform. Also, there was a risk of creating the conditions for excessive airborne fiber contamination as a result of tamping. Therefore it was decided to use only pre-cut blankets with the exception of a small volume above the air inlet which was filled with bulk fibers. The lower cavity was first insulated with one vertical layer of blankets installed against the container wall and then with a stack of horizontal blankets to restrict the flow of hot gas through gaps and minimize heat loss.

The first component to be installed after the stack was lowered in place within the container was the bottom exhaust manifold, Figure 22. This was a Foamfrax HD cast insulation material, approximately 30 pcf dry density, which fit between the stack and the exhaust outlet, Figure 23. A thermocouple was installed inside the transition channel to measure exhaust temperature. On the opposite side, the air inlet manifold shown in Figure 24, was covered with a metallic canopy and then the whole volume was filled with blankets up to the air inlet flange elevation. The remaining volume was then filled with bulk fibers.

After the fuel barrier was installed, work continued with installation of a multilayer assembly of fibrous ceramic blankets, 8 pcf density, cut oversized to account for fiber shrinkage in proximity of the hot face and to compensate for natural settlement. The thickness of each Durablanket-S layer is approximately 50 mm (~2 inches) and each layer extends over the two opposite sides of the previous layer. This staggered pattern arrangement, as shown in Figure 25 at mid elevation, allows effective overlapping of multiple layers preventing interstitial cracks between layers which may lead to radiation heat losses through the peripheral insulation package.

Particular care was taken to ensure that the blanket layers were installed snug against the stack liner pleats. Additional pieces of blanket material were installed in close proximity of the liner were the blanket edge was cut to clear the pleats.

After installation of the top Nickel foil and instrumentation wiring, shown in Figure 26, multiple layers of Saffil HD high purity alumina blankets were installed, Figure 27.. The uppermost layer in contact with the container cover lid was a layer of compliant Saffil LD mat.

Figure 22 - Exhaust Manifold on Bottom of Container

Figure 23 - Exhaust Manifold and Outlet Insulation Packing

Figure 24 - Air inlet Manifold (as viewed through the container hatch)

Figure 25 – Peripheral Insulation Blankets at Mid-elevation (fuel inlet side)

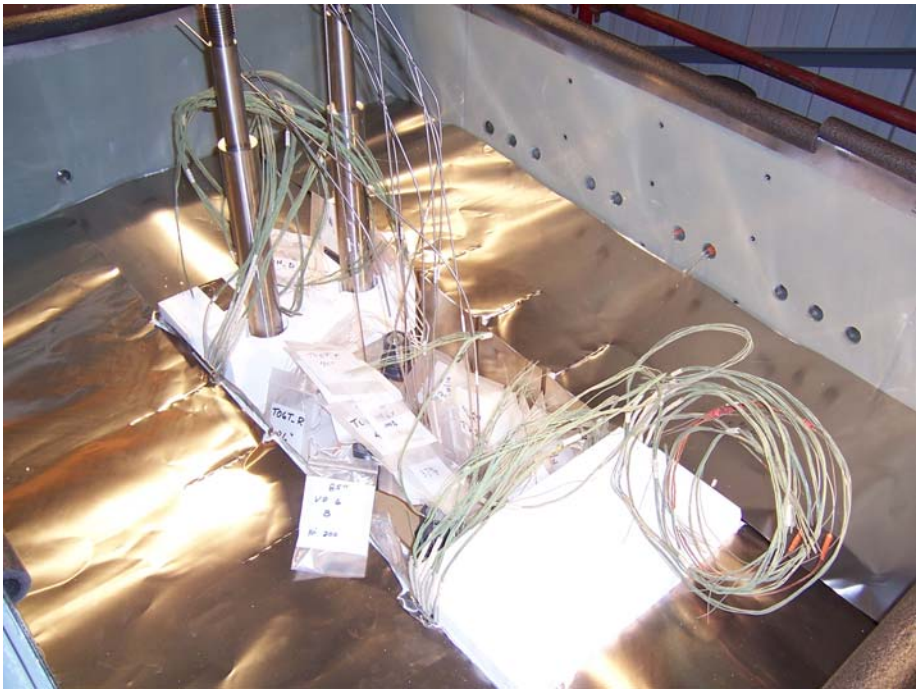

Figure 26 – Top of Low Purity Insulation and Nickel Foil Barrier

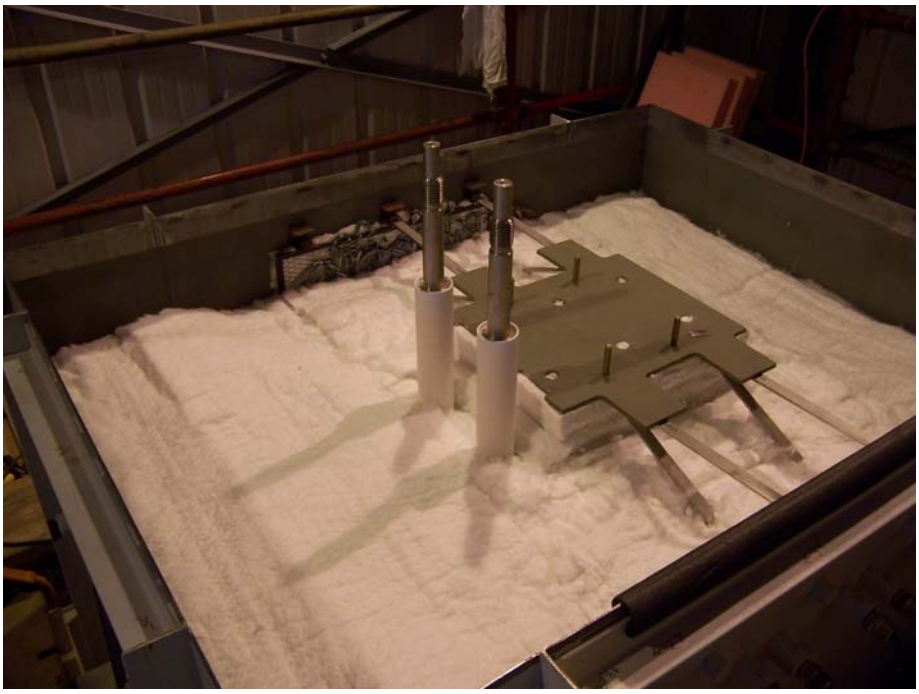

Figure 27 –High Purity Insulation Top Layers

The POCD8R1 Stack Test operated for approximately 400 hours during which time the container external walls were monitored to gather data to validate the analysis data. Thermocouples on the external container wall and surveys with infrared pyrometers indicated that the wall temperatures were lower than expected. Upon disassembly the insulation and container had considerable condensation, but no gaps were apparent in the insulation. Corrosion of the container wall was minimal. Fuel bypass through the insulation was slightly higher than expected.

TASK 7.1.6 – SPENT FUEL RECIRCULATOR

The existing design of the spent fuel recirculator was determined to be satisfactory and thus no design work was required.

TASK 7.1.7 - EXTERNAL RECIRCULATION LOOP

The purpose of this task was to design and procure the POCD8R! external recirculation loop piping, insulation, and instrumentation.

The design of the External Recirculation Loop was successfully executed. Individual components were fabricated and/or procured and tested. The recirculation loop and instrumentation were installed, insulated, and leak checked prior to the start of the POCD8R1 stack test.

Figure 28 shows the ejector/prereformer assembly, on a temporary stand, prior to installation. Fuel heater no. 1 and the connecting pipe spool on the actual loop support stand are shown in Figure 29 just prior to installation. A typical weld joint, in this case between fuel heater no. 2 and the container inlet feed-through, is shown in Figure 30.

The recirculation loop piping was insulated with five layers of 2.5 cm (one inch) thick Durablanket S. Figure 31 shows the recirculation loop piping insulation in progress. The finished piping was then wrapped in an alumina jacket, Figure 32.

The circulator, fuel heaters, and prereformer performed as expected during startup, operation, and shutdown. The individual components, and where possible the loop piping, were leak checked on a regular basis with no leaks detected throughput the period of operation.

Following shutdown of the stack test, after approximately 400 hours of operation, the ejector/prereformer assembly, fuel heater no. 2, and the recirculation inlet and outlet feed-throughs were removed and inspected. All were determined to be in good condition, Figures 33 through 36, respectively.

Figure 28 – Ejector/Prereformer Assembly

Figure 29 – Heater No. 1 and Recirculation Loop Pipe Spool

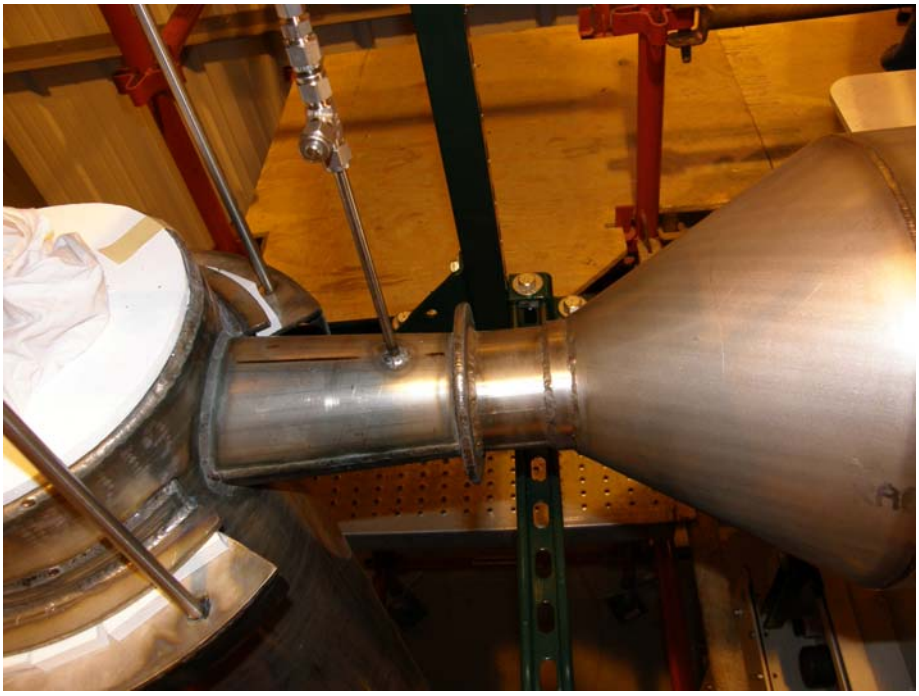

Figure 30 – Weld Joint between Fuel Heater 2 and Container Inlet Feed-through

Figure 31 – Recirculation Loop Piping Insulation in Progress

Figure 32 – Finished Recirculation Loop Pipe between Circulator and Fuel Heater No. 1

Figure 33 – Fuel Heater No. 2 and Container Inlet Feed-through with Insulation Removed (post-test)

Figure 34 – Bottom of Fuel Heater No. 2 (post-test)

Figure 35 – Feed-through Bellows (post-test)

Figure 36 – Prereformer Outlet Bellows (post-test)

TASK 7.1.8 - TOOLING & FIXTURES

The purpose of this task was to design, fabricate, and qualify tooling, fixtures, jigs, etc. that were needed to assemble and/or install the POCD8R1 test article.

The POCD8R1 stack test article consisted of 48 Delta8 cells, arrayed into six bundles (stacks), each containing eight cells. Individual bundles were configured into an integrated bundle assembly (IBA). Each of the six IBAs was comprised of the eight cell stack, recuperator, air delivery and distribution components, exhaust components, and air feed tubes. Three IBAs were then assembled in to a bundle row. Thus the stack test article contained two bundle rows with three IBAs per row.

The tooling required to assemble the IBA was redesigned to optimize the assembly process and address issues identified during the assembly of the first generation Delta8 stack test article (POCD8R0). Utilizing lessons learned from the POCD8R0 stack test article assembly and installation, new and improved tooling was successfully redesigned, built, and tested.

The IIBA tooling fixture allowed horizontal assembly of the IBA, as shown in Figure 37.

After assembly in the horizontal position, the fixture allowed vertical rotation for transportation to the next stage of assembly. Figures 38 shows the IBA being lifted into vertical position.

Bundle rows (consisting of three IBAs and associated components) were assembled in the row assembly tooling fixture, Figure 39. This fixture facilitated the assembly of an entire bundle. The fixture provided alignment and support of each IBA, permitted access for welding, inspection, and assembly of IBA instrumentation. The row assembly fixture was designed so that it could also to lift the entire row and transport and install it into the stack assembly station in preparation for the stack assembly. (Figure 40). The stack assembly station, Figure 41, was designed and assembled to support the two bundle rows during assembly of the remaining stack components.

A major effort was placed on the design, construction, and qualification of the Stack Lifting Fixture, considered to be the most critical tooling/assembly. This apparatus was designed to lift, transport, and position the assembled stack test article inside the container. Qualification included load proof testing prior to the actual lifting of the POCD8R1 stack test article and positioning it inside the container to ensure the fixture was functional, safe, and compliant with applicable standards

The design basis of the Stack Lifting Fixture design was a combination of two Row Lifters joined together to form the lifting structure for the POCD8R1 stack test article. The combined load of stack and lifting fixture was lifted using a commercial 3-ton (2722 kg) Strongbac® beam.

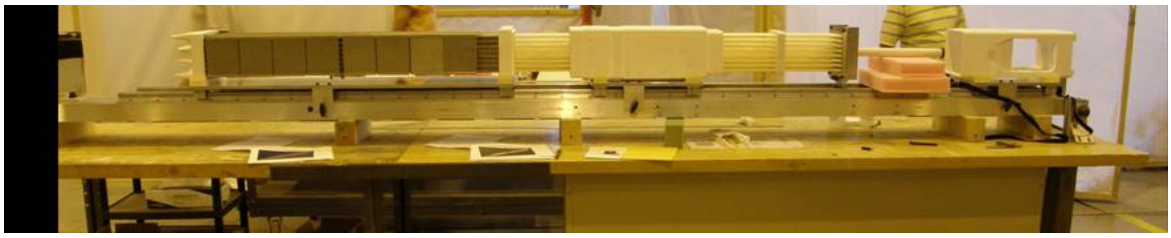

Figure 37 – IBA Assembly Fixture

Figure 38 – IBA Assembly Fixture (vertical)

Figure 39 –Bundle Row Assembly Fixture (left, two IBAs; right, three IBAs)

Figure 40 – Bundle Row Lift

Figure 41 – Stack Assembly Station

Four vertical channels were connected on the bottom to the row strongbacks, and at the top to a hanger assembly to form a rigid frame, shown schematically in Figure 42. The hanger assembly was made of three plates, spaced apart by two solid blocks, the whole assembly connected with four high strength bolts loaded in double shear.

All of the Stack Lifter critical components proved to have stresses that were below the allowable design loads.

The overall structure was designed to lift a completely assembled stack test article comprising two rows of three bundles each, weighing approximately 2700 lb (rated load). Including the Stack Lifting fixture which weighs approximately 730 lb; thus the total capacity of the lifting rig was 3,430 lb (1556 kg).

In compliance with OSHA 1926.251(a)(4) and ASME B30.20 standard requirements, the Stack Lifter was tested using a proof load that was 125% of the rated load capacity.

The Stack Lifter proof test was conducted by loading the fixture, with a 3,379 lb (1533 kg) dead weight. The dead weights were uniformly distributed as follows:

Two base I-beams, 80 lb each, tot. 160 lb (73 kg)

Three plates (30”x60”x1” thk), each 520 lb, tot. 1560 lb (707 kg)

Twentyone plates, each 79 lb, tot. 1659 lb (753 kg) for a total of 3,379 lb (1533 kg), equivalent to 125% of the R1 stack rated load.

The total combined weight of the Strongbac beam (180 lb) and Stack Lifter (731 lb) was 911 lb (413 kg). The estimated reading on the scale was therefore 4290 lb. The actual reading on the scale was 4290 lb (1946 kg). The lifting fixture was hoisted as high as the hook capacity allowed and the total clearance from ground was measured, Figure 43. The recorded height was 137" (11ft-5in) (3.48 m), which provided sufficient clearance between the bottom of the fixture and the container top edge at 133.5" (3.39 m).

At the completion of the test, a visual inspection of all fixture welds and structural members was conducted. No deformation, cracks, or other defects were found.

The fully assembled stack test article was subsequently lifted from the Stack Assembly Station and was positioned smoothly inside the container. The total weight reading on the scale, including Strongbac beam, Stack Lifting Fixture was 3020 lb (1370 kg). By subtracting the combined weight of Strongbac beam and Stack Lifting Fixture (911 lb), it was calculated that the as-built stack weight was 2109 lb (957 kg).

The POCD8R1 stack test article was successfully assembled, transported, and positioned inside the module container, as shown in Figures 44 and 45, within schedule and budget.

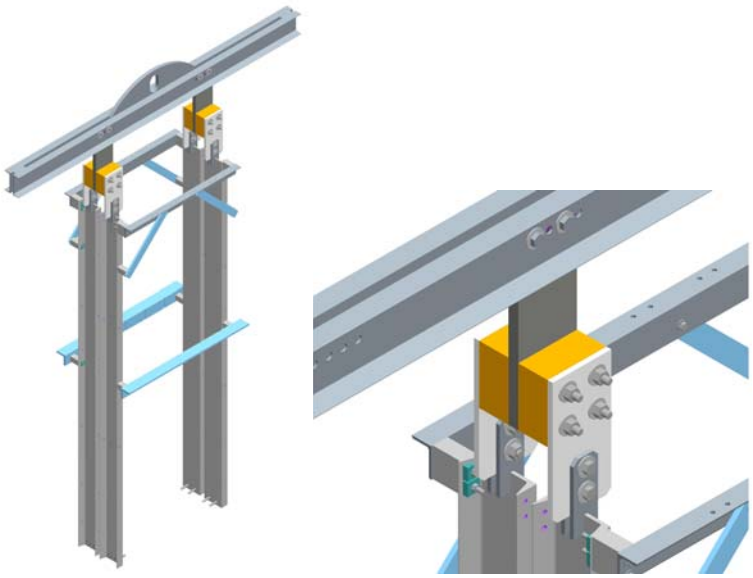

Figure 42 – R1 Stack Lifter Assembly with Detail of Structural Hanger

Figure 43 – Stack Lifting Fixture - Proof Load Test

Figure 44 – Stack Test Article Being Installed into Container

Figure 45 –Stack Test Article and Lifter Positioned Inside the Container

TASK 7.2 – POCD8R1 MODULE ASSEMBLY

The design of the POCD8R1 fuel cell module was the scope of companion program DE-FC26-05NT42613. A description of the module is included herein as background for the module assembly procedure.

The POCD8R1 stack test article contained 48 scandia-stabilized Delta8 cells with an active length of 100 cm, arranged in an array of six bundles, with each bundle containing eight cells. The design of the test article was intended to be a scaled version of the conceptual advanced module design, with the advanced module being one of the final deliveries in the SECA program. The stack test article featured numerous components and subassemblies identical to those intended for use in the advanced module. Design innovations and cost reduction features relative to the previous stack design (POCD8R0) were incorporated herein and their performance to be validated. Among the cost reduction features was the use of cast ceramic parts to replace machined ceramic boards and metallic parts. Significant key design feature included the installation of the cells with the open end down and the elimination of in-stack reformer boards..

A key design element was the modular subassembly element, the integrated bundle assembly (IBA). The IBA contained a number of net-shape, high purity alumina castings and an eight-cell Delta8 bundle. In addition to the eight cells, the IBA contained an integral cast ceramic recuperator, an air box with air feed tubes, a ceramic exhaust/base casting, a ceramic seal casting, and a closed-end casting. The fuel-to-air seal was

accomplished using custom machined alumina boards held in the seal casting. The IBA is shown schematically in Figure 46.

A carbon steel container housed the six IBAs. The IBAs are arranged in two rows of three bundles each. Electric guard heaters were located around the periphery of the cells to facilitate heatup and to reduce lateral thermal temperature gradients on the cells. The stack was surrounded by a nickel metal liner to prevent fuel bypass.

.

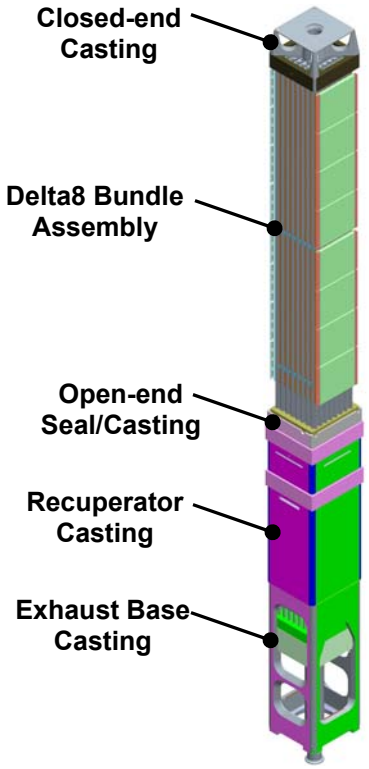

Figure 46 - Integral Bundle Assembly (IBA)

The stack was thermally insulated by a low purity ceramic blanket insulation (peripheral insulation) located outside of the stack liner. An exploded view of the stack is shown schematically in Figure 47. A fuel barrier, located at the elevation of the open end seal, was intended to limit fuel bypass through the peripheral insulation. The module, in turn, was enclosed in a carbon steel outer container, Figure 48

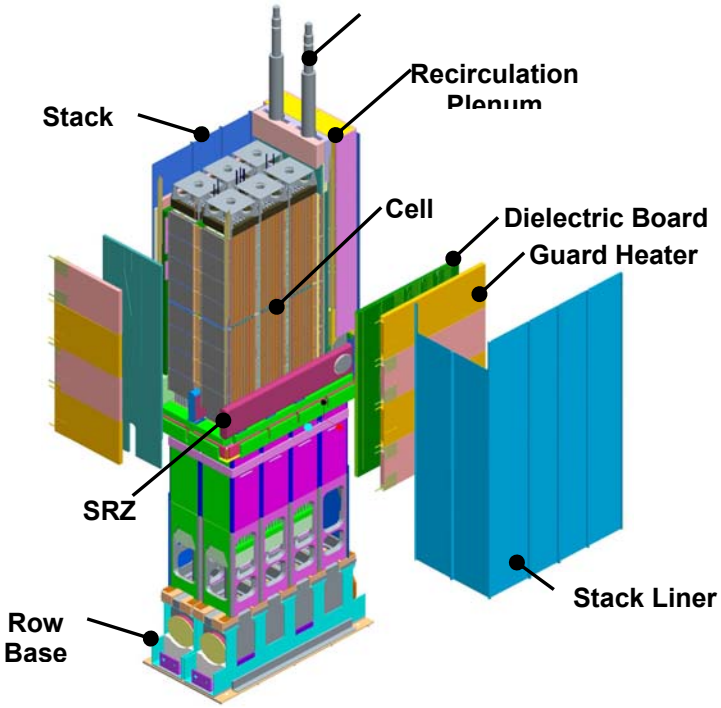

Figure 47 – Exploded Stack Assembly

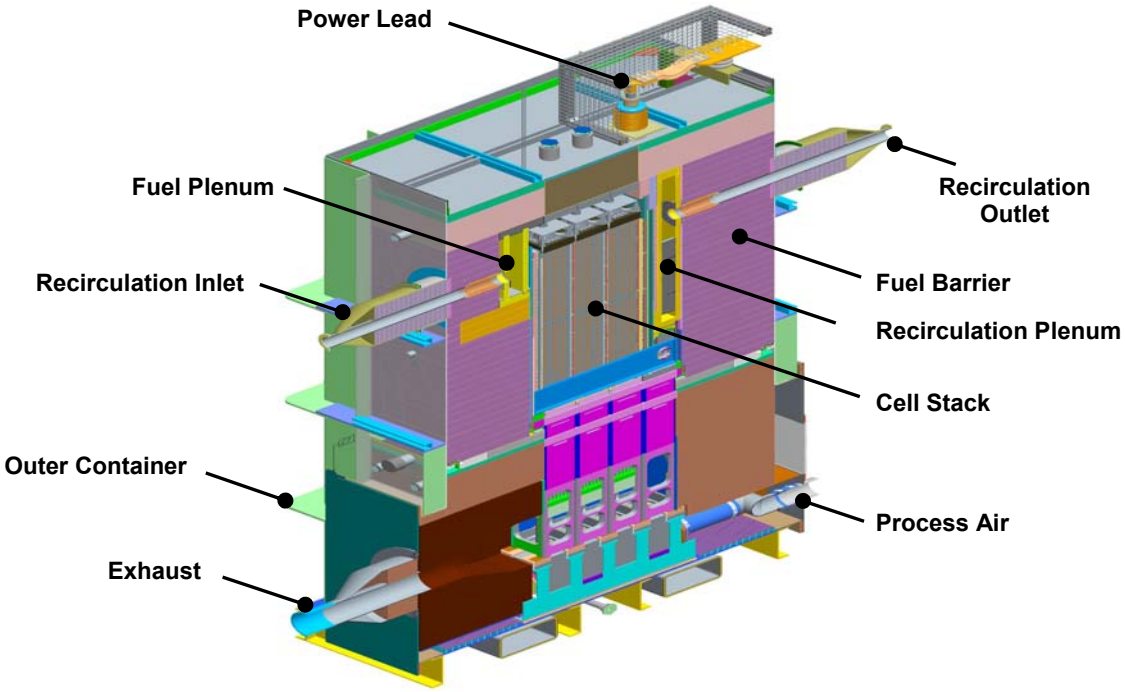

Figure 48 – Module Component Layout

Task 7.2.1 – Fabricate and Assemble Tooling & Fixtures

The objective of this task was to design, fabricate, assemble, and qualify specialized tooling, jigs, fixtures, etc. that were necessary to assemble the module. The effort under this task was synergistic with that of Task 7.1.8; thus, please refer to Section 7.1.8 for a detailed discussion of the work completed under this task.

TASK 7.2.2 – CELL AND BUNDLE MANUFACTURING

The objective of this task was to manufacture the Delta8 cells and bundles for use in the POCD8R1 stack test. The test article contained 48 scandia-stabilized zirconia Delta8 cells with an active length of 100 cm. The Delta8 cell geometry and materials are shown in Figure 49 and Table 1, respectively.

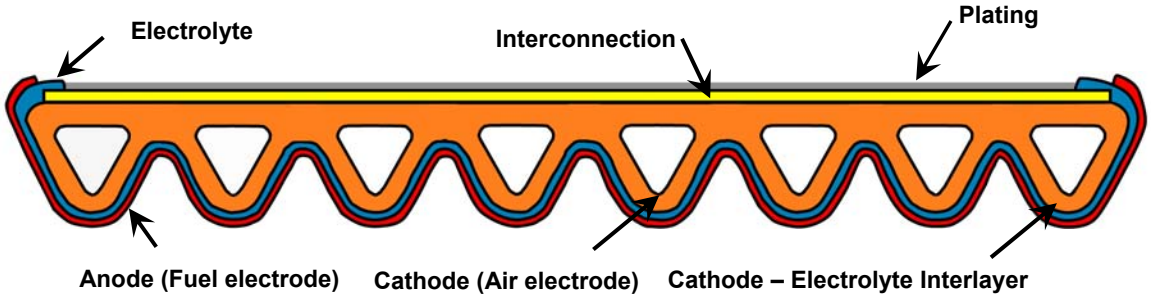

Figure 49 – Delta8 Cell Geometry

Delta8 Cell Materials	
Component	**Material**
Cathode (Air Electrode)	Doped lanthanum manganite
Cathode – Electrolyte Interlayer	50% cathode + 50% electrolyte
Electrolyte	Scandia stabilized zirconium oxide
Interconnection	Doped lanthanum chromite
Anode (Fuel Electrode)	Nickel – zirconium oxide cermet
Plating	Nickel

Table 1 – Delta8 Cell Materials

All cells were manufactured utilizing the most advanced manufacturing processing and materials at that point in time. During production of these cells and bundles, data was generated and analyzed to better understand and optimize each process step. In

addition, testing was conducted to improve yield. As yield issues occurred, analyses of potential causes were performed and, where appropriate, process improvements implemented. Cell production occurred in three manufacturing campaigns, with the goal being to improve yield with each subsequent campaign utilizing lessons learned from the previous campaign. Overall, cell manufacturing yield improved by more than 80% in the third campaign compared to the first campaign.

All cells and bundles for the POCD8R1 stack test were successfully manufactured and assembled. A single Delta8 cell is shown in Figures 50 and 51 and an eight-cell bundle in Figure 52.

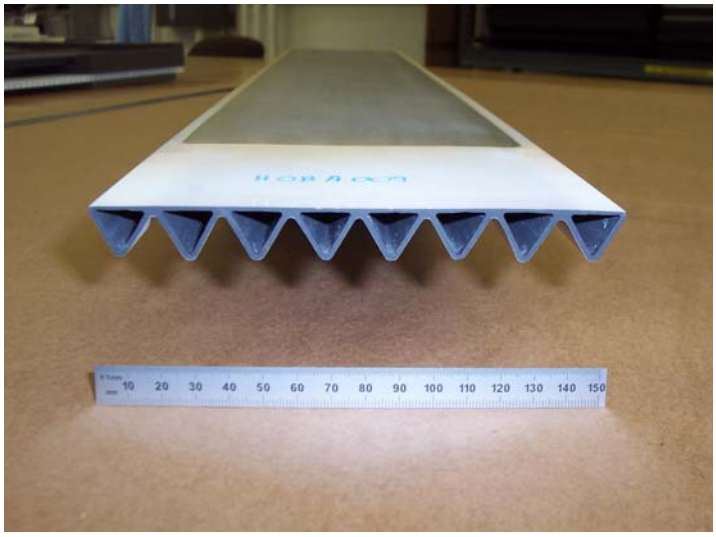

Figure 50 – Photograph of Delta8 Cell (open end)

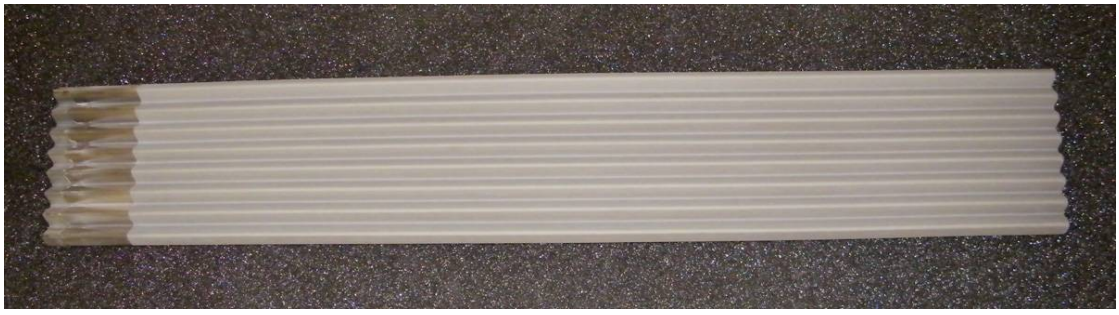

Figure 51 – Photograph of Delta8 Cell (open end at left)

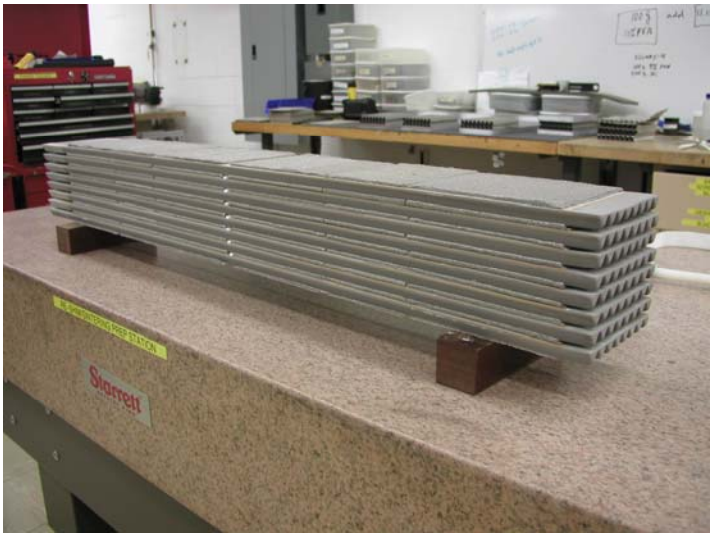

Figure 52 – Photograph of Eight-cell Bundle

TASK 7.2.3 - DEVELOPMENT MODULE ASSEMBLY DRAWINGS

This task supported the preparation of the documentation to fabricate and assemble the stack and module components supporting the activities discussed in Task 7.2.4.

Drawings and procedures were generated to determine the sequence of assembly, to identify tooling needs during assembly, and for verification of component design and fit-up. Several higher level assembly drawings were created to support the activities described in the module assembly task. Drawings were released as needed to support the stack and module assembly. The documentation was subsequently revised to reflect as-built information and design improvements that were made during the assembly.

TASK 7.2.4 - MODULE ASSEMBLY

The objective of this task was to assemble the module and prepare it for integration with the balance-of-plant. The integration of the module with the balance-of-plant and installation of the fully integrated (module and BOP) test article into the test facility were the scope of companion program FC26-05NT42613.

Fabrication of the modular subassembly, the IBA, was initiated upon the availability of the first (of six) completed bundle. Due to manufacturing tolerances of the cells and bundles, the open end of each bundle was mapped to insure proper interfacing with the open end seal. The mapped data was processed and used to machine the open end seal. After the open end seal was machined, the fit-up of the seal with the bundle was verified. At this point in the assembly process proceeds with the placement of the open end/casting subassembly and closed end seal casting assembly onto the respective ends of the bundle. Figure 53 shows the open-end of the IBA.

Each of the six IBAs contained an eight cell bundle, an integral cast ceramic recuperator, an air box with air feed tubes, a ceramic exhaust/base casting, a ceramic seal casting, and a closed-end casting. The fuel-to-air seal was accomplished using custom machined alumina boards held in the seal casting. The IBA was shown previously in Figure 46.

Figure 53 – Bundle Assembly Showing Open-end Seal, Casting and Instrumentation

The IBAs were assembled in the horizontal position, rotated to vertical, transported, and placed in to the bundle row assembly fixture (see Figures 37 through 39). A bundle row consisted of three IBAs, a common row base weldment, air inlet manifold, and one bus bar. The module thus contained two bundle rows of three IBAs per row.

The bundle row assembly fixture provided alignment and support of each IBA, permitted access for welding and inspection of the bundle-to-bundle electrical connectors, welding the bus bar to the bundle, and assembly of the IBA instrumentation. As discussed earlier in this report (Task 7.1.8), the bundle row assembly fixture was also used to lift the entire bundle row in to the stack assembly station

Each bundle row was then lifted and placed onto the stack tray which is positioned on the floor within the stack assembly station, Figure 54. The stack assembly station (shown previously in Figure 41), an open frame structure, was designed to temporarily support the two bundle rows during assembly of the remaining stack components.

Module assembly then continued with the installation of the SRZs, recirculation castings, and liner seal castings. Here, also, the power leads were welded to the bus bars and the row-to-row connections were welded to the complete the circuit. The dielectric board/instrumentation subassembly was completed and installed in to the stack. All of

the instrumentation along the outside surfaces of the boards, shown in Figure 55, was cemented into place within machined slots.

Figure 54 - Placement of Bundle Rows onto the Stack Tray

Figure 55 – Stack Assembly: Dielectric Boards, SRZs, and Recirculation Castings

The guard heaters subassemblies were completed and installed adjacent to the dielectric boards. The recirculation collection box was installed at the end of the stack and banded for support, Figure 56.

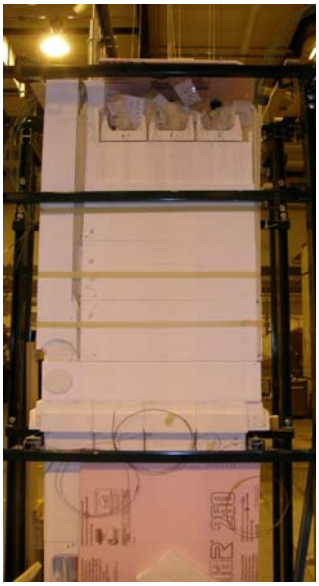

Figure 56 – Stack Assembly: Recirculation Collection Box

The stack liner was installed around the stack and welded into place, Figure 57.

Figure 57 – Stack LIner

The outer container (Figure 58) was leak tested and prepared to accept the stack test article.

Figure 58 – Outer Container

The stack lifting fixture (Figures 43 and 44) was used to place the stack test article into the container. After the stack was placed into the outer container (see Figure 59), module assembly continued with installation of the water barrier, process air piping, lower insulation, lateral shipping restraints, and fuel barrier around the stack. Upper insulation was then installed above the fuel barrier followed by installation of the recirculation feed-throughs Installation of the upper insulation continued above the feed-throughs,. The upper module is shown in Figure 60.

Figure 59 - Stack Inside Container

Figure 60 - Upper Module

The stack instrumentation (Figure 61) was routed from the stack to the container wall (Figure 62). Each instrumentation lead was fastened to a screen, to anchor the connection in a cold region (Figure 63).

Figure 61 – Stack Instrumentation

Figure 62 – Instrumentation from Stack to Container Wall

The upper insulation plug that resides above the stack was then assembled and installed into the container (Figure 64). The plate supporting the insulation rested on brackets that attach to the container wall. A blanket of insulation was placed in the area from the upper insulation plug to the container wall, as shown in Figure 65. The blanket was layered up to the elevation of the upper insulation plug support plate, Figure 66.

The container lid was then lowered down and set in place on top of the mounting brackets, as shown in Figure 67. Once the lid was in place, it was clamped to the container in preparation for welding. Using studs that were part of the upper insulation support plate, the plug was then drawn up to insure the upper insulation support plate was in contact with the container lid. The lid was then welded to the outer container.

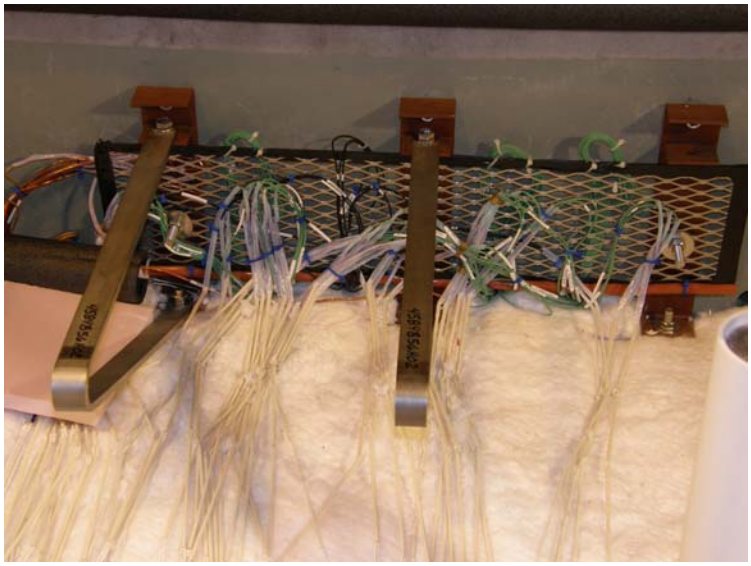

Figure 63 – Container Wall Instrumentation Anchoring

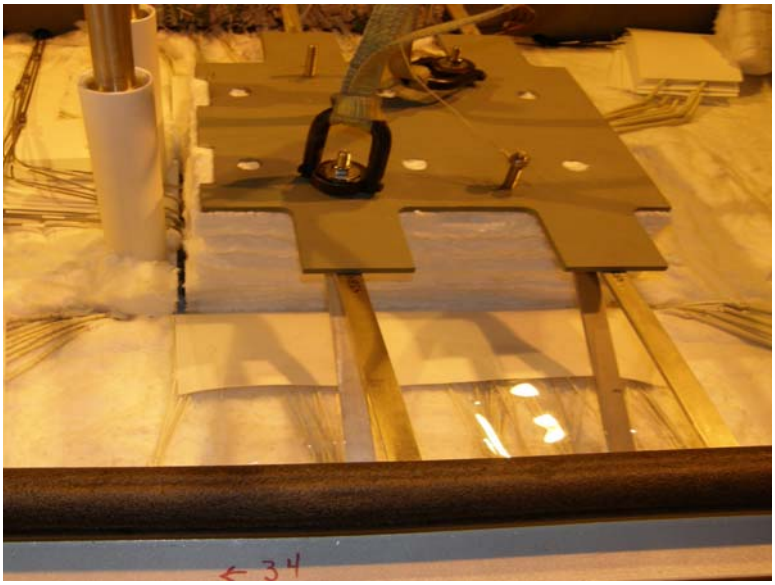

Figure 64 – Upper Insulation Plug

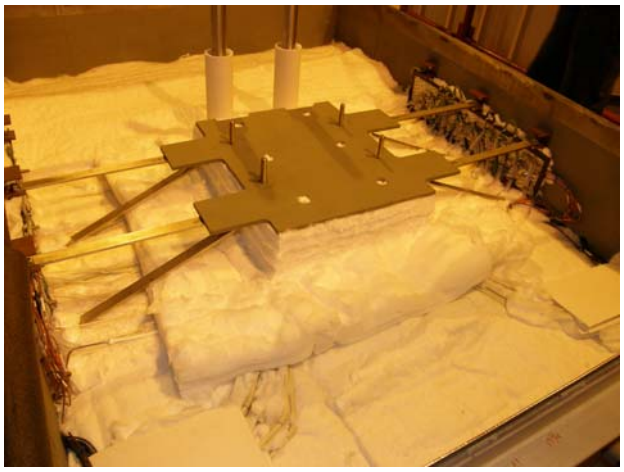

Figure 65 – Blanket Insulation around Plug

Figure 66 – Upper Insulation

Figure 67 – Outer Container Lid

The power lead bellows flange, Figure 68, was seal welded to the container lid. Assembly continued outside of the container with the power lead assembly and cables as shown in Figure 69.

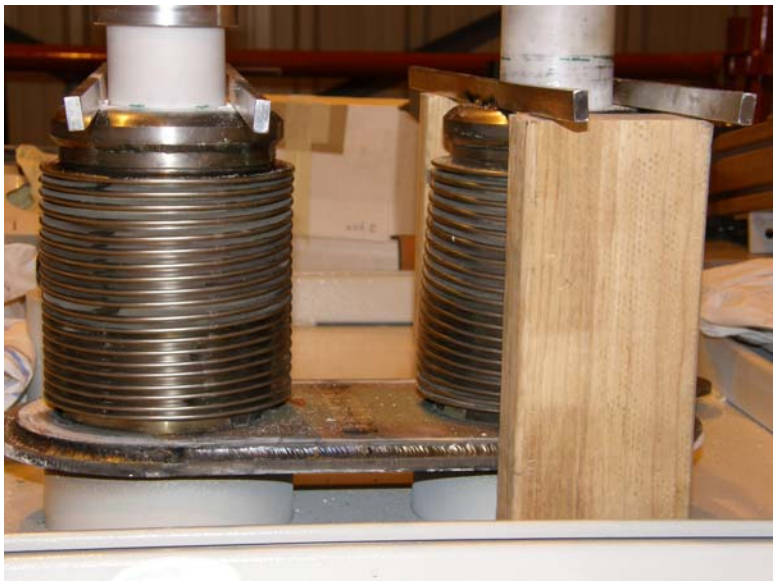

Figure 68 – Power Lead Assembly

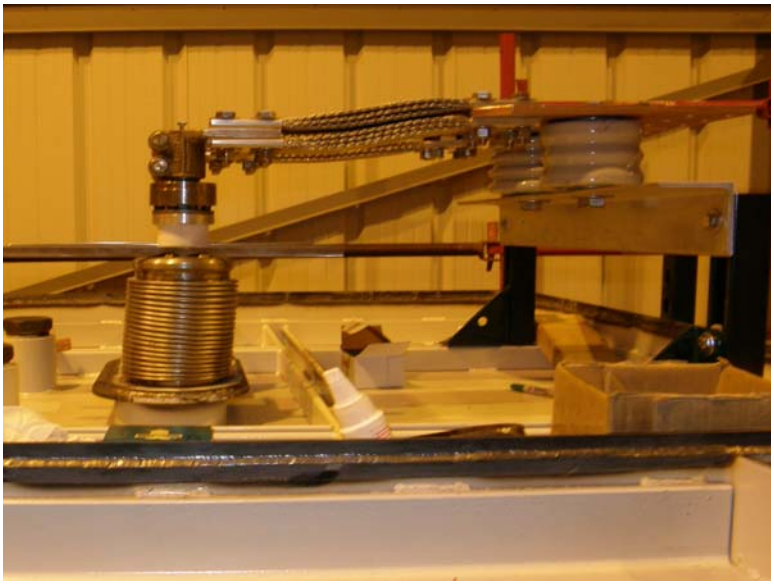

Figure 69 – Power Lead Cables

The next items to be assembled were the ejector and upper fuel heater, Figure 70. These components were lowered into place and supported from framework bolted onto the container. The circulator was then placed under the ejector and bolted to the floor. The lower heater was then installed and all pipe flanges were clamped in preparation for welding.

Figure 70 – Ejector, Prereformer, Circulator

The recirculation feed-throughs were welded to the container then the heater and ejector were welded to their respective feed-throughs (Figure 69). The external piping, upper and lower fuel heaters, and the ejector were all insulated. The piping and insulation was then wrapped with metal cladding to help protect it from damage (Figures 72 through 74, respectively).

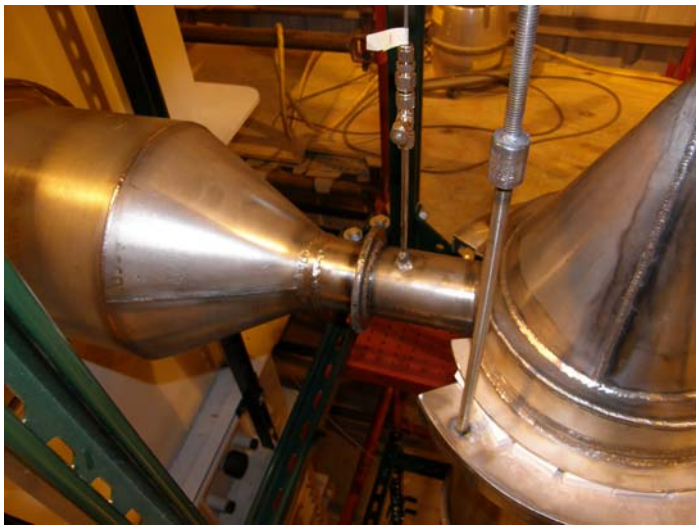

Figure 71 – Recirculation Feed-through (ejector side)

Figure 72 – External Loop Piping Insulation

Figure 73 – Insulated Lower Fuel Heater

Figure 74 – External Loop with Metal Cladding

Figure 75 shows the completely assembled stack test article installed with in the test facility.

Figure 75 – POCD8R1 Stack Test Article Installed in the Test Facility

A discussion on the startup, operation, and post-test analysis of the POCD8R1 stack test can be found in the final report for companion program DE-FC26-05NT42613.